MICROSCOPY AND NANOSCOPY OF ORGANIC SEMICONDUCTORS FOR STRUCTURAL AND ELECTRONIC ANALYSIS

CLEMENS LIEWALD

München 2018

MICROSCOPY AND NANOSCOPY OF ORGANIC SEMICONDUCTORS FOR STRUCTURAL AND ELECTRONIC ANALYSIS

CLEMENS LIEWALD

DISSERTATION

durchgeführt an der Fakultät für Physik
der Ludwig-Maximilians-Universität
München

vorgelegt von
Clemens Liewald
aus Weiden in der Oberpfalz

München, den 09.05.2018

"Die Wahrheit ist dadurch in Frage gestellt, dass sie politisiert wird."

Martin Buber

ZUSAMMENFASSUNG

Die Mikro- und Nanostruktur von organischen Halbleitern beeinflusst entscheidend die Leistung von elektronischen und optoelektronischen Bauelementen. Folglich sind experimentelle Untersuchungen mit geeigneten Mikroskopiemethoden erforderlich. In dieser kumulativen Dissertation präsentiere ich vier zugehörige Forschungsprojekte zur Bestimmung struktureller und elektronischer Eigenschaften von organischen molekularen Halbleitern. Diese Arbeit ist in zwei Teile gegliedert, erstens die Entwicklung und Anwendung neuartiger Mikroskopietechniken, und zweitens die Untersuchung der Photoantwort in Transistoren mit den Halbleitern Pentacen und Epindolidion.

Im ersten Teil werden zwei neuartige Mikroskopiemethoden, die mikrodiffraktive Bildgebung und die elektronische Terahertz Nanoskopie eingeführt. Für mikrodiffraktive Bildgebung werden fokussierte Röntgenstrahlen von der Probe gestreut, mit einer Ortsauflösung von $300\,\mathrm{nm} \times 3\,\mu\mathrm{m}$ bei $0.1\,\mathrm{nm}$ Wellenlänge. Mit dieser Methode untersuchen wir den Polymorphismus von Pentacen und die Kristallinität von Pentacen unter Goldkontakten.

Für die lokale Untersuchung von Ladungsdichten, entwickeln wir das elektronische Terahertz Nanoskop, die Kombination eines Raumtemperatur-Terahertz-Transceivers (Transmitters und Receivers) mit einem Raster-Nahfeldmikroskop (SNOM). Dieser Aufbau liefert Amplituden- und Phasenbilder mit $50\,\mathrm{nm}$ Ortsauflösung bei $0.5\,\mathrm{mm}$ Wellenlänge. Die Bilder einer Siliciumprobe belegen eine Leitfähigkeitsempfindlichkeit für Ladungsdichten bis hinunter zu $10^{16}\,\mathrm{cm}^{-3}$.

Im zweiten Teil wird die Raster-Photostrommikroskopie (SPCM) benutzt, um die elektronische Antwort von Feldeffekttransistoren auf eine lokale optische Stimulation zu untersuchen. Für Pentacen Transistoren demonstrieren wir, dass SPCM den Hauptmechanismus für Spannungsverlust aufzeigt. Dafür wird ein asymmetrischer Transistor untersucht. Je nach Betriebsrichtung zeigt dieser Transistor stark lokalisierte Exziton-Trennung am Quellkontakt, oder inhomogenes Freisetzen von gefangenen Ladungsträgern im Transistorkanal.

Im Gegensatz dazu besteht die Photoantwort von Epindolidion Transistoren aus einem schnellen Verschiebe-Beitrag unter den Kontakten und aus einem langsamen Beitrag durch Fallenentleerung im Transistorkanal. Wir folgern diese Mechanismen aus der Analyse der Photoantwort im Zeit- und Frequenzbereich, und aus dem Betrieb der Proben als Dioden und als Feldeffekttransistoren.

Die hier erzielten Ergebnisse sollten das Verständnis von organischen Halbleitern auf der Mikroskala und Nanoskala verbessern.

ABSTRACT

The micro- and nanostructure of organic molecular semiconductors crucially affects the performance of electronic and optoelectronic devices. Consequently, experimental investigations with suitable microscopy methods are required. In this cumulative dissertation, I present four related research projects for the determination of structural and electronic properties of organic molecular semiconductors. This work is organized in two parts, first, the development and application of novel microscopy methods, and second, the investigation of the photoresponse in field-effect transistors with the semiconductors pentacene and epindolidione.

In the first part, two novel microscopy methods, microdiffraction imaging and all-electronic terahertz nanoscopy are introduced. For microdiffraction imaging, focused X-rays are scattered from the sample, with a spatial resolution of $300\,\mathrm{nm} \times 3\,\mathrm{\mu m}$ at $0.1\,\mathrm{nm}$ wavelength. With this method, we assess the polymorphism of a pentacene thin film and probe the crystallinity of a pentacene film below gold contacts.

For the local charge density probing, we develop the all-electronic terahertz nanoscope, the combination of a room-temperature terahertz transceiver (sender and receiver) with a scanning near-field optical microscope (SNOM). This setup provides amplitude and phase images with $50\,\mathrm{nm}$ spatial resolution at $0.5\,\mathrm{mm}$ wavelength. The images of a silicon sample prove a conductance sensitivity for charge densities down to $10^{16}\,\mathrm{cm}^{-3}$.

In the second part, scanning photocurrent microscopy (SPCM) is used to investigate the electronic response of field-effect transistors on a local optical stimulation. For pentacene transistors, we demonstrate that SPCM highlights the main voltage loss mechanism. Therefore, an asymmetric transistor is investigated. Depending on the operating direction, this transistor shows either strongly localized exciton splitting at the source contact, or inhomogeneous charge de-trapping within the transistor channel.

In contrast, the photoresponse of epindolidione transistors consists of a fast displacement contribution under the contacts and of a slow de-trapping contribution within the transistor channel. We deduce these mechanisms from a photoresponse analysis in the time and frequency domain, and from the operation of the samples as diodes and as field-effect transistors.

The results achieved here should improve the understanding of organic semiconductors on the microscale and nanoscale.

CONTENTS

LIST OF FIGURES

ACRONYMS

2D	two-dimensional
AFM	atomic force microscope
Al	aluminum
Al_2O_3	aluminum oxide
Au	gold
BP	bulk phase
C10-BTBT	$2,7$-didecylbenzothienobenzothiophene
C12-BTBT-C12	didodecyl[1]benzothieno[3,2-b][1]-benzothiophene
CCD	charge-coupled device
COC	cyclic olefin copolymer
DI water	deionized water
Epi	epindolidione
ESRF	European Synchrotron Radiation Facility
F4-TCNQ	tetrafluorotetracyanoquinodimethane
FET	field-effect transistor
GIXS	grazing-indicence X-ray scattering
H_2O_2	hydrogen peroxide
H_2SO_4	sulfuric acid
H_2SO_5	peroxymonosulfuric acid
HeNe	helium-neon
HF	hydrofluoric acid
HOMO	highest occupied molecular orbital
IR	infrared
LUMO	lowest unoccupied molecular orbital
MIS	metal-insulator-semiconductor
MoS_2	molybdenum disulfide

N_2	nitrogen
NEXAFS	near-edge X-ray absorption fine structure
OFET	organic field-effect transistor
OLED	organic light-emitting diode
pH	potential of hydrogen
Pt	platinum
QCL	quantum cascade laser
Si	silicon
Si_3N_4	silicon nitride
SiO_2	silicon dioxide
SPCM	scanning photocurrent microscopy
s-SNOM	scattering-type scanning near-field optical microscopy
STXM	scanning transmission X-ray microscopy
TFP	thin-film phase
TFT	thin-film transistor
THz	terahertz
Ti	titanium
TTC	tetratetracontane
TTL	transistor-transistor logic

MOTIVATION

The digital revolution is driven by the mass production of electronic devices. Mobile computers, like tablets or smartphones, provide permanent information access, at any place and at any time. In addition, more and more analog devices are now equipped with electronics, and can process, store, send, and receive electronic data, like in smart homes or autonomous cars. The basic building blocks of this information technology are semiconducting electronic devices, especially silicon (Si) transistors. In the search for additional applications, novel semiconductors are investigated. Here, materials from organic chemistry, polymers and small molecules, have proven their capabilities, with simpler processing steps saving energy and time. Organic electronics employs these materials in electronic devices like transistors, sensors, solar cells, or light-emitting diodes [1, 2]. Currently, organic light-emitting diodes (OLEDs) are most advanced, building smartphone displays with high contrast and high brightness.

The physical properties of organic semiconductors are extensively described with concepts known from inorganic semiconductors. However, the inherent properties of both material systems need to be considered for finding new applications and designing best-performing devices. The charge mobility of organic semiconductors is lower compared to inorganic semiconductors [3], but the ability to synthesize organic materials in chemical laboratories allows to tailor the mechanical, electronic, and optical properties for novel applications. In this way, flexible and stretchable devices can be used for portable electronics, smart textiles, and medical diagnostics [4, 5]. Wearable and im-
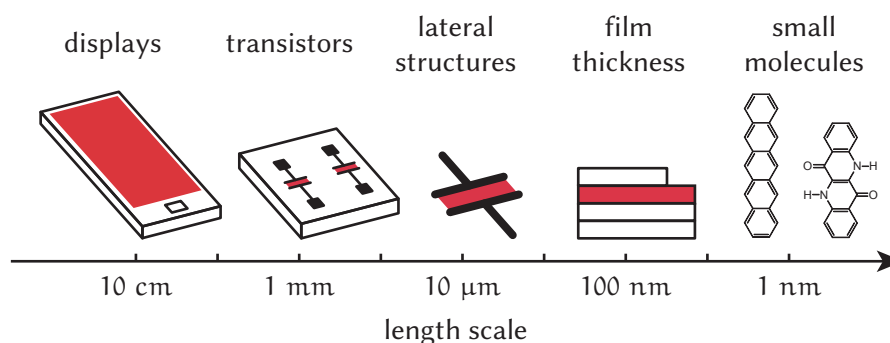
FIGURE 1: IMPORTANT LENGTH SCALES IN ORGANIC ELECTRONIC DEVICES.
The full device dimensions range from >10 cm for displays and solar cells to about 1 mm for individual transistors. Lateral dimensions are typically below 100 μm, while the individual film thickness ranges from several 100 nm down to about 1 nm for single molecules.

plantable devices work as enzyme-based electrochemical biosensors, with a label-free, selective, and sensitive detection [6]. These applications require the materials to be biocompatible, or even biodegradable [5, 7]. The strong interaction of organic materials with light can be used in optoelectronic devices like OLEDs, solar cells, light sensors, or for artificial photosynthesis [8, 9].

Important length scales in organic electronic devices extend over several orders of magnitude, from the centimeter scale down to the nanometer scale. Displays or solar cells reach dimensions of $>10\,\mathrm{cm}$ and require a constant performance over the whole area. Single organic transistors can be easily manufactured in the millimeter scale, with lateral structures $<100\,\mathrm{\mu m}$. Individual layers of such devices are typically $<100\,\mathrm{nm}$ thin, down to single molecule layers of about $1\,\mathrm{nm}$. The intermolecular spacing, which is important for charge transfer between the molecules, is typically also $<1\,\mathrm{nm}$.

To build electronic devices, various fabrication steps are required. Each processing step can influence the overall electronic properties, by changing the film structure across multiple length scales [10]. Most polymers are solution processable, which favors convenient processing steps without the need for high temperatures. However, polymer materials are also prone to impurities, for example from the chemical synthesis. Small molecules can be purified efficiently and can be deposited under vacuum conditions, in a clean and controlled process. Dependent on the substrate modification, organic materials can either show a de-wetting behavior with separated islands, or form closed and smooth films [11]. Individual molecules often build crystalline layers, with crystalline grain sizes from $<100\,\mathrm{nm}$ to $>10\,\mathrm{\mu m}$. The crystals can be very pure or can exhibit imperfections with static and energetic disorder. Furthermore, organic films can show polymorphism, the presence of different crystalline structures within the same film [12]. By incorporating guest molecules in molecular host layers, called molecular doping, the electronic potential near preferred aggregation areas is changed strongly [13, 14]. Finally, the organic layer can be damaged by the evaporation of metal top contacts, which can diffuse into the organic film, assembling to metal nano-clusters [15]. All these structural effects influence the electronic characteristics of the fabricated devices.

To identify performance bottlenecks and to understand the device properties in full detail, the local structural and the local electronic properties need to be understood. Therefore, various microscopy techniques can be used [16], like transmission electron microscopy (TEM) [17, 18], transmission X-ray microscopy (STXM) [17, 19], Kelvin probe force microscopy (KPFM) [20], infrared (IR) scattering-type scanning near-field optical microscopy (s-SNOM) [21, 22], scanning photocurrent microscopy (SPCM) [23–29], and electric-field-induced optical second-harmonic generation (EFISHG) [30, 31]. Novel mi-
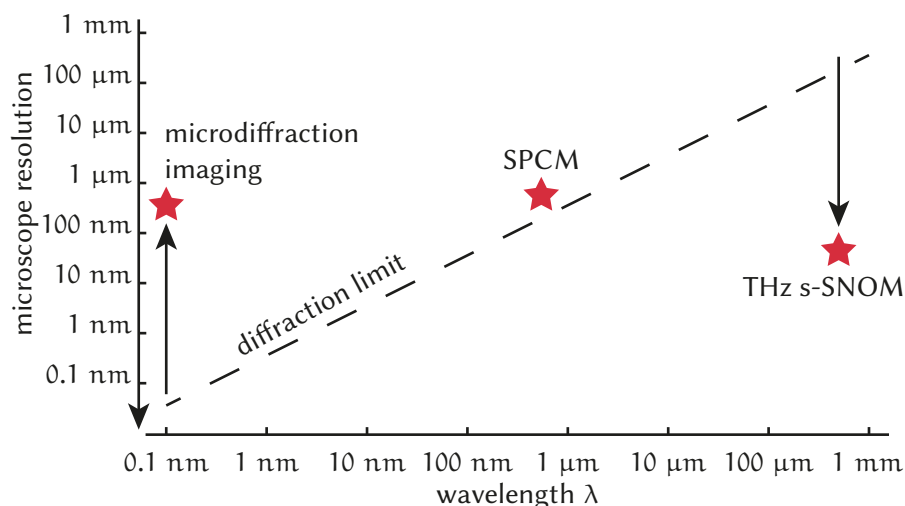
FIGURE 2: OVERVIEW OF THE USED MICROSCOPY METHODS.
In the course of this thesis, three microscopy methods were used: Microdiffraction imaging, using X-rays at 0.1 nm wavelength λ, scanning photocurrent microscopy (SPCM) with visible light at 488 nm and 633 nm, and terahertz (THz) scattering-type scanning near-field optical microscopy (s-SNOM) with a wavelength of 0.5 mm.

croscopy methods, which were successfully used with inorganic semiconductors, need to be tested carefully for organic semiconductors. The inherent softness of the organic materials might hinder a straightforward application.

1.1   THIS WORK

My research was driven by the goal of understanding structural and electronic effects in small molecule thin films and devices through the visualization of microscopic and nanoscopic properties. Accordingly, I pursued a two-fold strategy. One the one hand, novel microscopy techniques were developed and tested with organic samples. Microdiffraction imaging, which had been established for inorganic semiconductors shortly before this work, was demonstrated as a suitable tool for organic semiconductors [32]. All-electronic terahertz (THz) nanoscopy was developed, successfully operated with lowly doped Si [33], and tentatively applied to organic samples. On the other hand, pentacene [34] and epindolidione (Epi) [35] devices were investigated with photocurrent microscopy. For these materials, the different photoresponse mechanisms were determined and clarified. An overview of the used microscopy methods with the respective wavelength and the spatial resolution is shown in Figure 2. In summary, this thesis should help to understand the photoresponse effects in more detail, and should help to extend the toolset of microscopy methods for organic semiconductors. Common principles of the used microscopy methods are emphasized in the following.

Development and application of novel microscopy techniques
Both utilized methods, microdiffraction imaging and terahertz (THz) nanoscopy, employ an optical excitation and the detection of scattered light from the sample. With microdiffraction imaging, using hard X-rays at a wavelength of 0.1 nm, the light is diffracted from the crystalline planes of the measured samples. Here, we investigated the local crystallinity of pentacene thin films [32]. All-electronic THz nanoscopy is a super-resolution microscopy at a wavelength of 0.5 mm, achieving a spatial resolution orders of magnitude below the Abbe diffraction limit. Here, the light is scattered by the near-field interaction of a sharp, metallic tip with the probed sample. THz nanoscopy works purely optical but allows to investigate the local conduction properties of charge carriers at low densities. We demonstrated this sensitivity for a doped Si sample [33]. The desired near-field signal is separated from the large background by a periodic signal modulation a given frequency, and a demodulation of the measured light at the same frequency.

Photocurrent microscopy (SPCM) of organic field-effect transistors
With the SPCM measurements, the understanding of the electronic device response on illumination should be deepened. Here, the sample is excited optically, but analyzed electronically. The illumination is also modulated at a specific frequency, which allows separating the photoresponse from the background via frequency demodulation, similar to the s-SNOM. By analyzing the SPCM maps and transistor curves, we concluded that SPCM highlights the dominant voltage loss mechanism in pentacene field-effect transistors (FETs), either from contact resistance or from charge de-trapping [34]. For Epi FETs, we could separate the influence and photoresponse position of electrons and holes. The Epi FETs showed two kinds of photoresponse, a displacement current under the contacts and an enhanced conduction due to de-trapping in the transistor channel [35].

The following chapters provide a detailed introduction to my conducted research. Important concepts of semiconductors and small molecule semiconductors are described in chapters 2 and 3. Basic principles and results of microdiffraction imaging and THz nanoscopy are summarized in chapters 4 and 5. An introduction to SPCM and a summary of the results on pentacene and Epi FETs is provided in chapters 6 and 7. Furthermore, I discuss insights and considerations beyond the associated publications in the respective chapters. Finally, future prospects are outlined in chapter 8.

The results, which were published during this work, are attached as full articles in appendix A, with the supplementary material in appendix B. Detailed descriptions of the sample fabrication and the SPCM setup are provided in appendices C and D, respectively.

ELECTRONIC PROPERTIES OF SEMICONDUCTORS

Semiconductors are characterized as solid-state materials with the conductivity between conductors and insulators. This chapter provides an introduction to the basic concepts of semiconductors and the application in field-effect transistors (FETs), following the textbook of Simon M. Sze [36]. In semiconducting materials, electrons can occupy specific energy ranges, which are described by the electronic band structure. The closest bands to the Fermi level are called the valence band and conduction band. These bands are separated by the band gap, which cannot be occupied. The electrons, which partially fill the conduction band with an electron density n, can move around freely and respond to electric or magnetic forces. An almost completely filled valence band can be described by the concept of holes, positively charged particles with a hole density p and similar behaviors as electrons. For intrinsic semiconductors at finite temperatures, electrons are continuously excited from the valence to the conduction band, leaving holes in the conduction band. In thermal equilibrium, the charge carrier concentrations satisfy the relationship

$$pn = n_i^2 \ ,$$

where n_i is the intrinsic carrier concentration. The conductivity of a semiconductor can be varied by inducing impurities to the material, either electron donors or electron acceptors. Semiconductors with donors are named n-type, and semiconductors with acceptors are named p-type. The charge carriers with higher concentration are called majority carriers, the charge carriers with lower concentration are called minority carriers. For a p-type semiconductor, holes are the majority carriers and electrons are the minority carriers.

In an electric field E, the charge carriers drift along the field and contribute to a total current density j. This current density is the sum of the electron and hole current density in opposite directions,

$$j = j_n + j_p = \sigma E = (en\mu_n + ep\mu_p)E \ ,$$

with the conductivity σ, the elementary charge e, the electron mobility μ_n, and the hole mobility μ_p. An electron holds the charge $-e$, and a hole the charge e.

If there is a spatial variation of charge concentration in the semiconductor, a diffusion current can occur. The charges are moving from a region of high concentration to a region of low concentration. For

electrons in a one-dimensional gradient along the distance x, the drift current density is

$$j_n = eD_n \frac{dn}{dx} \quad ,$$

with the diffusivity D_n. The diffusivity is related to the mobility by the Einstein relation

$$D_n = \frac{kT}{e} \mu_n \quad ,$$

via the Boltzmann constant k, the temperature T, and the elementary charge e.

When an electrical field and a concentration gradient are present at the same time, both current contributions are flowing. Consequently, the current density equations for electrons and holes read as

$$j_n = en\mu_n E + eD_n \frac{dn}{dx} \quad , \qquad j_p = ep\mu_p E - eD_p \frac{dp}{dx} \quad .$$

If additional charge carriers are injected in the semiconducting material, $pn > n_i{}^2$, a non-equilibrium condition is present. These charge carriers are called excess carriers and can, for example, be injected by biasing or optical excitation. The optical excitation, creating an electron in the conduction band and a hole in the valence band, increases the electron and hole concentrations by the same amount. The non-equilibrium condition tends to relax to the equilibrium condition via charge recombination of electrons and holes. This recombination can be radiative, emitting a photon, or non-radiative, dissipating heat to the material.

For a direct band gap material, the thermal band-to-band generation rate G_{th} and recombination rate R_{th} describe the equilibrium charge densities for electrons n_{no} and hole p_{no}. When illuminating the semiconductor, an additional generation rate G_L is introduced. For a low optical injection in a p-type semiconductor, the lifetime of the excess minority electrons is described by the proportionality constant β and the equilibrium hole density,

$$\tau_n \equiv \frac{1}{\beta p_{no}} \quad .$$

In indirect band gap semiconductors, this direct recombination rate is very low because of the nonzero momentum difference between the electrons and holes. Instead, the recombination is mediated by localized energy states in the band gap. These energy states can act as generation and recombination states for electrons and holes, with the density N_t. The lifetime for excess minority electrons in a p-type

semiconductor, with low optical injection, and recombination centers in the middle of the band gap can be approximated as

$$\tau_n \equiv \frac{1}{v_{th}\sigma_n N_t} \quad,$$

with the thermal velocity of charge carriers v_{th}, and the capture cross section for electrons σ_n.

When all previous described effects, drift, diffusion, generation, and recombination occur at the same time in a semiconductor, the continuity equation for the density change over time t can be derived for electrons and holes,

$$\frac{\partial n}{\partial t} = \frac{1}{e}\frac{\partial j_n}{\partial x} + (G_n - R_n) \quad, \qquad \frac{\partial p}{\partial t} = -\frac{1}{e}\frac{\partial j_p}{\partial x} + (G_p - R_p) \quad.$$

Additionally, the electric field E is dependent on the semiconductor dielectric permittivity ε and the space charge density ρ via Poisson's equation,

$$\frac{dE}{dx} = \frac{\rho}{\varepsilon} \quad.$$

The space charge density is the algebraic sum of all negative and positive charge densities. In summary, the continuity equations together with Poisson's equation describe the most relevant effects, for charge transport in semiconductors.

2.1 FIELD-EFFECT TRANSISTORS

The investigated samples featured field-effect transistor (FET) geometries. FETs are three-terminal devices, in which the electrical response is controlled by an electrical field [36]. Organic FETs (OFETs) are usually fabricated as thin-film transistors (TFTs), by depositing and modifying several layers with a typical layer thickness below 100 nm. A schematic of an organic field-effect transistor (OFET) with top-contacts and a bottom-gate is shown in Figure 3. The semiconducting device channel between the source electrode and the drain electrode is separated from the gate electrode by an insulating, dielectric layer. The transistor current between source and drain depends strongly on the applied gate voltage. If the gate electric field accumulates charges at the semiconductor/dielectric interface, a current is flowing, and the transistor is switched on. If the channel is depleted from charge carriers, no current is flowing, and the transistor is switched off.

Different operating regimes can be distinguished in a FET, namely the subthreshold, the saturation, and the linear regime. In the subthreshold regime, the charge layer starts to be accumulated and the
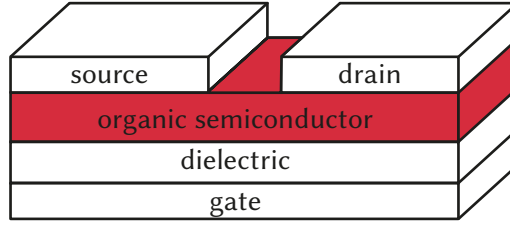
FIGURE 3: SCHEMATIC OF A TOP-CONTACT OFET.
The bottom-gate contact controls the current between the source and the drain, through the organic semiconductor.
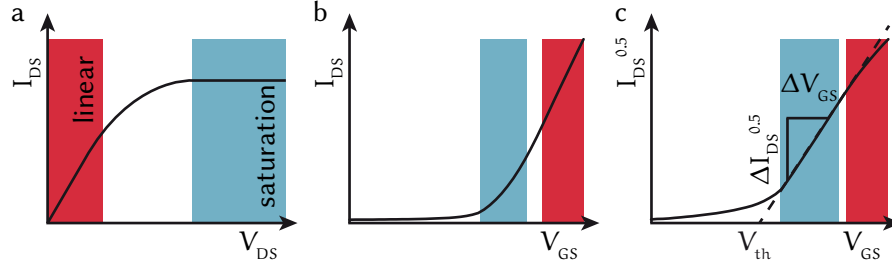
FIGURE 4: SCHEMATIC DEVICE CHARACTERISTICS OF A THIN-FILM TRANSISTOR.
a) Output curve I_{DS} vs. V_{DS}. b) Transfer curve I_{DS} vs. V_{GS}. c) Transfer curve $I_{DS}^{0.5}$ vs. V_{GS} for extracting the mobility and the threshold voltage.

current rises exponentially with the gate potential. In the saturation regime, the charge layer is accumulated, but not over the whole transistor channel. Near the drain contact, all charge carriers are collected by the drain, leading to a space charge transport in this region. The transistor current I_{DS} in the saturation regime is given by

$$I_{DS} = \frac{W}{2L} \mu C_i (V_{GS} - V_{th})^2 \ ,$$

with the channel width W, the channel length L, the mobility μ, the capacitance per area C_i, the gate voltage V_{GS}, and the threshold voltage V_{th} of the transistor. Finally, in the linear regime, the charge layer is accumulated over the whole transistor channel. Here, I_{DS} is proportional to the applied drain voltage V_{DS}.

To operate FETs at low voltages with high current, a high mobility μ and a low threshold voltage V_{th} is desired. The mobility μ of the transistor can be extracted from measuring the slope $\Delta I_{DS}^{0.5}/\Delta V_{GS}$, as shown in Figure 4c. This mobility is not the intrinsic mobility of the semiconductor but the mobility of the whole device. Therefore, it can depend on various parameters, such as the contact resistance between the top contacts and the semiconductor, or the interface quality to the dielectric layer. Often, the contact resistance is gate-dependent, changing the estimated mobility by one magnitude or more [37].

SMALL MOLECULE ORGANIC SEMICONDUCTORS

Small molecule organic semiconductors typically contain aromatic compounds with delocalized π-electrons. The π-electrons are shared between the atoms of the aromatic compound, which can even extend over the whole molecule. In aggregated solids, the π-electrons can also be exchanged between neighboring molecules, making the solid a (semi)conductor. The π-electrons fill the molecular orbitals up to the highest occupied molecular orbital (HOMO). The next, empty molecular orbital is called the lowest unoccupied molecular orbital (LUMO), which is separated from the HOMO by an energy gap. The molecules can aggregate to molecular crystals, forming large single crystals, or polycrystalline thin films. In the solid-state form, the energy levels for charge transport are also referred as HOMO and LUMO.

Charge transport in molecular semiconductors occurs within the range of two limiting boundaries, namely band-like transport and hopping transport. The band-like regime features a delocalization of the charges over several molecules, whereas, in the hopping regime, the charges are localized on single molecules. Charge transport in organic devices is often dominated by trap states for the charge carriers, meaning that the charges get localized on specific positions. Further descriptions about the principles of organic electronics can be found in the in the textbooks of Martin Pope & Charles E. Swenberg [1], and of Markus Schwoerer & Hans C. Wolf [2].

3.1 PIGMENT SEMICONDUCTORS

A variety of molecules can be used as organic semiconductors. Traditionally, these molecules form van der Waals crystals, driven by the search for large π-electron systems. One drawback of the weak van der Waals forces is the low stability against environmental influences, which can cause device degradation. Higher stability was shown for pigment molecules, an emerging class of molecular semiconductors. These pigment molecules feature polar groups, which form the stronger hydrogen bonds to neighboring molecules. Therefore, on the one hand, the π-electron systems of individual pigment molecules are smaller; but, on the other hand, the molecules can be packed more tightly, due to the higher intermolecular forces. This tighter molecular packing enhances the charge transfer between the neighboring molecules, which is needed for good semiconductors. For the interested reader, a broader overview of the field of pigment

semiconductors is provided in the reviews of Eric D. Głowacki et al. [38], and of Marcel Gsänger et al. [39].

3.2 PHOTOGENERATION OF CHARGE CARRIERS

Organic materials, especially pigments, feature a strong light absorption. Upon illumination, an absorbed photon forms an electron-hole pair (exciton), that is bound by the Coulomb attraction potential

$$V = \frac{e^2}{4\pi\varepsilon\varepsilon_0 r} \quad,$$

with the electron charge e, the relative permittivity ε, the vacuum permittivity ε_0, and the electron-hole distance r. The Coulomb potential of organic materials is typically in the order of a few $100\,\mathrm{meV}$, caused by the low permittivity ($\varepsilon = 2 - 4$). With the thermal energy of $25.7\,\mathrm{meV}$ at $25\,^\circ\mathrm{C}$ room temperature, the excitons do not dissociate spontaneously, like in inorganic materials ($\varepsilon = 11.7$ in Si). For the charge separation, an additional driving force is needed, like excess energy, a local electrostatic environment, or an applied electric field. A prevalent method to increase the yield of charge separation is the introduction of donor-acceptor heterojunctions in the organic devices.

This sensitivity of organic semiconductors to illumination is employed in solar cells, FETs, and photodiodes. Organic phototransistors are commonly described by two different effects, the photovoltaic and the photoconductive effect. The photovoltaic effect features exciton splitting with charge separation. In contrast, the photoconductive effect comprises an enhanced conduction from secondary processes like contact-resistance lowering or charge detrapping. This model has been derived for inorganic transistors [40, 41] and applied for organic phototransistors [42], but the overall description is not entirely reliable [43]. The optoelectronic phenomena of organic semiconductors and devices surely are material-dependent and require an experimental investigation and verification. For further detailed descriptions of organic optoelectronic materials, the curious reader is referred to the reviews of Oksana Ostroverkhova [8], and of Kang-Jun Baeg et al. [42].

3.3 PENTACENE

Pentacene ($C_{22}H_{14}$) is one of the best characterized organic semiconductors, showing high charge mobilities $\mu = 2\,\mathrm{cm^2\,V^{-1}\,s^{-1}}$ to $5\,\mathrm{cm^2\,V^{-1}\,s^{-1}}$ [44, 45]. The molecules consist of five benzene rings, fused to a linear molecule from the class of polyacenes. Individual molecules form van der Waals crystals in a herringbone structure and can assemble in four different crystal polymorphs [46]. Two of these
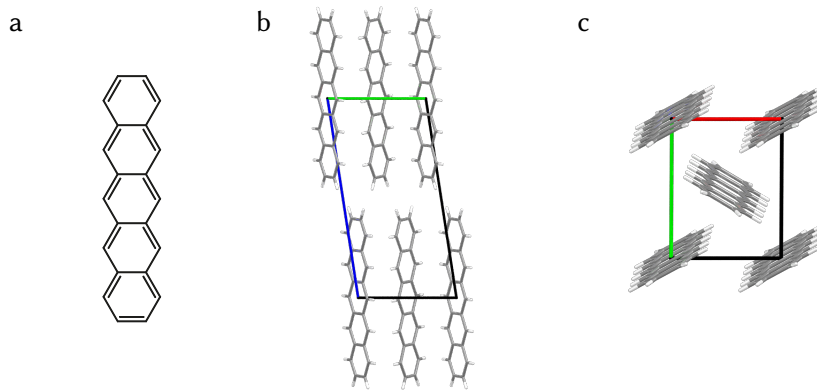
FIGURE 5: STRUCTURE OF PENTACENE.
a) Structural formula of pentacene, consisting of five benzene rings. b) View along the a-axis of the thin-film phase (TFP) unit cell. c) View along the c-axis of the TFP unit cell, showing the herringbone structure.

polymorphs occur in electronic thin film devices, the Campbell or bulk phase (BP) [47, 48], and the thin-film phase (TFP) [49]. The thin-film phase is substrate induced during growth and can undergo a phase transition into the thermodynamically stable bulk phase. Note that the name convention for the lattice parameters of pentacene unit cells has changed since the original publications of R. B. Campbell et al. [50]. The unit cell of TFP pentacene is shown in Figure 5, created with the software *Mercury* [51]. Pentacene thin films are prepared in high vacuum conditions via molecular beam deposition. On hydrophobic substrates, the pentacene molecules stand upright and form molecular layers with a layer spacing of 15.4 Å (TFP) and 14.4 Å (BP). BP pentacene can grow in small crystallites within the surrounding TFP pentacene. These crystallites appear as perpendicular ellipsoids with a length up to several microns, as shown by IR s-SNOM [22]. This study was mainly conducted by Christian Westermeier, the results are shown in appendices A.8 and B.6. Upon illumination of a pentacene film, singlet excitons are generated, undergoing an ultrafast fission into triplet excitons [52, 53]. These triplet excitons are tightly bound, can react with trapped charges, or decay radiationless. The photocurrent effects of pentacene devices are summarized in the review of Amrita Masurkar & Ioannis Kymissis [24].

3.4 EPINDOLIDIONE

Epindolidione (Epi) is a pigment semiconductor, typically used by the coloring industry as a yellow colorant. The semiconducting properties of Epi were pioneered by Eric D. Głowacki, showing a charge mobility up to $1.5\,cm^2\,V^{-1}\,s^{-1}$ [54, 55]. Neighboring Epi molecules form hydrogen bonds, adding up to long molecular chains. These chains are stacked to a brick-wall crystal structure with small intermolecular distances, favoring charge transfer between adjacent chains [55,

a   b   c
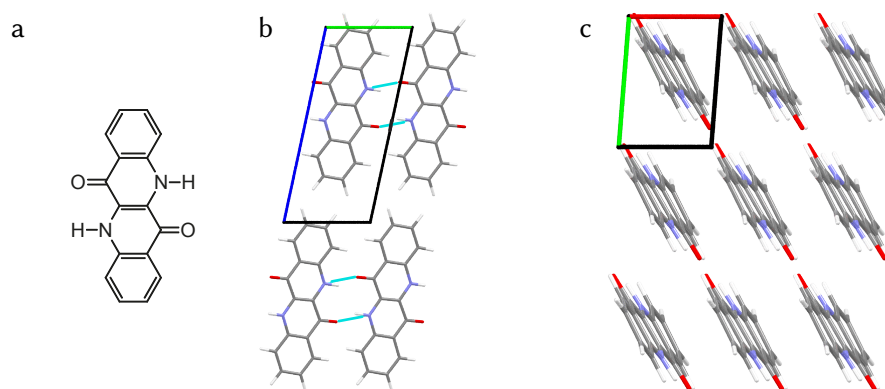
FIGURE 6: STRUCTURE OF EPINDOLIDIONE (EPI).
a) Structural formula of Epi. b) View along the a-axis of the unit cell, with hydrogen bonds between the neighboring molecules, indicated as cyan lines. c) View along the c-axis of the unit cell, showing the brick-wall structure.

56]. The crystal structure of Epi is shown in Figure 6, calculated with the software *Mercury* [51]. The relative permittivity of Epi is currently not determined. Like pentacene thin films, Epi thin films are produced with molecular beam deposition. A key advantage of Epi is its outstanding chemical stability. The devices can be operated in aqueous buffer solutions from pH 3 to pH 10 [55], can catalyze water into hydrogen peroxide (H_2O_2) [57], and can be functionalized with proteins [58].

MICRODIFFRACTION IMAGING

Part of the findings presented in this chapter have been published [32]. The full article can be found in appendix A.1.

X-ray diffraction measures the periodic distances of atomic or molecular crystals in the reciprocal space [59]. The development of modern X-ray synchrotron beamlines leads to higher photon flux, smaller beam diameters, and advanced data handling. At the beamline ID01 of the European Synchrotron Radiation Facility (ESRF), an optimized method of scanning X-ray microscopy has been developed shortly before this work [60]. For this method, the X-ray beam is focused by a Fresnel zone plate to a sub-μm spot, the sample and the X-ray detector are set to a Bragg position of the investigated crystalline material:

$$n\lambda = 2d\sin(\theta) \ ,$$

with $n \in \mathbb{N}$, λ the wavelength, d the lattice spacing, and θ the angle between the lattice plane and the incoming beam. The momentum transfer q can be calculated with

$$q = \frac{4\pi}{\lambda}\sin(\theta) \ .$$

Now, the sample is scanned over the beam, recording a two-dimensional (2D) map of the Bragg intensities.

During beamtime at ID01, we have successfully imaged a polymorphic pentacene sample with BP and TFP pentacene at the different BP
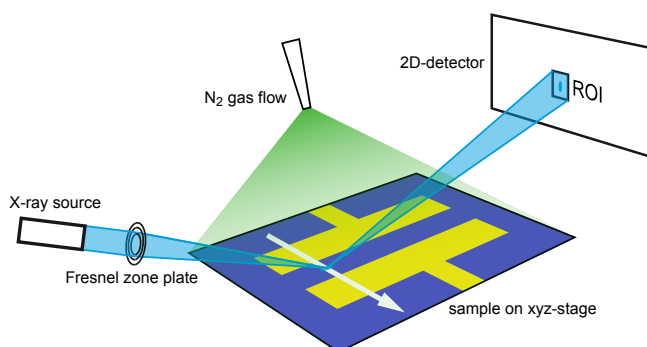
Figure 7: Schematic of microdiffraction imaging.
The X-ray beam is focused with a Fresnel zone plate on the sample. The scattered X-rays are recorded by a two dimensional detector. To avoid beam damage, the sample is blowed with dry N_2. For imaging, the sample is scanned with respect to the X-ray beam. Reprinted from [32].
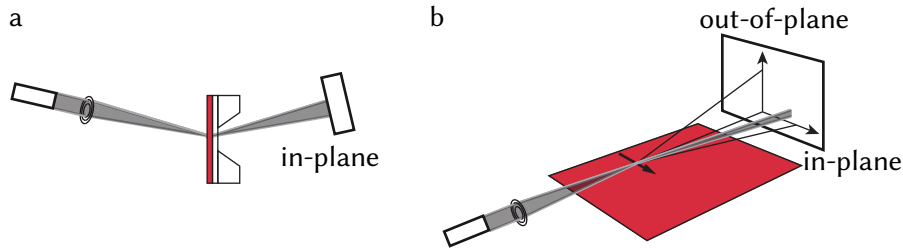
FIGURE 8: SCHEMATIC OF X-RAY SCATTERING TECHNIQUES FOR IN-PLANE ANALYSIS. a) Transmission X-ray scattering. b) Grazing-incidence X-ray scattering (GIXS).

and TFP Bragg positions, respectively. The 2D maps, recorded at the same sample area show a mutually exclusive BP and TFP distribution. The longer lattice distances, compared to inorganic semiconductors, require lower scattering angles and lead therefore to a larger beam footprint, and a lower spatial resolution. Furthermore, a pentacene transistor was measured with a microdiffraction line scan, showing that the crystal structure of the pentacene under the gold (Au) top contacts was not damaged by the Au layer. The findings are presented in appendix A.1.

4.1   AZIMUTHAL ANALYSIS OF POLYCRYSTALLINE PENTACENE

When pentacene is deposited on a heated Si substrate, a polymorphism of BP and TFP pentacene can develop. The amount of BP pentacene even grows over time, often in the shape of approximately perpendicular ellipsoids within the surrounding TFP pentacene matrix [22]. While IR s-SNOM identifies the local crystal structure of pentacene, it cannot determine the azimuthal (in-plane) orientation of the pentacene crystallites. This additional information can be provided by scattered hard X-rays. A possible technique is the transmission geometry, shown in Figure 8a, where the focused X-rays hit the sample almost perpendicular. The scattered X-rays, with a momentum transfer parallel to the sample plane, are detected behind the sample. To avoid absorption of the Si substrate, 15 nm pentacene was evaporated on a free-standing, 50 nm thin silicon nitride (Si_3N_4) membrane. For a successful measurement, the sample needs to be in the center of rotation, while standing upright on the sample holder. These geometrical requirements could not be met during our beam time at ID01 so that no successful measurement was recorded.

Another method to determine the azimuthal crystalline orientation is grazing-indicence X-ray scattering (GIXS) [61]. Here, the incoming X-ray beam hits the sample at a small angle, almost parallel to the substrate surface, and undergoes total reflection, as shown in Figure 8b. For macroscopic X-ray beams, this method is restricted to single crystals because all orientations of polycrystalline samples are present
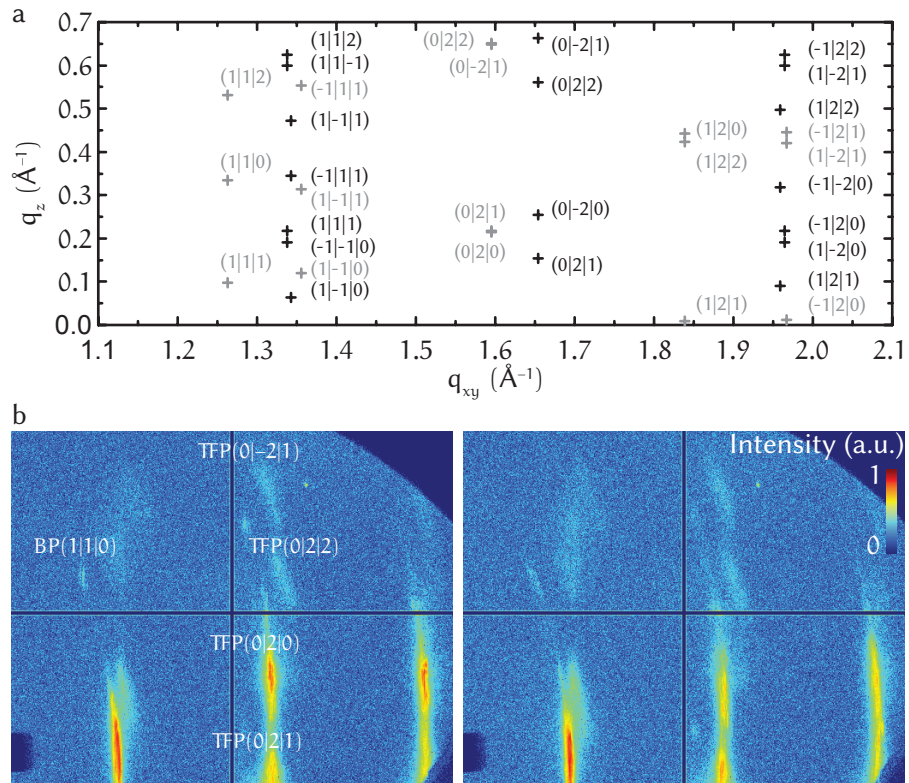
FIGURE 9: MICROFOCUSED GIXS OF POLYMORPHIC PENTACENE.
a) Calculated diffraction indices for thin-film phase (TFP) pentacene (black) and bulk phase (BP) pentacene (gray). b) Microfocused grazing-indicence X-ray scattering (GIXS) detector images at different sample positions of a 15 nm thin pentacene film, showing scattering intensity variations of the diffraction peaks. The two images were representatively chosen from a spatial line scan.

in the beam. With a micro- or nanofocused beam, the X-rays are scattered only from a small area of the sample with a reduced number of crystalline orientations. The Bragg conditions of the scattered X-ray beam contain an in-plane component q_{xy}, and an out-of-plane component q_z. The calculated diffraction indices for BP and TFP pentacene, generated with the software package *simDiffraction* [62], are shown in Figure 9a. The GIXS measurements were recorded with an incident beam angle of 0.1°, corresponding to a beam footprint of $200\,\mu m \times 350\,nm$ on the sample. As the grain size of the pentacene film was about $2\,\mu m^2$, and therefore, the X-ray beam was scattered from a limited number of grains. The sample was moved perpendicular to the beam path and a line scan of GIXS maps was recorded. The two representative GIXS maps in Figure 9b show a varying scattering intensity for different diffraction peaks, indicating a change in the grain rotation. As the measured pentacene film was only $15\,nm$ thin, the diffraction features were broadened perpendicular to the substrate [59]. Therefore, composite diffraction features were formed from the individual scattering peaks, and the azimuthal orientation of BP pentacene within TFP pentacene could not be determined.

In-plane information can also be gathered from scanning transmission X-ray microscopy (STXM) and near-edge X-ray absorption fine structure (NEXAFS), using focused soft X-rays, that excite electronic transitions from an atomic core level. With a focus size in the order of $20\,nm$, the spatial resolution of these methods is comparable to the spatial resolution of an s-SNOM. The X-ray absorption can be tuned to be sensitive to the film thickness or to the azimuthal rotation, and, therefore, can determine the orientation of individual pentacene grains [63, 64]. In the course of this thesis, we investigated polymorphic pentacene in a combined study with IR s-SNOM, STXM, and NEXAFS. With IR s-SNOM, I determined the position of the BP ellipsoids of $15\,nm$ pentacene on a free-standing Si_3N_4 membrane. The STXM and NEXAFS at the same sample positions measurements were performed by Xiaoyan Du, FAU Erlangen-Nürnberg. We could determine that the BP ellipsoids hold the same azimuthal orientation as the surrounding TFP matrix. However, the growth direction of the ellipsoids could not be fully identified. The results of this study can be found in the dissertation of Xiaoyan Du [65].

TERAHERTZ NANOSCOPY

Part of the findings presented in this chapter have been published [33]. The full article can be found in appendix A.2 and the supplementary material in appendix B.1.

Scattering-type scanning near-field optical microscopy (s-SNOM) allows bypassing the Abbe diffraction limit by focusing light on the small metallic tip of an atomic force microscope (AFM) [21]. At the tip apex, the light is strongly enhanced, and interacts with the probed sample, if the tip is near the sample. The lateral resolution of an s-SNOM is determined by the size of the tip apex, typically below $50\,\mathrm{nm}$. The near-field interaction can be qualitatively described by a point dipole at the tip apex, which induces a mirror dipole in the sample, scattering light with the amplitude s and the phase φ as

$$se^{i\varphi} \propto \frac{\alpha}{1 - \frac{\alpha\beta}{16\pi(a+z)^3}} \quad .$$

Here, α is the point-dipole polarizability of the tip, $\beta = (\varepsilon-1)/(\varepsilon+1)$ is the response function of the sample, and z is the distance between the tip and the sample surface. This point-dipole model was extended to a finite-dipole model, for a quantitative prediction of the material contrasts [66]. By oscillating the tip at the frequency Ω, corresponding to tapping mode AFM, the near-field interaction is periodically switched on and off. Therefore, the near-field signal can be separated from the large background a signal demodulation at harmonics of the tip frequency $n\Omega$. Thus, near-field microscopy allows determining the local permittivity of the probed material in a small area under the metallic tip.

An important application of s-SNOM is the near-field conductivity mapping of semiconductors. As in far-field spectroscopy, the collective motion of charge carriers is excited and analyzed optically. By measuring and analyzing the optical spectra, electronic properties, such as the charge density and charge mobility can be extracted. For a broader introduction to s-SNOM conductivity measurements, the interested reader is directed to the review of Fritz Keilmann et al. [67], and of Mengkun Liu et al. [68].

Semiconductors with a low charge density can be assessed with light at frequencies f around $1\,\mathrm{THz}$ ($\lambda = 0.3\,\mathrm{mm}$). In this region, sufficiently fast and sensitive detectors with a high dynamic ratio are still under development. During the course of this work, we coupled two emerging methods of THz light detection to an s-SNOM.
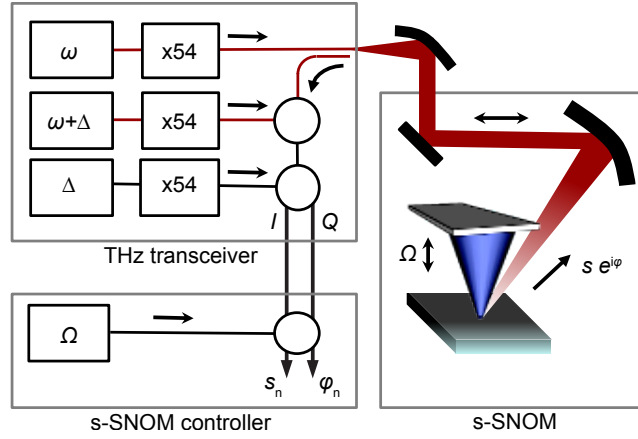
FIGURE 10: SCHEMATIC OF ALL-ELECTRONIC TERAHERTZ NEAR-FIELD MICROSCOPY.
The emitted light from the THz transceiver is focused with a parabolic mirror on
the oscillating tip in the s-SNOM, and the back-scattered light is guided on the
same optical path back into the THz transceiver. In the transceiver, the light is
electronically detected and mixed to two quadrature signal outputs with a 90° phase
shift, I and Q. These signals are demodulated at the harmonic frequencies $n\Omega$ of
the tip frequency Ω, and the scattered near-field amplitude s_n and phase φ_n are
calculated from the quadrature signals. Reprinted from [33].

First, laser self-detection of a liquid helium cooled quantum cascade
laser (QCL), where the signal is measured as voltage fluctuations of
the laser driving voltage [69, 70]. The results of this work are shown
in appendix A.6. Second, an all-electronic detection with a room
temperature transceiver (transmitter and receiver), that generates and
measures the THz radiation electronically. As the characteristic prop-
erty of both methods, the scattered light is guided back into the light
source, on the same optical path as the emitted light. Thus, the experi-
mental setup can be very compact, omitting, for example, an external
beam splitter.

With the all-electronic terahertz (THz) nanoscopy, we demonstrated
background-free amplitude and phase images of Si at 0.6 THz, equiva-
lent to $\lambda = 0.5\,\mathrm{mm}$ wavelength. The Si sample contained well-defined
nanosctructures in topography and doping density. One area of inter-
est was a p-n transition from a region, doped at an electron density
$n_e \approx 2 \times 10^{17}\,\mathrm{cm}^{-3}$, to a substrate region with a hole density $n_h =
2 \times 10^{16}\,\mathrm{cm}^{-3}$. By measuring this p-n transition and calculating the
corresponding near-field spectra, we could prove a lateral resolution
of $50\,\mathrm{nm} = 10^{-4}\lambda$. The results of our measurements are shown in
appendix A.2.

In addition to the experiments, we could confirm the measured
near-field contrasts by calculations, described in the following para-
graph. Under illumination, the free charges follow the oscillation
of the incoming electromagnetic field, for frequencies ω up to the
so-called plasma frequency ω_p. Semiconductors appear metallic for
frequencies below ω_p and transparent for higher frequencies. This
behavior is described by the Drude model
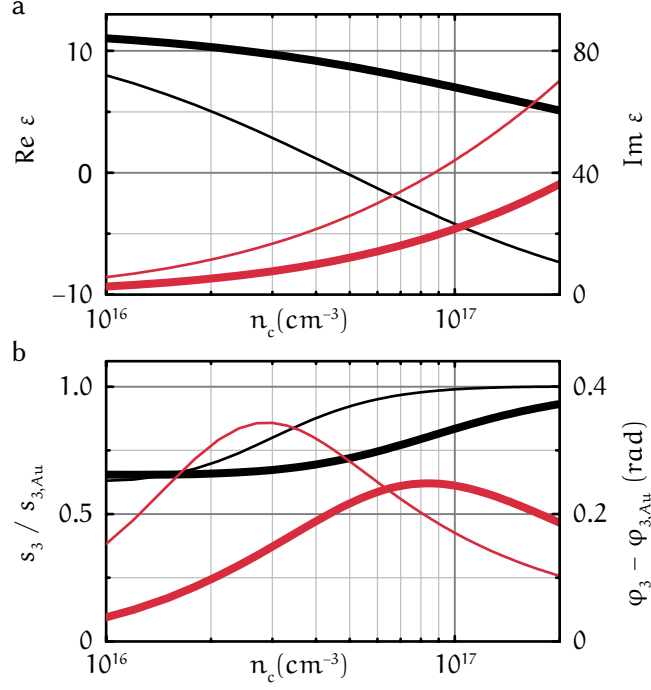
FIGURE 11: CALCULATED PERMITTIVITY AND NEAR-FIELD RESPONSE OF SI AT 0.6 THz.
a) Real part Re ε (black) and imaginary part Im ε (red) of the Si permittivity. b)
Scattering amplitude s_3 (black) and phase φ_3 (red), normalized to Au. The calcula-
tions were performed for electrons (thin curves) and holes (thick curves). Adapted
from [33].

$$\varepsilon = \varepsilon_\infty - \frac{\omega_p^2}{\omega(\omega + i\tau^{-1})} \quad,$$

with the high-frequency permittivity of the material ε_∞, and the
mean free time between charge collisions τ. The plasma frequency
strongly depends on the charge carrier density and ranges from the
infrared region for highly conducting semiconductors to the THz re-
gion for lowly conducting semiconductors [67]. With $\omega_p = \sqrt{\frac{ne^2}{\varepsilon_0 m}}$,
and $\tau = \frac{m\mu}{e}$, the permittivity can be written as

$$\varepsilon = \varepsilon_\infty - \frac{\frac{ne^2}{\varepsilon_0 m}}{\omega(\omega + i\frac{e}{m\mu})} \quad.$$

Here, n is the charge density, e the elementary charge, ε_0 the
vacuum permittivity, m the effective charge carrier mass, and μ the
charge mobility. Note that the mobility μ is often dependent on the
charge density n [71–73]. The calculated real part Re ε and imagi-
nary part Im ε of the permittivity for p-doped and n-doped Si are
shown in Figure 11a. For this calculation, the frequency was set to
0.6 THz ($\omega = 20\,\text{cm}^{-1}$), and literature values for the mass and density-
dependent mobility of electrons and holes were used [71, 74]. The

shift between the p-doped and n-doped resonance can be mostly attributed to the lower mobility of holes compared to electrons in the low density regime. Using this permittivity, the near-field response was calculated with the finite dipole model (effective tip length of $600\,\mathrm{nm}$, tip radius of $50\,\mathrm{nm}$, illumination angle of $60°$) [21, 66]. Normalized to Au, the third harmonic scattering amplitude $s_3/s_{3,\mathrm{Au}}$ and scattering phase $\varphi_3 - \varphi_{3,\mathrm{Au}}$ are shown in Figure 11b.

5.1 APPLICABILITY TO ORGANIC SEMICONDUCTORS

THz spectroscopy of organic semiconductors allows measuring intrinsic properties of the investigated materials because the excited charge carriers oscillate on the nanometer scale. Thin films of small molecule organic semiconductors typically grow in a polycrystalline structure, with crystalline grain sizes up to several microns [22, 54]. Therefore, most charge carriers are not affected by the grain boundaries. The analysis of THz spectra provides insight about the electronic properties in organic materials, characterizing band transport and charge trapping of optically or electrically injected charge carriers [75–79]. Characteristic values for didodecyl[1]benzothieno[3,2-b][1]-benzothiophene (C12-BTBT-C12), $\mu = 9.3\,\mathrm{cm^2 V^{-1} s^{-1}}$, $m = 2m_e$ were extracted by Arend et al. [79], assuming a background permittivity $\varepsilon_\infty = 3.5$ [80].

With these values, the permittivity and near-field response can be calculated, as shown in Figure 12. Here, the mobility was treated as a constant but should be considered density-dependent in more precise calculations. The calculation shows the Drude resonance for charge densities in the range of $10^{17}\,\mathrm{cm^{-3}}$ to $10^{19}\,\mathrm{cm^{-3}}$. Compared to Si, these densities are higher, which can be assumed as a general trend of organic semiconductors, owed to the lower mobility and higher charge mass. These calculated charge densities can be accumulated in FETs, achieving a sheet density $n_{2\mathrm{D}} = 10^{12}\,\mathrm{cm^{-2}}$ in the approximately $1\,\mathrm{nm}$ thin accumulation layer [79], yielding a charge density of $10^{19}\,\mathrm{cm^{-3}}$ in the accumulation layer. However, the $50\,\mathrm{nm}$ probing depth of the s-SNOM [81] would reduce the near-field signal drastically if it came from the $1\,\mathrm{nm}$ thin charge sheet. Another method of adjusting charge densities in organic semiconductors is chemical or molecular doping, which can induce densities of $>10^{20}\,\mathrm{cm^{-3}}$ throughout the molecular film [13]. Thus, in principle, organic semiconductors hold the required properties for a THz s-SNOM analysis.

As a first experimental test, the organic semiconductor 2,7-didecyl-benzothienobenzothiophene (C10-BTBT), doped with tetrafluorotetracyanoquinodimethane (F4-TCNQ), was investigated. Upon doping with F4-TCNQ, dimers of C10-BTBT and F4-TCNQ are formed [82]. The samples were kindly supplied by the group of Norbert Koch, HU Berlin. The local electronic distribution of the doping should be
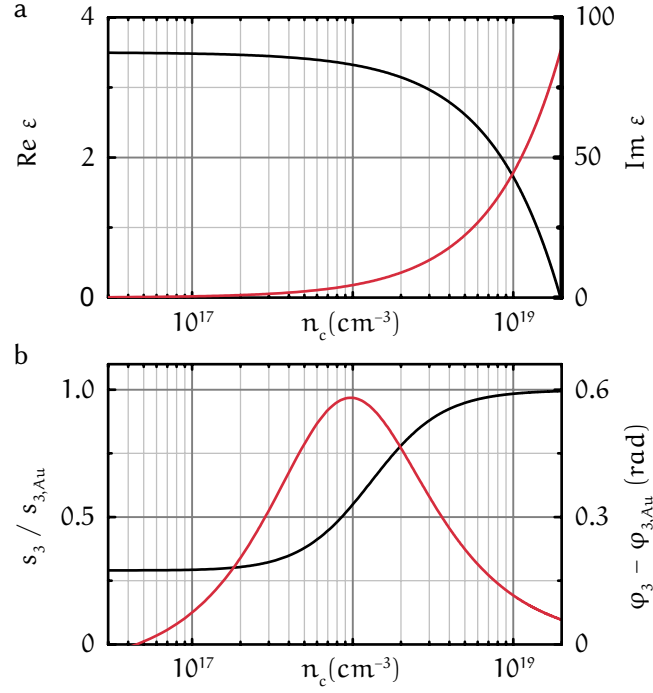
FIGURE 12: CALCULATED PERMITTIVITY AND NEAR-FIELD RESPONSE OF C12-BTBT-C12
AT 0.6 THz.
a) Real part Re ε (black) and imaginary part Im ε (red) of the C12-BTBT-C12 permittivity. b) Scattering amplitude s_3 (black) and phase φ_3 (red), normalized to Au.

examined with THz s-SNOM. Accordingly, the recorded measurement at 0.6 THz, with a full platinum (Pt) tip and 194 nm tapping amplitude, is shown in Figure 13. Recorded from left to right, the images show a strong correlation of the topography with the optical near-field amplitude s_1 and s_2. While the topography was increasing through the scan, the near-field amplitude was decreasing. Most probably, the organic material was adsorbed at the tip, creating a dielectric layer around the metallic tip, because the molecules were only loosely bound to the substrate. This layer around the metallic tip suppressed the periodic near-field enhancement between the tip and the substrate, which is crucial for operating an s-SNOM. Therefore, no stable experimental conditions were found. For future THz s-SNOM experiments with organic semiconductors, this adsorption behavior needs to be understood.
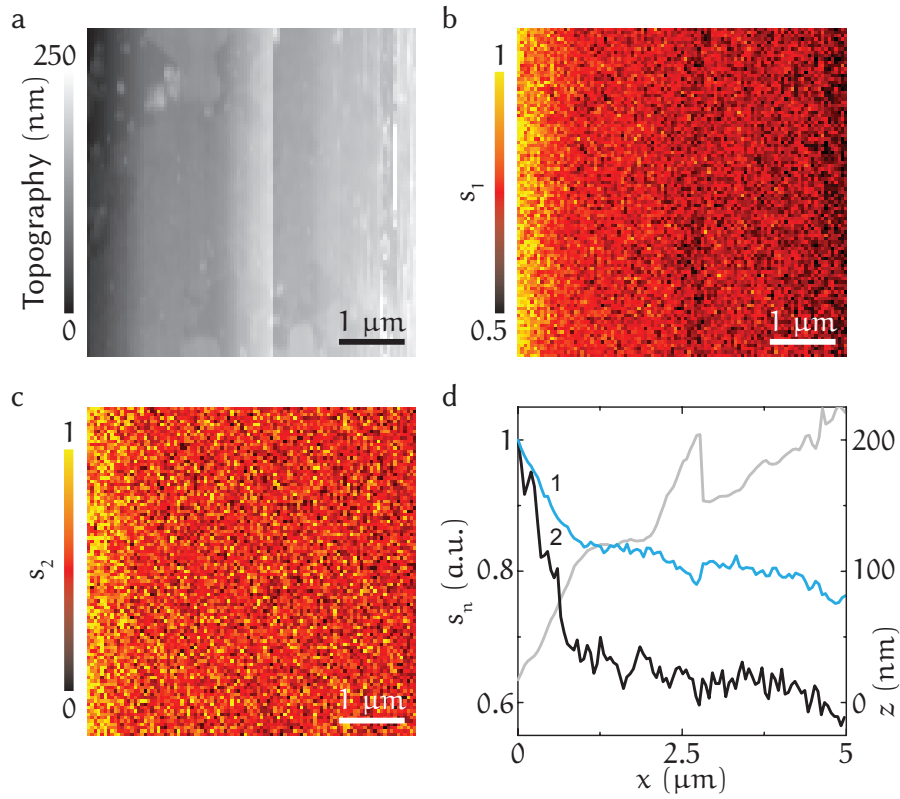
FIGURE 13: SINGLE-FREQUENCY 0.6 THz s-SNOM IMAGE OF C10-BTBT:F4TCNQ.
Simultaneously recorded a) topography, b) THz amplitude s_1, c) THz amplitude s_2, d) extracted profiles, averaged over all lines. The image was recorded column by column, from left to right. During the scan, the topography increased and the THz amplitude decreased.

CONTACT RESISTANCE AND CHARGE CARRIER TRAPS IN PENTACENE

Part of the findings presented in this chapter have been published [34]. The full article can be found in appendix A.3 and the supplementary material in appendix B.2.

Scanning photocurrent microscopy (SPCM) describes the electronic device response on a localized optical modulation [23]. The incoming light is pulsed with a fixed frequency f, and the current is demodulated at the same frequency, extracting the photocurrent I_{photo}. A schematic of the measurement principle is shown in Figure 14. Detailed descriptions of the home-made SPCM setup, used in this work, are presented in appendix D.

Previous SPCM studies of pentacene FETs have identified distinct photoresponse contributions, with different spatial signatures [24]. Confined to the edge of the source contact, the photoresponse was attributed to an enhanced injection or a lowering of the contact resistance [25, 26]. An SPCM signal near the contacts and in the channel was assigned to contact resistance and a varying mobility in the channel [27]. Also in the channel, an inhomogeneous photoresponse distribution was found, marking hotspots of charge carrier traps [28]. Here, the trapped positive charges (holes) are released by the prevalent triplet excitons, generated after light absorption. Recently, the channel formation of pentacene transistors was mapped by varying the applied drain and gate voltage [29]. In summary, there are two main effects, contributing to the photoresponse in pentacene FETs, exciton-splitting with charge-separation near the contacts, and charge de-trapping within the channel. These effects can be separated, using different pulse frequencies f of the exciting laser [28]. The de-trapping can be measured up to $f = 100\,kHz$, whereas the confined contribution at the contact also occurs at higher frequencies. However, it had been unclear which kind of photoresponse could be expected from freshly prepared pentacene FETs.

In the course of this dissertation, we could determine the device characteristics, that cause the different photoresponse contributions. This work was done together with Daniel Reiser during his master's thesis [83]. For this deduction, a pentacene FET with asymmetric source/drain contacts was investigated. Asymmetric contacts can occur from imperfections in the device fabrication and feature a strongly direction-dependent transistor current due to an asymmetric contact resistance R_C. In the high R_C direction, the SPCM maps mainly showed the photoresponse at the source contact. In the other
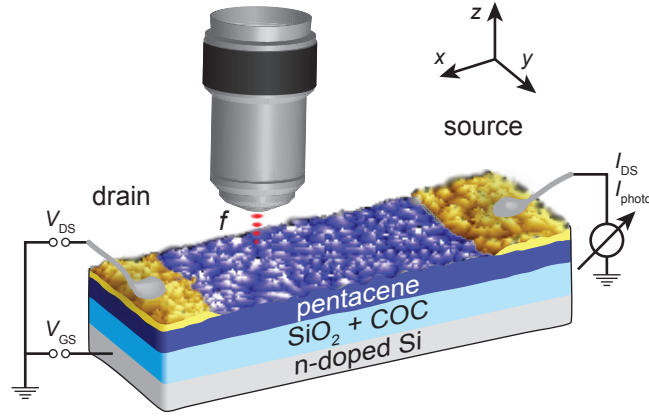
FIGURE 14: SCHEMATIC OF PHOTOCURRENT MICROSCOPY.
Visible light with a pulse frequency f is focused with an objective on a field-effect transistor (FET), where the drain voltage V_{DS} and gate voltage V_{GS} is applied. The current at the source contact I_{DS} is demodulated at the pulse frequency f, providing the photocurrent I_{photo}. Reprinted from [34], with the permission from AIP Publishing.

direction with low R_C, the maps revealed the inhomogeneous photoresponse distribution within the transistor channel. Thus, we concluded that the SPCM maps of pentacene FETs highlight the dominant voltage loss mechanism, hindering the optimal charge transport. The findings are presented in appendix A.3.

6.1 RESISTOR NETWORK SIMULATION MODEL

For SPCM measurements, a focused laser excites the devices locally, but the current is measured globally, over the entire contact area. The extracted photocurrent ΔI_{photo} is typically three orders of magnitude lower than the dark current I_{dark}. In a theoretical study, it was investigated, if the local thin-film properties can be reconstructed from the SPCM maps. The main work of this study was done by Mohammed Darwish, TU Munich. As the basic principle, trapped holes in the transistor channel are illuminated at the position **r** and released into the HOMO energy level, as shown in Figure 15a. Being released from the traps, the holes contribute to the charge transport in the transistor channel. The transistor was modeled as a 2D resistor network, and reduced to an equivalent resistor R. An inhomogeneous trap distribution was initialized by assigning different values to the individual resistors. Blocks of four resistors represented the illuminated position and were sequentially manipulated, as shown in Figure 15b. At each position, the current response, corresponding to a reduced equivalent resistor $R - \Delta R$, was calculated. In this way, an SPCM map was constructed. Finally, the SPCM maps were compared to the initialized trap distribution. This comparison showed indeed the variations of the local trap density in the SPCM maps. However, near
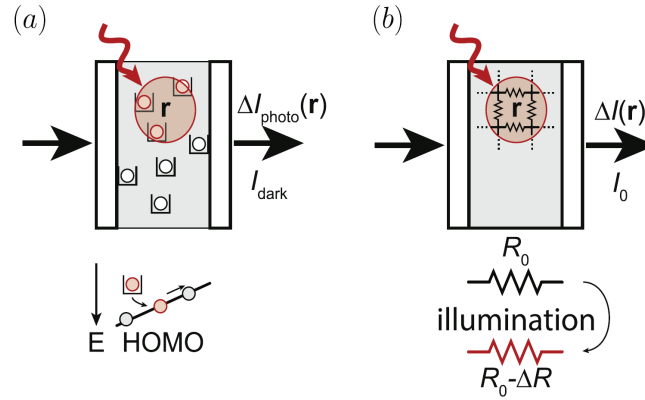
FIGURE 15: PRINCIPLE OF PHOTOCURRENT SIMULATION WITH A RESISTOR NETWORK.
a) Schematic of trap states, illuminated at the position $\mathbf{r}$. The trapped charges are released into the HOMO and contribute to the transistor current with $\Delta I_{photo}(\mathbf{r})$.
b) The transistor is modeled as a resistor network, which can be simplified to an equivalent resistor R. Under illumination, the equivalent resistor is reduced to $R - \Delta R$. Reprinted with permission from [84].

the contacts, the high conduction of the source/drain contacts was dominating the SPCM maps, so that the trap density could not be seen anymore. The results of this study are shown in appendices A.5 and B.4. Our earlier experiments also show an increase of the photoresponse near the contacts, but the trap distribution is still clearly visible (c.f. Figure 3a of appendix A.3). Thus, the strength of these two effects, found by calculation, could be adjusted in future investigations.

ELECTRONS AND HOLES IN EPINDOLIDIONE

Part of the findings presented in this chapter have been published [35]. The full article can be found in appendix A.4 and the supplementary material in appendix B.3.

The following chapter describes our investigations of the photoresponse in Epi FETs. This work was done together with Simone Strohmair, who has finished her master's thesis in the course of this dissertation [85], and with Henrik Hecht, who is currently working on his master's thesis. Our SPCM measurements allowed to characterize the kinetics of electrons and holes in Epi transistors. In contrast to previous SPCM measurements of pentacene [28, 83], the Epi devices showed a strong photoresponse at positive gate voltages V_{GS}, while the holes were depleted from the semiconducting layer. A comprehensive understanding of the Epi photoresponse, containing drift, diffusion, generation, and recombination, was achieved by a time and frequency domain analysis at different voltage configurations. Applying a negative drain voltage V_{DS}, the device was operated as a FET, while for $V_{DS} = 0\,V$, it was operated as a metal-insulator-semiconductor (MIS) diode. The SPCM measurements at different pulse frequencies f of the incident light allowed us to identify the photoresponse as a fast displacement current under the semitransparent source/drain contacts. The charge carriers for this contributions were generated by exciton-splitting in the electric field between the gate and the top contacts. In the FET configuration, the device showed an additional low-frequency response, that was recognized as exciton-assisted de-trapping of holes in the transistor channel. The findings are presented in appendix A.4.

7.1 EFFECTS OF CONTACT RESISTANCE ON THE DISPLACEMENT PHOTORESPONSE

The photoresponse contribution from displacement currents was measured for positive and negative gate voltages V_{GS} with respect to the threshold voltage V_{th}, yet at different pulse frequencies f. For $V_{GS} > V_{th}$, the illumination-induced a higher total charge in the Epi layer, and the displacement current was measured also at lower frequencies, compared to $V_{GS} < V_{th}$. Here, less charge was induced on illumination, and the process finished faster. A similar effect can be observed for two different FETs at negative gate voltages V_{GS}. These transistors presumably had a different contact resistance R_C, resulting from a varying fabrication protocol. The high contact resistance
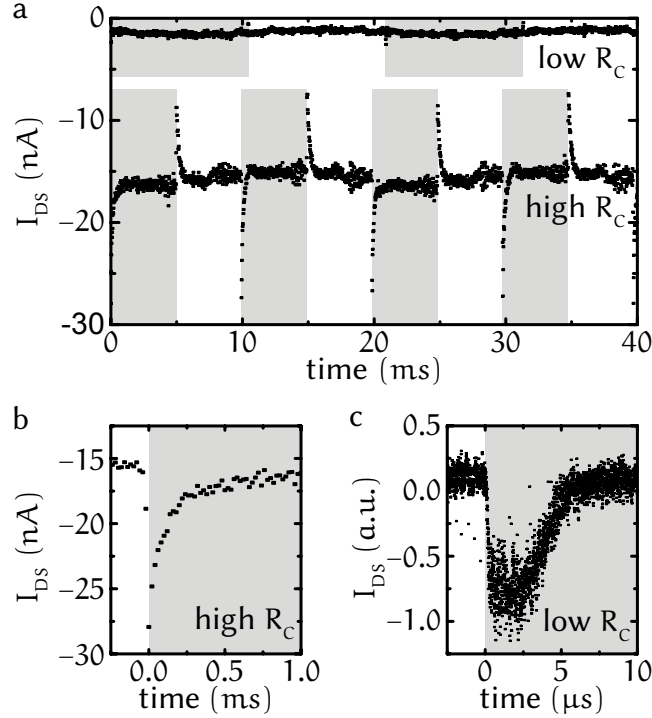
FIGURE 16: TRANSIENT PHOTOCURRENT OF EPI FETs.
a) Comparison of two Epi FETs with high and low contact resistance R_C. Gray areas mark the times under illumination. b) The transient of the high R_C transistor decays within 0.5 ms. c) The transient of the low R_C transistor decays within 5 μs

was the result of a titanium (Ti) adhesive layer under the slowly evaporated Au top contacts. The low contact resistance was achieved by omitting the Ti layer and evaporating the Au contacts at a higher rate of $11 \, \text{Å} \, \text{s}^{-1}$. With the applied $V_{GS} < V_{th}$ and $V_{DS} = 0$, holes are accumulated at the Epi/tetratetracontane (TTC) interface but are not drifting from source to drain. This configuration is equivalent to MIS diodes with ohmic contacts of different quality. The response of the devices to pulsed, global illumination is shown in Figure 16. Upon illumination, negative transients are induced, with a fast rise time and a slower decay. The transients of the high R_C device show a decay within 0.5 ms, the low R_C device is two orders of magnitude faster, with a rise time of 0.2 μs and a decay within 5 μs. For low R_C, the holes are efficiently injected into the Epi layer and accumulated at the TTC interface. Only a small amount of holes does not reach the interface, due to traps within the Epi layer. For high R_C, the hole injection is hindered, meaning that the hole density at the TTC interface is lower. The excitons in the Epi layer are split by the electric field under the top contacts and positive charges are shifted toward the TTC interface. The negative charges are drawn toward the top contacts and eventually get extracted. Thus, for high R_C, a higher net charge needs to be shifted to the TTC interface, meaning that this process is slower.

OUTLOOK

In this work, the microscopic and nanoscopic properties of organic thin-films and organic transistors were investigated. A comprehensive SPCM analysis of pentacene and Epi revealed distinct, material-specific contributions to the photoresponse. For pentacene FETs, the SPCM maps highlight the dominant voltage-loss mechanism, either contact resistance at the source contact, or trap states in the transistor channel. Epi FETs show fast, light-induced displacement currents, determined as electron-hole dissociation in the electric field under the contacts. Additionally, in the channel, a slow response was measured, increasing the transistor current due to de-trapping of holes. Besides resolving these SPCM contributions, organic thin-films were analyzed with microdiffraction imaging and with THz s-SNOM. Microdiffraction imaging characterizes the local crystal structure, also under metal contacts. THz nanoscopy probes the local charge density. A limiting factor are the fairly large lattice constants, which increase the beam footprint for the Bragg scattering conditions in the case of microdiffraction. The weak intermolecular binding compared to the adhesivity of the metal AFM tip causes the molecules to attach to the tip, and, therefore, to damp the periodic near-field interaction of the THz nanoscopy. These issues need to be considered in future investigations with these methods.

Futures studies could the combine the available microscopy methods to gain an in-depth understanding of the structure-function relationship in organic semiconductors. Some prospects are given in the following, final paragraphs of this thesis.

Heterostructures of 2D Materials and Organic Semiconductors
Hybrid heterojunctions of 2D materials and organic semiconductor nanosheets promise to combine the best properties of these two material systems [86–90]. The organic layer strongly absorbs light, the interface to the 2D material is used for efficient charge separation, and the 2D material features efficient charge transport. For an excellent device performance, the interface quality is crucial, which is hard to achieve with poor growth of organic semiconductors on the 2D materials. Therefore, a method, developed mainly by Simon Noever in our laboratories, is used to stabilize and transfer the organic thin films from a substrate with superior thin-film growth onto arbitrary substrates [91]. The results of this work are shown in appendices A.7 and B.5. With these hybrid heterojunctions, the device response on charge separation, electron transport and hole transport can be ex-

perimentally investigated. The first investigated hybrid devices with pentacene and molybdenum disulfide (MoS_2) require N_2 atmosphere for operation. This atmosphere is provided by an encapsulation of the sample stage, which shows first promising results at the moment.

Single-charge measurements of THz s-SNOM

In the presented results, the achieved lateral solution of $50\,nm$ also implies a probing depth of the order of $50\,nm$, giving a probing volume of $(50\,nm)^3$ [81]. From this probing volume and a measured charge density of $2 \times 10^{16}\,cm^{-3}$, the mean number of charges in the probing volume is calculated to be 2.5. The limiting charge sensitivity in the used setup is certainly lower because the acquisition time per pixel can be chosen longer, giving a higher signal to noise ratio. Furthermore, a lower THz frequency, which is sensitive to even lower charge densities, will probably enable a direct probing of single-charge phenomena.

A

PUBLICATIONS

PEER-REVIEWED FIRST AUTHOR PUBLICATIONS THAT ARE PART
OF THIS CUMULATIVE THESIS

Microdiffraction imaging—a suitable tool to characterize organic electronic devices
C. Liewald, S.J. Noever, S. Fischer, J. Roemer, T.U. Schülli, and
B. Nickel
AIMS Materials Science (2015) [32]

All-electronic terahertz nanoscopy
C. Liewald, S. Mastel, J. Hesler, A.J. Huber, R. Hillenbrand, and
F. Keilmann
Optica (2018) [33]

Photocurrent microscopy of contact resistance and charge carrier traps in organic field-effect transistors
C. Liewald, D. Reiser, C. Westermeier, and B. Nickel
Applied Physics Letters (2016) [34]

Scanning photocurrent microscopy of electrons and holes in the pigment semiconductor epindolidione
C. Liewald, S. Strohmair, H. Hecht, E. Głowacki, and B. Nickel
Organic Electronics (2018) [35]

FURTHER PEER-REVIEWED PUBLICATIONS

A resistor network simulation model for laser-scanning photo-current microscopy to quantify low conductance regions in organic thin films
M. Darwish, H. Boysan, **C. Liewald**, B. Nickel, and A. Gagliardi
Organic Electronics (2018) [84]

Phase-resolved terahertz self-detection near-field microscopy
M.C. Giordano, S. Mastel, **C. Liewald**, L.L. Columbo, M. Brambilla,
L. Viti, A. Politano, K. Zhang, L. Li, A.G. Davies, E.H. Linfield, R. Hillenbrand, F. Keilmann, G. Scamarcio, and M.S. Vitiello
Optics Express (2018) [92]

Transferable Organic Semiconductor Nanosheets for Application in Electronic Devices
S.J. Noever, M. Eder, F. del Giudice, J. Martin, F.X. Werkmeister, S. Hallwig, S. Fischer, O. Seeck, N.-E. Weber, **C. Liewald**, F. Keilmann, A. Turchanin, and B. Nickel
Advanced Materials (2017) [91]

Sub-micron phase coexistence in small-molecule organic thin films revealed by infrared nano-imaging
C. Westermeier, A. Cernescu, S. Amarie, **C. Liewald**, F. Keilmann, and B. Nickel
Nature Communications (2014) [22]

A.1 MICRODIFFRACTION IMAGING—A SUITABLE TOOL TO CHARACTERIZE ORGANIC ELECTRONIC DEVICES

Clemens Liewald, Simon Noever, Stefan Fischer, Janina Roemer, Tobias U. Schülli, and Bert Nickel

Abstract

Tailoring device architecture and active film morphology is crucial for improving organic electronic devices. Therefore, knowledge about the local degree of crystallinity is indispensable to gain full control over device behavior and performance. In this article, we report on microdiffraction imaging as a new tool to characterize organic thin films on the sub-micron length scale. With this technique, which was developed at the ID01 beamline at the ESRF in Grenoble, a focused X-ray beam (300 nm diameter, 12.5 keV energy) is scanned over a sample. The beam size guarantees high resolution, while material and structure specificity is gained by the choice of Bragg condition. Here, we explore the possibilities of microdiffraction imaging on two different types of samples. First, we measure the crystallinity of a pentacene thin film, which is partially buried beneath thermally deposited gold electrodes and a second organic film of fullerene C_{60}. The data shows that the pentacene film structure is not impaired by the subsequent deposition and illustrates the potential of the technique to characterize artificial structures within fully functional electronic devices. Second, we investigate the local distribution of intrinsic polymorphism of pentacene thin films, which is very likely to have a substantial influence on electronic properties of organic electronic devices. An area of 40 µm by 40 µm is scanned under the Bragg conditions of the thin-film phase and the bulk phase of pentacene, respectively. To find a good compromise between beam footprint and signal intensity, third order Bragg condition is chosen. The scans show complementary signal distribution and hence demonstrate details of the crystalline structure with a lateral resolution defined by the beam footprint (300 nm by 3 µm). The findings highlight the range of applications of microdiffraction imaging in organic electronics, especially for organic field effect transistors and for organic solar cells.

Contribution

I fabricated the polymorphic pentacene sample. All data were taken by Simon Noever, Bert Nickel and myself. I analyzed the data on polymorphic pentacene, wrote the major part of the manuscript, and prepared the final manuscript.

http://www.aimspress.com/

Research article

Microdiffraction imaging—a suitable tool to characterize organic electronic devices

Clemens Liewald [1,2], Simon Noever [1,2], Stefan Fischer [1], Janina Roemer [1], Tobias U. Schülli [3], and Bert Nickel [1,2,*]

[1] Fakultät für Physik & Center for NanoScience (CeNS), Ludwig-Maximilians-Universität München, Geschwister-Scholl-Platz 1, 80539 Munich, Germany

[2] Nanosystems Initiative Munich, Schellingstrasse 4, 80799 Munich, Germany

[3] ID01/ESRF, 71 avenue des Martyrs, CS 40220, F-38043 Grenoble Cedex 9, France

* Correspondence: Email: nickel@lmu.de.

Abstract: Tailoring device architecture and active film morphology is crucial for improving organic electronic devices. Therefore, knowledge about the local degree of crystallinity is indispensable to gain full control over device behavior and performance. In this article, we report on microdiffraction imaging as a new tool to characterize organic thin films on the sub-micron length scale. With this technique, which was developed at the ID01 beamline at the ESRF in Grenoble, a focused X-ray beam (300 nm diameter, 12.5 keV energy) is scanned over a sample. The beam size guarantees high resolution, while material and structure specificity is gained by the choice of Bragg condition.

Here, we explore the possibilities of microdiffraction imaging on two different types of samples. First, we measure the crystallinity of a pentacene thin film, which is partially buried beneath thermally deposited gold electrodes and a second organic film of fullerene C_{60}. The data shows that the pentacene film structure is not impaired by the subsequent deposition and illustrates the potential of the technique to characterize artificial structures within fully functional electronic devices. Second, we investigate the local distribution of intrinsic polymorphism of pentacene thin films, which is very likely to have a substantial influence on electronic properties of organic electronic devices. An area of 40 μm by 40 μm is scanned under the Bragg conditions of the thin-film phase and the bulk phase of pentacene, respectively. To find a good compromise between beam footprint and signal intensity, third order Bragg condition is chosen. The scans show complementary signal distribution and hence demonstrate details of the crystalline structure with a lateral resolution defined by the beam footprint (300 nm by 3 μm).

The findings highlight the range of applications of microdiffraction imaging in organic

electronics, especially for organic field effect transistors and for organic solar cells.

1. Introduction

Organic electronics allow for large scale, low cost, and low energy device fabrication. Today, organic electronics have found mass market application in digital displays consisting of organic light emitting diodes (OLED). In order to improve the performance of organic electronic devices, a detailed understanding of the device physics is essential. The challenge for highly ordered materials is twofold; on the one hand side, intrinsic properties, such as charge carrier mobility, depend on details of the pi-electron overlap [1] and polymorphism. Polymorphism is common among a variety of organic small molecule semiconductors [2–5]. Consequently, the domain size and the mutual distribution of the polymorphs are of great concern [6]. On the other hand, processing steps and interface phenomena often induce additional structural changes at the nm to micron scale, which may influence device performance. Close attention should be paid to contact regions because metal top contacts can influence the underlying organic layer by metal clusters diffusing in the organic film [7], while the growth mode of many organic materials on bottom contact metals is strongly disturbed, which changes the energy alignment of these materials [8]. In practice, top contact configuration in pentacene thin film transistors shows preferable device characteristics when not employing bottom contact electrodes which are functionalized [9]. Furthermore, the manufacturing of multilayer devices, such as organic light emitting diodes, organic photovoltaics and ambipolar organic field effect transistors (OFETs), demands the application of various sequential processing steps, including photolithography, imprint, shadow masks, spin casting, and annealing [10]. These subsequent processing steps can also modify the structure of subjacent films [11].

An experimental approach that allows nm-resolved, non-destructive probing of the crystal structure of organic devices, e.g. on top or below metal contacts of an OFET and in the conduction channel, would be very attractive. Recently, we introduced scattering-type scanning near field infrared optical microscopy (s-SNOM) to probe polymorphism in organic films [6]; however, this gentle technique does not work below Au contacts, which reflect back the IR light so that no information from below is accessible. Transmission electron microscopy (TEM) instead allows to image depth profiles of organic devices with close to molecular resolution, revealing interdiffusion of Au, originating from the top contact deposition [7]. However, the demanding cross section preparation requires cutting the device apart and the electron flux alters [12] or even disintegrates the molecular structure at prolonged exposure.

In principle, X-ray techniques combine all needed properties: X-ray reflectometry, for example, is used to depth profile stratified media on sample surfaces as well as buried layers [13], whereas scattering geometries, such as grazing incidence X-ray scattering allow for surface sensitive probing of thin organic single and multilayers [14,15]. Although X-rays are commonly used to probe rather large areas, typically several hundred microns squared, there is so far only a small amount of reports on scanning X-ray diffraction with a sub-micron focused X-ray beam [16–19]. This microdiffraction imaging was used to study inorganic materials and can for example resolve local strain and lattice

orientation of semiconductors like Si and Ge. Studies using microdiffraction techniques on organic semiconductors are mostly limited to transmission measurements which resolve depth profiles of organic devices [20]. Ideally, the energy should be in the vicinity of ~ 20 keV because irradiating organic carbon compounds with high flux per area X-rays at lower energy leads to severe beam damage by incoherent scattering [21]. Here, we employ microdiffraction imaging in reflection geometry to study organic films, using a beam of 300 nm diameter at an energy of 12.5 keV, and cannot observe any beam damage. In this experiment, we map the lateral distribution of artificial and intrinsic structures in organic single- and multilayer thin-film devices. With microdiffraction imaging, it is possible to resolve the local crystalline structure on the surface and in buried layers, by scanning the beam over the sample and recording the intensity at specific angles, matching designated Bragg conditions. Furthermore, we discuss the current limitations of the lateral resolution and possible applications for this method.

2. Materials and Method

2.1. Sample preparation

The organic semiconductor pentacene served as a model system for our microdiffraction experiments. When grown on silicon oxide, pentacene thin films are known to crystallize in two main structural phases, the so-called thin-film phase (TFP) and bulk phase (BP) [4,5,22–24].

For measuring buried organic structures in working multilayer devices, an ambipolar organic field-effect transistor (OFET) was fabricated. Here, a 40 nm layer of pentacene was used as p-type semiconductor, followed by 40 nm gold top contacts, and finally 30 nm of fullerene C_{60} as n-type semiconductor. The channel width and length were 2 mm and 50 μm, respectively. Highly n-doped silicon with 300 nm SiO_2 acted as combined gate/dielectric substrate. After consecutively sonicating in acetone, isopropyl alcohol, and de-ionized water for 10 min each, the sample was cleaned with oxygen plasma for 180 s. Prior to pentacene deposition, the dielectric surface was finished with a ~ 5 nm thick layer of cyclic-olefin-copolymere (COC), by spin casting a 0.25% solution of COC in toluene for 30s at 6000 rpm and annealing at 100 ℃ for 60 s. Pentacene and fullerene C_{60} layers were produced at room temperature and ~ 90 ℃, respectively, by molecular vapor deposition, at a rate of 0.1 Å/s, respectively, and gold contacts were fabricated by electron beam deposition, at a rate of 1 Å/s. All structures were defined by shadow masks under ultra high vacuum conditions. The upper part of the pentacene layer (~ 5 nm) was cross-linked by e-beam irradiation prior to gold evaporation.

To study the polymorphism of TFP and BP pentacene, a 60 nm thick pentacene film was prepared on a silicon wafer with 20 nm thick SiO_2. The substrate was cleaned by sonicating, as described above, and the pentacene film was deposited by molecular vapor deposition, at a rate of 0.1 Å/s. With this deposition rate, pentacene crystallizes at room temperature in the TFP with the [001] direction perpendicular to the substrate surface. However for this sample, a substrate temperature between 40 ℃ and 50 ℃ was chosen, which is known to induce mixed growth of TFP and BP pentacene [5,22–24] and to exhibit ellipsoidal structures on a sub-micron length scale [6]. The coexistence of the two phases on this sample was verified with an in-house reflectometer prior to the reported experiment.

2.2. *X-ray diffraction*

2.2.1. Reflectometry

The X-ray reflectometry curve shown here was measured at the P08 beamline at PETRA III at DESY in Hamburg, Germany [25]. Here, the X-ray energy E was set to 18 keV, which corresponds to a wavelength λ of 0.6888 Å.

2.2.2. Microdiffraction imaging

Microdiffraction imaging was performed at the beamline ID01 at the European Synchrotron Radiation Facility (ESRF) in Grenoble, France. Here, the synchrotron X-ray beam with an energy of 12.5 keV, which corresponds to a wavelength λ of 0.9919 Å, was focused by a Fresnel zone plate with a central beam stop, followed by an order sorting aperture (to block unfocused beam parts and higher diffraction orders) to a nominal beam size of 300 nm (for further details, we refer to [17]). A sketch of the measurement geometry is shown in Figure 1a. Here, the angle of the incident beam θ was adjusted to a Bragg condition of the film and the diffracted beam was recorded with a 2D detector (MAXIPIX, 516×516 pixels², 55×55 μm² pixel size) [26] with adjusted regions of interest (ROI) at about 40 cm distance from the sample holder. Additionally, lead tape between the incident beam and the detector was used as a beam knife-edge to prevent air scattering from disturbing the recorded signal. To avoid radiation damage from reactive oxygen species, the sample was blown with dry nitrogen. First, the sample was positioned with a light microscope, illuminating from the top. Subsequently, the sample was continuously mapped in real space with a piezoelectric stage for short distances (<100 μm) or a hexapod (>100 μm) with step size resolutions of 5 nm and 100 nm, respectively. This so-called K-Map, a quick mapping procedure developed at ID01 has significantly reduced the measurement time needed for these scans, by optimizing positioning, exposure, and data acquisition [17]. The K-Maps in this report had a size of 40×40 μm² and a resolution of 80×40 pixels² (0.5×1 μm²), leading to a total measuring time of only 16 min and 43 min, corresponding to a pixel time of 0.3 s and 0.8 s, respectively.

However, the lateral resolution of the K-Maps is inherently limited by the footprint f of the beam. In the direction perpendicular to the X-ray beam, the footprint $f_\perp$ corresponds to the diameter b of the focused beam, which was set to 300 nm during our experiments. Additionally, in the direction parallel to the incident X-ray beam, the geometrically enlarged footprint $f_\parallel$ is given by

$$f_\parallel = \frac{b}{\sin(\theta)}, \tag{1}$$

with the beam diameter b and the incident angle θ. Consequently, the footprint $f_\parallel$ is smaller for higher incident angles θ, which improves the lateral resolution of the K-Maps. A good lateral resolution in both directions can be achieved with inorganic crystals like VO_2, Si, or Ge [16–19], owing to their high crystallinity. However, it is difficult to record K-Maps at high incident angles θ for organic crystals, because of their overall lower scattered intensity and their larger lattice constants. Therefore, finding a suitable compromise between footprint size and signal to noise ratio is essential, when measuring crystalline organic thin films. Here, the pentacene samples were measured at the (002) and (003) Bragg conditions.

3. Results and Discussion

We characterized an ambipolar pentacene-C_{60} OFET as a representative sample for multilayer devices, as they are commonly used in organic electronics. A sketch of the experimental geometry is shown in Figure 1 a). Here, the source and drain electrode of the transistor are indicated by the T-structures and the scan profile is indicated by the white arrow. At this position, the gold contacts had a length of 100 µm, each, which adds, together with the channel length of 50 µm, to a total device length of 250 µm. An illustration of the vertical section of the device is shown in Figure 1 b), with the C_{60} layer depicted on top of the gold and the pentacene layer. The pentacene top contact configuration is needed to optimize charge carrier injection in bi-layer ambipolar transistors [15].

To investigate the pentacene layer beneath the gold contacts, we measured two 400 µm scans over the device. First, we performed a reference measurement, to determine the exact sample position [Figure 1 c)]. The incidence angle θ was set to the Au (111) Bragg condition, i.e. 12.15 °, which is very pronounced, since vacuum deposited gold on SiO_2 crystallizes in fcc structure in [111] direction [27]. Here, the footprint size parallel to the beam $f_\parallel$ corresponded to 1.43 µm, according to equation (1). The scan was done using the hexapod because the scan width of 400 µm exceeded the hardware limitation of the high-resolution piezoelectric stage. As seen from Figure 1, the intensity profile of the scan traces the channel geometry quite well. Second, we set the incidence angle to the pentacene TFP (002) Bragg condition, i.e. to 3.69 °, which corresponded to a footprint $f_\parallel$ of 4.65 µm. This led to good signal strength with an acceptable footprint. The intensity profile of the TFP (002) scan indicates a complementary behavior to the Au (111) scan [Figure 1 c)]. The drop in intensity beneath the gold contacts can be explained rather well by absorption of X-rays while passing through the gold layer. The absorption of a planar layer is given by:

$$I_r = I_0 * \exp\left(-\frac{2d}{\mu * \sin(\theta)}\right) \qquad (2)$$

where d is the nominal gold layer thickness, θ the incident angle, µ = 3.2 µm the attenuation length of gold and I_0 the scattered intensity without gold. The factor two in the exponent accounts for the way in and out of the gold layer. As a result, the signal intensity should calculate to $I_r \sim 0.68 * I_0$. However, the acquired signal only drops about 20% and is thus higher than expected from this calculation. One explanation for this observation might be the uncertainty of the actual Au film thickness deposited onto the pentacene layer. The quartz microbalances, which were used to read out the nominal Au thickness, do not address any eventual deviations from growth on e.g. smooth SiO_2 surfaces.

For these reasons, the decrease of the pentacene signal beneath the gold contacts could be ascribed to the absorption of the beam propagating through the gold film. Thus, we have no indication that the top contact strongly reduces the crystallinity of the pentacene film.

Furthermore, the pentacene signal increased only slowly with growing distance to the right gold contact, even though no electrode material was present in the beam pathway. Here, the preparation of the contact geometry could have led to a damaged film. For example, removing the shadow mask could have led to a mechanical damage of the subjacent pentacene film after contact fabrication.

Moreover, it is necessary to address the large variations in the pentacene (002) signal, compared to the Au (111) signal. The grain size of pentacene is usually on the micron scale, far larger than for Au, and its topography shows thickness variations of the order of the nominal film thickness when grown on SiO_2. Therefore, the scattered intensity should depend strongly on the beam position on the

pentacene surface.
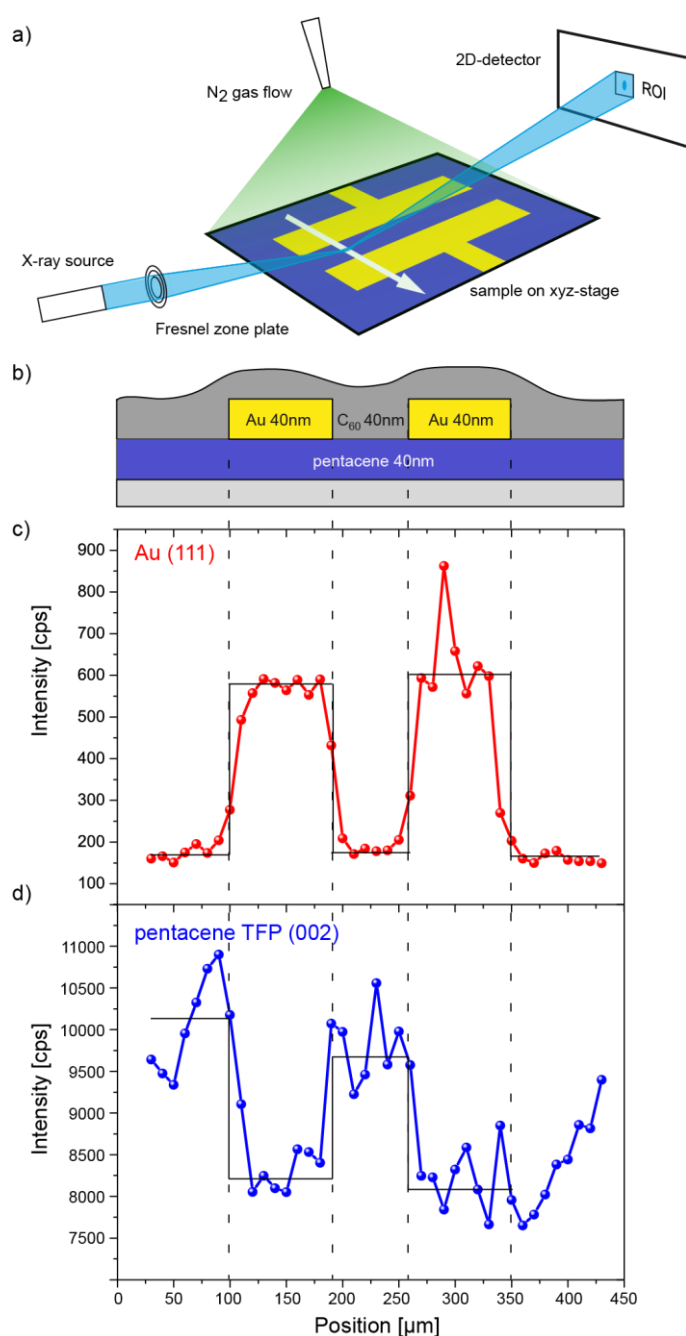
Figure 1. Schematic and X-ray line scans of an ambipolar pentacene-C_{60} OFET. a) Sketch of the experiment geometry. b) Cross section of the sample geometry. c) Incident angle adjusted to the gold (111) Bragg condition. d) Incident angle adjusted to the pentacene TFP (002) Bragg condition.

As a representative sample for investigating the local polymorphic structure of organic thin films and to determine the potential of the setup to resolve sub-micron features, we investigated a pentacene thin film, which exhibits three different Bragg signatures from the thin-film phase [TFP (00L)], the bulk phase [BP (00L)] and the lying phase, as verified via X-ray reflectometry (Figure 2 a). The crystalline lying phase nucleates after a critical film thickness, which is strongly dependent

on the substrate temperature during the pentacene deposition (>100 nm at room temperature, 30 nm at 87 ℃) [24,28]. In contrast, the coexistence of TFP and BP pentacene is induced by temperature dependent stress at the SiO_2 interface [5,6,22–24]. Here, we focus on this coexistence of TFP and BP pentacene. Using s-SNOM with a lateral resolution as small as 20 nm has shown that, in fact, the lateral distribution of TFP and BP pentacene exhibits ellipsoidal structures on a length scale of 100 nm [6]. However, the s-SNOM probes to a depth of typically 30–50 nm [29], whereas X-ray microdiffraction yields information of the whole depth of the film.

To resolve the intrinsic lateral distribution of TFP and BP pentacene, we recorded two 2D K-Maps of the same sector of the sample surface, one for each polymorph. To gain high lateral resolution, we used the piezoelectric motors to move the sample stage. The incident angle θ was set to 5.54 ° and 5.93 °, which corresponded to a footprint of 3.10 μm and 2.90 μm at the TFP (003) and BP (003) Bragg condition, respectively. Choosing the (003) Bragg conditions therefore reduced the footprint by 33% compared to the (002) Bragg conditions. For this system, choosing higher order Bragg conditions led to an undesirable signal to noise ratio. The K-Maps were recorded with the incident beam along the slow scan direction. To image a lateral inhomogeneity with full resolution, the scan size was set to 40 μm and the motor steps were set to 500 nm in the fast scan direction and 1 μm in the slow scan direction.
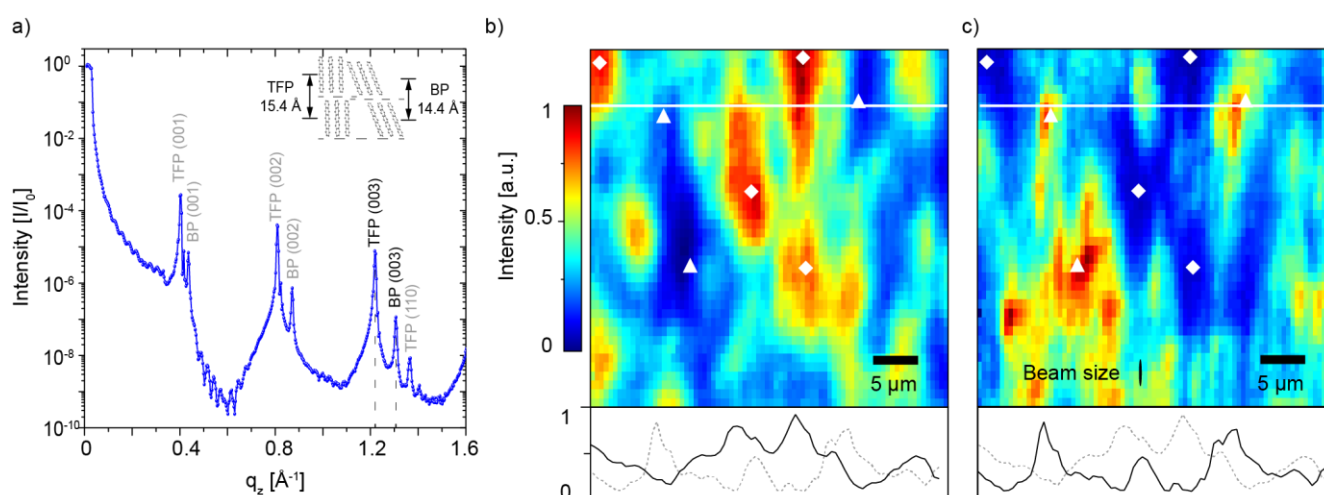
Figure 2. a) Wide (normal) beam X-ray reflectivity of a 60 nm thick pentacene film with the indicated Bragg series of TFP and BP pentacene. Inset shows a sketch of TFP and BP pentacene. b) and c) K-Maps of the microdiffraction X-ray intensity of the same sample area, measured at the TFP(003) and BP(003) Bragg condition, respectively. Diamonds and triangles indicate maxima in TFP and BP intensity, respectively. The continuous line profiles at the bottom correspond to the white section indicated in the map (the dashed lines compare the profile to the respective other phase).

We have blown the samples with dry nitrogen during all measurements to minimize radiation damage from reactive oxygen species, activated by hard X-rays in ambient air. During the short exposure times of the maps and scans shown here (typically several seconds per data point), we could not observe any beam damage for repeated measurements, i.e. loss of Bragg signal, and thus conclude that microdiffraction imaging is suited for investigating organic thin films. Recent test

measurements indicate that beam damage can be further minimized by using higher beam energies, i.e. at 20 keV exposure times of several minutes are possible.

As result, we obtained a map of the TFP and the BP distribution within the thin film [Figure 2 b) and c)]. The two K-Maps show a complementary intensity profile, revealing micron scaled domains exclusively grown in TFP (diamonds) and BP (triangles), respectively. This behavior can also be seen in the line profiles of TFP and BP pentacene. The elongated beam footprint indicated in Figure 2 c) leads to an overall smearing of the signal parallel to the beam direction.

4. Conclusion

We used microdiffraction imaging with a focused X-ray beam to study the structure of organic thin films. Within these films, we were able to resolve intrinsic structures as well as artificial structures, which are used to build organic electronic devices like multilayer ambipolar OFETs. We demonstrated a lateral resolution for organic thin films of 300 nm in the direction perpendicular to the beam and about 3 μm in the direction parallel to the beam. To acquire K-maps with the lateral resolution of the focus size in both directions, two subsequent K-Maps at the same sample position with a sample rotation of 90 ° would be needed. By further improving the focusing optics, ID01, for example, offers a beam size of 100 nm diameter after its upgrade in 2014 and it will be interesting to see, if this is confirmed in microdiffraction experiments.

Furthermore, changing the measurement geometry from reflection to transmission, could avoid the problem of large footprints parallel to the beam. This transmission geometry would require thinner substrates, e.g. sapphire [30] or ultra-thin Si_3N_4 membranes, which are commonly used for scanning transmission X-ray microscopy (STXM) [31,32].

Nevertheless, the current resolution is already well suited to study organic electronic devices, e.g. organic thin-film transistors, because the commonly used channel lengths of these devices are in the range of 20 μm to 50 μm. Furthermore, the local nanostructure of state of the art organic solar cells, fabricated by self-organization or nanoimprint [33], could also be examined, even with metallic contacts on top. X-ray microdiffraction therefore complements to other scanning techniques, like STXM [32], s-SNOM [6,16], scanning photoresponse microscopy [34], or micro-Raman spectroscopy [19], to gain a deeper understanding of fundamental device physics.

Conflict of Interest

The authors report no conflict of interests in this research.

References

1. Bredas JL, Beljonne D, Coropceanu V, et al. (2004) Charge-transfer and energy-transfer processes in pi-conjugated oligomers and polymers: A molecular picture. *Chem Rev* 104: 4971–5003.
2. He T, Stolte M, Burschka C, et al. (2015) Single-crystal field-effect transistors of new Cl2-NDI polymorph processed by sublimation in air. *Nat Commun* 6: 5954.
3. Tang Q, Zhang DQ, Wang SL, et al. (2009) A Meaningful Analogue of Pentacene: Charge Transport, Polymorphs, and Electronic Structures of Dihydrodiazapentacene. *Chem Mater* 21: 1400–1405.
4. Schiefer S, Huth M, Dobrinevski A, et al. (2007) Determination of the crystal structure of substrate-induced pentacene polymorphs in fiber structured thin films. *J Am Chem Soc* 129: 10316–10317.
5. Mattheus CC, Dros AB, Baas J, et al. (2003) Identification of polymorphs of pentacene. *Synth Met* 138: 475–481.
6. Westermeier C, Cernescu A, Amarie S, et al. (2014) Sub-micron phase coexistence in small-molecule organic thin films revealed by infrared nano-imaging. *Nat Commun* 5: 5101.
7. Durr AC, Schreiber F, Kelsch M, et al. (2002) Morphology and thermal stability of metal contacts on crystalline organic thin films. *Adv Mater* 14: 961–963.
8. Kahn A, Koch N, Gao WY (2003) Electronic structure and electrical properties of interfaces between metals and pi-conjugated molecular films. *J Polym Sci Part B Polym Phys* 41: 2529–2548.
9. Necliudov PV, Shur MS, Gundlach DJ, et al. (2003) Contact resistance extraction in pentacene thin film transistors. *Solid State Electron* 47: 259–262.
10. Klauk H, (2006) *Organic Electronics: Materials, Manufacturing, and Applications,* 1 Eds., Wiley-VCH.
11. Dam HF, Andersen TR, Pedersen EBL, et al. (2015) Enabling flexible polymer tandem solar cells by 3D ptychographic imaging. *Adv Energy Mater* 5: 1400736.
12. Fuller T, Banhart F (1996) In situ observation of the formation and stability of single fullerene molecules under electron irradiation. *Chem Phys Lett* 254: 372–378.
13. Tolan M, (2013) *X-Ray Scattering from Soft-Matter Thin Films: Materials Science and Basic Research*, Springer.
14. Fritz SE, Martin SM, Frisbie CD, et al. (2004) Structural characterization of a pentacene monolayer on an amorphous SiO2 substrate with grazing incidence X-ray diffraction. *J Am Chem Soc* 126: 4084–4085.
15. Noever SJ, Fischer S, Nickel B (2013) Dual Channel Operation Upon n-Channel Percolation in a Pentacene-C60 Ambipolar Organic Thin Film Transistor. *Adv Mater* 25: 2147–2151.
16. Qazilbash MM, Tripathi A, Schafgans AA, et al. (2011) Nanoscale imaging of the electronic and structural transitions in vanadium dioxide. *Phys Rev B* 83: 165108.
17. Chahine GA, Richard MI, Homs-Regojo RA, et al. (2014) Imaging of strain and lattice orientation by quick scanning X-ray microscopy combined with three-dimensional reciprocal space mapping. *J Appl Crystallogr* 47: 762–769.
18. Chahine GA, Zoellner MH, Richard M-I, et al. (2015) Strain and lattice orientation distribution in SiN/Ge complementary metal–oxide–semiconductor compatible light emitting microstructures by quick x-ray nano-diffraction microscopy. *Appl Phys Lett* 106: 071902.

19. Zoellner MH, Richard M-I, Chahine GA, et al. (2015) Imaging Structure and Composition Homogeneity of 300 mm SiGe Virtual Substrates for Advanced CMOS Applications by Scanning X-ray Diffraction Microscopy. *ACS Appl Mater Interfaces* 7: 9031–9037.

20. Paci B, Bailo D, Albertini VR, et al. (2013) Spatially-resolved in-situ structural study of organic electronic devices with nanoscale resolution: the plasmonic photovoltaic case study. *Adv Mater* 25: 4760–4765.

21. Reich C, Hochrein MB, Krause B, et al. (2005) A microfluidic setup for studies of solid-liquid interfaces using x-ray reflectivity and fluorescence microscopy. *Rev Sci Instrum* 76.

22. Dimitrakopoulos CD, Brown AR, Pomp A (1996) Molecular beam deposited thin films of pentacene for organic field effect transistor applications. *J Appl Phys* 80: 2501–2508.

23. Knipp D, Street RA, Volkel A, et al. (2003) Pentacene thin film transistors on inorganic dielectrics: Morphology, structural properties, and electronic transport. *J Appl Phys* 93: 347–355.

24. Yanagisawa H, Tamaki T, Nakamura M, et al. (2004) Structural and electrical characterization of pentacene films on SiO_2 grown by molecular beam deposition. *Thin Solid Films* 464: 398–402.

25. Seeck OH, Deiter C, Pflaum K, et al. (2012) The high-resolution diffraction beamline P08 at PETRA III. *J Synchrotron Radiat* 19: 30–38.

26. Ponchut C, Rigal JM, Clément J, et al. (2011) MAXIPIX, a fast readout photon-counting X-ray area detector for synchrotron applications. *J Instrum* 6: C01069.

27. Kaefer D, Ruppel L, Witte G (2007) Growth of pentacene on clean and modified gold surfaces. *Phys Rev B* 75.

28. Bouchoms IPM, Schoonveld WA, Vrijmoeth J, et al. (1999) Morphology identification of the thin film phases of vacuum evaporated pentacene on SiO_2 substrates. *Synth Met* 104: 175–178.

29. Govyadinov AA, Mastel S, Golmar F, et al. (2014) Recovery of Permittivity and Depth from Near-Field Data as a Step toward Infrared Nanotomography. *ACS Nano* 8: 6911–6921.

30. Seiki N, Shoji Y, Kajitani T, et al. (2015) Rational synthesis of organic thin films with exceptional long-range structural integrity. *Science* 348: 1122–1126.

31. Collins BA, Cochran JE, Yan H, et al. (2012) Polarized X-ray scattering reveals non-crystalline orientational ordering in organic films. *Nat Mater* 11: 536–543.

32. Hub C, Burkhardt M, Halik M, et al. (2010) In situ STXM investigations of pentacene-based OFETs during operation. *J Mater Chem* 20: 4884–4887.

33. Weickert J, Dunbar RB, Hesse HC, et al. (2011) Nanostructured Organic and Hybrid Solar Cells. *Adv Mater* 23: 1810–1828.

34. Westermeier C, Fiebig M, Nickel B (2013) Mapping of trap densities and hotspots in pentacene thin-film transistors by frequency-resolved scanning photoresponse microscopy. *Adv Mater* 25: 5719–5724.

Clemens Liewald, Stefan Mastel, Jeffrey Hesler, Andreas J. Huber, Rainer Hillenbrand, and Fritz Keilmann

Abstract
Probing conductivity in a contactless way with nanoscale resolution is a pressing demand in such active fields as quantum materials, superconductivity, and molecular electronics. Here, we demonstrate a laser- and cryogen-free microwave-technology-based scattering-type scanning near-field optical microscope powered by an easily aligned free-space beam with a tunable frequency up to $0.75\,\text{THz}$. It uses Schottky diode components to record background-free amplitude and phase nano-images, for the first time in the terahertz range, which is uniquely sensitive for assessing conduction phenomena. Images of Si with doped nanostructures prove a conductance sensitivity corresponding to $10^{16}\,\text{cm}^{-3}$ mobile carriers, at $50\,\text{nm}$ spatial resolution.

Contribution
Experimental work for setting up the instrumentation was done by Stefan Mastel, Jeffrey Helser, Fritz Keilmann, and myself. I measured, calculated, and analyzed the data. The Manuscript was written by Fritz Keilmann and myself.

All-electronic terahertz nanoscopy

Clemens Liewald,[1,2] Stefan Mastel,[3] Jeffrey Hesler,[4] Andreas J. Huber,[5] Rainer Hillenbrand,[6,7] and Fritz Keilmann[1,*]

[1]Fakultät für Physik & Center for NanoScience (CeNS), Ludwig-Maximilians-Universität, 80539 München, Germany
[2]Nanosystems Initiative Munich, 80799 München, Germany
[3]CIC nanoGUNE, 20018 Donostia-San Sebastián, Spain
[4]Virginia Diodes Inc., Charlottesville, Virginia 22901, USA
[5]Neaspec GmbH, 82512 Martinsried, Germany
[6]CIC nanoGUNE and UPV/EHU, 20018 Donostia-San Sebastián, Spain
[7]IKERBARSQUE, Basque Foundation of Science, 48013 Bilbao, Spain
*Corresponding author: fritz.keilmann@lmu.de

Probing conductivity in a contactless way with nanoscale resolution is a pressing demand in such active fields as quantum materials, superconductivity, and molecular electronics. Here, we demonstrate a laser- and cryogen-free microwave-technology-based scattering-type scanning near-field optical microscope powered by an easily aligned free-space beam with a tunable frequency up to 0.75 THz. It uses Schottky diode components to record background-free amplitude and phase nano-images, for the first time in the terahertz range, which is uniquely sensitive for assessing conduction phenomena. Images of Si with doped nanostructures prove a conductance sensitivity corresponding to 10^{16} cm^{-3} mobile carriers, at 50 nm spatial resolution.   © 2018 Optical Society of America under the terms of the OSA Open Access Publishing Agreement

1. INTRODUCTION

Scattering-type scanning near-field optical microscopy (s-SNOM) provides ~20 nm resolution at any frequency from ultraviolet to microwave [1], where the far-infrared region is in high demand in solid-state physics. Signatures of Drude-type semiconductors allow quantification of carrier concentration to low values, while signatures of non-Drude materials such as transition metal oxides and organic conductors reveal underlying rich physics of correlated electrons entangled by charge, orbital, spin, and lattice degrees of freedom [2]. Such behavior leads to exotic materials like correlated quantum matter, highly susceptible to external perturbation and hence showing intrinsic phase complexities, examples of which are unconventional superconductors, multiferroics, or Mott insulators [3]. Characteristic length scales of intrinsic phase separation reach far below an infrared wavelength and thus call for applying advanced near-field nanoscopy methods that have emerged over the past two decades. In s-SNOM, a metal AFM tip is illuminated by a focused light that concentrates at the tip apex and interacts with a sample. Scattered light is coherently detected, simultaneously with topography, such that scanning generates two optical images, one of the scattering efficiency amplitude s, the other of the phase φ of scattering [1]. A former attempt at far-infrared s-SNOM imaging suffered from demanding instrumentation, especially a liquid He-cooled detector with

inadequate dynamic range that was inadequate for determining phase contrast [4]. Pioneering microwave s-SNOMs [5,6] based on waveguide-connected tips demonstrated [5] the principle of tip-confined optical nanoscopy, the use of interferometry to record amplitude and phase images, and the value of electrostatic theory for understanding the near-field interaction mechanism. Here, we introduce a terahertz (THz) s-SNOM where a high-frequency microwave circuit connects via free space with a standard s-SNOM (Fig. 1) and achieves high S/N and thus fast imaging, with no need to use a beamsplitter for cooling, or an external detector.

2. EXPERIMENT

The THz transceiver, custom-built by Virginia Diodes Inc., features high-harmonic (54th) generation of a synthesized microwave at frequency ω, which is precisely and quickly tunable from 9 to 14 GHz, to launch a vertically polarized, diverging THz beam of ~10 μW from a 1.3 mm × 2.5 mm aperture, tunable from 0.5 to 0.75 THz. The solid-state multiplication chain consists of transistor-based amplifiers and Schottky diodes mounted in a hollow metal waveguide (depicted as red in the circuit scheme of Fig. 1). By band filtering and the use of balanced multiplier designs, a clean 54th-harmonic output is achieved. In addition, the transceiver redirects any THz radiation that propagates backward from the launching aperture via an internal
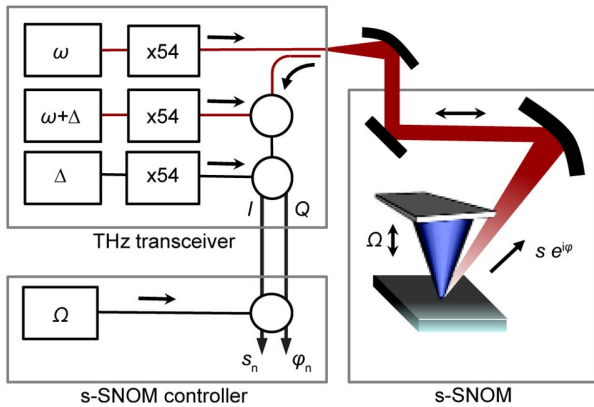
Fig. 1. Sketch of s-SNOM illuminated by a free-space THz beam, tunable between 0.5 and 0.75 THz, from a microwave–harmonic transceiver circuit that also provides heterodyne detection of back-propagating THz waves and generates output signals I and Q. These signals become demodulated in the s-SNOM controller at low-order harmonics n of the tip tapping frequency Ω, to generate simultaneous, background-free near-field amplitude and phase images together with topography.

waveguide directional coupler, and downconverts it to a 50 MHz signal using a Schottky diode mixer (see operation principle in Supplement 1) depicted as the upper circle in Fig. 1. For this heterodyne detection process, in our realization of backscattered THz light from the probing tip, the reference wave is generated by ×54 multiplication of a synthesized microwave at frequency $\omega + \Delta$ with $\Delta = 0.926$ MHz chosen such that the mixer generates the IF (intermediate frequency) signal at a fixed frequency of $54 \times 0.926 = 50$ MHz, independently of the tuning of ω (i.e., of both THz frequencies).

A single 90° off-axis paraboloidal mirror of 50 mm effective focal length couples the THz beam to and from a standard s-SNOM (NeaSNOM of Neaspec GmbH; see photograph in Supplement 1 [Fig. S1]); its alignment is facilitated by a pilot beam (not shown) from the second, opposite input port of the NeaSNOM. A commercial full-metal tip of 80 μm shaft length (Rocky Mountain 25PT200B-H), five times longer than in common infrared s-SNOMs, provides sizable (even if not optimal) antenna efficiency at the long wavelength of 500 μm corresponding to 0.6 THz. An initial alignment of the s-SNOM's internal paraboloidal mirror is uncritical as expected from the large focal volume.

Note that the IF signal faithfully replicates amplitude s and phase φ of the tip-backscattered THz radiation, and furthermore, that the present scheme is a low-frequency analog of the first heterodyne, complex-contrast and background-free s-SNOM that worked in the visible [7]. The IF signal is fed to an I-Q Schottky mixer, depicted as the middle circle in Fig. 1, together with a reference signal at $54 \times \Delta$. This unit forms two output signals, I and Q, because it contains two mixers of which one has its reference wave delayed by 90°. Both are fed into the standard electronics controller of the s-SNOM, which determines their modulation components simultaneously for several harmonics of the tip tapping frequency Ω. Recall the tip oscillates normally to the sample surface; in this work with 200 nm amplitude, it oscillates at the cantilever's resonance frequency of 70 KHz. Selecting a component with a harmonic number high enough guarantees suppression of unwanted background-scattered radiation, and thus pure near-field imaging [1]. A unique practical advantage of synthesized microwaves is their

tight control of frequency to <1 Hz, because this allows a temporarily offsetting of Δ by a few Hz, such that both I-Q mixer outputs visibly oscillate between their extreme levels and thus facilitate the final alignment of the s-SNOM's internal paraboloidal mirror in all translational degrees of freedom.

3. RESULTS

The THz s-SNOM's performance is demonstrated with an all-Si sample (SRAM, available from Bruker Nano Inc.) that exhibits multiply repeated nanostructures of various doping levels and also high topographic steps that allow their recognition in any microscope. Figure 2 displays the 0.6 THz image (cut from the larger one in Supplement 1, Fig. S2, left) of the SRAM sample. Both amplitude s_3 and phase φ_3 images exhibit topography-induced stripes next to high topography steps due to an "edge-darkening" effect [1]. Otherwise, the THz images distinguish several regions with differing amplitude and phase contrasts, indicating varied conditions of the free carrier population; namely, carrier type, density, and mobility. In passing, note dark dots in the amplitude image that correlate with topography humps; we assign them to low-refractive-index dust particles of about 50 nm height, preventing the tip from reaching the surface whereby they reduce the strength of the near-field interaction but not its phase. Four regions (A–D) are depicted in Fig. 2 by dashed boxes, which show homogeneous THz contrasts and are assigned by the supplier of
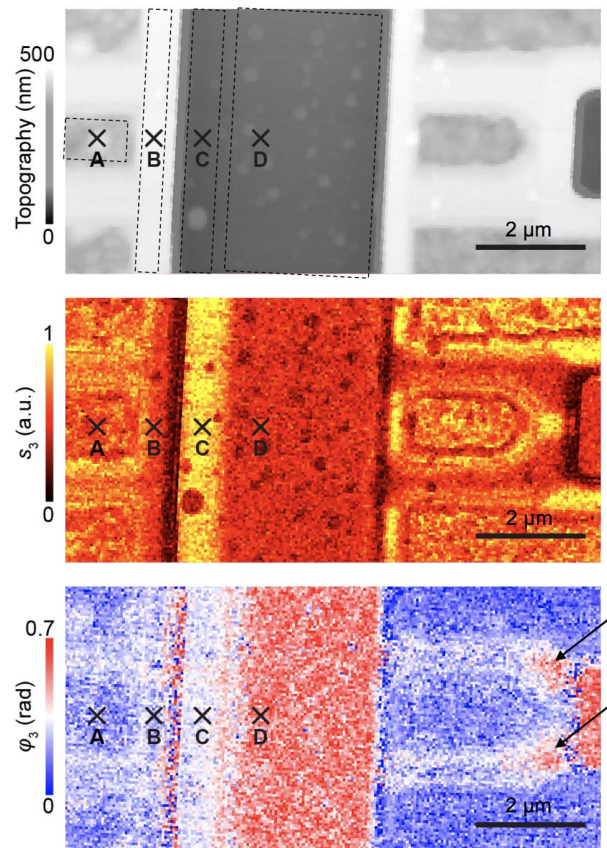
Fig. 2. Single-frequency 0.6 THz s-SNOM of Si exhibiting topographical as well as doping nanostructures, namely, the simultaneously recorded topography (top), THz amplitude s_3 (mid), and THz phase φ_3 nano-images (bottom); acquisition time, 10 min.
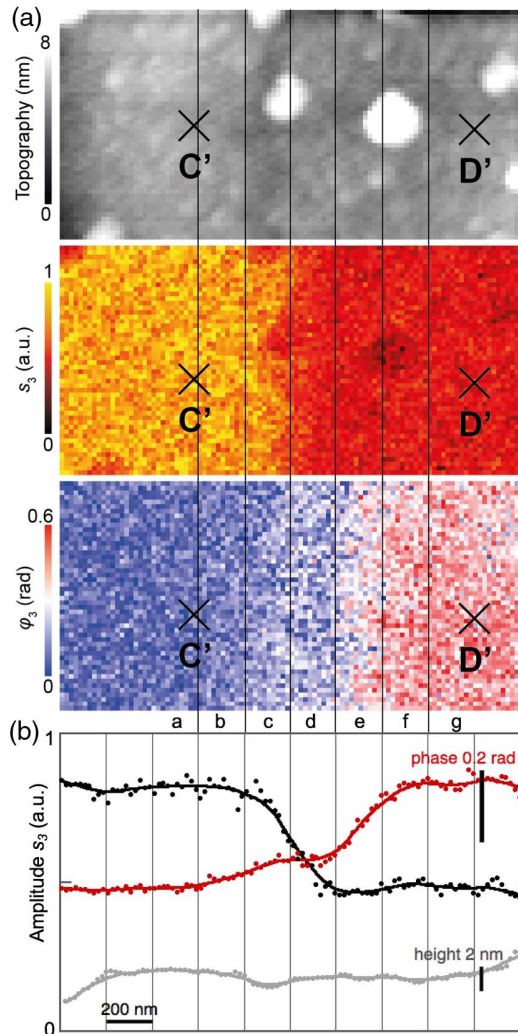
Fig. 3. Single-frequency 0.6 THz s-SNOM image (1 μm × 2 μm) of Si as in Fig. 2 extending over the edge of the ion-implanted region C'. (a) Simultaneously recorded topography (top), THz amplitude s_3 (mid), and THz phase φ_3 (bottom); acquisition time, 2.5 min; (b) Line profiles (dots) along the full 2 μm width of the image (a), height (grey), amplitude (black), and phase (red) obtained by averaging the lower 400 nm each of the respective images; curves are obtained by smoothing.

the Si test structure with the following characteristics. D is the homogeneously p-doped substrate with nominal hole density of $2 \cdot 10^{16}$ cm^{-3}. The others are ion implanted: A, p-type with hole density $4 \cdot 10^{19}$ cm^{-3}; and B and C, n-type with electron densities of $2 \cdot 10^{20}$ cm^{-3} and $2 \cdot 10^{17}$ cm^{-3}, respectively.

At the tapping amplitude of 200 nm used in Figs. 2 and 3, and Supplement 1, Fig. S2, left, the scattering signals are nearly background-free already in the second tapping harmonic, and certainly background-free in the third harmonic images presented in this work. This is proven by approach curves in the Supplement 1, Fig. S3, where the THz amplitude s_3 decays to 20% at a tip-sample distance z of about 50 nm. This behavior is compatible with the specified tip radius of the order of 50 nm, and thus, with a 50 nm lateral resolution as well as a 50 nm effective probing depth into the Si sample [1].

The arrows in the phase image of Fig. 2 point to two ∼500 nm wide regions of distinct contrast, which are not mentioned in the sample's description; also, they are not visible in its mid-infrared s-SNOM nano-image (Supplement 1, Fig. S2b). While following their origin would be beyond the scope of the present paper, they directly illustrate our method's sensitivity to low carrier density.

Next, we demonstrate the capability of 0.6 THz s-SNOM to map low carrier-density gradients, by recording a higher-resolved image of the transition region between areas C and D. The images in Fig. 3 reveal an interesting substructure across the doping edge, as each of the three observables in s-SNOM, topography, THz amplitude, and THz phase seemingly have the edge at different positions, offset up to hundreds of nm. As seen in Fig. 3(b) in detail, the amplitude decreases evenly over a ∼300 nm distance covering sections b and c; the topography features a 1 nm deep depression within section b only; the phase increases monotonically over ∼500 nm distance covering sections a to e, but stays constant within section c. Obviously, the transition between n-type and p-type regions studied here extends over a ∼500 nm distance.

4. THEORY

To understand these contrasts, we recall that the dielectric response due to charge carriers of density n_c moving freely in a neutral medium (plasma) is governed by the dynamical conductivity $\sigma(\omega)$, which in Drude approximation is constant from DC up to the plasma frequency ω_p. The plasma frequency scales with the carrier density n_c and mass m_c as $\omega_p \approx \sqrt{n_c/m_c}$, and lies in the visible for metals. Near-field interaction with a Drude-type semiconductor leads to a resonant response characterized by a phase peak and an amplitude step near ω_p, as was first predicted using the point dipole model of near-field interaction and verified experimentally at high $n_c \approx 10^{19}$ cm^{-3} in the mid-infrared [8]. The first far-infrared nano-imaging of carrier distributions at 2.5 THz [4] demonstrated sensitivity from the 10^{18} to below 10^{17} cm^{-3} range, which is centrally important for semiconductor science and technology (that demonstration was a *tour de force* because of the required, low-dynamic-range superconducting detector [4]). To focus on our observed contrasts in Fig. 3, we calculate the complex near-field response at 0.6 THz using the finite dipole model of tip-sample near-field interaction (effective tip length 600 nm, tip radius 50 nm, illumination angle 60°) [1,9]. The extended Drude dielectric data of Si were calculated from literature values for the mass and mobility of electrons and holes, respectively [10,11,12]. The theory result in Fig. 4 demonstrates a clear difference between electrons and holes, especially that a Drude resonance at 0.6 THz can arise from either an electron density of $3 \cdot 10^{16}$ cm^{-3} or a hole density of $8 \cdot 10^{16}$ cm^{-3}. Such densities are of the same order of magnitude as those specified by the sample supplier for areas C and D depicted in Fig. 2. In passing, we point out that our s-SNOM imaging of the same sample in the mid-infrared (see Supplement 1, Fig. S2) shows no contrast in areas C and D; indeed, at that 45-fold higher frequency (27 THz), a Drude resonance would necessitate a 2000-fold higher carrier density.

5. DISCUSSION

The curves in Fig. 4 predict that for Si, even a single-frequency measurement of s-SNOM amplitude and phase at 0.6 THz can
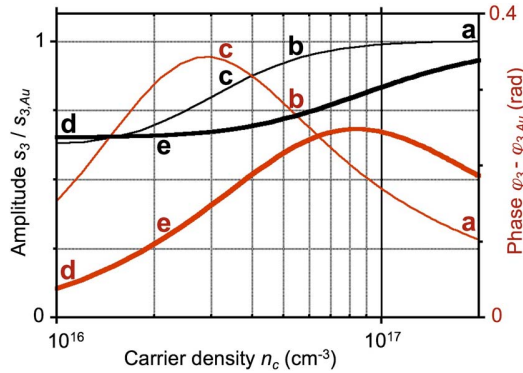
Fig. 4. Predicted 0.6 THz s-SNOM scattering amplitude s_3 (black) and scattering phase φ_3 (red) of Si, relative to Au, versus carrier density for electrons (thin curves) and holes (thick curves). Letters tentatively placed next to these curves correspond to the sections a–e of the n-p transition region investigated in Fig. 3.

both identify the carrier type and quantify the carrier density in the 10^{16} to $>10^{17}$ cm^{-3} range. To do so, the mass and mobility of electrons and holes must be known and the measurement must be calibrated with a known reference material such as Au. This calibration was not attempted in the present study, however, considering that the unknown depth profile of ion implantation in area C should cause problems of interpretation. Clearly, a similarly qualitative and quantitative material characterization is possible with our method, not only for doped semiconductors but for any conducting or even dielectric system whose dielectric function exhibits contrast in the THz region.

The predictions of Fig. 4 can qualitatively explain several features of the experimental near-field profiles of Fig. 3(b). Consider first the region D', which represents p-type Si substrate of nominal density $n_h = 2 \cdot 10^{16}$ cm^{-3}, certainly a standard substrate homogeneous throughout the depth of the probing near-field into the sample. Approaching the edge of the doped area C', starting from around D' along sections e and d, reveals that the phase decreases but the amplitude stays constant, just as predicted by the thick curves in Fig. 4, for the case that n_h decreases from about $2 \cdot 10^{16}$ cm^{-3} to a lower value because of recombination with electrons. A second example is the approach to the edge from around C' along sections a, b, and c, where we observe a decreasing amplitude and an increasing phase, also just as Fig. 4 (thin curves) would predict for an electron density decrease from $n_e \approx 2 \cdot 10^{17}$ cm^{-3} to $\approx 3 \cdot 10^{16}$ cm^{-3}. Other observed features, such as a mismatch of predicted phases in sections c and d close to the edge, need further consideration that goes beyond the scope of this paper. In fact, the significant depression of the surface in section b is an indication that the doping/annealing process may have produced a more complex nanostructure in the n-p transition than simple in-plane density gradients (one process step for area C' was implanting 900 kV P^+ ions that, according to literature, deposit acceptors primarily in 1 ± 0.5 μm depth below the surface).

6. OUTLOOK

There are two promising extensions of the presented nano-imaging, which would allow further insight. One is the established tomography method of s-SNOM, which can detect

sub-surface layers and quantify depth profiles by systematically varying the tapping conditions or analyzing different demodulation orders [12–15]. The other is to repeat nano-imaging at precisely varied (>8 digits of precision) transceiver frequencies anywhere between 0.5 and 0.75 THz with the present device (0.75 to 1.1 THz with a new model being developed). Tuning can currently be achieved within 3 ms and should enable fast spectroscopic s-SNOM acquiring half-octave-wide THz point spectra in a matter of seconds. For comparison, time-domain THz nano-spectroscopy covering a decade of frequencies centered around 0.7 THz has matured from early demonstrations [16,17] into a commercial product (neaspec.com) that has recently enabled taking amplitude-and-phase point spectra of the present sample in a few min/pixel acquisition time [18,19].

7. CONCLUSION

We conclude that our all-electronic THz nano-imaging is capable of quantifying conductivity of lowly doped semiconductors not only on the 50 nm scale in a matter of few min acquisition time for a 10,000 pixel image, but also at sub-order-of-magnitude precision in carrier density, including identification of carrier type, without a calibration procedure, as required with microwave-impedance-measuring AFMs [6,20]. Moreover, all-electronic THz s-SNOM is ready for correlative microscopy using infrared or Raman channels to be operated from the second port of the NeaSNOM nanoscope. A practical advantage of our all-electronic THz nanoscope is that THz generation and coherent detection are both contained and permanently aligned inside a compact device. No cryogenic detectors are needed, as is the case with lasers or synchrotrons, and, indeed, no external detector must be operated, as with time-domain THz systems.

All-electronic THz nanoscopy opens up fast and simple nanoscale probing to a wealth of actively studied physics phenomena and materials exhibiting low, exotic, and/or non-Drude conduction mechanisms, such as in high-Tc superconductivity, ballistic transport, charge density wave, or electronic phase separation, in conventional as well as in quantum materials like topological insulators and polaritonic two-dimensional materials, or in molecular electronics.

See Supplement 1 for supporting content.

REFERENCES

1. F. Keilmann and R. Hillenbrand, "Near-field nanoscopy by elastic light scattering from a tip," in *Nano-Optics and Near-Field Optical Microscopy*, A. V. Zayats and D. Richards, eds. (Artech House, 2009).
2. S. V. Dordevic and D. N. Basov, "Electrodynamics of correlated electron matter," Ann. Phys. **15**, 545–570 (2006).
3. M. Liu, A. J. Sternbach, and D. Basov, "Nanoscale electrodynamics of strongly correlated quantum materials," Rep. Prog. Phys. **80**, 014501 (2016).

4. A. J. Huber, F. Keilmann, J. Wittborn, J. Aizpurua, and R. Hillenbrand, "Terahertz near-field nanoscopy of mobile carriers in single semiconductor nanodevices," Nano Lett. **8**, 3766–3770 (2008).

5. F. Keilmann, D. W. V. D. Weide, T. Eickelkamp, R. Merz, and D. Stöckle, "Extreme sub-wavelength resolution with a scanning radio-frequency transmission microscope," Opt. Commun. **129**, 15–18 (1996).

6. A. Imtiaz, S. M. Anlage, J. D. Barry, and J. Melngailis, "Nanometer-scale material contrast imaging with a near-field microwave microscope," Appl. Phys. Lett. **90**, 143106 (2007).

7. R. Hillenbrand and F. Keilmann, "Complex optical constants on a sub-wavelength scale," Phys. Rev. Lett. **85**, 3029–3032 (2000).

8. B. Knoll and F. Keilmann, "Infrared conductivity mapping for nanoelectronics," Appl. Phys. Lett. **77**, 3980–3982 (2000).

9. A. Cvitkovic, N. Ocelic, and R. Hillenbrand, "Analytical model for quantitative prediction of material contrasts inscattering-type near-field optical microscopy," Opt. Express **15**, 8550–8565 (2007).

10. G. Masetti, M. Severi, and S. Solmi, "Modeling of carrier mobility against carrier concentration in arsenic-, phosphorus-, and boron-doped silicon," IEEE Trans. Electron. Devices **30**, 764–769 (1983).

11. D. M. Riffe, "Temperature dependence of silicon carrier effective masses with application to femtosecond reflectivity measurements," J. Opt. Soc. Am. B **19**, 1092–1100 (2002).

12. J. M. Stiegler, A. J. Huber, S. L. Diedenhofen, J. Gomez Rivas, R. E. Algra, E. Bakkers, and R. Hillenbrand, "Nanoscale free-carrier profiling of individual semiconductor nanowires by infrared near-field nanoscopy," Nano Lett. **10**, 1387–1392 (2010).

13. J. Sun, J. C. Schotland, R. Hillenbrand, and P. S. Carney, "Nanoscale optical tomography using volume-scanning near-field microscopy," Appl. Phys. Lett. **95**, 121108 (2009).

14. M. Eisele, T. L. Cocker, M. A. Huber, M. Plankl, L. Viti, D. Ercolani, L. Sorba, M. S. Vitiello, and R. Huber, "Ultrafast multi-terahertz nano-spectroscopy with sub-cycle temporal resolution," Nat. Photonics **8**, 841–845 (2014).

15. K. Moon, H. Park, J. Kim, Y. Do, S. Lee, G. Lee, H. Kang, and H. Han, "Subsurface nanoimaging by broadband terahertz pulse near-field microscopy," Nano Lett. **15**, 549–552 (2014).

16. F. Buersgens, H.-T. Chen, and R. Kersting, "Terahertz microscopy of charge carriers in semiconductors," Appl. Phys. Lett. **88**, 112115 (2006).

17. H.-G. von Ribbeck, M. Brehm, D. W. van der Weide, S. Winnerl, O. Drachenko, M. Helm, and F. Keilmann, "Spectroscopic THz near-field microscope," Opt. Express **16**, 3430–3438 (2008).

18. F. Huth and Y. Abate, (personal communication, 2017).

19. M. C. Giordano, S. Mastel, C. Liewald, L. L. Columbo, M. Brambilla, L. Viti, A. Politano, K. Zhang, L. Li, A. G. Davies, E. H. Linfield, R. Hillenbrand, F. Keilmann, G. Scamarcio, and M. S. Vitiello are preparing a manuscript to be called "Phase-resolved terahertz self-detection near-field microscopy."

20. A. Imtiaz, T. M. Wallis, S.-H. Lim, H. Tanbakuchi, H.-P. Huber, A. Hornung, P. Hinterdorfer, J. Smoliner, F. Kienberger, and P. Kabos, "Frequency-selective contrast on variably doped p-type silicon with a scanning microwave microscope," J. Appl. Phys. **111**, 93727 (2012).

a.3 photocurrent microscopy of contact resistance and charge carrier traps in organic field-effect transistors

Abstract

We use a pentacene transistor with asymmetric source drain contacts to test the sensitivity of scanning photocurrent microscopy (SPCM) for contact resistance and charge traps. The drain current of the device strongly depends on the choice of the drain electrode. In one case, more than 94 % of the source drain voltage is lost due to contact resistance. Here, SPCM maps show an enhanced photocurrent signal at the hole-injecting contact. For the other bias condition, i.e., for ohmic contacts, the SPCM signal peaks heterogeneously along the channel. We argue from basic transport models that bright areas in SPCM maps indicate areas of large voltage gradients or high electric field strength caused by injection barriers or traps. Thus, SPCM allows us to identify and image the dominant voltage loss mechanism in organic field-effect transistors.

Contribution

I designed the experiments. Daniel Reiser and myself prepared the samples, recorded and analyzed the data. Furthermore, I wrote the manuscript.

Photocurrent microscopy of contact resistance and charge carrier traps in organic field-effect transistors

C. Liewald,[1,2] D. Reiser,[1] C. Westermeier,[1] and B. Nickel[1,2,a]

[1]*Fakultät für Physik and Center for NanoScience (CeNS), Ludwig-Maximilians-Universität München, Geschwister-Scholl-Platz 1, 80539 Munich, Germany*
[2]*Nanosystems Initiative Munich, Schellingstrasse 4, 80799 Munich, Germany*

We use a pentacene transistor with asymmetric source drain contacts to test the sensitivity of scanning photocurrent microscopy (SPCM) for contact resistance and charge traps. The drain current of the device strongly depends on the choice of the drain electrode. In one case, more than 94% of the source drain voltage is lost due to contact resistance. Here, SPCM maps show an enhanced photocurrent signal at the hole-injecting contact. For the other bias condition, i.e., for ohmic contacts, the SPCM signal peaks heterogeneously along the channel. We argue from basic transport models that bright areas in SPCM maps indicate areas of large voltage gradients or high electric field strength caused by injection barriers or traps. Thus, SPCM allows us to identify and image the dominant voltage loss mechanism in organic field-effect transistors. *Published by AIP Publishing.*
[http://dx.doi.org/10.1063/1.4960159]

Organic field-effect transistors (OFETs) have a planar arrangement of the contacts which is beneficial for the investigation of charge transport on the micro- to nanoscale by scanning probe and microscopy techniques.[1–4] Injection barriers and electronic trap states obstruct the intrinsic charge transport of OFETs and pose critical challenges to the reproducibility of organic devices. Here, we explore scanning photocurrent microscopy (SPCM)[5] to obtain insight into the predominant limitation of an OFET. In SPCM, a focused laser is modulated and scanned across the transistor channel at ambient conditions. The light-induced current, the so-called photocurrent, is separated from the dark current by lock-in techniques. Previous SPCM measurements of pentacene OFETs showed qualitatively different spatial distributions of the SPCM signal.[6] One experiment with a line-shaped laser focus showed a strong SPCM signal near both contacts and was explained by a varying mobility and a distributed contact resistance.[7] In other experiments with a diffraction-limited, point-like laser beam, an inhomogeneous distribution along the source contact dominated the signal. This enhancement was attributed to the dissociation of excitons, charge extraction, and enhanced injection of holes by lowering the injection barrier.[8,9] On the other hand, large area illumination of trap states in pentacene diodes was also reported to cause photoresponse by trap release.[10] Indeed, SPCM allowed observing a dispersed and structured SPCM signal within the transistor channel, interpreted as charge release from local trap densities.[11] However, a consistent description that combines the microscopic phenomena for thin-film transistors near contacts and within the channel is still missing.

Here, we elucidate the physical mechanisms that evoke SPCM signals in OFETs by making use of a pentacene transistor with asymmetric contacts. Asymmetric contacts are present in the case of a contact resistance which depends on the polarity of the source-drain voltage, i.e., the injection barrier for one of the source-drain contacts is considerably larger.[12] Such a behavior unintentionally occurs in some devices, due to fabrication imperfections. However, the asymmetric device can be used for studying the sensitivity of SPCM toward contact resistance and other imperfections. Switching the source-drain voltage polarity without changing other physical parameters allows for imaging the same device in high and low contact resistance mode. We find that an operation in high contact resistance mode results in a SPCM enhancement exclusively at the contacts, whereas an operation of the same device in low contact resistance mode allows us to observe the SPCM signal deep within the channel, due to trap states. We argue that high contact resistance acts as a voltage divider, significantly reducing the potential and electric field within the transistor channel.[4,13] SPCM is sensitive to areas with high electric field, which occur at the contacts for injection-limited devices and at areas of high trap densities for devices with low resistance ohmic contacts.

The investigated pentacene transistors were fabricated on highly n-doped silicon wafers (CrysTec) with an 82 nm thick, thermally grown SiO_2 layer as a gate dielectric. To clean the substrate, it was subsequently sonicated in acetone and isopropyl alcohol, for 10 min each, and rinsed with deionized (DI) water. Afterward, the substrate was cleaned in piranha solution, with three parts of sulfuric acid (H_2SO_4) and one part of hydrogen peroxide (H_2O_2), for 35 min and rinsed with DI water. Finally, the substrate was cleaned with oxygen plasma for 3 min. On top of the cleaned SiO_2 layer, a 5 nm thick film of cyclic olefin copolymer (COC, TOPAS 6013S-04) was spin-coated from a 0.25 wt. % solution in toluene and subsequently annealed for 2 min at 100 °C. A 30 nm thick layer of pentacene was evaporated with a deposition rate of 0.08 Å/s at a substrate temperature of about 60 °C and a pressure of 4×10^{-8} mbar. As source and drain top contacts, a 2 nm thick titanium layer was evaporated with a deposition rate of 0.5 Å/s, followed by a 30 nm thick gold layer with a

a)Electronic mail: nickel@lmu.de

deposition rate of 0.8 Å/s. The contacts were defined by shadow masks, resulting in a transistor length of 23 μm and a width of 1 mm. After the deposition process, the sample was glued with conductive silver lacquer into a chip-carrier and wire-bonded. A scheme of the complete transistor layout is shown in Figure 1. On this sample, the two investigated transistors are referred to as transistor I and transistor II.

The working principle of the used SPCM setup is also shown in Figure 1. A HeNe laser at 633 nm wavelength impinges on the OFET with a rectangular pulse shape at a frequency of 5.5 kHz. At this pulse frequency, SPCM is sensitive to both signal contributions, the depopulation of trap states and the exciton dissociation.[11] The intensity of the focused, diffraction-limited laser spot is set to 2 μW and is typically Gaussian distributed with a diameter of about 600 nm. To scan the transistor channel in x- and y-direction across the fixed laser focus, the sample is mounted on an xyz-stage (ANPx/z101/RES, ANC350, Attocube Systems). Two power supply units (7651, Yokogawa) are used to apply the drain and gate voltages with respect to source. The source contact is grounded via a current-to-voltage converter (DLPCA-200, Femto), which is read out by a voltmeter (34410A, Agilent) and a lock-in amplifier (7265, SIGNAL RECOVERY). The voltmeter reads out the DC transistor current I_{DS} between the source and drain, while the lock-in amplifier reads out the AC signal $I_{photo}(\vec{x})$ induced from the pulsed laser at the position $\vec{x} = (x, y)$. For an illumination with a diffraction-limited spot, the amplitude of $I_{photo}(\vec{x})$ is at least three orders of magnitude lower than the dark transistor current I_{DS}.[9,11,14] To ensure a precise positioning of the sample and to correct possible drifts of the piezo step motors, the reflection intensity of the HeNe laser is simultaneously recorded with a photodiode. The used setup is described elsewhere in more detail.[8,11] We call the 2D representation of the $I_{photo}(\vec{x})$ signal a scanning photocurrent microscopy (SPCM) map.

The transfer curves of transistor I for both polarities of the applied drain voltage $V_{DS} = -20$ V are shown in Figure 2(a). Technically, the polarization change was obtained by exchanging the wires at the source-drain contacts named A and B. In the preferential direction (AB direction—electrode A is source
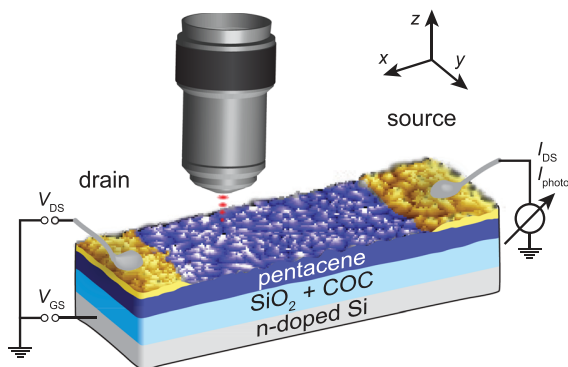
FIG. 1. Schematic of the SPCM setup. The drain voltage V_{DS} and gate voltage V_{GS} are applied against ground, the transistor current I_{DS} is detected between the source contact and ground. For recording a SPCM map, the pulsed laser is focused on the transistor channel and the sample is raster scanned in the xy-plane. The transistor current I_{DS} is analyzed with a lock-in amplifier to read out the SPCM signal I_{photo}.
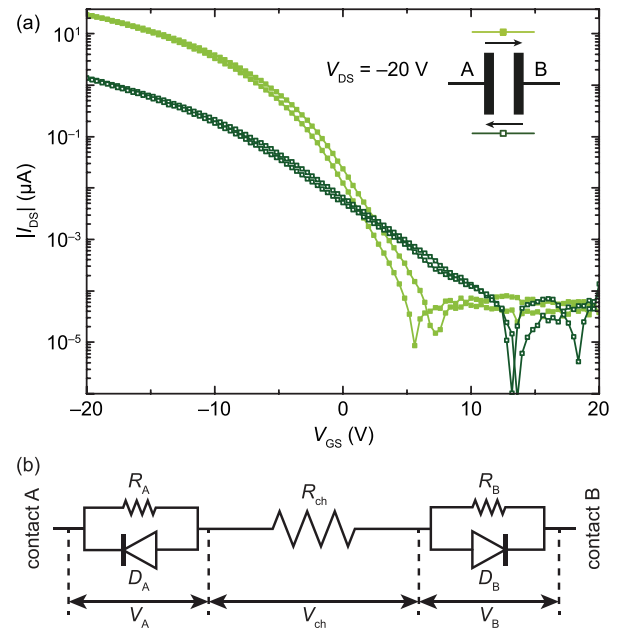
FIG. 2. (a) Transfer curves (forward and backward sweep) of transistor I for both bias polarities. The preferred AB direction (light green) exhibits a higher current and a lower turn-on voltage compared to the defective BA direction (dark green). Inset: schematic of the source drain contacts with the arrows indicating the polarity of the electric field. (b) Equivalent circuit for a field-effect transistor, represented by a diode and a resistance in parallel at each contact, and the channel resistance between the contacts. The resistances result in a voltage drop V_A, V_{ch}, and V_B, respectively.

and electrode B is drain), the charge carrier mobility was about 15 times higher than in the BA direction ($\mu_{AB} = 1.2 \times 10^{-2}$ cm^2 V^{-1} s^{-1}, $\mu_{BA} = 7.8 \times 10^{-4}$ cm^2 V^{-1} s^{-1})[15] if contact resistance is neglected. In other words, transistor I showed reasonable transfer characteristics in the AB direction but poor characteristics in the BA direction. The transfer curves, together with the mobility calculations for transistor I and, as a comparison, for the symmetric transistor II are summarized in the supplementary material.[15] As the channel itself acts as a tunable ohmic resistor R_{ch}, an injection barrier at the hole injecting electrode B in the BA configuration is most likely the origin of the asymmetric behavior.[8,12,16,17] To quantify this hypothesis, we adapt a minimal equivalent circuit from Elhadidy et al.,[18] which is shown in Figure 2(b). Here, each contact is represented by a diode and a resistance in parallel, and the channel is represented by an ohmic resistance. At the source contact (e.g., contact A in the AB direction), the diode D_A is biased in the reverse direction and the transistor current I_{DS} entirely flows through the resistance R_A, which accounts for the hole injection barrier at contact A. At the drain contact (e.g., contact B in AB direction), the diode D_B is biased in the forward direction and therefore, the transistor current entirely flows through this diode, assuming that hole extraction is not hindered. Thus, the applied drain-source bias V_{DS} drops across $R_A + R_{ch}$ in the AB direction and across $R_B + R_{ch}$ in the BA direction. Here, V_A and V_B are the potential drops across the specific contact and V_{ch} is the potential drop across the connecting channel. In order to estimate the contact resistance of the poor electrode B, we analyze the transistor behavior at negative gate bias ($V_{GS} = -20$ V).[17,19,20] The preferred AB direction sets an upper limit of the channel resistance

$R_{\rm ch} \leq R_{\rm A} + R_{\rm ch} = \frac{V_{\rm DS}}{I_{\rm DS}} = 0.84\,{\rm M\Omega}$. The contact resistance $R_{\rm B}$ at electrode B, which reduces the current in BA direction, is calculated from the total resistance in BA direction $R_{\rm BA}$ minus the channel resistance $R_{\rm ch}$ according to $R_{\rm B} = R_{\rm BA} - R_{\rm ch} \geq 15\,{\rm M\Omega} - 0.84\,{\rm M\Omega} \approx 14\,{\rm M\Omega}$. These two resistors act as a voltage divider. From this analysis, the main conclusion is that in the BA direction, approximately 94% of the voltage drops at the hole-injecting electrode B and only 6% drops across the channel. Note that this decomposition into channel and contact resistance can only be applied to an asymmetric device where one contact resistance $R_{\rm B}$ is much larger than the channel resistance $R_{\rm ch}$, which itself is much larger than the other contact resistance $R_{\rm A}$ (i.e., $R_{\rm B} \gg R_{\rm ch} \gg R_{\rm A}$). For symmetric devices, a different method for extracting the contact resistance needs to be applied.[17,19,20]

In the following, we apply SPCM in order to verify conclusions of the equivalent circuit model by a local probe. The recorded SPCM maps of transistor I, operated in AB and BA directions, are shown in Figure 3. Both maps were measured at the same sample area. The top part of each SPCM

map was recorded outside of the channel, i.e., beyond the extension of the pentacene film; thus, no signal is observed at this position. The boundaries of the source and drain electrodes are indicated as white dotted lines. The slight bending of the boundaries can be attributed to a drift of the piezo stepping motors. The operation in the AB direction ($V_{\rm DS} = -8\,{\rm V}$, $V_{\rm GS} = -16\,{\rm V}$, linear regime) is shown in Figure 3(a). Here, the SPCM map shows local hotspots of high photoresponse across the whole channel region. The characteristic timescale of the release and capture of trapped charges was determined by frequency resolved SPCM measurements.[11] Areas with high photoresponse are areas of high trap density, which contribute to the photocurrent via the depopulation of occupied charge traps by triplet excitons.[11]

In contrast, the SPCM map in the BA direction is strikingly different (Figure 3(b)). An inhomogeneous signal next to the B electrode dominates the SPCM map, which can be attributed to dissociation of excitons into free charge carriers and to an enhanced injection of holes by lowering the injection barrier.[8,9] Logarithmic line profiles of the SPCM maps across both electrodes and the transistor channel (single line and the averaged profile over 50 lines) are shown in Figure 3(c). In the BA direction, they reveal a faint SPCM signal (0.015 nA) in the center of the transistor channel. In the supplementary material, balanced SPCM maps of the symmetric transistor II are shown for comparison.[15]

Apparently, the SPCM maps correlate directly with the regions of high electric field strength, which is at electrode B for high contact resistance in the inferior BA bias direction and within the channel in regions of high trap density in the superior AB bias direction. To quantify this assumption, we rationalize that illuminating a pentacene OFET locally (600 nm) gives rise to an enhanced current density $\vec{j}_{\rm photo} = \sigma \vec{E}$. Two contributions to the current density $\vec{j}_{\rm photo} = \vec{j}_{\rm pr} + \vec{j}_{\rm pc}$ have been identified. The first one is photoresponse $\vec{j}_{\rm pr} = p_{\rm released}(\vec{x})\,e\mu\vec{E}(\vec{x})$, originating from the release of trapped charge carriers due to triplet excitons from a local illumination. Here, $p_{\rm released}(\vec{x})$ is the density of released charge carriers, μ is the intrinsic mobility, and $\vec{E}(\vec{x})$ is the lateral field strength at the spot of illumination. The second contribution is photocurrent $\vec{j}_{\rm pc} = p_{\rm split}(\vec{E}, \vec{x})e\mu\vec{E}(\vec{x})$, evoked by exciton splitting and charge separation at the illuminated point. Note that photocurrent $\vec{j}_{\rm pc}$ does not occur at low field strengths because free charge carriers recombine with charged trap states,[21] i.e., significant charge carrier densities $p_{\rm split}(\vec{E}, \vec{x})$ are only expected in regions of large voltage drops. Both contributions scale with the electric field strength $\vec{E}(\vec{x})$ along the channel. Qualitatively, SPCM is sensitive to regions of high electric field, i.e., large voltage drops due to traps and contact barriers. Therefore, SPCM can be added to the group of microscopy methods which map the local electric field, like optical second-harmonic generation[3,20] and Kelvin probe microscopy.[1,4,5] A detailed analysis of SPCM maps combined with the electric potential measured by, e.g., Kelvin probe would be an interesting endeavor to separate photocurrent and photoresponse in OFET devices, i.e., charge separation and trap release, respectively.

In summary, we analyzed scanning photocurrent microscopy maps from a pentacene OFET with asymmetric contacts. Devices with large injection barriers show an enhanced

FIG. 3. SPCM maps of transistor I in the linear regime. The boundaries of the contacts A and B are indicated by the white, dotted lines. The arrows indicate the polarity of the electric field. (a) AB direction. The SPCM map shows photoresponse with local hotspots of areas with high trap density. (b) BA direction. The SPCM map shows photocurrent, mainly located at the boundary of the source contact, with decreasing intensity underneath the contact and a suppressed photoresponse within the transistor channel. (c) Logarithmic line profile of a single line (AB direction: filled squares, BA direction: open squares) and averaged over 50 lines (continuous lines).

SPCM signal at the limiting contact. For ohmic contacts, SPCM maps peak in the regions of high trap state density within the accumulation channel of the OFET. In both cases, the SPCM signal scales qualitatively with the local electric field. SPCM is a valuable microscopy technique allowing for imaging of the dominant defective regions in organic devices with a lateral resolution of about 600 nm at ambient conditions. SPCM can also be applied to heterojunction devices of 2D materials, which intrinsically show high electric fields,[22] or to connected devices in an integrated circuit. Here, SPCM could be adapted for quality control.

Note added in Proof. Recently, insufficient gate overlap was reported to cause asymmetric contact resistance in organic transistors.[23]

[1]K. P. Puntambekar, P. V. Pesavento, and C. D. Frisbie, Appl. Phys. Lett. **83**, 5539 (2003); M. Ando, S. Heike, M. Kawasaki, and T. Hashizume, *ibid.* **105**, 193303 (2014).

[2]J. Zaumseil, R. H. Friend, and H. Sirringhaus, Nat. Mater. **5**, 69 (2006); C. Hub, M. Burkhardt, M. Halik, G. Tzvetkov, and R. Fink, J. Mater. Chem. **20**, 4884 (2010); C. Westermeier, A. Cernescu, S. Amarie, C. Liewald, F. Keilmann, and B. Nickel, Nat. Commun. **5**, 4101 (2014); C. Liewald, S. Noever, S. Fischer, J. Roemer, T. U. Schülli, and B. Nickel, AIMS Mater. Sci. **2**, 369 (2015).

[3]T. Manaka, E. Lim, R. Tamura, and M. Iwamoto, Nat. Photonics **1**, 581 (2007).

[4]R. Scholz, D. Lehmann, A. D. Müller, F. Müller, and D. R. T. Zahn, Phys. Status Solidi A **205**, 591 (2008).

[5]R. Graham and D. Yu, Mod. Phys. Lett. B **27**, 1330018 (2013).

[6]A. Masurkar and I. Kymissis, Appl. Phys. Rev. **2**, 031101 (2015).

[7]Z. Jia, S. Meng, and I. Kymissis, IEEE Electron Device Lett. **31**, 761 (2010).

[8]M. Fiebig, C. Erlen, M. Göllner, P. Lugli, and B. Nickel, Appl. Phys. A **95**, 113 (2009).

[9]A. W. Tsen, F. Cicoira, G. G. Malliaras, and J. Park, Appl. Phys. Lett. **97**, 023308 (2010).

[10]X. Qiao, C. Zhao, B. Chen, and L. Luan, Appl. Phys. Lett. **105**, 033303 (2014).

[11]C. Westermeier, M. Fiebig, and B. Nickel, Adv. Mater. **25**, 5719 (2013).

[12]W. Chen, S. Qin, X.-A. Zhang, S. Zhang, J. Fang, G. Wang, C. Wang, L. Wang, and S. Chang, Appl. Phys. Lett. **104**, 083115 (2014).

[13]M. Gruber, F. Schürrer, and K. Zojer, Org. Electron. **13**, 1887 (2012).

[14]M. Breban, D. B. Romero, S. Mezhenny, V. W. Ballarotto, and E. D. Williams, Appl. Phys. Lett. **87**, 203503 (2005).

[15]See supplementary material at http://dx.doi.org/10.1063/1.4960159 for an evaluation of the transfer curves of both transistors and SPCM maps of transistor II.

[16]L. Bürgi, H. Sirringhaus, and R. H. Friend, Appl. Phys. Lett. **80**, 2913 (2002).

[17]M. Gruber, E. Zojer, F. Schürrer, and K. Zojer, Adv. Funct. Mater. **23**, 2941 (2013).

[18]H. Elhadidy, J. Sikula, and J. Franc, Semicond. Sci. Technol. **27**, 015006 (2012).

[19]D. J. Gundlach, L. Zhou, J. A. Nichols, T. N. Jackson, P. V. Necliudov, and M. S. Shur, J. Appl. Phys. **100**, 024509 (2006).

[20]M. Nakao, T. Manaka, M. Weis, E. Lim, and M. Iwamoto, J. Appl. Phys. **106**, 014511 (2009).

[21]R. R. Chance and C. L. Braun, J. Chem. Phys. **59**, 2269 (1973).

[22]H. Chen, N. Cheng, W. Ma, M. Li, S. Hu, L. Gu, S. Meng, and X. Guo, ACS Nano **10**, 436 (2016); D. Jariwala, S. L. Howell, K.-S. Chen, J. Kang, V. K. Sangwan, S. A. Filippone, R. Turrisi, T. J. Marks, L. J. Lauhon, and M. C. Hersam, Nano Lett. **16**, 497 (2016); Z. Yang, R. Grassi, M. Freitag, Y.-H. Lee, T. Low, and W. Zhu, Appl. Phys. Lett. **108**, 083104 (2016).

[23]K. Zojer, T. Rothländer, J. Kraxner, R. Schmied, C. Palfinger, H. Plank, W. Grogger, A. Haase, H. Gold, and B. Stadlober, Sci. Rep. **6**, 31387 (2016).

A.4 SCANNING PHOTOCURRENT MICROSCOPY OF ELECTRONS AND HOLES IN THE PIGMENT SEMICONDUCTOR EPINDOLIDIONE

Clemens Liewald, Simone Strohmair, Henrik Hecht, Eric Głowacki, and Bert Nickel

Abstract

Photocurrent microscopy is used to characterize the kinetics of electrons and holes in organic field-effect transistors (FETs) with the hydrogen-bonded pigment epindolidione as active layer. The method relies on electrons and holes, generated on local illumination, which are provided after exciton splitting, to probe charge trapping. In the dark, hole conduction is observed for negative gate voltage while no electron conduction is observed for positive gate voltage. However, under illumination, a fast displacement current with 60 µs onset time and 1 ms exponential decay occurs for positive gate voltage, which can be explained by exciton splitting underneath the semitransparent top contact followed by subsequent electron trapping and hole extraction. Afterward, trapped electrons hop via further trap states within the film to the insulator into interface traps (13 ms exponential decay) which induce a positive threshold voltage shift in the FET transfer curves for hole transport. Photocurrent microscopy confirms that the displacement current occurs only for illumination under and near the semitransparent source/drain contacts, which act here as metal-insulator-semiconductor (MIS) diodes. For negative gate voltage instead, the photocurrent comprises an enhanced hole current in the FET channel between the contacts. In the channel region, the detrapping of holes at the interface with the insulator (3 ms time constant) enhances the transistor current at low frequencies <1 kHz, whereas the displacement current between the contacts and the gate is observed only at frequencies >10 kHz. Thus, we show here that photocurrent microscopy allows to identify the kinetics of electrons and holes in traps close to the contacts and in the FET channel of pigment transistors.

Contribution

I designed the experiments and tailored the SPCM setup accordingly. Simone Strohmair and myself prepared the Epi samples. Simone Strohmair, Henrik Hecht, and myself recorded and analyzed the data. Furthermore, I wrote the manuscript.

Scanning photocurrent microscopy of electrons and holes in the pigment semiconductor epindolidione

C. Liewald[a,b], S. Strohmair[a], H. Hecht[a], E.D. Głowacki[c], B. Nickel[a,b,*]

[a] Faculty of Physics and CeNS, Ludwig-Maximilians-Universität München, 80539, Munich, Germany
[b] Nanosystems Initiative Munich (NIM), 80799, Munich, Germany
[c] Laboratory of Organic Electronics, Department of Science and Technology, Campus Norrköping, Linköpings Universitet, Bredgatan 33, SE-601 74, Norrköping, Sweden

ABSTRACT

Photocurrent microscopy is used to characterize the kinetics of electrons and holes in organic field-effect transistors (FETs) with the hydrogen-bonded pigment epindolidione as active layer. The method relies on electrons and holes, generated on local illumination, which are provided after exciton splitting, to probe charge trapping. In the dark, hole conduction is observed for negative gate voltage while no electron conduction is observed for positive gate voltage. However, under illumination, a fast displacement current with 60 µs onset time and 1 ms exponential decay occurs for positive gate voltage, which can be explained by exciton splitting underneath the semitransparent top contact followed by subsequent electron trapping and hole extraction. Afterward, trapped electrons hop via further trap states within the film to the insulator into interface traps (13 ms exponential decay) which induce a positive threshold voltage shift in the FET transfer curves for hole transport. Photocurrent microscopy confirms that the displacement current occurs only for illumination under and near the semitransparent source/drain contacts, which act here as metal-insulator-semiconductor (MIS) diodes. For negative gate voltage instead, the photocurrent comprises an enhanced hole current in the FET channel between the contacts. In the channel region, the detrapping of holes at the interface with the insulator (3 ms time constant) enhances the transistor current at low frequencies < 1 kHz, whereas the displacement current between the contacts and the gate is observed only at frequencies > 10 kHz. Thus, we show here that photocurrent microscopy allows to identify the kinetics of electrons and holes in traps close to the contacts and in the FET channel of pigment transistors.

1. Introduction

Hydrogen-bonded pigments have emerged in recent years as a new class of organic semiconductors [1,2]. One representative is the pigment epindolidione (Epi), which is typically used as a yellow colorant in the printing and coating industry. Utilized as a semiconductor, Epi shows a hole transport mobility up to $1\,cm^2\,V^{-1}s^{-1}$, combined with outstanding chemical stability in the pH range 3–10 [3,4]. Polycrystalline Epi films consist of linear chains of H-bonded molecules that are π-π stacked in a close, brick-wall arrangement, favoring charge transport between the individual Epi chains [3,5]. These properties allow for multidisciplinary applications with Epi thin films, such as photoelectrodes for H_2O_2 production or the bioconjugation with functional proteins in an aqueous environment [6,7]. Field-effect transistors (FETs) with a semiconducting Epi layer show bipolar charge transport of electrons or holes if proper metal contacts for charge injection are employed [3]. In Epi FETs, electron transport with reduced mobility of $2 \times 10^{-3}\,cm^2\,V^{-1}\,s^{-1}$ is observed in N_2 atmosphere, suggesting that electron traps hinder the conduction at ambient conditions even further. The formation of defects in organic films can furthermore occur from interface effects, polymorphism, or mechanical strain [8,9]. A full picture of trap states and trap dynamics in Epi thin films is crucial for an optimization of the various devices produced with this material. As charge carrier trap states are a limitation of many organic semiconductor devices, elaborating methods for the evaluation of majority and minority carriers is a primary motivation behind this work. Following common descriptions of organic semiconductors, the high-mobility holes are here named majority charge carriers, and the low-mobility electrons are named minority charge carriers [10].

Using photoresponse microscopy measurements, we image the kinetics of electron and hole trap filling in p-type Epi transistors at ambient conditions. A variation of the applied drain voltage V_{DS} allows for using the tested devices in two operating modes, as FETs with $V_{DS} < 0\,V$, or as metal-insulator-semiconductor (MIS) diodes with

---

$V_{DS} = 0$ V [11]. Also, the gate voltage V_{GS} controls the charge distribution in the different device layers. For negative V_{GS}, holes are injected from the source/drain contacts into the Epi layer. Here, ohmic contacts but also injection barriers are possible, affecting the device performance strongly [12]. For positive V_{GS}, electrons are blocked at the source/drain-Epi interface. This electron barrier can induce a high electric field $E > 10^5$ V/cm in the Epi below the contacts, sufficient for charge separation in organic semiconductors [13].

The photoresponse microscopy maps for these different operation modes differ profoundly, and they show two major contributions. First, operated as FETs with negative V_{GS}, i.e. in hole accumulation, the devices show a conduction enhancement in the FET channel region due to de-trapping of holes. This de-trapping mechanism has previously been used for imaging of trap densities in pentacene films [14,15]. In addition to this FET photoresponse, a MIS photoresponse of Epi is observed, spatially confined to the area below the top contacts. We argue that this response stems from electron and holes obtained by exciton dissociation in the high-field region between the contacts and the gate. Subsequently, the generated charges move toward the contact and the gate insulator, similar to a time-of-flight setting. Time and frequency resolved measurements reveal fast and slow components due to different trapping behavior of majority and minority charge carriers (holes and electrons) for negative and positive V_{GS}, respectively. With pentacene devices, however, no significant photocurrent was observed for positive V_{GS} [14]. This missing contribution for pentacene could be owed to the ultrafast singlet fission and generation of triplet excitons in pentacene preventing charge separation [16]. Thus, photocurrent microscopy allows to identify electron and hole traps under the contacts and within the transistor channel. The method introduced here can be applied to a range of semiconductor materials, which show photoresponse in thin film geometry, including Perovskites, 1D and 2D materials [17–30].

The investigated Epi transistors were fabricated by deposition and formation of different functional layers in a bottom-gate/top-contact device geometry. A schematic of the transistor structure with electrical connections for biasing and measuring the drain-source current I_{DS} and the photocurrent I_{photo} is shown in Fig. 1. Further descriptions of the used materials and methods are provided in the **Experimental section**.

2. Results and discussion

First, we discuss the photoresponse for global illumination of the Epindolidione devices in FET mode ($V_{DS} = -10$ V). The transfer curves in the dark and under illumination are shown in Fig. 2. A full set of transfer and output curves is shown in the Supplementary Information. Typical for p-type organic semiconductors, these transfer curves allow to define two distinct operating conditions. At positive gate voltages V_{GS}, no significant current was measured. At sufficiently negative gate voltages, a linear increase of $I^{1/2}$ indicates that a conductive hole channel formed. In the fabricated transistors, the work function difference between the Al gate and Au top contacts induced a negative
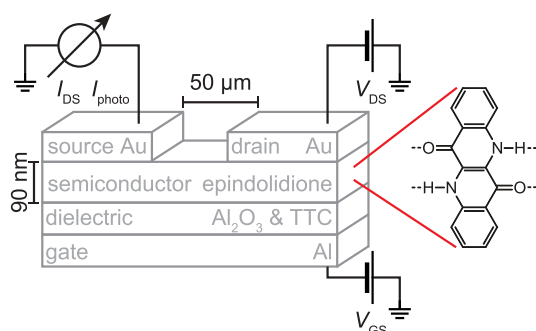
Fig. 1. Schematic of the transistor geometry with the pigment semiconductor epindolidione, building hydrogen-bonds between neighboring molecules.

threshold voltage V_{th}, calculated with a linear fit on $I_{DS}^{1/2}$ vs. V_{GS}.

The effect of global illumination on the transfer curves is investigated with the following experiment, shown in Fig. 2a: Starting in the dark with $V_{GS} = -15$ V at a chosen $I_{DS,0}$, the gate voltage was gradually increased to $V_{GS} = 5$ V (A), with a sweep rate of 1 V/1.13 s. Then, a blue laser with $\lambda = 488$ nm wavelength uniformly illuminated the transistor with 2 mW cm^{-2} for 2 s (B). Afterward, again in the dark, the gate voltage was gradually decreased to $V_{GS} = -15$ V (C), followed by a waiting time, here 140 s, until I_{DS} reached the starting value $I_{DS,0}$. The consecutive control experiment in dark showed only a slight increase of I_{DS}. The extracted transfer curves in Fig. 2b show a significant hysteresis, i.e. a transfer curve shift toward more positive V_{GS} due to illumination [31]. This bias stress is quantified by calculating the threshold voltage difference between the sweeps C and A, here $\Delta V_{th} = 2.1$ V for the illumination time $t = 2$ s. In contrast, only little bias stress, $\Delta V_{th} = 0.25$ V, was observed in the dark. The extracted voltage shifts ΔV_{th} for different illumination times (ms to s) are drawn in Fig. 2c and show a substantial increase for longer illumination. By comparing the dark value to ΔV_{th} under illumination, we could detect light-induced bias stress for illumination times as low as 2 ms, or 4 μJ cm^{-2}. Often, bias stress is induced by localized charges, i.e. filled trap states, at the semiconductor-dielectric interface. Trap filling can be quantified by the relation $\Delta Q = -c \, \Delta V_{th}$. Here, a positive ΔV_{th} is induced by the negative charge of trapped electrons [31]. In the dark, only little bias stress was observed because the high energy barrier between the work function of Au and the lowest unoccupied molecular orbital (LUMO) of Epi prohibits electron injection, so that electron traps cannot be filled from the contacts [3].

As a 30 nm thick Au layer shows 13% transmission at $\lambda = 488$ nm [32], the incoming light reached the Epi layer below the Au contacts, creating excitons. Thus, it is reasonable to assume that the trapped electrons, causing the bias stress upon illumination, originate from exciton splitting in the high field between the blocking top contact and the gate.

In the following, the kinetics of bias stress is further analyzed with time-resolved current measurements, recording the transient response of I_{DS} on global illumination. These measurements are shown in Fig. 3a) and **b)** for $V_{GS} = 5$ V and $V_{GS} = -15$ V, respectively. Here, the transistor was exposed to pulsed light with a pulse frequency $f = 48$ Hz, i.e. switching every 10.4 ms between full illumination and dark; gray areas mark the times during illumination. For light exposure at $V_{GS} = 5$ V, I_{DS} reached its maximum value of 3.5 nA within 60 μs and decreased slowly to a finite value above zero. Switching from light to dark, I_{DS} peaked equally fast at a minimum value of -1.6 nA and likewise decreased to a finite value above zero. For $V_{GS} = -15$ V, an average current of -2.78 μA was measured. Here, the current changed on the ms time scale from -2.74 μA in the dark to -2.82 μA during illumination. Both time-resolved current measurements follow a bi-exponential behavior, depicted by the red lines, with two decay time constants $\tau_1 = 1$ ms and $\tau_2 = 13$ ms for $V_{GS} = 5$ V, and $\tau_1 = 0.6$ ms and $\tau_2 = 3$ ms $V_{GS} = -15$ V. Such a bi-exponential behavior of a transient current implies that several effects contribute [33]. Assuming an uncharged Epi layer for $V_{GS} = 5$ V in the dark due to the blocking top contact, illumination created excitons, and the electric field between the top contacts and the gate could then separate these electron-hole pairs. The observed displacement current suggests that the electrons were driven against the electric field to the Epi-TTC interface, filling electron traps in bulk Epi or at the interface. The holes were extracted at the contacts.

Within this scenario, the fast component with rising time < 60 μs and decay constant $\tau_1 = 1$ ms represents the initial displacement current due to electrons and holes moving in the Epi layer and from electron trapping in bulk Epi, in close vicinity of where the excitons were split. After this initial process, a slower displacement current follows, namely due to electron hopping from bulk traps toward the Epi-TTC interface ($\tau_2 = 13$ ms). The decrease to a finite value above zero could originate from a leakage in the dielectric, or from an overall
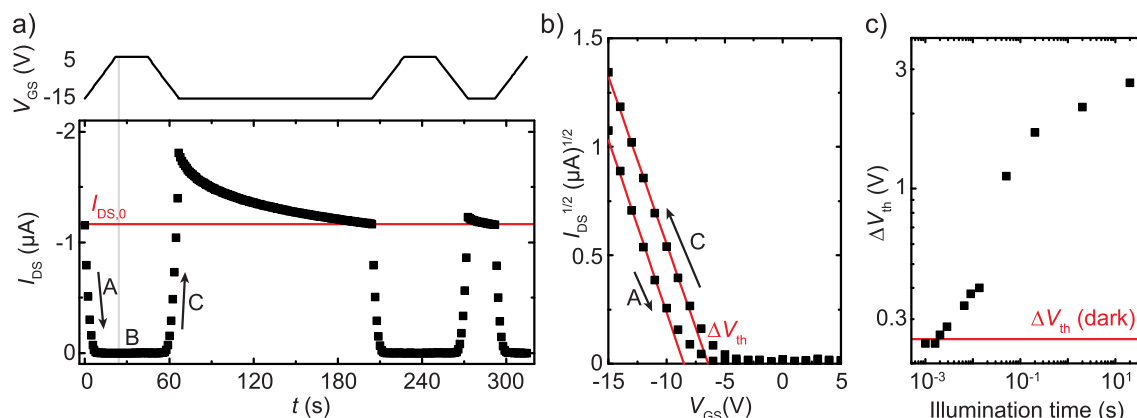
Fig. 2. a) Time-resolved measurement of the drain current I_{DS} for an epindolidone FET, while varying the gate voltage V_{GS}. Starting in dark at $I_{DS,0}$ (red horizontal line), V_{GS} was changed from $-15\,V$ to $5\,V$ (A). Now, the FET was illuminated for 2 s (B), and V_{GS} was changed back to $-15\,V$ (C). Here, I_{DS} was increased compared to $I_{DS,0}$ and was decreasing slowly. After the starting value $I_{DS,0}$ was reached, a control measurement without illumination was done. Here, I_{DS} was only slightly increased. **b)** Extracted transfer curves (A, C) from the time-resolved measurement. For 2 s illumination, a positive threshold voltage shift $\Delta V_{th} = 2.1$ was observed. The red lines indicate linear fits on the measured data points. **c)** Threshold voltage shift ΔV_{th} vs. illumination time at 5 V. The red line at 0.25 V marks ΔV_{th} in the dark. (For interpretation of the references to color in this figure legend, the reader is referred to the Web version of this article.)
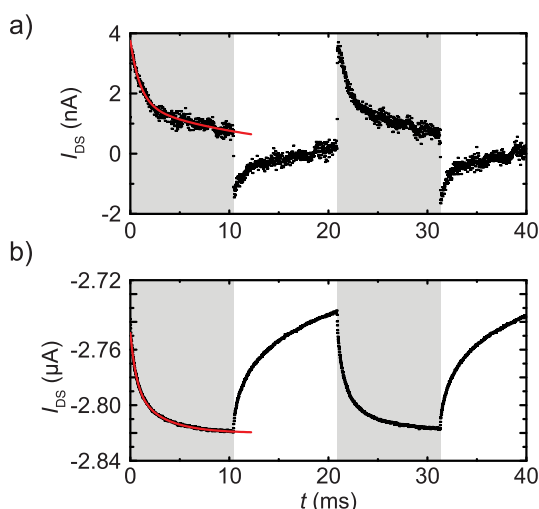
Fig. 3. Time-resolved drain current I_{DS} for pulsed illumination, **a)** $V_{GS} = 5\,V$, and **b)** $V_{GS} = -15\,V$, at 48 Hz pulse frequency. The gray areas mark the times under illumination; the red curves depict bi-exponential fits to the measurement points. (For interpretation of the references to color in this figure legend, the reader is referred to the Web version of this article.)

displacement of electrons in the Epi layer toward the Epi/TTC interface. While we cannot fully exclude the leakage current, we rationalize this observation by considering the experimental procedure for this measurement. The experiment was performed by sweeping V_{GS} from $-15\,V$ to 5 V and back, with a similar sweep rate like in Fig. 2. Therefore, the condition $V_{GS} > V_{th}$ was only fulfilled for a few seconds, where the ΔV_{th} was not completely saturated. Thus, the remaining positive I_{DS} originates most probably from a displacement of electrons toward the Epi/TTC interface, while the deep traps with release times longer than the period of the light pulses remain essentially filled, not affecting the current transients. The transient after turning off the light should be induced by the free and trapped electrons, which undergo a thermally-activated back-diffusion toward the source contact, due to a chemical gradient from the high electron concentration at the Epi/TTC interface. Thus, we explain the observed effects by an equilibrium of light-induced charge generation, field-induced electron displacement toward the Epi/TTC interface, and electron back-diffusion toward the top contacts, due to the induced chemical gradient.

When the polarity of the gate electric field is switched to

$V_{GS} = -15\,V$, the current difference between illumination and dark $\Delta I_{DS} = 60\,nA$ is much larger. We assign this effect to an enhanced conductivity of the Epi transistor, either by lowering the contact resistance or by releasing trapped holes in the transistor channel, as observed before for pentacene transistors [14,15].

To test our hypothesis of exciton splitting beneath top contacts for positive V_{GS}, we probed the transistor with spatially-resolved and frequency-resolved photocurrent measurements. That is, the laser was now focused to a diffraction-limited spot and scanned in a straight line across the transistor structure. At each position, a photocurrent spectrum for $f = 48\,Hz$ - 250 kHz was recorded with a lock-in amplifier. The scanned photocurrent I_{photo} is shown for $V_{GS} = 5\,V$ in Fig. 4a) and for $V_{GS} = -15\,V$ in Fig. 4b), while the drain voltage was set to $V_{DS} = -10\,V$. For illustration purposes, the complex photocurrent
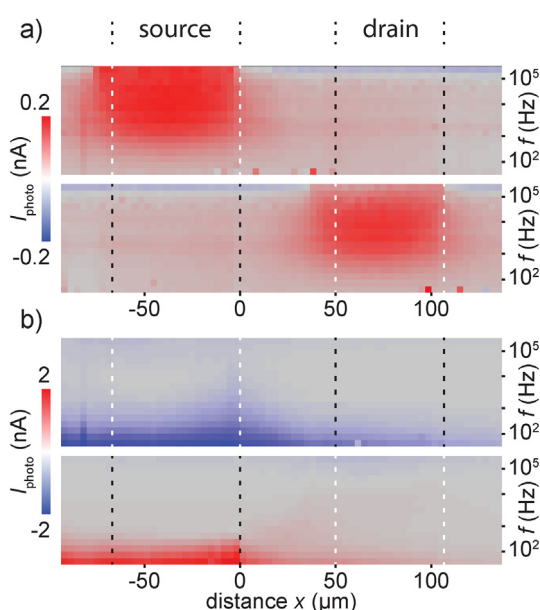
Fig. 4. Photocurrent I_{photo} as a function of pulse frequency f across the lateral transistor structure. **a)** $V_{GS} = 5\,V$, with a high-frequency contribution at the contacts. **b)** $V_{GS} = -15\,V$, with a low-frequency contribution and its maximum at 0 µm. Dotted lines indicate the transistor channel ($x = 0\,µm$ - 50 µm) between the left source contact and the right drain contact; the contacts marked with white lines were connected to the transimpedance amplifier.

I_{photo} was projected on the photocurrent phase $\theta_{photo} = -30°$. Red color marks I_{photo} in phase and blue color marks I_{photo} in opposite phase. Dotted lines indicate the edges of the gold contacts, simultaneously measured with reflectivity, defining the transistor channel ($x = 0\,\mu m$ - $50\,\mu m$) between the left source contact and the right drain contact. For subsequent measurements, the lock-in amplifier was connected to the contacts marked with white lines, measuring I_{photo} at the source and the drain contact, respectively [34]. By doing so, we could determine if the measured I_{photo} was passing only the source or drain contact, or was passing both contacts. A further experimental description is provided in the Supplementary Information.

Indeed, for $V_{GS} = 5\,V$, a positive photocurrent with 0.2 nA magnitude was measured, mainly located at the contacts and several μm around the contacts. This contribution started with a small amplitude at low frequencies, increased, and remained constant above 1 kHz. Photocurrent was only measured at illumination positions near contact connected to the lock-in amplifier, implying that the generated holes were driven to the top contact closest to illumination and were extracted there. This behavior confirms the displacement character between the top contacts and the gate. As I_{photo} showed no sharp confinement to the contacts but also appeared near to the contacts, we exclude a photoelectric injection of electrons from Au into Epi. A comparison of the sharp spatial resolution of reflectivity and photocurrent is shown in the Supplementary Information. Note that photocurrent for positive V_{GS} was not observed in previous measurements of pentacene FETs [14], presumably because exciton splitting in pentacene is complicated by singlet fission.

After having identified the process of photocurrent generation for $V_{GS} = 5\,V$, we now discuss the line scans for $V_{GS} = -15\,V$ (Fig. 4b). Here, I_{photo} dominates at low frequencies with 2 nA magnitude, i.e. one magnitude larger than the photocurrent for $V_{GS} = -15\,V$. At low frequencies, I_{photo} was distributed over the whole transistor. At higher frequencies, the broad distribution was more confined to a region in the channel and under the source contact, with a maximum at the beginning of the channel, $x = 0\,\mu m$. This spatial shape of I_{photo} resembles photocurrent maps of other materials [14,17]. In contrast to the line scans for $V_{GS} = 5\,V$, the spatial position with the maximum at $x = 0\,\mu m$ did not change, whether the lock-in amplifier was connected to the source or drain contact. Instead, the sign of the photocurrent changed, showing a negative I_{photo} when connected to the source contact, and a positive I_{photo} when connected to the drain contact. This behavior can be explained as follows. In a p-type FET, positive charge carriers drift from the source via the channel to the drain, leading to a negative net current at the source contact and a positive net current at the drain contact. The charge carriers pass both contacts, source and drain. Photocurrent effects can arise due to a lowering of contact resistance and de-trapping of hole traps within the channel. Both effects exhibit a different spatial signature in photocurrent microscopy. A lowering of the contact resistance is strongly confined to the edge of the Au contact while de-trapping occurs in a broader range within the transistor channel [15]. As I_{photo} was dominating several microns around $x = 0\,\mu m$, we assign this low-frequency component to the release of trapped holes in the transistor channel, which enhance the overall transistor current.

Finally, we evaluate the influence of charge carrier densities by a variation of the voltage configurations. The model of photocurrent generation is refined by measuring and analyzing the photocurrent amplitude $|I_{photo}|$ and phase θ_{photo}. For these measurements, the device was illuminated at the source contact ($x = -10\,\mu m$), where the signal showed the highest levels. Applying different drain voltage levels allowed to measure spectra in MIS configuration ($V_{DS} = 0\,V$) and FET configuration ($V_{DS} = -10\,V$). Also, the gate voltage controlled the charge distribution in the different layers, hole injection into Epi for $V_{GS} = -15\,V$ and electron blocking at the Au-Epi interface for $V_{GS} = 5\,V$. The recorded spectra are shown in Fig. 5. Black filled squares correspond to $V_{GS} = -15\,V$ and $V_{DS} = -10\,V$; black filled
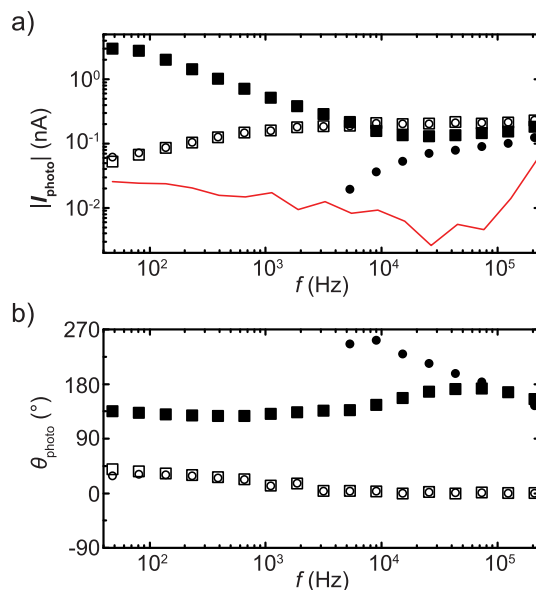
Fig. 5. Local photocurrent spectra at the source contact, **a)** amplitude $|I_{photo}|$ and **b)** phase θ_{photo}, with different voltage combinations: $V_{GS} = -15\,V$ (black filled symbols) and $V_{GS} = 5\,V$ (white filled symbols), $V_{DS} = -10\,V$ (squares) and $V_{DS} = 0\,V$ (circles). The red line marks the spectral background of the measurement setup, recorded in the dark. (For interpretation of the references to color in this figure legend, the reader is referred to the Web version of this article.)

circles to $V_{GS} = -15\,V$ and $V_{DS} = 0\,V$; white filled squares to $V_{GS} = 5\,V$ and $V_{DS} = -10\,V$; white filled circles to $V_{GS} = 5\,V$ and $V_{DS} = 0\,V$. As expected, the strongest signal was measured in the FET spectra for $V_{GS} = -15\,V$, at low frequencies $f < 10^3\,Hz$. This signal decreased by one magnitude for higher frequencies and remained constant for $f > 10^4\,Hz$. In this frequency regime, the MIS spectrum at $V_{GS} = -15\,V$ converged with the FET spectrum. We therefore conclude that the high-frequency spectra at $V_{GS} = -15\,V$ were not affected by the drain voltage. The same independence on the drain voltage can be seen for the photocurrent at $V_{GS} = 5\,V$, confirming the displacement character of these spectra. Moreover, the 180° phase difference between the spectra for $V_{GS} = -15\,V$ and $V_{GS} = 5\,V$ indicates that the photocurrent was, as expected for displacement currents, induced in opposite directions. Note that the line scans for $V_{GS} = -15\,V$ (Fig. 4b) also contain this high-frequency displacement current, but it can rarely be seen due to the color scale. The same line scans, highlighting this high-frequency component with a different color scale, are shown in the Supplementary Information. This high-frequency displacement current for $V_{GS} = -15\,V$ can be explained with residual contact resistance of the Au-Epi interface or with trapped holes in the bulk Epi below the contacts. In either case, illumination promotes the holes closer to the Epi-TTC interface, generating a displacement current. This process, measured only at high frequencies $f > 10^4\,Hz$, decays much faster than the displacement current for $V_{GS} = 5\,V$ because the hole trap density is much lower than the electron trap density (see Fig. 5a).

3. Conclusion

In summary, we have imaged and analyzed the kinetics of electron and hole traps in Epindolidone films and have identified two photocurrent contributions. The excitons, generated upon illumination, can enhance the FET current by de-trapping holes in the channel, or they can dissociate into electrons and holes due to the high electric field between the contacts and the gate. For $V_{GS} = 5\,V$, exciton-splitting and charge separation leads to two successive displacement currents. Initially, hole extraction and electron bulk trapping occur, followed by

electron hopping from bulk traps to interface traps. These interface traps cause bias stress, shifting the threshold voltage of the FET transfer curves. Line scans of frequency-resolved photocurrent reveal that electron trapping occurs under and also several μm next to the Au contacts. For negative gate voltages V_{GS}, the photocurrent also contains this displacement contribution, and additionally a component assigned to the de-trapping of holes. This de-trapping enhances the FET current, mainly under the source contact and within the transistor channel. The here presented methods of spatial distribution and dynamics analysis of trap states should apply to a variety of emerging electronic materials like other organic semiconductors, Perovskites, 1D and 2D materials.

4. Experimental section

4.1. Transistor fabrication

Transistors were fabricated by thermal evaporation under high vacuum, and the transistor structures were defined by shadow masks. A 100 nm thick Al layer was deposited as gate contact on glass substrates. The Al layer was electrochemically oxidized to 32 nm Al_2O_3 in an acidic solution with pH 6 and 20 V anodization voltage. Afterward, 34 nm tetratetracontane (TTC) was deposited and thermally annealed for 16 h at 60 °C under N_2 atmosphere to form the gate dielectric together with Al_2O_3. 90 nm of purified Epindolidione was evaporated as the semiconducting layer. Finally, 30 nm Au serve as source and drain contacts. The fabricated transistor channel was of 50 μm length and 2 mm width, defined with shadow masks. The sample was glued to a chip-carrier and wire bonded for measuring.

4.2. Photocurrent measurements

A diode laser system (iPulse, TOPTICA Photonics) with a wavelength of 488 nm was electronically controlled and used for excitation of the Epindolidione layer, matching the absorption spectrum of Epindolidione [3]. The pulse shape of the illumination was used in two operational modes. First, in a rectangular mode, with a pulse frequency f and a fixed pulse duty of 50%. Second, in a single-shot mode, emitting only one light pulse of arbitrary pulse length. The Al gate contact and one Au top contact were connected to power supply units (7651, Yokogawa), the other Au top contact was connected to ground via a transimpedance amplifier (DHPCA-100, Femto) at 10^6 V/A. Thus, the transimpedance amplifier converted the current between the connected contact and ground into a voltage output. The amplifier output was analyzed with a digital multimeter (34411A, Agilent), measuring the drain current I_{DS}, and with a lock-in amplifier (7280, Signal Recovery). The lock-in amplifier extracted the complex photocurrent I_{photo} at the reference pulse frequency of the used laser. I_{photo} can be decomposed into amplitude $|I_{photo}|$ and phase θ_{photo}. Photocurrent spectra were measured by subsequently changing the laser pulse frequency and measuring I_{photo}. More details of the used setup are described elsewhere [14,15,34].

Acknowledgments

Appendix A. Supplementary data

Supplementary data related to this article can be found at http://dx.doi.org/10.1016/j.orgel.2018.05.032.

References

[1] E.D. Glowacki, M. Irimia-Vladu, S. Bauer, N.S. Sariciftci, Hydrogen-bonds in molecular solids - from biological systems to organic electronics, J. Mater. Chem. B 1 (2013) 3742–3753 https://doi.org/10.1039/c3tb20193g.

[2] M. Gsänger, D. Bialas, L. Huang, M. Stolte, F. Würthner, Organic semiconductors based on dyes and color pigments, Adv. Mater. 28 (2016) 3615–3645 https://doi.org/10.1002/adma.201505440.

[3] E.D. Głowacki, G. Romanazzi, C. Yumusak, H. Coskun, U. Monkowius, G. Voss, M. Burian, R.T. Lechner, N. Demitri, G.J. Redhammer, N. Sünger, G.P. Suranna, S. Sariciftci, Epindolidiones—versatile and stable hydrogen-bonded pigments for organic field-effect transistors and light-emitting diodes, Adv. Funct. Mater. 25 (2015) 776–787 https://doi.org/10.1002/adfm.201402539.

[4] R. Lassnig, B. Striedinger, A.O.F. Jones, B. Scherwitzl, A. Fian, E.D. Glowacki, B. Stadlober, A. Winkler, Temperature and layer thickness dependent in situ investigations on epindolidone organic thin-film transistors, Synth. Met. 218 (2016) 64–74 https://doi.org/10.1016/j.synthmet.2016.05.003.

[5] A.O.F. Jones, C. Röthel, R. Lassnig, O.N. Bedoya-Martínez, P. Christian, I. Salzmann, B. Kunert, A. Winkler, R. Resel, Solution of an elusive pigment crystal structure from a thin film: a combined X-ray diffraction and computational study, CrystEngComm 19 (2017) 1902–1911.

[6] E.D. Glowacki, R.R. Tangorra, H. Coskun, D. Farka, A. Operamolla, Y. Kanbur, F. Milano, L. Giotta, G.M. Farinola, N.S. Sariciftci, Bioconjugation of hydrogen-bonded organic semiconductors with functional proteins, J. Mater. Chem. C 3 (2015) 6554–6564 https://doi.org/10.1039/C5TC00556F.

[7] M. Jakešová, D.H. Apaydin, M. Sytnyk, K. Oppelt, W. Heiss, N.S. Sariciftci, E.D. Głowacki, Hydrogen-bonded organic semiconductors as stable photoelectrocatalysts for efficient hydrogen peroxide photosynthesis, Adv. Funct. Mater. 26 (2016) 5248–5254 https://doi.org/10.1002/adfm.201601946.

[8] T. Cramer, L. Travaglini, S. Lai, L. Patruno, S. De Miranda, A. Bonfiglio, P. Cosseddu, B. Fraboni, Direct imaging of defect formation in strained organic flexible electronics by scanning kelvin probe microscopy, Sci. Rep. 6 (2016) 38203.

[9] C. Westermeier, A. Cernescu, S. Amarie, C. Liewald, F. Keilmann, B. Nickel, Submicron phase coexistence in small-molecule organic thin films revealed by infrared nano-imaging, Nat. Commun. 5 (2014) 4101 https://doi.org/10.1038/ncomms5101.

[10] Y. Hu, V. Pecunia, L. Jiang, C.A. Di, X. Gao, H. Sirringhaus, Scanning kelvin probe microscopy investigation of the role of minority carriers on the switching characteristics of organic field-effect transistors, Adv. Mater. 28 (2016) 4713–4719 https://doi.org/10.1002/adma.201503812.

[11] S. Grecu, M. Bronner, A. Opitz, W. Brütting, Characterization of polymeric metal-insulator–semiconductor diodes, Synth. Met. 146 (2004) 359–363 https://doi.org/https://doi.org/10.1016/j.synthmet.2004.08.014.

[12] M. Gruber, F. Schürrer, K. Zojer, Relation between injection barrier and contact resistance in top-contact organic thin-film transistors, Org. Electron. 13 (2012) 1887–1899 https://doi.org/ https://doi.org/10.1016/j.orgel.2012.05.009.

[13] T. Hahn, S. Tscheuschner, C. Saller, P. Strohriegl, P. Boregowda, T. Mukhopadhyay, S. Patil, D. Neher, H. Bässler, A. Köhler, Role of intrinsic photogeneration in single layer and bilayer solar cells with C60 and PCBM, J. Phys. Chem. C 120 (2016) 25083–25091 https://doi.org/10.1021/acs.jpcc.6b08471.

[14] C. Westermeier, M. Fiebig, B. Nickel, Mapping of trap densities and hotspots in pentacene thin-film transistors by frequency-resolved scanning photoresponse microscopy, Adv. Mater. 25 (2013) 5719–5724 https://doi.org/10.1002/adma.201300958.

[15] C. Liewald, D. Reiser, C. Westermeier, B. Nickel, Photocurrent microscopy of contact resistance and charge Carrier traps in organic field-effect transistors, Appl. Phys. Lett. 109 (2016) 053301 https://doi.org/10.1063/1.4960159.

[16] M.W.B. Wilson, A. Rao, B. Ehrler, R.H. Friend, Singlet exciton fission in polycrystalline pentacene: from photophysics toward devices, Accounts Chem. Res. 46 (2013) 1330–1338 https://doi.org/10.1021/ar300345h.

[17] L. Caranzi, G. Pace, M. Sassi, L. Beverina, M. Caironi, Transparent and highly responsive phototransistors based on a solution-processed, nanometers-thick active layer, embedding a high-mobility electron-transporting polymer and a hole-trapping molecule, ACS Appl. Mater. Interfaces 9 (2017) 28785–28794 https://doi.org/10.1021/acsami.7b05259.

[18] S.J. Oh, J. Kim, J.M. Mativetsky, Y.-L. Loo, C.R. Kagan, Mapping the competition between exciton dissociation and charge transport in organic solar cells, ACS Appl. Mater. Interfaces 8 (2016) 28743–28749 https://doi.org/10.1021/acsami.6b07810.

[19] H. Chen, N. Cheng, W. Ma, M. Li, S. Hu, L. Gu, S. Meng, X. Guo, Design of a photoactive Hybrid bilayer dielectric for flexible nonvolatile organic memory transistors, ACS Nano 10 (2016) 436–445 https://doi.org/10.1021/acsnano.5b05313.

[20] R. Xiao, Y. Hou, Y. Fu, X. Peng, Q. Wang, E. Gonzalez, S. Jin, D. Yu, Photocurrent mapping in single-crystal methylammonium lead iodide perovskite nanostructures, Nano Lett. 16 (2016) 7710–7717 https://doi.org/10.1021/acs.nanolett.6b03782.

[21] S. Liu, L. Wang, W.-C. Lin, S. Sucharitakul, C. Burda, X.P.A. Gao, Imaging the long transport lengths of photo-generated carriers in oriented perovskite films, Nano Lett. 16 (2016) 7925–7929 https://doi.org/10.1021/acs.nanolett.6b04235.

[22] D. Zheng, H. Fang, P. Wang, W. Luo, F. Gong, J.C. Ho, X. Chen, W. Lu, L. Liao, J. Wang, W. Hu, High-performance ferroelectric polymer side-gated CdS nanowire ultraviolet photodetectors, Adv. Funct. Mater. 26 (2016) 7690–7696 https://doi.org/10.1002/adfm.201603152.

[23] C. Karnetzky, L. Sponfeldner, M. Engl, A.W. Holleitner, Ballistic and resonant negative photocurrents in semiconducting carbon nanotubes, Phys. Rev. B 95 (2017) 161405.

[24] T. Wang, S. Hu, B. Chamlagain, T. Hong, Z. Zhou, S.M. Weiss, Y.-Q. Xu, Visualizing light scattering in silicon waveguides with black phosphorus photodetectors, Adv. Mater. 28 (2016) 7162–7166 https://doi.org/10.1002/adma.201506277.

[25] J. Zhang, Y. Wei, F. Yao, D. Li, H. Ma, P. Lei, H. Fang, X. Xiao, Z. Lu, J. Yang, J. Li, L. Jiao, W. Hu, K. Liu, K. Liu, P. Liu, Q. Li, W. Lu, S. Fan, K. Jiang, SWCNT-MoS2-SWCNT vertical point heterostructures, Adv. Mater. 29 (2017) 1604469-n/a https://doi.org/10.1002/adma.201604469.

[26] J.D. Mehew, S. Unal, E. Torres Alonso, G.F. Jones, S. Fadhil Ramadhan, M.F. Craciun, S. Russo, Fast and highly sensitive ionic-polymer-gated WS2–graphene photodetectors, Adv. Mater. 29 (2017) 1700222-n/a https://doi.org/10.1002/adma.201700222.

[27] W.J. Yu, Q.A. Vu, H. Oh, H.G. Nam, H. Zhou, S. Cha, J.-Y. Kim, A. Carvalho, M. Jeong, H. Choi, A.H. Castro Neto, Y.H. Lee, X. Duan, Unusually efficient photocurrent extraction in monolayer van der Waals heterostructure by tunnelling through discretized barriers, Nat. Commun. 7 (2016) 13278 https://doi.org/10.1038/ncomms13278.

[28] Y. Guo, J. Yin, X. Wei, Z. Tan, J. Shu, B. Liu, Y. Zeng, S. Gao, H. Peng, Z. Liu, Q. Chen, Ge-states-induced disruption to the energy band alignment at thickness-modulated molybdenum sulfide junctions, Advanced Electronic Materials 2 (2016) 1600048-n/a https://doi.org/10.1002/aelm.201600048.

[29] S. Mashhadi, D.L. Duong, M. Burghard, K. Kern, Efficient photothermoelectric conversion in lateral topological insulator heterojunctions, Nano Lett. 17 (2017) 214–219 https://doi.org/10.1021/acs.nanolett.6b03851.

[30] Q. Ma, S.-Y. Xu, C.-K. Chan, C.-L. Zhang, G. Chang, Y. Lin, W. Xie, T. Palacios, H. Lin, S. Jia, P.A. Lee, P. Jarillo-Herrero, N. Gedik, Direct optical detection of Weyl fermion chirality in a topological semimetal, Nat. Phys. 13 (2017) 842 https://doi.org/10.1038/nphys4146.

[31] R. Liguori, W.C. Sheets, A. Facchetti, A. Rubino, Light- and bias-induced effects in pentacene-based thin film phototransistors with a photocurable polymer dielectric, Org. Electron. 28 (2016) 147–154 https://doi.org/10.1016/j.orgel.2015.10.029.

[32] A. Axelevitch, B. Gorenstein, G. Golan, Investigation of optical transmission in thin metal films, Physics Procedia 32 (2012) 1–13 https://doi.org/10.1016/j.phpro.2012.03.510.

[33] H.H. Choi, M.S. Kang, M. Kim, H. Kim, J.H. Cho, K. Cho, Decoupling the bias-stress-induced charge trapping in semiconductors and gate-dielectrics of organic transistors using a double stretched-exponential formula, Adv. Funct. Mater. 23 (2013) 690–696 https://doi.org/10.1002/adfm.201201545.

[34] M. Fiebig, C. Erlen, M. Göllner, P. Lugli, B. Nickel, Spatially resolved photoresponse measurements on pentacene thin-film transistors, Appl. Phys. Mater. Sci. Process 95 (2009) 113–117 https://doi.org/10.1007/s00339-008-5009-x.

A.5 A RESISTOR NETWORK SIMULATION MODEL FOR LASER-SCANNING PHOTO-CURRENT MICROSCOPY TO QUANTIFY LOW CONDUCTANCE REGIONS IN ORGANIC THIN FILMS

Mohammed Darwish, Hakan Boysan, Clemens Liewald, Bert Nickel, and Alessio Gagliardi

Abstract

Organic field effect transistors (OFETs) show considerable variation from device to device and batch to batch. For the basic understanding of the microscopic origins of these variations, it is crucial to develop both experimental and theoretical methods that allow to localize ineffective regions in a device. Raster techniques, which manipulate conductivity locally, combined with global current readout may provide this information, e.g. it has been suggested that diffraction limited illumination of OFETs by laser scanning photo-current microscopy provides trap density distribution maps. However, the question arises whether local variation of conductivity is indeed suited for localization of such defects given that the detected photo-current passes through the whole network of conductance in the thin film device. In this study, we present a simulation model based on resistor networks to investigate the effect of defective regions in organic thin films. We show that varying conductances locally allows indeed to reconstruct the spatial distributions of ineffective areas. We also demonstrate how such simulations can be applied to interpret photo-current microscopy maps in terms of trap densities.

Contribution

I provided ideas and feedback from an experimental point of view, designed Figure 1, and wrote respective parts of the manuscript.

A resistor network simulation model for laser-scanning photo-current microscopy to quantify low conductance regions in organic thin films☆

M. Darwish[a,*], H. Boysan[a], C. Liewald[b,c], B. Nickel[b,c], A. Gagliardi[a,c]

[a] Institute for Nanoelectronics, Department of Electrical and Computer Engineering, Technische Universität München, Munich, 80333, Germany
[b] Fakultüt für Physik and Center for NanoScience (CeNS), Ludwig-Maximilians-Universität, Munich, 80539, Germany
[c] Nanosystems Initiative Munich (NIM), Munich, 80799, Germany

ABSTRACT

Organic field effect transistors (OFETs) show considerable variation from device to device and batch to batch. For the basic understanding of the microscopic origins of these variations, it is crucial to develop both experimental and theoretical methods that allow to localize ineffective regions in a device. Raster techniques, which manipulate conductivity locally, combined with global current readout may provide this information, e.g. it has been suggested that diffraction limited illumination of OFETs by laser scanning photo-current microscopy provides trap density distribution maps. However, the question arises whether local variation of conductivity is indeed suited for localization of such defects given that the detected photo-current passes through the whole network of conductance in the thin film device. In this study, we present a simulation model based on resistor networks to investigate the effect of defective regions in organic thin films. We show that varying conductances locally allows indeed to reconstruct the spatial distributions of ineffective areas. We also demonstrate how such simulations can be applied to interpret photo-current microscopy maps in terms of trap densities.

1. Introduction

Research into organic electronics has gathered a lot of pace over the past decade. Organic based devices can complement current technologies, but also possess numerous advantages over their inorganic counterparts. From the possibility of low cost production on a large scale (utilizing the vast array of different materials), to obtaining devices with bendable (flexible) capabilities, this has merited the extensive effort put into studying such a technology. The main building block of these devices, the materials themselves, are categorized into two different groups, small molecules and polymers respectively. Small molecules come with some degree (usually high) of crystallinity, while polymers are more towards being amorphous in nature. However, there are also materials that can come as a combination of both structural forms, such as Poly (3-hexylthiophene) [1–3]. Furthermore, small molecules can be evaporated in vacuum chambers, while polymers on the other hand are solution processed (which is regarded as a simpler process). An extensive database of the different materials can be found here [4]. Both types are under investigation to realize various devices for different applications. Examples include organic-field effect

transistors (OFETs for radio frequency identification tags or sensors) [5–9], light emitting diodes (OLEDs for displays) [10–13], and solar cells (OSCs for energy harvesting) [14–16]. Whichever device is chosen, they all must exhibit and maintain good performance measures. In OFETs which are the main focus in this study, these measures are high charge carrier mobilities, low operating voltages, and device stability.

With all the promise that OFETs show, there still are factors that limit their usage on a large commercial scale. One of these factors is the presence of ineffective regions within the channel of a device. These regions act as defects that limit device performance in terms of the measures mentioned previously and can originate from several sources (i.e. structural or energetic defects). Furthermore, this might lead to charge carrier trapping. To this day, measurements taken from OFETs are usually done in either ambient atmosphere for shorts periods of time or inside vacuum chambers. Prolonged operation under ambient atmosphere typically leads to performance degradation. One famous example is oxidized pentacene species, where oxygen atoms bond with the pentacene central rings leading to the formation of traps states within the band gap [17,18]. Furthermore, OFETs are not made up of only organic materials (eventhough efforts have been made to achieve

exactly that). Other materials include metals (i.e. for the source and drain contacts) and inorganic oxides. Therefore, interface quality has a large effect on how OFETs perform. Charge transport in organic materials commonly occurs within the first few monolayers at the organic-oxide interface [19,20], hence careful consideration must be taken into account for which materials should be chosen for optimum device performance.

The aforementioned sources of traps states in organic materials are a consequence of the fabrication procedure or the operating conditions. But a major source of traps states in organic semiconductors relates to their nature (i.e. they are inherently present). This highly depends on the partial localization of quantum states in space, due to energy and spatial disorder. Consequently, a broadening of the energy levels in the density of states is generated as a result of such disorder. This has been famously described before by Bässler [21] as the Gaussian Disorder Model (GDM). One of the main parameters of the GDM is called the energetic disorder (denoted as σ and given in milli-electronvolts). With higher energetic disorder, the tail of the Gaussian distribution will extend into the band gap. As the charge transport in organics often relies on hopping from one site to the next, a certain amount of these sites will act as trap states. This energetic disorder can be found in both small molecules and polymers, but are more pronounced in the latter.

As far as how traps affect device performance, this highly depends on their position relative to the transport level. There are two different classifications of traps, shallow and deep traps respectively. Both have very different effects on OFETs. Shallow traps target charge carrier mobilities [22–24]. Charges are momentarily trapped as they travel from the source to the drain. Such an effect is outlined by the multiple trap and release model (MTR) [25,26]. This model takes into consideration the amount of time a certain charge spends trapped as well as the time it takes to travel between traps. If charges are trapped for longer periods of time, this leads to hysteresis when switching from forward to backward biases [24,27]. MTR is usually applied to organics being more crytalline than amorphous because they have both localized and delocalized states. This leads to a transition from localized to delocalized levels, hence transport becomes based on multi-trapping and releasing of charges. On the other hand, deep traps lead to threshold voltage shifts and the need for higher operating voltages [28,29]. This is obvious since more energy is required to free charges to participate in transport.

For all these reasons, it is crucial to have an in-depth and full understanding of defective regions in organic based devices. This requires extracting possible low conductive regions for subsequent analysis of the identified areas (e.g. identifying polymorphs as a potential source of traps states [30]). In this study, the investigation will be more on the theoretical side but the experimental procedure will be presented as well (in Section 2). This is followed by presenting the analytical model used for our simulations and its validation in Sections 3 and 4 respectively. Finally in Section 5, results are presented and comparisons drawn between the simulation and experimental results.

2. Experimental setup

From an experimental perspective, the method chosen for our investigation is called "Scanning Photo-Current Microscopy" (SPCM) [31]. The measurement setup using SPCM is illustrated in Fig. (1a). SPCM relies on scanning the surface of an organic thin film with submicron precision. A laser light is shone onto a specific spot along the length of the film with a certain wavelength. Under this illumination, charges at that location gain the required energy to become de-trapped and start flowing in the direction of the electric field applied between the source and drain contacts. In pentacene, the de-trapping is governed by the reaction of the prevalent triplet excitons [32,33] with trapped charges [31,34]. With such a setup, the photo-response current can be measured and a map can be drawn to show the strength of the current difference (i.e between pre- and post-illumination) with respect to the
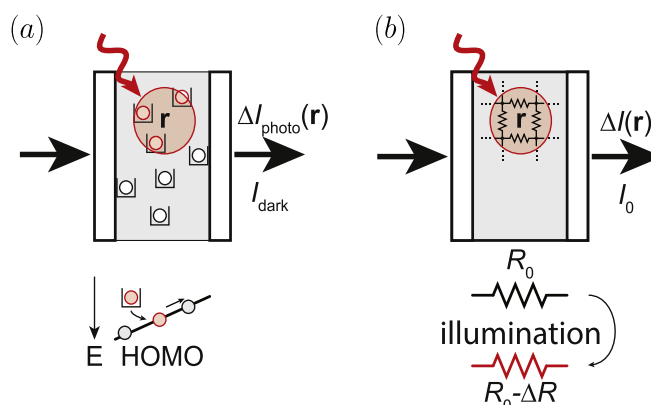
Fig. 1. (a) Illustration of the SPCM measurement technique, and **(b)** its curcuit equivalent based on a network of resistors. The organic film is illuminated by a laser light (block resistances manipulated) focusing on sub-micron sized spots. As a consequence of this illumination (manipulation) charges are de-trapped and the photo-current is measured.

illuminated spot.

Our previous experimental SPCM studies of pentacene transistors showed inhomogeneous SPCM maps, which were explained with an inhomogeneous trap distribution, revealed by exciton-assisted de-trapping [31,35,36]. According to the Thevenin theorem, any complex network of resistors can be simplified to an equivalent circuit with just one resistor. In this investigation, we determine the equivalent simplified network (i.e. the current before and after illumination), as shown in Fig. (1b). Here, we want to address the question to which extent does the total current change still contains information of the local resistance change. We address this issue by simulations of resistors networks. This simulation model (introduced in the following section) will also be used to evaluate the density of traps.

3. Theoretical model

Our simulation model is based on a theory of resistor networks presented in Ref. [37]. It is important to begin by noting that investigations of transistor operations using circuit elements has been proposed before by Shockley [38] and Brews [39] (i.e charge sheet model). More recently, such models have also been extended to investigate both organic and inorganic ambipolar transistors [40–42]. Here we start by considering a two dimensional resistance network with N nodes numbered $i = 1,2,3, ...,N$ respectively (as shown in Fig. 2). The conductance between two neighbouring nodes is given by $c_{ij} = r_{ij}^{-1} = c_{ji}$, and according to Kirchhoff's law[1]

$$\sum_{j=1}^{N} {}'c_{ij}(V_i - V_j) = I_i {}^1, \quad i = 1,2,3, ...,N \tag{1}$$

where I and V are the current and voltage respectively. Eq. (1) can be rewritten in the following form:

$$L\vec{V} = \vec{I} \tag{2}$$

From Eq. (2), L is defined as a conductance matrix (referred to as the "Laplacian" matrix in Ref. [37]). The off diagonal elements of this matrix correspond to the conductance between a pair of nodes. It also should be noted that this matrix is an adjacency matrix, which means if there is no resistor present between nodes i and j, the conductance is equal to zero. The final representation of the conductance matrix is

---

[1] the prime stands for the omission of the term $j = i$.
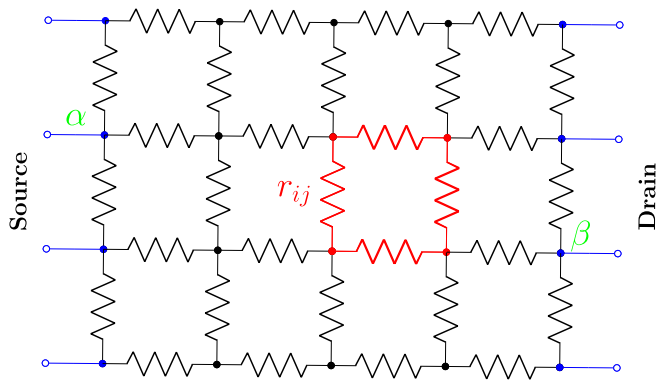
Fig. 2. A simple schematic of a 2D resistor network. The block highlighted in red represents a single spot. Letters i and j represent the position of an individual resistor, while α and β (in green) denote the chosen nodes for which the network resistance is calculated between them. (For interpretation of the references to color in this figure legend, the reader is referred to the Web version of this article.)

$$L = \begin{pmatrix} c_{11} & -c_{12} & \cdots & -c_{1N} \\ -c_{21} & c_{22} & \cdots & -c_{2N} \\ \vdots & \vdots & \ddots & \vdots \\ -c_{N1} & -c_{N2} & \cdots & c_{NN} \end{pmatrix},$$

$$(3)$$

$$L\Psi_i = \lambda_i \Psi_i \qquad i = 1,2,3, \ldots,N \tag{4}$$

where Ψ_i and λ_i are the eigenvectors and eigenvalues of the conductance matrix respectively. Using Eqs. (1)–(4), one can calculate the overall resistance between two arbitrary nodes α and β with the following expression:

$$R_{\alpha\beta} = \sum_{i=2}^{N} \frac{1}{\lambda_i} \left| \Psi_{i\alpha} - \Psi_{i\beta} \right|^2 \tag{5}$$

As the sum of all columns/rows are equal to zero, one of the eigenvalues is zero. This is usually the first eigenvalue (i.e at $i = 1$), that is why the summation in Eq. (5) goes from $i = 2$ to N. Care should also be taken when differentiating the usage of i, j, α, and β since they all represent the same entity (i.e nodes). Variables i and j are referred to when constructing the network and consequently the conductance matrix. On the other hand, α and β represent two nodes that have been chosen, and the resistance of the network is calculated with respect to them (see Fig. (2)). Therefore, the lowercase r are the values for the individual resistances between the nodes within the network. The uppercase R refers to the resistance of the entire network between two specific nodes. Such reference will stay the same from here onwards.

Each block inside the network consists of 4 resistors r and hence represents a spot to be "illuminated". Once a spot has been chosen (at random or otherwise), all 4 resistors are changed accordingly. This change is applied through the relation between the carrier density and resistance given in Eqs. (6) and (7). The carrier density is raised to a specific value which provides 4 new resistances r assigned to a block. In this way, we can mimic the effect of the illumination process onto a specific spot. Pre- and post-illuminated block resistances are always calculated in this fashion.

$$r = \rho \frac{l}{wt} \tag{6}$$

$$\rho = \frac{1}{qp\mu_{(p/n)}} \tag{7}$$

where,

a) ρ is the resistivity of the organic semiconductor.
b) l, w, t are the length, width, and thickness of the spot size.
c) q is the electronic charge.

d) p is the charge carrier density (main simulation parameter).
e) $\mu_{(p/n)}$ is the charge carrier mobility.

Once the manipulation process is complete, the new conductance matrix built, and the final network resistance calculated, a voltage is applied across the channel to calculate the "photo-response" current using Eq. (2). It should be taken into consideration that all nodes on both the source and drain sides must be at the same potential assigned to them (i.e ground on the source, a voltage V on the drain). With that in mind, this insures that the current entering from any node on the source will have all possible pathways available to choose from in reaching the drain. This dictates how the conductance matrix is set up.

4. Model validation

We begin by validating the model to ensure that its functionality is sound. Two approaches have been chosen for this validation. The first one will be simulating a homogeneous network. This means that all block resistances r are assigned the same initial value. The entire network is then manipulated block by block in a sequential manner, and a color map of the network is drawn at the end. Since the network is homogeneous and the manipulation process (i.e increasing the carrier density) is the same for every block, it should be expected that "sister" blocks (i.e. same distance from the edges but on opposite sides) will result in the same photo-response current and consequently the same current difference. That is indeed the case, as illustrated by the color map in Fig. (3) which shows horizontal and vertical symmetry. One important observation, is how the difference between the "dark" current and the photo-response current (in terms of current density) increases as we get closer to the contact edges in contrast to the central region of the channel. However this does not affect the symmetry. More on this observation will be discussed in detail in the following section, where simulation and experimental results are compared.

With the previous approach the entire network was scanned block by block. In our second approach, we wanted to manipulate specific blocks that were identified beforehand in order to draw out a certain image. The image of choice in this case was one of the author's affiliation logo. From Fig. (4), it can be seen that the initials are visible and clearly readable. The intensity is slightly different across the logo as this depends on the position of the block in question. Pre-illumination current and charge densities were $0.28A/cm^2$ and $10^{14}cm^{-3}$, with post illumination densities are $10^{17}cm^{-3}$ respectively. This provides adequate proof that the model responds well to a predefined input, giving the expected output. Furthermore, this allows us to extract local properties of the network (i.e. effect of specific positions with respect to the entire network).

5. Results: simulation vs. experimental

In terms of running the model to compare simulation and experimental results, a few changes need to applied to that of the validation procedure. Firstly, charge densities are not homogeneously distributed across the transistor channel. Hence, for a more realistic approach the network in question must be of an inhomogeneous nature. This has been done by providing the model with a range of charge densities, to both choose from and assign individual resistances in a random fashion. Furthermore, results of this model are to be compared with that of an OFET, hence we must insure that the network is operating under the same conditions similar to an OFET in order to have a justifiable comparison. In addition to the random assignment of charges across the network, both the effects of the gate and the drain-source must be implemented. For the former, this is done implicitly, as for the latter it is explicitly addressed.

In an OFET, the gate is responsible for inducing charges inside the channel. This attribute is added by providing the network with a specific value for the charge density. A Gaussian distribution with a pre-
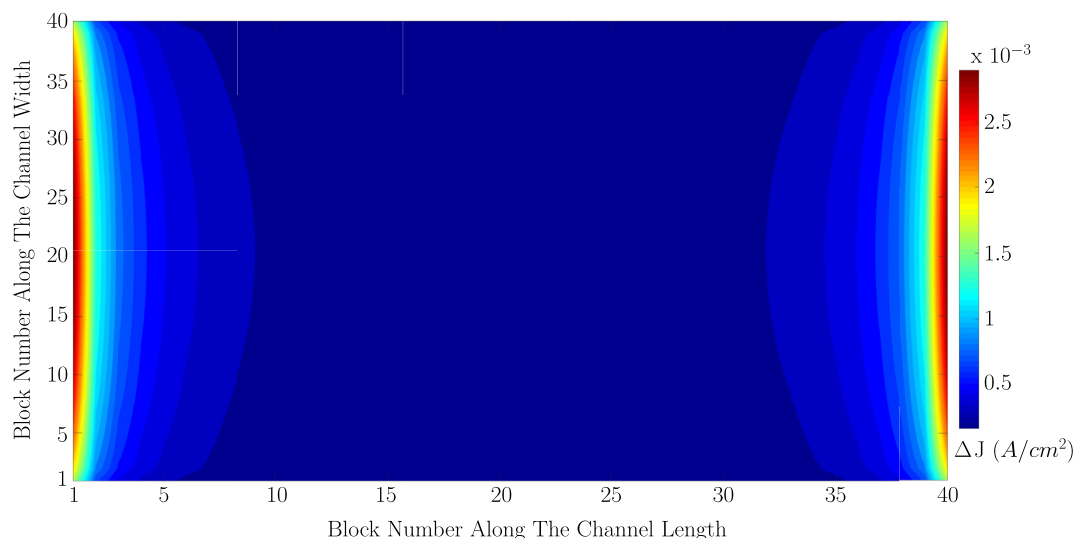
Fig. 3. A color map representation of the manipulation process of a homogeneous network. During the manipulation process, each block was returned to it's initial state before moving to the next one. Symmetry is present (taken either horizontally or vertically) meaning that "sister" blocks on opposite sides give the same intensity. This is expected since all blocks share the same initial state. (For interpretation of the references to color in this figure legend, the reader is referred to the Web version of this article.)
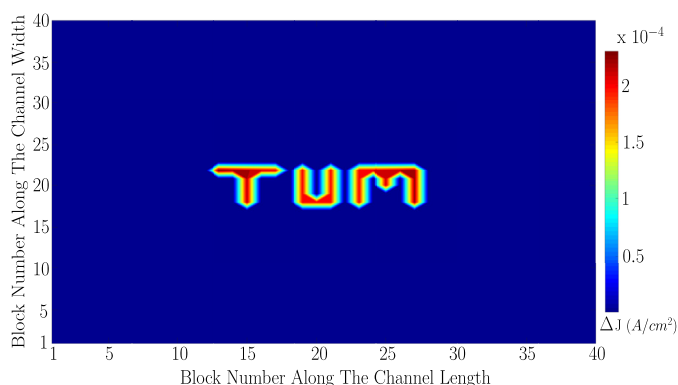
Fig. 4. Illustration of the TUM logo. Specific blocks were chosen and manipulated to draw this image.

defined standard deviation is centered around this value. For the drain-source effect, we assume that the charge density across the channel should decrease linearly as we move from the source towards the drain. Here the network is divided into multiple segments, where a set of values corresponding to the charge densities are assigned to each segment (based on the standard deviation of the Gaussian distribution). The distribution is then simply shifted to a lower value while maintaining the same standard deviation. This is repeated from one segment to the next until we reach the drain. To insure that these assumptions are correct, we ran a drift-diffusion (DD) simulation on a bottom gate/bottom contact Pentacene OFET and extracted the density profile across the channel region. This profile is shown in Fig. (S1) of the Supplementary Information. Fig. (S1) shows the same linear drop, hence consolidating the approach described earlier. Nevertheless, closer to the drain contact we observe that the density profile deviates from this linear behaviour. More on this aspect with be discussed shortly. To summarize, in this fashion we are able to implicitly include the gate effect (i.e. charge density value based on a Gaussian distribution), the linear decrease in density due to the explicit drain-source effect (i.e. shifting the distribution accordingly), and finally the inhomogeneity of charge density assignment based on the given standard deviation.

Results presented here will be based on a Pentacene OFET, but the model can be generally applied to other materials by properly adjusting

Table 1
Summary of the parameters used for the simulation of a Pentacene OFET.

Simulation Parameters	
Channel Length	$20\,\mu m$
Channel Width	$20\,\mu m$
Channel Thickness	2 nm
Spot Size	500 nm × 500 nm
Charge Density	$1.15 \times 10^{17}\,cm^{-3} - 1.35 \times 10^{17} cm^{-3}$
Carrier Mobility	$6.5 \times 10^{-3} cm^2/Vs$

the parameters. The parameters used for our simulations are summarized in Table 1. The operating point of the network is at a gate voltage of 20 V and drain-source voltage of 10 V respectively. For the used charge density range, a total of 24 values were chosen to cover the entire range, 6 for each segment in decreasing order. This ensures the linear drop across the channel is present. To find out how the charge densities are assigned to the network, their corresponding number of individual resistances were extracted (i.e for each segment). Fig. (5) shows this assignment, and indicates that all values (i.e charge densities) given to a specific segment of the network are more or less evenly distributed. Only three values are higher as they are common between
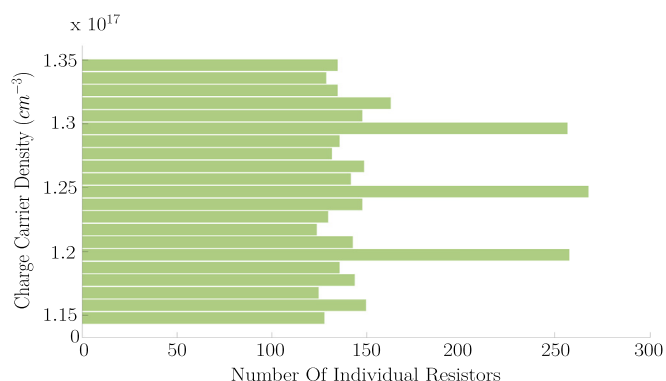
Fig. 5. Bar chart showing the distribution of the charge carrier densities and corresponding number of resistors across the four sections of the network. Densities are more or less fairly distributed, except three values which are shared between two adjacent sections.
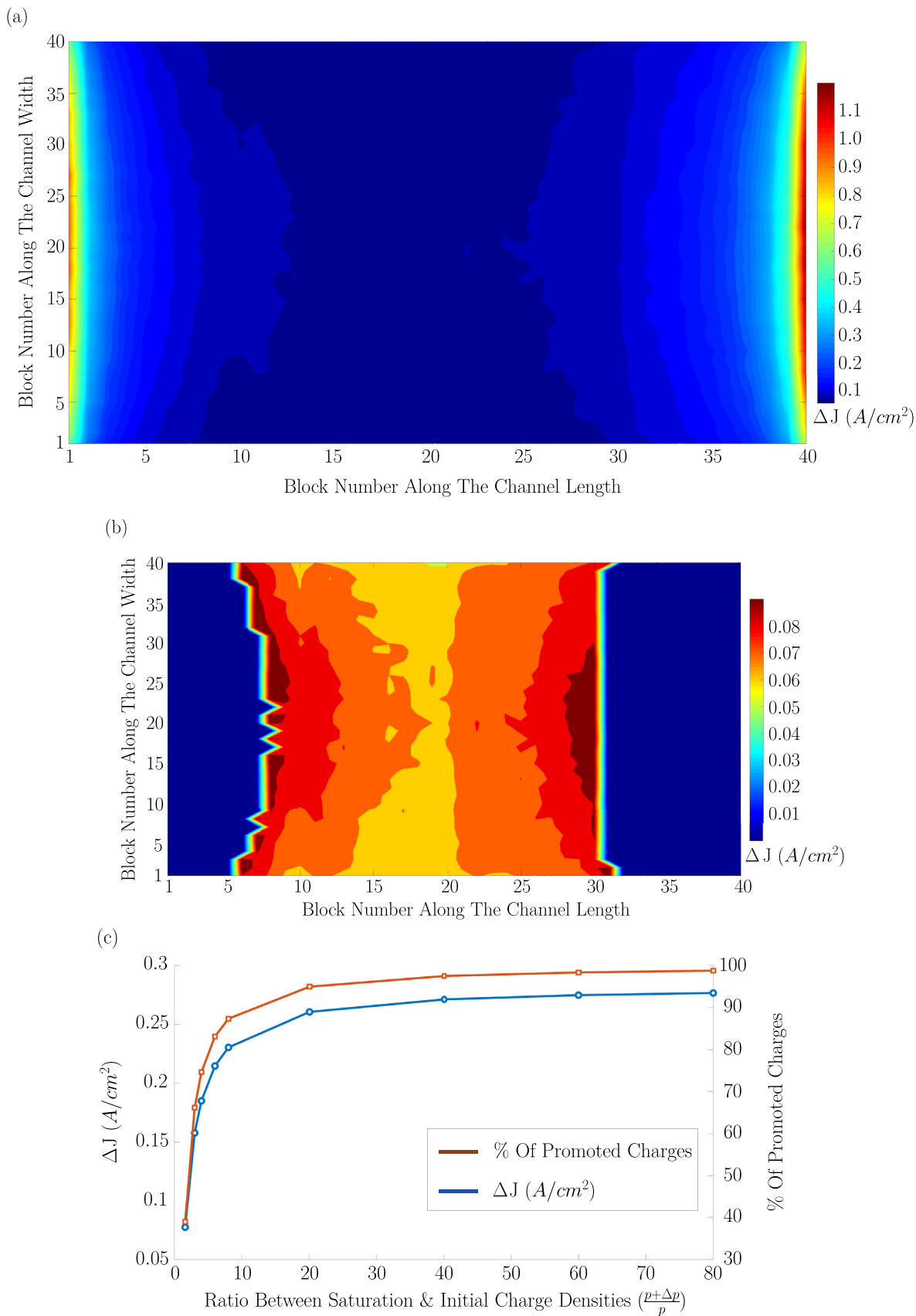
Fig. 6. (a) Color map of the entire network after the manipulation process. High current density difference between pre- and post-manipulation obseerved near the contacts relating to the position of the block rather than local effects. **(b)** A detailed view of the central region of the network where a more local effect due to de-trapping is observed. **(c)** Effect on both the promoted charges (orange) and ΔJ (blue) with respect to the ratio between saturation and initial charge densities. (For interpretation of the references to color in this figure legend, the reader is referred to the Web version of this article.)

Table 2

Comparison between experimental measurements and simulation results.

	Experimental	Simulation
Dark Current Density	350 A/cm^2	355A/cm^2
ΔJ	0.01 A/cm^2 - 0.07 A/cm^2	0.01A/cm^2 - 0.08A/cm^2
Trap Density	4.4×10^{18}cm^{-3} (From Table I in Ref. [43])	4.85×10^{18}cm^{-3}

two adjacent segments. The network was divided into 4 segments.

Now that the model has been appropriately adjusted, the entire network will be manipulated block by block. In this manner the positions which contribute to the highest (and lowest) photo-response current and hence the corresponding defective regions are identified. The resulting color map is depicted in Fig. (6a). The principle of SPCM and the model used is based on the effect of illumination which triggers the de-trapping mechanism at a specific spot, therefore identifying a local effect relating a certain density of traps to a specific location in the transistor channel. Similar to SPCM we can use the simulated maps to interpret these low conductive (i.e. defective) regions in terms of traps densities. A recurring observation from Figs. (3) and (6a) is the rather large difference in current density near the contact edges. This raises the question, is what being observed near the contact edges a local effect that de-trapping is much more significant there in contrast to the central region, or is it a global effect due to the close proximity to the contacts that it becomes relevant or even overshadows the effect of de-trapping. We believe it is the latter, because these edge effects are present regardless of the type of network in question. The closer we move towards the edges, the position of the block (i.e. global aspect) has a greater effect on the current than the change applied to the block itself (i.e local aspect).

Focusing on the central region of the channel, we investigate all blocks positioned approximately $3\,\mu$m–$5\,\mu$m away from either contact edges. This allows us to exclude the non-linear behaviour previously mentioned (see Fig. (S1)). Furthermore, this non-linearity is present at high drain voltages (i.e 35 V), on the other hand the network is operating at a lower drain voltage of 10 V. We observe a varying intensity of the color map as shown in Fig. (6b), and the corresponding range of ΔJ lies between 0.01A/cm^2 - 0.08A/cm^2. This range is similar to what has been measured experimentally in Ref. [31]. In order to achieve this agreement we raised the charge density for the manipulation process to 2×10^{17}cm^{-3}. To calculate the density of traps in the central region, we extracted information from the two blocks resulting in both the highest and lowest ΔJ. Combining Eqs. (6) and (7), the resistances r can be rewritten as

$$r_{dark} = \frac{l}{qp\mu_p A} \tag{8}$$

and

$$r_{illum} = \frac{l}{q(p + \Delta p)\mu_p A}, \tag{9}$$

where r_{dark} and r_{illum} are the resistances before and after the manipulation process, A and Δp are the area and trap density respectively. Finally, the trap density is expressed as

$$\Delta p_{avg} = \frac{l}{(r_{dark} - r_{illum})_{avg}q\mu_p A} \tag{10}$$

Both the trap density and the block resistances have a subscript "average" because there are 4 resistors per block and hence why the average value is calculated. Using Eq. (10) the average trap density was evaluated to be between 7.6×10^{16}cm^{-3} - 8×10^{16}cm^{-3}. This corresponds to approximately 40% of the trapped charges are promoted for transport. Given that only 40% of charges were de-trapped, increasing

the density of the manipulation process would further promote more charges. Naturally the ΔJ will continue to increase but only up to a certain point, at which it saturates irrespective of any further manipulation (i.e. all charges are de-trapped). To find out this onset of saturation, Fig. (6c) shows the effect on both the promoted charges and the ΔJ for for different densities of the manipulation process. From Fig. (6c), almost all charges are de-trapped (i.e. 97%) when the strength of the manipulation is 40 times higher than the initial state of a chosen block. This corresponds to a total local charge density of 5×10^{18}cm^{-3} and hence a trap density of 4.85×10^{18}cm^{-3}.

The charge mobility given in Table 1 was chosen to obtain the aforementioned trap densities. The mobility itself was extracted from a DD simulation. Fig (S2) in the Supplementary Information shows the mobility profile along the channel region of a Pentacene transistor. At the desired operating point of our network, the mobility is almost constant and is estimated to be 6.5×10^{-3}cm^2/Vs. Using this mobility, we managed to achieve a very good agreement between simulated and experimentally evaluated trap densities, as given in Table 2.

Finally, given that the above analysis was based on certain approximations such as how the gate and drain-source effects are included or even how we mimic the illumination process, this same investigation can be done on the DD level. Using DD all aspects of a transistor operation are explicitly considered through solving both the Poisson and current equations. Moreover, the channel can be divided up into smaller segments where trap states at a specific energy can be defined for each and every segment. Then, a similar analysis as done previously (i.e. on the resistor network) can be carried out using DD. But given that organic transistors usually have channel lengths in the range of tens of microns, then dividing up such long channels into sub-micron segments and monitoring the effect on the output current due to a change in a specific segment, it becomes increasingly complicated and time consuming. Furthermore, if the channel width is taken into consideration (i.e. going from 2- to 3- dimensions) it would then be nearly impossible to carry out an investigation similar to the SPCM procedure. Thus if an "on the fly" investigation of the effect of traps in organic transistors is required, the proposed resistor network model can act as an appropriate tool for that purpose given that we have to rely on certain approximations. Nevertheless, the analysis is done considering all important aspects of a transistor operation and on an adequate time-scale. More importantly, we have shown that the model can be used to quantify low conductive regions in terms of trap densities and their effect on the output current. Hence, we demonstrated that the local effect is more pronounced than the global state of the entire network (i.e. which defines the resistance pathway the current will undertake). This is critical as the aim is to trace the effect of traps back to a specific location in the organic film, as done by the SPCM procedure.

6. Conclusion

In this study we presented a simulation model based on a network of resistors to investigate traps states in organic thin films. The model is used to interpret the results provided by scanning photo-current microscopy. Blocks of resistors are chosen and manipulated accordingly to mimic charge carrier de-trapping through an illumination process. Initially, the model has been successfully validated. This is followed by appropriately extending the model for a more realistic approach to identify defective regions in organic thin films. Quantifying these defective regions in term of trap densities, our analysis shows that the difference in current observed as a result of spot illumination, can be related to charges being de-trapped at that same spot. This is true assuming that we are not too close to the edges (approximately $3\,\mu$m–$5\,\mu$m away from the edges), where the effect of the contacts becomes predominant and the local property due to charge de-trapping is greatly overshadowed. Furthermore, to record a ΔJ similar to that of SPCM measurements, we found that only 40% of charges were promoted. Yet a higher manipulation process (i.e. 40 times higher) was

required to promote almost all trapped charges. This corresponds to a trap density of $4.85 \times 10^{18} cm^{-3}$ which is also in agreement with experimentally measured trap densities.

Appendix A. Supplementary data

Supplementary data related to this article can be found at https://doi.org/10.1016/j.orgel.2018.08.002.

References

[1] M. Brinkmann, Structure and morphology control in thin films of regioregular poly (3-hexylthiophene), J. Polym. Sci. B Polym. Phys. 49 (17) (2011) 1218–1233, https://doi.org/10.1002/polb.22310.

[2] W. Xie, Y.Y. Sun, S.B. Zhang, J.E. Northrup, Structure and sources of disorder in poly(3-hexylthiophene) crystals investigated by density functional calculations with van der waal interactions, Phys. Rev. B 83 (18) (2011) 184117, https://doi.org/10.1103/PhysRevB.83.184117.

[3] M. Wirix, P. Bomans, H. Friedrich, N. Sommerdijk, G. de With, Three-dimensional structure of P3HT assemblies in organic solvents revealed by cryo-tem, Nano Lett. 14 (4) (2014) 2033–2038, https://doi.org/10.1021/nl5001967.

[4] A.B. Mallik, J. Locklin, S. Mannsfeld, C. Reese, M.E. Roberts, M.L. Senatore, H. Zi, Z. Bao, Design, synthesis, and transistor performance of organic semiconductors, in: Z. Bao, J. Locklin (Eds.), Organic Field-Effect Transistors, Taylor & Francis, 2007, pp. 161–228 Ch. 3.1.

[5] K. Myny, S. Steudel, S. Smout, P. Vicca, F. Furthner, B. van der Putten, A.K. Tripathi, G.H. Gelinck, J. Genoe, W. Dehaene, P. Heremans, Organic RFID transponder chip with data rate compatible with electronic product coding, Org. Electron. 11 (7) (2010) 1176–1179, https://doi.org/10.1016/j.orgel.2010.04.013.

[6] B.K.C. Kjellander, W. Smaal, K. Myny, J. Genoe, W. Dehaene, P. Heremans, G.H. Gelinck, Optimized circuit design for flexible 8-bit RFID transponders with active layer of ink-jet printed small molecule semiconductors, Org. Electron. 14 (3) (2013) 768–774, https://doi.org/10.1016/j.orgel.2012.12.027.

[7] T. Someya, A. Dodabalapur, J. Huang, K.C. See, H.E. Katz, Chemical and physical sensing by organic field-effect transistors and related devices, Adv. Mater. 22 (34) (2010) 3799–3811, https://doi.org/10.1002/adma.200902760.

[8] S. Han, X. Zhuang, W. Shi, X. Yang, L. Li, J. Yu, Poly(3-hexylthiophene)/polystyrene (P3HT/PS) blends based organic field-effect transistor ammonia gas sensor, Sensor. Actuator. B 225 (31) (2016) 10–15, https://doi.org/10.1016/j.snb.2015.11.005.

[9] M. Yun, A. Sharma, C. Fuentes-Hernandez, D.K. Hwang, A. Dindar, S. Singh, S. Choi, B. Kippelen, Stable organic field-effect transistors for continuous and non-destructive sensing of chemical and biologically relevant molecules in aqueous environment, ACS Appl. Mater. Interfaces 6 (3) (2014) 1616–1622, https://doi.org/10.1021/am404460j.

[10] J. Nishide, H. Nakanotani, Y. Hiraga, C. Adachi, High-efficiency white organic light-emitting diodes using thermally activated delayed fluorescence, Appl. Phys. Lett. 104 (23) (2014) 233304, https://doi.org/10.1063/1.4882456.

[11] H. Nakanotani, T. Higuchi, T. Furukawa, K.Masui, K. Morimoto, M. Numata, H. Tanaka, Y. Sagara, T. Yasuda, C. Adachi, High-efficiency organic light-emitting diodes with fluorescent emitters, Nature Commun. 5:4016. https://doi.org/10.1038/ncomms5016.

[12] J.H. Jou, S. Kumar, A. Agrawal, T.H. Li, S. Sahoo, Approaches for fabricating high efficiency organic light emitting diodes, J. Mater. Chem. C 3 (13) (2015) 2974–3002, https://doi.org/10.1039/C4TC02495H.

[13] T. Miwa, S. Kubo, K. Shizu, T. Komino, C. Adachi, H. Kaji, Blue organic light-emitting diodes realizing external quantum efficiency over 25% using thermally activated delayed fluorescence emitters, Nature Sci. Rep. 7 (284).https://doi.org/10.1038/s41598-017-00368-5.

[14] L. Lu, T. Zheng, Q. Wu, A.M. Schneider, D. Zhao, L. Yu, Recent advances in bulk heterojunction polymer solar cells, Chem. Rev. 115 (23) (2015) 12666–12731, https://doi.org/10.1021/acs.chemrev.5b00098.

[15] J. Yuan, J. Gu, G. Shi, J. Sun, H. Q. Wang, W. Ma, High efficiency all-polymer tandem solar cells, Nature Sci. Rep. 6 (26459). https://doi.org/10.1038/srep26459.

[16] J. Lui, et al., Fast charge separation in a non-fullerene organic solar cell with a small driving force, Nature Energy 1. doi:10.1038/nenergy.2016.89.

[17] D. Knipp, J.E. Northhup, Electric-field-induced gap states in pentacene, Adv. Mater. 21 (24) (2009) 2511–2515, https://doi.org/10.1002/adma.200802173.

[18] J.E. Northhup, M.L. Chabinyc, Gap states in organic semiconductors: hydrogen- and oxygen-induced states in pentacene, Phys. Rev. B 68 (4) (2003) 041202, , https://doi.org/10.1103/PhysRevB.68.041202.

[19] R. Ruiz, A. Papadimitratos, A.C. Mayer, G.G. Malliaras, Thickness dependence of

[20] mobility in pentacene thin-film transistors, Adv. Mater. 17 (14) (2005) 1795–1798, https://doi.org/10.1002/adma.200402077.

[20] A. Hoppe, T. Balster, T. Muck, V. Wagner, Scaling limits and MHz operation in thiophene-based field-effect transistors, Phys. Status Solidi 205 (3) (2008) 612–625, https://doi.org/10.1002/pssa.200723442.

[21] H. Bässler, Charge transport in disordered organic photoconductors: a Monte Carlo simulation study, Phys. Status Solidi 175 (1) (1993) 15–56, https://doi.org/10.1002/pssb.2221750102.

[22] C. Li, L. Duan, H. Li, Y. Qiu, Universal trap effect in Carrier transport of disordered organic semiconductors: transition from shallow trapping to deep trapping, J. Phys. Chem. C 118 (20) (2014) 10651–10660, https://doi.org/10.1021/jp5022906.

[23] M.F. Calhoun, C. Hsieh, V. Podzorov, Effect of interfacial shallow traps on polaron transport at the surface of organic semiconductors, Phys. Rev. Lett. 98 (9) (2007) 096402, , https://doi.org/10.1103/PhysRevLett.98.096402.

[24] V. Podzorov, E. Menard, A. Borissov, V. Kiryukhin, J.A. Rogers, M.E. Gershenson, Intrinsic charge transport on the surface of organic semiconductors, Phys. Rev. Lett. 93 (8) (2004) 086602, , https://doi.org/10.1103/PhysRevLett.93.086602.

[25] A. Salleo, T.W. Chen, A.R. Völkel, Y. Wu, P. Liu, B.S. Ong, R.A. Street, Intrinsic hole mobility and trapping in a regioregular poly(thiophene), Phys. Rev. B 70 (11) (2004) 115311, https://doi.org/10.1103/PhysRevB.70.115311.

[26] R. Noriega, A. Salleo, Charge transport theories in organic semiconductors, in: H. Klauk (Ed.), Organic Electronics II: More Materials and Applications, Wiley-VCH, 2012, pp. 67–103 Ch. 3.

[27] C. Ucurum, H. Goebel, F.A. Yildirim, W. Bauhofer, W. Krautschneider, Hole trap related hysteresis in pentacene field-effect transistors, J. Appl. Phys. 104 (2008), https://doi.org/10.1063/1.2999643 084501.

[28] J. Zaumseil, H. Sirringhaus, Electron and ambipolar transport in organic field-effect transistors, Chem. Rev. 107 (4) (2007) 1296–1323, https://doi.org/10.1021/cr0501543.

[29] H. Sirringhaus, Reliability of organic field-effect transistors, Adv. Mater. 21 (38) (2009) 3859–3873, https://doi.org/10.1002/adma.200901136.

[30] C. Westermeier, A. Cernescu, S. Amarie, C. Liewald, F. Keilmann, B. Nickel, Sub-micron phase coexistence in small-molecule organic thin films revealed by infrared nano-imaging, Nat. Commun. 5 (4101). http://dx.doi.org/10.1038/ncomms5101.

[31] C. Westermeier, M. Fiebig, B. Nickel, Mapping of trap densities and hotspots in pentacene thin-film transistors by frequency-resolved scanning photoresponse microscopy, Adv. Mater. 25 (40) (2013) 5719–5724, https://doi.org/10.1002/adma.201300958.

[32] M.W.B. Wilson, A. Rao, B. Ehrler, R.H. Friend, Singlet exciton fission in poly-crystalline pentacene: from photophysics towards devices, Acc. Chem. Res. 46 (6) (2013) 1330–1338, https://doi.org/10.1021/ar300345h.

[33] H. Marciniak, M. Fiebig, M. Huth, S. Schiefer, B. Nickel, F. Selmaier, S. Lochbrunner, Ultrafast exciton relaxation in microcrystalline pentacene films, Phys. Rev. Lett. 99 (17) (2007) 176402, https://doi.org/10.1103/PhysRevLett.99.176402.

[34] D.V. Lang, X. Chi, T. Siegrist, A.M. Sergent, A.P. Ramirez, Amorphouslike density of gap states in single-crystal pentacene, Phys. Rev. Lett. 93 (8) (2004) 086802, , https://doi.org/10.1103/PhysRevLett.93.086802.

[35] M. Fiebig, C. Erlen, M. Göllner, P. Lugli, B. Nickel, Spatially resolved photoresponse measurements on pentacene thin-film transistors, Appl. Phys. A 95 (1) (2009) 113–117, https://doi.org/10.1007/s00339-008-5009-x.

[36] C. Liewald, D. Reiser, C. Westermeier, B. Nickel, Photocurrent microscopy of contact resistance and charge Carrier traps in organic field-effect transistors, Appl. Phys. Lett. 109 (2016), https://doi.org/10.1063/1.4960159 053301.

[37] F.Y. Wu, Theory of resistor networks: the two-point resistance, J. Phys. Math. Gen. 37 (26) (2004) 6653–6673, https://doi.org/10.1088/0305-4470/37/26/004.

[38] W. Shockley, A unipolar "field-effect" transistor, Proc. I.R.E. 40 (11) (1952) 1365–1376, https://doi.org/10.1109/JRPROC.1952.273964.

[39] J.R. Brews, A charge-sheet model of the mosfet, Solid State Electron. 21 (2) (1978) 345–355, https://doi.org/10.1016/0038-1101(78)90264-2.

[40] R. Schmechel, M. Ahles, H. von Seggern, A pentacene ambipolar transitor: experiment and theory, J. Appl. Phys. 98 (8) (2005) 084511, , https://doi.org/10.1063/1.2106009.

[41] D. Knipp, K.Y. Chan, A. Gordijn, M. Marinkovic, H. Stiebig, Ambipolar charge transport in microcrystalline silicon thin-film transistors, J. Appl. Phys. 109 (2) (2011), https://doi.org/10.1063/1.3531990 02504.

[42] A. Risteska, K.Y. Chan, T.D. Anthopoulos, A. Gordijn, H. Stiebig, M. Nakamura, D. Knipp, Designing organic and inorganic ambipolar thin-film transistors and inverters: theory and experiment, Org. Electron. 13 (12) (2012) 2816–2824, https://doi.org/10.1016/j.orgel.2012.08.038.

[43] W.L. Kalb, B. Batlogg, Calculating the trap density of states in organic field-effect transistors from experiment: a comparison of different methods, Phys. Rev. B 81 (3) (2010), https://doi.org/10.1103/PhysRevB.81.035327 035327(1–13).

A.6 PHASE-RESOLVED TERAHERTZ SELF-DETECTION NEAR-FIELD MICROSCOPY

Maria C. Giordano, Stefan Mastel, Clemens Liewald, Lorenzo L. Columbo, Massimo Brambilla, Leonardo Viti, Antonio Politano, Kai Zhang, Lianhe Li, A. Giles Davies, Edmund H. Linfield, Rainer Hillenbrand, Fritz Keilmann, Gaetano Scamarcio, and Miriam S. Vitiello

Abstract

At terahertz (THz) frequencies, scattering-type scanning near-field optical microscopy (s-SNOM) based on continuous wave sources mostly relies on cryogenic and bulky detectors, which represents a major constraint for its practical application. Here, we devise a THz s-SNOM system that provides both amplitude and phase contrast and achieves nanoscale (60-70nm) in-plane spatial resolution. It features a quantum cascade laser that simultaneously emits THz frequency light and senses the backscattered optical field through a voltage modulation induced inherently through the self-mixing technique. We demonstrate its performance by probing a phonon-polariton-resonant CsBr crystal and doped black phosphorus flakes.

Contribution

I did preliminary experiments in the mid IR region and recorded the first terahertz self-detection near-field signal. Furthermore, I had the idea and calculated the averaged profiles for Figure 2e-g. In addition, I noticed and calculated the phase shift during tip approach for Figure 3a, b.

Phase-resolved terahertz self-detection near-field microscopy

Maria C. Giordano,[1] Stefan Mastel,[2] Clemens Liewald,[3,4] Lorenzo L. Columbo,[5,6] Massimo Brambilla,[5,7] Leonardo Viti,[1] Antonio Politano,[8] Kai Zhang,[9] Lianhe Li,[10] A. Giles Davies,[10] Edmund H. Linfield,[10] Rainer Hillenbrand,[11,12] Fritz Keilmann,[3] Gaetano Scamarcio,[5,7,*] and Miriam S. Vitiello[1]

[1]NEST, CNR - Istituto Nanoscienze and Scuola Normale Superiore, Piazza San Silvestro 12, I-56127 Pisa, Italy
[2]CIC nanoGUNE Consolider, 20018 Donostia—San Sebastian, Spain
[3]Fakultät für Physik & Center for NanoScience (CeNS), Ludwig-Maximilians-Universität München, Geschwister-Scholl-Platz 1, 80539 Munich, Germany
[4]Nanosystems Initiative Munich, Schellingstrasse 4, 80799 Munich, Germany
[5]CNR- Istituto di Fotonica e Nanotecnologie, Sede di Bari, via Amendola 173, I-70126 Bari, Italy
[6]Dipartimento di Elettronica e Telecomunicazioni, Politecnico di Torino, Corso Duca degli Abruzzi 24, 10129 Torino, Italy
[7]Dipartimento Interateneo di Fisica, Università degli Studi e Politecnico di Bari, via Amendola 173, I-70126 Bari, Italy
[8]Fondazione Istituto Italiano di Tecnologia, Graphene Labs, via Morego 30, 16163, Genova, Italy
[9]i-Lab, Suzhou Institute of Nano-Tech and Nano-Bionics, Chinese Academy of Sciences, Suzhou, Jiangsu, China
[10]School of Electronic and Electrical Engineering, University of Leeds, Leeds LS2 9JT, UK
[11]IKERBASQUE, Basque Foundation for Science, 48013 Bilbao, Spain
[12]CIC nanoGUNE and UPV/EHU, 20018 Donostia-San Sebastian, Spain
*gaetano.scamarcio@uniba.it

Abstract: At terahertz (THz) frequencies, scattering-type scanning near-field optical microscopy (s-SNOM) based on continuous wave sources mostly relies on cryogenic and bulky detectors, which represents a major constraint for its practical application. Here, we devise a THz s-SNOM system that provides both amplitude and phase contrast and achieves nanoscale (60-70nm) in-plane spatial resolution. It features a quantum cascade laser that simultaneously emits THz frequency light and senses the backscattered optical field through a voltage modulation induced inherently through the self-mixing technique. We demonstrate its performance by probing a phonon-polariton-resonant CsBr crystal and doped black phosphorus flakes.

OCIS codes: (180.4243) Near-field microscopy; (180.5810) Scanning microscopy; (140.5965) Semiconductor lasers, quantum cascade; (110.6795) Terahertz imaging; (110.3175) Interferometric imaging; (310.6628) Subwavelength structures, nanostructures.

References and links

1. F. Keilmann and R. Hillenbrand, "Near-Field Nanoscopy by Elastic Light Scattering from a Tip", in Nano-Optics and Near-Field Optical Microscopy, Zayats, & A. D. Richards, eds., Artech House, Boston, London (2009).
2. A. J. Huber, F. Keilmann, J. Wittborn, J. Aizpurua, and R. Hillenbrand, "Terahertz Near-Field Nanoscopy of Mobile Carriers in Single Semiconductor Nanodevices," Nano Lett. **8**(11), 3766–3770 (2008).
3. R. Hillenbrand and F. Keilmann, "Complex Optical Constants on a Subwavelength Scale," Phys. Rev. Lett. **85**(14), 3029–3032 (2000).
4. N. Ocelic, A. Huber, and R. Hillenbrand, "Pseudo-heterodyne Detection for Background-Free Near-Field Spectroscopy," Appl. Phys. Lett. **89**(10), 101124 (2006).
5. H. G. von Ribbeck, M. Brehm, D. W. van der Weide, S. Winnerl, O. Drachenko, M. Helm, and F. Keilmann, "Spectroscopic THz near-field microscope," Opt. Express **16**(5), 3430–3438 (2008).

6. H.-T. Chen, S. Kraatz, G. C. Cho, and R. Kersting, "Identification of a resonant imaging process in apertureless near-field microscopy," Phys. Rev. Lett. **93**(26), 267401 (2004).
7. C. Liewald, S. Mastel, J. Hesler, A. J. Huber, R. Hillenbrand, and F. Keilmann, "All-electronic terahertz nanoscopy," Optica **5**(2), 159 (2018).
8. A. J. L. Adam, "Review of Near-Field Terahertz Measurement Methods and Their Applications," J. Infrared Millim. Terahertz Waves **32**(8-9), 976–1019 (2011).
9. W. L. Chan, J. Deibel, and D. M. Mittleman, "Imaging with terahertz radiation," Rep. Prog. Phys. **70**(8), 1325–1379 (2007).
10. P. Dean, O. Mitrofanov, J. Keeley, I. Kundu, L. Li, E. H. Linfield, and A. Giles Davies, "Apertureless near-field THz imaging using the self-mixing effect in a quantum cascade laser," Appl. Phys. Lett. **108**(9), 091113 (2016).
11. R. Degl'Innocenti, R. Wallis, B. Wei, L. Xiao, S. J. Kindness, O. Mitrofanov, P. Braeuninger-Weimer, S. Hofmann, H. E. Beere, and D. A. Ritchie, "Terahertz nanoscopy of plasmonic resonances with a quantum cascade laser," ACS Photonics **4**(9), 2150–2157 (2017).
12. T. Taimre, K. Bertling, Y. L. Lim, P. Dean, D. Indjin, and A. D. Rakić, "Methodology for materials analysis using swept-frequency feedback interferometry with terahertz frequency quantum cascade lasers," Opt. Express **22**(15), 18633–18647 (2014).
13. M. S. Vitiello, G. Scalari, B. S. Williams, and P. De Natale, "Quantum cascade lasers: 20 years of challenges," Opt. Express **23**(4), 8462–8475 (2015).
14. G. Giuliani and S. Donati, "Laser interferometry", in Unlocking Dynamical Diversity, John Wiley & Sons, Ltd, pp. 217–255 (2005).
15. T. Taimre, M. Nikolić, K. Bertling, Y. L. Lim, T. Bosch, and A. D. Rakić, "Laser feedback interferometry: a tutorial on the self-mixing effect for coherent sensing," Adv. Opt. Photonics **7**(3), 570–631 (2015).
16. F. P. Mezzapesa, L. L. Columbo, M. Brambilla, M. Dabbicco, S. Borri, M. S. Vitiello, H. E. Beere, D. A. Ritchie, and G. Scamarcio, "Intrinsic stability of quantum cascade lasers against optical feedback," Opt. Express **21**(11), 13748–13757 (2013).
17. F. P. Mezzapesa, L. L. Columbo, C. Rizza, M. Brambilla, A. Ciattoni, M. Dabbicco, M. S. Vitiello, and G. Scamarcio, "Photo-generated metamaterials induce modulation of CW terahertz quantum cascade lasers," Sci. Rep. **5**(1), 16207 (2015).
18. F. P. Mezzapesa, L. L. Columbo, M. Brambilla, M. Dabbicco, M. S. Vitiello, and G. Scamarcio, "Imaging of free carriers in semiconductors via optical feedback in terahertz quantum cascade lasers," Appl. Phys. Lett. **104**(4), 041112 (2014).
19. R. Lang and K. Kobayashi, "External optical feedback effects on semiconductor injection laser properties," IEEE J. Quantum Electron. **16**(3), 347–355 (1980).
20. T. G. Fiske and L. B. Coleman, "Longitudinal-optical phonons in thin films of rubidium iodide, potassium iodide, rubidium bromide, cesium iodide, and cesium bromide," Phys. Rev. B Condens. Matter **45**(3), 1414–1424 (1992).
21. T. Taubner, F. Keilmann, and R. Hillenbrand, "Nanomechanical Resonance Tuning and Phase Effects in Optical Near-Field Interaction," Nano Lett. **4**(9), 1669–1672 (2004).
22. L. Viti, J. Hu, D. Coquillat, A. Politano, C. Consejo, W. Knap, and M. S. Vitiello, "Heterostructured hBN-BP-hBN Nanodetectors at Terahertz Frequencies," Adv. Mater. **28**(34), 7390–7396 (2016).
23. L. Viti, J. Hu, D. Coquillat, W. Knap, A. Tredicucci, A. Politano, and M. S. Vitiello, "Black Phosphorus Terahertz Photodetectors," Adv. Mater. **27**(37), 5567–5572 (2015).
24. O. Mitrofanov, L. Viti, E. Dardanis, M. C. Giordano, D. Ercolani, A. Politano, L. Sorba, and M. S. Vitiello, "Near-field terahertz probes with room-temperature nanodetectors for subwavelength resolution imaging," Sci. Rep. **7**, 44240 (2017).
25. M. A. Huber, F. Mooshammer, M. Plankl, L. Viti, F. Sandner, L. Z. Kastner, T. Frank, J. Fabian, M. S. Vitiello, T. L. Cocker, and R. Huber, "Femtosecond photo-switching of interface polaritons in black phosphorus heterostructures," Nat. Nanotechnol. **12**, 207 (2017).
26. M. S. Vitiello and L. Viti, "Photonic Devices Based On Black-Phosphorus and Combined Hybrid 2D nanomaterials," Riv. Nuovo Cim. **39**, 371–398 (2016).
27. J. Abate, S. Gamage, Z. Li, V. Babicheva, M. H. Javani, H. Wang, S. B. Cronin, and M. I. Stockman, "Nanoscopy reveals surface-metallic black phosphorus," Light Sci. Appl. **5**(10), e16162 (2016).
28. Y. Xu, J. Yuan, L. Fei, X. Wang, Q. Bao, Y. Wang, K. Zhang, and Y. Zhang, "Selenium-Doped Black Phosphorus for High-Responsivity 2D Photodetectors," Small **12**(36), 5000–5007 (2016).
29. F. Xia, H. Wang, and Y. Jia, "Rediscovering black phosphorus as an anisotropic layered material for optoelectronics and electronics," Nat. Commun. **5**(1), 4458 (2014).
30. M. S. Vitiello and A. Tredicucci, "Tunable emission in Terahertz quantum cascade lasers," IEEE Trans. Terahertz Sci. Technol. **1**(1), 76–84 (2011).
31. D. Burgoff, T.-Y. Kao, N. Han, C. W. I. Chan, X. Cai, Y. Yang, D. J. Hayton, J.-R. Gao, J. L. Reno, and Q. Hu, "Terahertz laser frequency combs," Nat. Photonics **8**(6), 462–467 (2014).
32. M. Rosch, G. Scalari, M. Beck, and J. Faist, "Octave spanning semiconductor laser," Nat. Photonics **9**(1), 42–47 (2015).
33. N. Rotenberg and L. Kuipers, "Mapping nanoscale light fields," Nat. Photonics **8**(12), 919–926 (2014).
34. S. Amarie and F. Keilmann, "Broadband-infrared assessment of phonon resonance in scattering-type near-field microscopy," Phys. Rev. B **83**(4), 045404 (2011).

35. L. L. Columbo and M. Brambilla, "Multimode regimes in quantum cascade lasers with optical feedback," Opt. Express **22**(9), 10105–10118 (2014).
36. M. S. Vitiello, L. Consolino, S. Bartalini, A. Taschin, A. Tredicucci, M. Inguscio, and P. De Natale, "Quantum limited frequency fluctuations in a terahertz laser," Nat. Photonics **6**(8), 525–528 (2012).
37. M. Ravaro, S. Barbieri, G. Santarelli, V. Jagtap, C. Manquest, C. Sirtori, S. P. Khanna, and E. H. Linfield, "Measurement of the intrinsic linewidth of terahertz quantum cascade lasers using a near-infrared frequency comb," Opt. Express **20**(23), 25654–25661 (2012).

1. Introduction

Terahertz (THz) frequency electromagnetic waves (30–300 μm wavelength) can resonantly interact with fundamental excitations of molecules and solids and thus offer an ideal tool for the optical characterization of emerging low-dimensional materials and biological-systems. Scattering-type scanning near-field optical microscopy (s-SNOM) displayed an exceptional potential for nanoscale imaging of material properties [1] as has been demonstrated also at 2.5 THz [2]. In s-SNOM, an incident light beam is focused on a sharp atomic force microscope (AFM) metallic tip strongly confining the radiation to the near-field region of its nanometric apex. Nanoscale resolved (10 - 100 nm) optical images can be retrieved by analyzing the scattered radiation as a function of tip position, placing the tip in close proximity to the sample surface.

Coherent imaging, i.e. detection of amplitude and phase contrast, is crucial to get information on the real and imaginary parts of the dielectric response and hence several interferometric approaches have been developed allowing amplitude and phase resolved s-SNOM imaging in the visible and infrared spectral ranges [3, 4]. Solutions based on fs pulsed laser sources and electro-optic sampling detection in the THz range [5, 6] or solutions based on microwave circuitry in the sub-THz range [7] have been reported. However, in spite of a strong demand to extend in the far-infrared the spectral coverage of coherent nano-imaging based on *continuous-wave (CW) compact sources*, conventional interferometric techniques [2, 8, 9] have suffered from the poor dynamic range of cryogenically cooled bolometric detectors needed to measure the typically small s-SNOM signals [2]. Progress in coherent THz nano-imaging would therefore greatly benefit from compact, room-temperature operating and fast detection systems for THz frequency operation.

Here we tackle the problem by conceiving a simple, potentially fast and compact s-SNOM system based on a THz quantum cascade laser (QCL) operated CW in the self-detection (SD) mode. A similar approach has been recently exploited to produce THz images with sub-wavelength spatial resolution [10, 11]. In this work, we demonstrate amplitude- and phase-resolved background-free SD-s-SNOM imaging with 60-70 nm spatial resolution comparable to the scattering tip size, providing a key step forward to make THz nanoscopy a widely used tool. Our approach, based on a simple 2-parameter fitting of self-mixing interferograms, outperforms by far all previously reported attempts based on the use of self-mixing and either attaining incoherent near-field s-SNOM imaging, or using a rather complex 6-parameter fitting procedure for amplitude-like and phase-like images at diffraction-limited resolutions (> 100 μm) [12].

2. Results and discussion

2.1 The general concept of SD-s-SNOM

In our experimental configuration, we use the radiation source, a THz quantum cascade laser (QCL) [13], (see Experimental Methods) not only for illuminating the tip but also for detecting the radiation field scattered from the tip, therefore avoiding the use of bulky THz cryogenic detectors. The near-field scattering is measured through the voltage change (ΔV) across the electrical contacts of the THz QCL, induced by the self-mixing effect [14, 15]. This effect is based on the reinjection of a small fraction (10^{-4} 10^{-2}) of the emitted field that coherently interferes within the laser cavity.

The inherent stability of QCLs against optical feedback [16] has been recently exploited in a number of self-mixing interferometry (SMI) configurations, providing an interesting method to control the emission of THz QCLs by reconfigurable photo-generated anisotropic metamaterials [17], to trace the free carrier distribution in a semiconductor target [18], and to map the real and imaginary refractive index of polymeric materials [12], for example.

In our system (Fig. 1(a)), the 2.7 THz QCL radiation is focused onto the apex of a Pt tip, which is sinusoidally dithered, normally and in close proximity to the sample surface at frequency Ω. The scattered field E_s is collected by a parabolic mirror and focused back onto the QCL front facet along the same incident optical path, inducing the changes in the QCL voltage (ΔV) (see details on the experimental arrangement in Appendix 1). Hence, ΔV measures the optical response of the sample. To quantify this properly, we relied on the well-established Lang-Kobayashi (LK) model [19], and extended it to encompass a complex sample permittivity. In the very weak feedback limit, the voltage change at the QCL terminals can be written (see Appendix 2):

$$\Delta V \propto s \cos(\omega_0 \frac{2L}{c} - \varphi) \tag{1}$$

where s and φ are the amplitude and phase, respectively, of the ratio between scattered and incident electrical fields of THz radiation, $\omega_0 = 2\pi c / \lambda$ is the unperturbed laser frequency, and L is the laser-to-tip distance which varies by the tip dithering and by the piezoelectric mirror (PZM) displacement. By using an optical attenuator (A), the feedback remains sufficiently low to keep the system in the validity range of Eq. (1). In this regime, the proposed experimental layout is similar to a single-arm homodyne interferometer [14], in which the laser output facet and the tip define the external cavity of our self-mixing interferometer.

Equation (1) contains all necessary physical quantities to predict observable amplitude and phase contrasts in SD-s-SNOM images. Although in conventional s-SNOM, the phase contrast is extracted by analyzing the detector signal variations induced by changing the optical path length of the reference beam of an interferometer, in SD-s-SNOM the amplitude and phase information is obtained from the analysis of the ΔV as a function of ΔL as explained below.
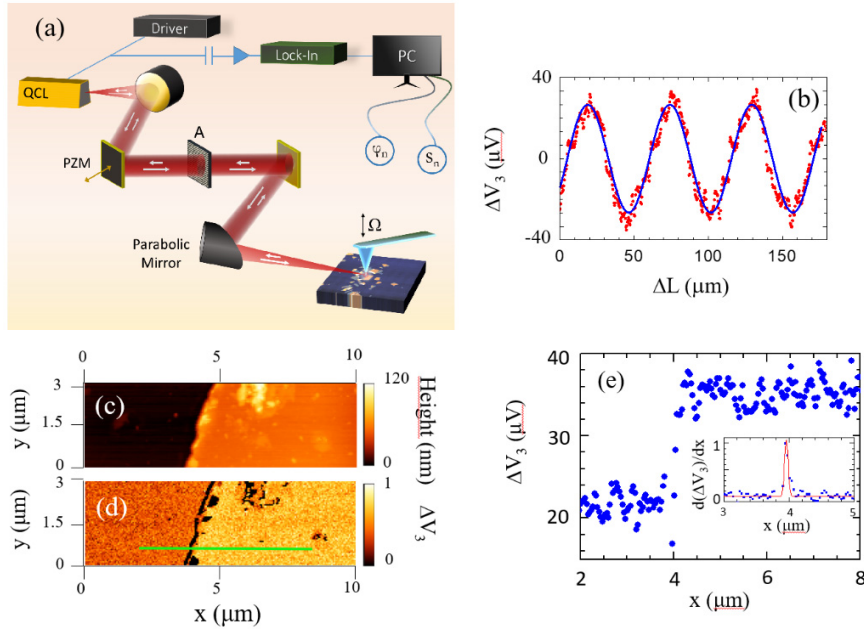
Fig. 1. Self-detection scattering type near field optical microscope with nanometer resolution at terahertz frequencies. (a) Schematic diagram showing the experimental arrangements. The same optical components (two paraboloid mirrors, an attenuator (A), one fixed mirror and one piezo-actuated mirror (PZM)) focus the THz beam emitted by the QCL onto the apex of a Pt tip sinusoidally dithered at frequency Ω in close proximity to the sample surface and feeds the scattered radiation back into the QCL cavity to produce self-mixing. The distance $L \approx 60$ cm between the QCL front facet and the tip can be varied by translating the PZM. (b) Self-mixing induced modulation from a Au surface of the voltage drop across the QCL obtained using the experimental arrangement (a) and measured by a lock-in amplifier to the $n = 3$ demodulation order, as a function of ΔL. The dots are the experimental data and the solid line is the best-fitted curve obtained using Eq. (2). The ΔV_3 signal show the expected $\lambda/2$ periodicity characteristic of self-mixing. (c) AFM topographic and (d) 3rd harmonic near-field THz imaging of the Au-on-silicon sample at a fixed mirror position. (e) Edge response profile extracted from (d) by averaging seven adjacent rows of pixels along the green horizontal line. The inset shows the corresponding spatial derivative, which has been fitted by a Gaussian function (red curve) with a full-width-at-half-maximum of 65 nm.

2.2 The implementation of SD-s-SNOM

In our arrangement, as is typical in s-SNOM for effectively distinguishing the near-field scattering from background scattering [1], ΔV is demodulated at low-order harmonics of the dither frequency using a lock-in amplifier, and the measured harmonic amplitudes ΔV_n are recorded up to the order $n = 5$ as a function of the displacement ΔL. Decomposing ΔV into harmonic components $\Delta V = \sum_{n=0}^{+\infty} \Delta V_n \cos(n\Omega t)$, we show that the demodulated signals equivalently carry information on the optical amplitude and phase components s_n and φ_n (see Appendix 2):

$$\Delta V_n \propto s_n \cos(\omega_0 \frac{2L(t)}{c} - \varphi_n) \tag{2}$$

The experimental $\Delta V_n \, vs \, \Delta L$ curves (e.g. ΔV_3 in Fig. 1(b)) demonstrates that our SD-s-SNOM system behaves similarly to an external interferometer and produces approximately

sinusoidal interference fringes, as predicted by Eq. (2). Figures 1(c)-(d) provide direct proof that the SD-s-SNOM signal is sufficiently stable for homodyne THz imaging.

2.3 Deep sub-wavelength in-plane spatial resolution

Comparison between the AFM (Fig. 1(c)) and the self-detected (Fig. 1(d)) images of a gold film deposited on a SiO_2-coated silicon substrate demonstrates the capability of our THz imaging system to achieve an in-plane resolution comparable with the employed tip apex sizes (50-70nm). Figure 1(e) shows the ΔV_3 signal collected along the green horizontal line in panel 1d traversing the edge of the gold-coated region. The inset of Fig. 1(e) shows the corresponding first-order spatial derivative. From the full-width-at-half-maximum of the Gaussian curve interpolating the derivative function (red curve in the inset of Fig. 1(e)), we can retrieve a remarkable spatial resolution of $\sigma_x = 68$ nm along the horizontal (fast) axis, corresponding to $\sim\lambda/1500$.

2.4 Amplitude and phase contrast imaging capability

The phase-contrast at THz frequencies between gold and SiO_2 is negligibly small, as is usual for all combinations of non-resonant materials [9]. Hence, to provide a proof-of-principle of the amplitude and phase contrast imaging capability of the SD-s-SNOM, we selected a polar crystal (CsBr), which exhibits a strong phonon-polariton (Reststrahlen) resonance in the range 2.2 – 3.3 THz [20]. We simulated the SD-s-SNOM near-field amplitude (s_3) (Fig. 2(a)) and phase (φ_3) signals (Fig. 2(b)) for both CsBr and Au as a function of wave number, using a single phonon oscillator model in the framework of the finite dipole model (see Appendix 2). Our findings show that, although Au exhibits the expected flat amplitude response and negligible phase throughout the THz frequency range investigated, CsBr shows a four-times stronger s_3 peak at 90 cm^{-1}, and a large phase signal $\varphi_3 \approx 150°$ at this wave number. Hence, we prepared a suitable sample comprising a CsBr crystal, coated with a thin (100 nm) Au film, and selected a THz QCL that operated single mode in continuous wave at 90.3 cm^{-1} (2.7 THz). These choices should ensure a strong near-field amplitude and phase contrast at CsBr/Au steps obtained by mechanically scratching the Au thin film to expose the underlying CsBr surface.

Figures 2(c)-2(d) compare the AFM topography (Fig. 2(c)) and the SD-s-SNOM image (Fig. 2(d)) of a CsBr/Au step, simultaneously obtained while raster-scanning in the x-y plane underneath the tip and recording ΔV_3 at each pixel. To show the L dependence of both the ΔV_3 signal and the optical contrast between CsBr and Au, we changed the optical phase $(\omega_0 \frac{2\Delta L}{c})$ over a 2π range in $\pi/3$ steps ($\Delta L = 9.25\,\mu m$), every $\Delta y = 0.5$ μm during the acquisition. We thus observe 13 striped regions in Fig. 2(d). In order to retrieve amplitude and phase from the collected optical images, each line in Fig. 2(c) and 2(d) were preliminarily horizontally shifted to straighten the CsBr/Au edge. Then the signal ΔV_3 was vertically averaged in each stripe and associated with the corresponding ΔL value. Finally, sinusoidal functions (Eq. (2)) were fitted to the $<\Delta V_3>$ vs ΔL curves to extract the amplitude s_3 and phase φ_3 as a function of the horizontal distance from the CsBr/Au edge (Fig. 2(f) and Fig. 2(g)). Then the height (Fig. 2(e)) and the signal ΔV_3 were vertically averaged on each stripe and associated with the corresponding L value. From the steep rise of the optical signal at the edge the Au film on the CsBr crystal, we can estimate the optical spatial resolution. To address the issue we have followed the same procedure detailed for Fig. 1(e). The full-width-at-half-maximum of the Gaussian curves interpolating the derivative function of the amplitude and phase signals (red curves in the insets of Figs. 2(f) and 2(g)), give estimates of the spatial resolutions: 54 nm and 60 nm for the amplitude and phase signals, respectively.
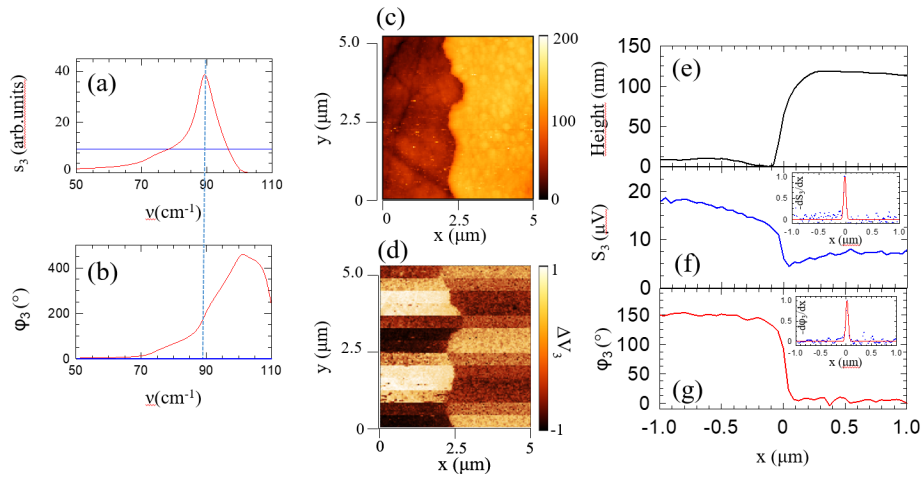
Fig. 2. Amplitude and phase resolved THz nanoscopy on a resonant polar crystal. (a-b) Simulated, near-field resonant dielectric response of CsBr (red lines) and Au (blue lines): amplitude (s_3) and phase (φ_3) plots as a function of wave number. The dashed vertical line corresponds to the probing laser frequency. (c) Atomic force microscope image of a 5 μm x 5.5 μm area of the CsBr/Au sample. Step sizes of $\Delta x = \Delta y$ = 41.6 nm were used. (d) Self-detected near field 3rd order signal. Every Δy = 0.5 μm the PZM mirror position is changed in order to shorten the optical path by ΔL = - 9.25 μm. (e-g) average topography (e), amplitude s_3 (f), and phase φ_3 (g) as a function of the position with respect to the CsBr/Au edge. The insets in Figs. 2(f) and 2(g) show the spatial derivative of the amplitude 2(f) and phase 2 (g) signals, which have been fitted by Gaussian functions (red curves) with full-width-at-half-maxima of 54 nm and 60 nm, respectively.

In Fig. 3, we demonstrate the strong sensitivity of SD-s-SNOM to changes in the amplitude and phase of the effective polarizability of the coupled tip-sample system. For this, we exploited the strong dependence of s_3 and φ_3 on the tip sample distance z (see Appendix 2) [21] and recorded ΔV_3 during approach curves obtained by progressively stepping the PZM position by ΔL = 9.25 μm. For each value of z, s_3 (Fig. 3(a)) and φ_3 (Fig. 3(b)) were extracted by fitting sinusoidal functions (Eq. (2) to the ΔV_3 vs L curves. The prevalent near-field nature of 3rd harmonic signals is shown by the monotonic decrease of both the amplitude and phase signals for increasing z, with s_3 becoming negligible and φ_3 saturating for z > 60 nm. The approach curves of Fig. 3(a)-3(b) are nicely reproduced by the calculated near-field amplitudes (s_3) (Fig. 3(c)) and phases (φ_3) (Fig. 3(d)) of CsBr and Au, solving the full set of transcendental coupled LK equations, with no approximations, at each experimental L value (see Appendix 2). Similarly, our technique is expected to measure changes of the real and imaginary part of the effective polarizability as a function of the incident laser wavelength.
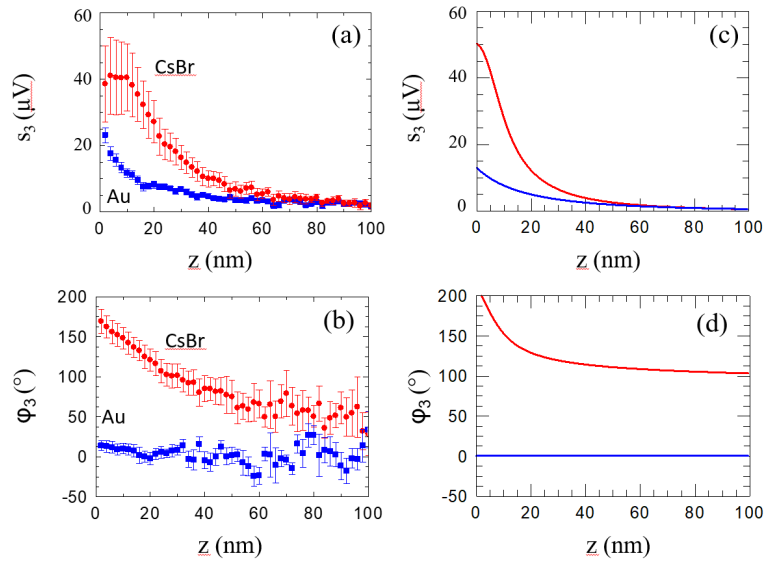
Fig. 3. THz near field amplitude and phase as a function of tip-sample distance (approach curves). (a-b) Comparison between the experimental amplitude (a) and phase (b) of CsBr (red) and Au (blue), collected as a function of the tip-sample distance z, using dither amplitude 106 nm and setting L such that ΔV_3 is maximum at $z = 0$; (c-d) Calculated near-field amplitudes (s_3) (c) and phases (φ_3) (d) of CsBr (red curves) and Au (blue curves) (see Appendix 2).

2.5 Application for 2D material imaging

Finally, we demonstrate the capability of SD-s-SNOM to image doped van der Waals layered materials. We selected black phosphorus (BP), an emerging layered semiconductor, which has been recently demonstrated to be a suitable material system in the THz for photodetectors [22, 23], and near-field optical probes [25]. Here we study BP flakes with different thickness and carrier densities (see the estimate of free carrier density in black phosphorus flakes in Experimental Methods section) that were transferred onto a Si/SiO$_2$ substrate by mechanical exfoliation [23, 26]. A thin (5 nm) SiO$_2$ protection layer was deposited via sputtering to encapsulate the material system and avoid degradation under ambient exposure, ensuring that flakes remained clean and stable for several months [22, 23].

Figure 4 compares the topography images (Figs. 4(a), 4(c), and 4(e) and the corresponding ΔV_3 signals (Figs. 4(b), 4(d), and 4(f) collected on Se-doped BP flakes. A near-field contrast is clearly observed between the Se-doped BP-flakes and the SiO$_2$ substrate in the 2D scans of ΔV_3 shown in Fig. 4(b), 4(d). This effect is also evident in the profile of ΔV_3 measured across the edge of the Se-doped BP flakes (Figs. 4 (l) and 4(m)). In Fig. 4(f) the optical phase was changed at constant steps of 0.39π ($\Delta L = 5.5 \mu m$), every $\Delta y = 0.21$ μm during the scan.

To extract the amplitude and phase from the optical images, each line in Fig. 4(e) and 4(f) were preliminarily horizontally shifted to straighten the BP/SiO$_2$ edge, in analogy to the analysis performed on the CsBr/Au sample (Figs. 2(c)-2(g)). Then, the height (Fig. 4(g)) was vertically averaged on each stripe and associated with the corresponding L value. From the striped image of Fig. 4(f) we extracted the near field amplitude s_3 (Fig. 4(h)) and phase φ_3 (Fig. 4(i)) profiles at the BP/SiO$_2$ step edge. Apparently, no phase contrast between BP and SiO$_2$ is observed, due to the off-resonance excitation of both materials, as expected since in both cases optical phonon resonances fall in the mid-IR [27]. Incidentally, the detected near-field scan results highly sensitive to the presence of oxidation-induced clusters on the surface of the investigated BP flake, which causes an abrupt change of the detected optical signal.
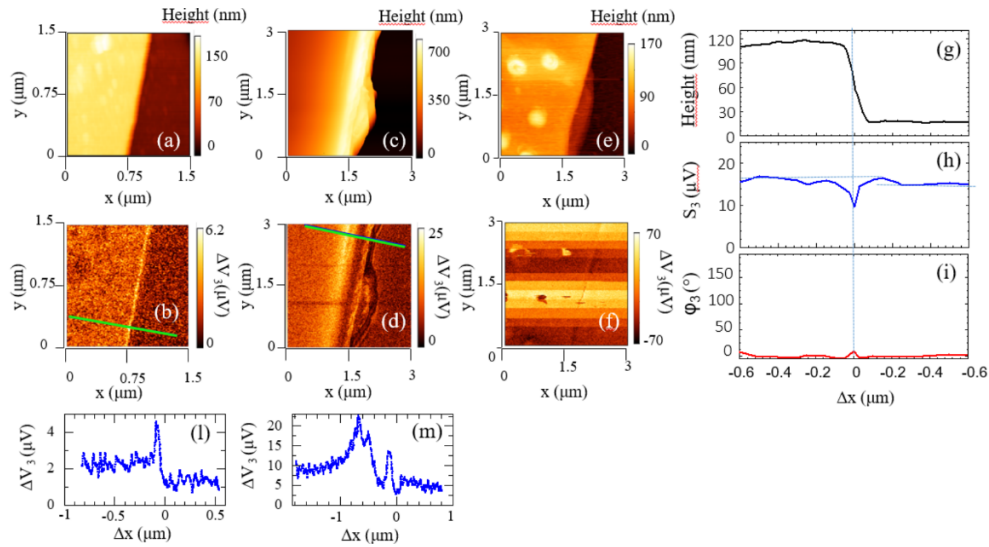
Fig. 4. SD s-SNOM nanoscopy at THz frequencies of doped black-phosphorus. (a, c, e) AFM tomographic images and (b, d, f) corresponding ΔV_3 near field optical signal collected on a set of representative Se-doped BP flakes having thickness 130 nm (a), 300 nm (c) 100 nm (e); (f) Self- detected near field 3rd order signal. Every $\Delta y = 0.21$ μm the PZM mirror position is changed in order to shorten the optical path by $\Delta L = 5.5$ μm. (g-i) average topography (g), amplitude s_3 (h), and phase φ_3 (i) as a function of the position with respect to the Se-doped BP/SiO$_2$ edge. The sharp features in panels (h) and (i) at $\Delta x = 0$ are known edge artifacts arising at the sharp edges of the mechanical exfoliated black phosphorus flakes. The dashed vertical line in panels (h-i) corresponds to the BP/SiO$_2$ edge. The horizontal dashed lines in panel (g) mark the amplitude contrast between the two materials. (l-m) ΔV_3 profiles averaged over seven adjacent rows of pixels along the green lines in panels (b) and (d), respectively

3. Conclusion

In conclusion, we have demonstrated a detector-less s-SNOM system operating at THz frequencies that provides both amplitude and phase contrast with deep sub-wavelength (60-70 nm) in-plane spatial resolutions. These achievements are expected to have a profound impact on the flourishing field of QCL-based THz imaging, in which near-field coherent detection has been missing, so far. The ability of SD-s-SNOM to resolve both the amplitude and phase of the THz field opens up the possibility of mapping the complex permittivity of a target using QCLs with a high spatial resolution, down to a few tens of nanometers. The proved sensitivity to thin-layered samples of our novel THz SD s-SNOM opens the way to further investigations of resonant 2D-materials and combined Van der Waals heterostructures, with potential impacts in plasmonics and optoelectronics.

Future experiments could make use of the tunable bandgap of BP [28] to control its mode-activation energy as well as exploiting resonant excitation to retrieve plasmonic features. The in-plane asymmetry of BP [29] may also allow for further tunability. Looking forward, complex heterostructures that combine BP with graphene, transition-metal dichalcogenides and hexagonal boron nitride have the potential to provide a robust technological platform for THz nanophotonics and ultrafast plasmonics.

Further development of SD-s-SNOM will also benefit from the availability of broadly tunable THz QCLs [30] and THz QCL combs [31, 32]. Also, the inherent ultrafast response of QCLs to optical feedback perturbations, associated with their unipolar nature and the ps-long lifetimes of inter-subband transitions, raises a compelling perspective for new time-resolved hyper spectral THz imaging systems with deep sub-wavelength spatial resolutions (< 100 nm or λ/1000).

The unique features of SD-s-SNOM, i.e. the inherent field sensitivity and compactness, can in principle lead to further elimination of intermediate optical elements and true access to near-field radiation, opening the way to many applications in fields ranging from biosensing to quantum optics [33]. Also, a full integration of sample and nanoscopy set-up inside the same cryostat may become possible, thereby allowing to exploit in situ the potential of coherent THz nanoscopy at cryogenic temperatures and under high magnetic fields, for understanding fundamental excitations, such as phonons, magnons, polaritons, and phase transitions in exotic semiconductor and organic nanostructures, superconductors, multiferroics, and metamaterials, just to mention a few examples.

Appendix 1

Experimental arrangement

A bound-to-continuum single longitudinal mode THz QCL emitting, at a wavelength $\lambda = 111$ μm (2.7 THz, 90.3 cm^{-1}) with a surface plasmon waveguide, was grown by molecular beam epitaxy employing a GaAs/Al$_{0.15}$Ga$_{0.85}$As heterostructure on a nominally undoped GaAs substrate. The 10-μm-thick active region was embedded between a doped ([Si] = 3.0×10^{18} cm^{-3}) 700-nm-thick GaAs bottom layer, and a doped ([Si] = 5.0×10^{18} cm^{-3}) 200-nm-thick GaAs top contact layer. The GaAs semi-insulating substrate was lapped down to a thickness of 150 μm. Laser bars 1.5 mm long and 150 μm wide were cleaved and mounted on a copper bar.

The QCL was mounted in a liquid helium continuous-flow cryostat fitted with a polymethylpentene window, and maintained at a fixed heat sink temperature of 15 K. To maximize the sensitivity to coherent optical feedback [14, 15], the QCL was driven in continuous wave at a current $I = 450$ mA ($J = 132$ A/cm^2) which is just 5% higher than the threshold current density ($J_{th} = 125$A/cm^2), using a highly stable current generator (Lightwave Electronics, mod. QCL 2000). The emitted THz beam was collimated using a 90° off-axis parabolic mirror with an effective focal length of 50 mm, and reflected by a mirror mounted on a piezo-controlled translator stage into the entrance optical port of a commercial near-field microscope (Mod. NeaSNOM, Neaspec, Martinsried, Germany). A 5 dB substrate-free, metal-mesh diffractive attenuator (Mod. 224, Lasnix, Berg, Germany) was placed in the beam. In the microscope, a second paraboloid mirror with an equivalent focal length of 25 mm focused the beam onto a Pt tip (Bruker, mod. RMN-25PT300) having a nominal apex radius of 50 nm, a shank length of 80 μm, and which was sinusoidally dithered at its resonant frequency $\Omega = 15380$ Hz. The laser polarization lay in the plane containing the tip in order to induce an oscillating dipole in the tip efficiently. The average optical path length from the QCL front facet to the tip was $L \approx 60$ cm. The scattered radiation was collected by the same focusing paraboloid mirror and coupled back into the laser cavity along the same incident optical path. The voltage modulation across the QCL terminals produced by the self-mixing effect was pre-amplified using a low-noise amplifier (DL Instruments, mod. 1201) and demodulated up to the highest harmonic order ($n = 5$) allowed by the electronic card of the NeaSNOM.

The density of free carriers n_e in the black phosphorus samples was estimated by performing transport analysis on field effect transistors FET having flakes with identical thickness as active channels [20–22, 24, 25]. n_e is connected with the FET threshold voltage V_{th} via the relation $n_e = \dfrac{C_G \Delta V_{th}}{q A_G}$, where C_G is the gate-to channel capacitance, A_G the gated BP area, and q is the electron charge. We measured $n_e \approx 4.0 \times 10^{17}$ cm^{-3} for the flake shown in Figs 4(a)-4(b), $n_e \approx 7.0 \times 10^{17}$ cm^{-3} for the flake shown in Figs. 4(c)-4(d) and $n_e \approx 1.5 \times 10^{17}$ cm^{-3} for the flake shown in Figs. 4(e)-4(f).

Appendix 2

Theory of self-detection scattering-type scanning near-field optical microscopy (SD s-SNOM)

The near-field scattering is modeled according to the finite-dipole model, in which the tip, described as a spheroid having an effective length L_t and apex radius a, polarizes the sample. The latter, in turn, acts back on the tip, yielding a near-field interaction specific to the sample material. The radiation scattered by a tip, placed with its apex at a distance z from a target surface, is proportional to the effective polarizability α_{eff} and can be written as

$$\sigma = \frac{E_s}{E_i} \propto (1+r_p)^2 \; \alpha_{eff}, \; \text{where [34]}$$

$$\alpha_{eff} = a^2 L_t \frac{L_t(\epsilon_t - 1)(2L_t \sqrt{1-\frac{a}{L_t}} + a \ln \frac{\left(1-\sqrt{1-\frac{a}{L_t}}\right)^2}{\frac{a}{L_t}})}{2L_t \sqrt{1-\frac{a}{L_t}}(L_t - a\epsilon_t) - aL_t(\epsilon_t - 1)ln \frac{\left(1-\sqrt{1-\frac{a}{LL_t}}\right)^2}{\frac{Ra}{L_t}}} \cdot (2 + \frac{\beta\left(g\frac{a+z}{LL_t}\right)\ln\left(\frac{4L_t}{4z+2a}\right)}{\ln\left(\frac{4L_t}{a}\right) - \beta\left(g - \frac{3a+4z}{4L_t}\right)\ln\left(\frac{2L_t}{2z+a}\right)}). \tag{3}$$

Here, E_i and E_s are the incident and scattered fields, respectively, and r_p is the far-field Fresnel reflection coefficient for p-polarized incidence. The sample dielectric permittivity ε_s enters through the so-called surface response function $\beta = (\varepsilon_s - 1) / (\varepsilon_s + 1)$, and ε_t is the tip dielectric function. The apex-sample surface distance z oscillates with frequency Ω and amplitude $2z_A$ as $z(t) = z_A + z_A \cos(\Omega t)$; g, is a complex factor related to the fraction of the total charge induced in the spheroid.

The complex effective scattering efficiency is represented in terms of amplitude and phase as $\sigma(t) = s(t)e^{i\varphi(t)}$, where both s and φ show a nonlinear dependence as a function of z. We have found a good agreement with the experimental results by using the values $L_t = 530$ nm, and $g = 0.98e^{0.08i}$.

Coherent optical feedback in a semiconductor laser cavity is described by the Lang-Kobayashi (LK) model [14, 15, 35], in which two coupled differential equations describe the evolution of the excited state population $N(t)$ and the optical field $E(t)$. The crucial feedback contribution in this model is provided by an additive term, representing the retarded field re-entering the laser cavity.

The LK equations read [35]:

$$\frac{dE(t)}{dt} = \frac{1}{2}(1+i\alpha_H)\left[G_n\left(N(t) - N_0\right) - \frac{1}{\tau_p}\right]E(t) + \frac{\gamma}{\tau_c}E(t-\tau)e^{-i\omega_0\tau}$$

$$\frac{dN(t)}{dt} = \frac{J\eta}{qd} - \frac{N(t)}{\tau_e} - G_n\left(N(t) - N_0\right)|E(t)|^2 \tag{4}$$

where N_0 is the carrier density at transparency, G_n is the gain coefficient, $\tau = 2L/c$, $\tau_p = 30$ ns and $\tau_c = 35$ ns are the photon life time and the cavity round trip time inside the QCL cavity, respectively, and τ_e is the carriers decay time ($1-10\,ps$), J is the current density, η is the internal quantum efficiency, d is the active layer thickness and q is the electron charge, γ is the feedback strength parameter, i.e. the fraction of the back-scattered field that efficiently

couples with the lasing mode. A value $\alpha_H = 1.5$ for the linewidth enhancement factor was used, which is appropriate for a THz QCL close to threshold [36, 37].

In our theoretical approach, we consider a feedback field provided only by the tip-scattered field E_s and neglect any contribution from the background field. The latter is a component well-known in s-SNOM that can be experimentally suppressed by recording signals at higher harmonics of Ω. Considering that the feedback path $2L$ depends on the oscillating tip position, we assume:

$$\gamma(t) \propto \sigma(t) = s(t)e^{i\varphi(t)} = \sum_{n=-\infty}^{+\infty} \sigma_n e^{in\Omega t} = \sum_{n=-\infty}^{+\infty} s_n e^{i\varphi_n} e^{in\Omega t}. \qquad (5)$$

The optical feedback coefficient C is defined as $C = |\gamma|\sqrt{1+\alpha_H^2}\,\dfrac{2L}{c\tau_c}$. In the very weak feedback limit, when $C \approx 10^{-2}$, as appropriate under our experimental condition, the perturbation induced on the laser frequency can be neglected and one can assume that the frequency of the retro-injected laser coincides with ω_0, radically simplifying the self-mixing formalism [14–16]. In fact, the sinusoidal line shapes unveiled in the experiments of Fig. 1 confirm that the system is in the very weak feedback self-mixing regime [19], with estimated values of the feedback coefficient $C \approx 0.03 - 0.1$. Hence, the LK equations are solved for the steady-state value of the carrier variation ΔN induced by the self-mixing (with respect to the free running laser value at threshold), assuming the tip and the PZM dynamics are slow with respect to field and carrier timescales:

$$\Delta N = -2|\gamma|\frac{\tau_p}{\tau_c}\cos(\omega_0\frac{2L(t)}{c} - \varphi(t)) \qquad (6)$$

noting that ΔV is proportional to ΔN [16], we find the following expression:

$$\Delta V(t) \propto s(t)\cos(\omega_0\frac{2L(t)}{c} - \varphi(t)) \qquad (7)$$

Due to the tip oscillation, the laser-tip distance varies as $L(t) = L_0 + 2z_A - z(t)$, where $L_0 + 2z_A$ is the laser-target distance which may vary, if the PZM is moved, on time scales much longer than the tip period $2\pi/\Omega$.. Moreover, we approximate $L \approx L_0$ in the following, since in our experimental configuration $z_A \ll \lambda$.

By introducing the spectral representation of the scattered amplitude in Eq. (4), we can rewrite the steady state equations accordingly, where the RHS term of Eq. (7) becomes:

$$\Delta V(t) \propto \sum_{n=-\infty}^{+\infty} S_n \cos\left(\omega_0\frac{2L}{c} - \varphi_n - \Omega_n t\right) \qquad (8)$$

$$= \sum_{n=0}^{\infty}\left[s_n\cos\left(\omega_0\frac{2L}{c} - \varphi_n - \Omega_n t\right) + s_{-n}\cos\left(\omega_0\frac{2L}{c} - \varphi_{-n} + \Omega_n t\right)\right] - s_0\cos\left(\omega_0\frac{2L}{c} - \varphi_0\right) = \sum_{n=0}^{\infty} s_n\left[\cos\left(\omega_0\frac{2L}{c} - \varphi_n - \Omega_n t\right) + \cos\left(\omega_0\frac{2L}{c} - \varphi_n + \Omega_n t\right)\right] - s_0\cos\left(\omega_0\frac{2L}{c} - \varphi_0\right)$$

$$= \sum_{n=0}^{\infty} 2s_n\left[\cos\left(\omega_0\frac{2L}{c} - \varphi_n\right)\cos(\Omega_n t)\right] - s_0\cos\left(\omega_0\frac{2L}{c} - \varphi_0\right)$$

where $\Omega_n = n\Omega$, and $s_n = s_{-n}$, since ΔV is an even function of time (ΔV depends on time only through z). Equation (8) allows information retrieval on the medium optical response since it provides the link between the demodulated SMI signal and the phase and amplitude spectral components of the scattering amplitude σ.

$$\Delta V_n \propto s_n \cos(\omega_0\frac{2L}{c} - \varphi_n). \qquad (9)$$

The simulated plots presented in Figs. 2(a)-2(b) and 3(c)-3(d) have been obtained by solving in steady state Eq. (7) in the case of moving mirror PZM, assuming a total

displacement ΔL of three interferometric fringes, where each fringe is $\dfrac{\lambda}{2} \approx 55.5\,\mu m$ corresponding to a phase shift $\dfrac{\omega_0 2\Delta L}{c} = 2\pi$ (Fig. 1). The oscillating laser voltage ΔV is then processed with a fast Fourier transform algorithm (equivalent to the lock-in filtering in the experiment) to recover the components ΔV_n corresponding to each mirror displacement. The amplitude and phase values s_n and φ_n, $n = 1...5$, are finally extracted by a fitting procedure based on Eq. (9).

A.7 TRANSFERABLE ORGANIC SEMICONDUCTOR NANOSHEETS FOR APPLICATION IN ELECTRONIC DEVICES

Simon J. Noever, Michael Eder, Fabio del Giudice, Jan Martin, Franz X. Werkmeister, Stefan Hallwig, Stefan Fischer, Oliver Seeck, Nils-Eike Weber, Clemens Liewald, Fritz Keilmann, Andrey Turchanin, and Bert Nickel

Abstract

A method has been developed to stabilize and transfer nanofilms of functional organic semiconductors. The method is based on crosslinking of their topmost layers by low energy electron irradiation. The films can then be detached from their original substrates and subsequently deposited onto new solid or holey substrates retaining their structural integrity. Grazing incidence X-ray diffraction, X-ray specular reflectivity, and UV–Vis spectroscopy measurements reveal that the electron irradiation of $\approx 50\,\mathrm{nm}$ thick pentacene films results in crosslinking of their only topmost $\approx 5\,\mathrm{nm}$ (3–4 monolayers), whereas the deeper pentacene layers preserve their pristine crystallinity. The electronic performance of the transferred pentacene nanosheets in bottom contact field-effect devices is studied and it is found that they are fully functional and demonstrate superior charge injection properties in comparison to the pentacene films directly grown on the contact structures by vapor deposition. The new approach paves the way to integration of the organic semiconductor nanofilms on substrates unfavorable for their direct growth as well as to their implementation in hybrid devices with unusual geometries, e.g., in devices incorporating free-standing sheets.

Contribution

I tested the feasibility of the transferred nanosheets for possible applications with IR s-SNOM. I prepared Figure 4 for the final submission during the review process.

Transferable Organic Semiconductor Nanosheets for Application in Electronic Devices

Simon J. Noever, Michael Eder, Fabio del Giudice, Jan Martin, Franz X. Werkmeister, Stefan Hallwig, Stefan Fischer, Oliver Seeck, Nils-Eike Weber, Clemens Liewald, Fritz Keilmann, Andrey Turchanin,* and Bert Nickel*

A method has been developed to stabilize and transfer nanofilms of functional organic semiconductors. The method is based on crosslinking of their topmost layers by low energy electron irradiation. The films can then be detached from their original substrates and subsequently deposited onto new solid or holey substrates retaining their structural integrity. Grazing incidence X-ray diffraction, X-ray specular reflectivity, and UV–Vis spectroscopy measurements reveal that the electron irradiation of ≈50 nm thick pentacene films results in crosslinking of their only topmost ≈5 nm (3–4 monolayers), whereas the deeper pentacene layers preserve their pristine crystallinity. The electronic performance of the transferred pentacene nanosheets in bottom contact field-effect devices is studied and it is found that they are fully functional and demonstrate superior charge injection properties in comparison to the pentacene films directly grown on the contact structures by vapor deposition. The new approach paves the way to integration of the organic semiconductor nanofilms on substrates unfavorable for their direct growth as well as to their implementation in hybrid devices with unusual geometries, e.g., in devices incorporating free-standing sheets.

The transfer and microfabrication techniques of graphene and other 2D materials have revolutionized the fabrication of novel layered materials and their implementation in electronic, optoelectronic, and nano-electromechanical devices.[1–5] By mechanical stacking of various atomically thin sheets (e.g., graphene, MoS$_2$, or BN), novel van der Waals (vdW) heterostructures are engineered, even if these material combinations cannot be grown directly by physical vapor deposition techniques.[6] In this way, vdW heterostructures with tailored electronic and optoelectronic properties can be generated by combining metallic, insulating and semiconducting sheets.[7] Nanofilms of organic semiconductors are promising candidates to extend this material toolbox for building hybrid devices, which would profit from the physical properties of both inorganic and organic materials.[8,9] To this end, they have to be prepared in the form of mechanically stable and transferable sheets. However, in contrast to graphene, where atoms are linked via strong covalent bonds, small aromatic molecules in pristine organic semiconductor films are bound via weak vdW forces. Therefore, it is not possible to peel off and deposit organic films to create electronic devices, in contrast to thicker organic crystals, which have been transferred successfully.[10] Here we demonstrate the preparation and implementation in field effect transistors (FETs) of transferable pentacene nanosheets, stabilized via electron irradiation-induced crosslinking of their surface layers. The irradiated films possess high mechanical stability and therefore they can be removed from the growth substrate and transferred onto

Dr. S. J. Noever, M. Eder, F. del Giudice, J. Martin, Dr. F. X. Werkmeister, S. Hallwig, S. Fischer, C. Liewald, Dr. F. Keilmann, Dr. B. Nickel
Faculty of Physics and CeNS
Ludwig-Maximilians-Universität München
80539 Munich, Germany
E-mail: nickel@physik.uni-muenchen.de

Dr. S. J. Noever, C. Liewald, Dr. B. Nickel
Nanosystems Initiative Munich (NIM)
80799 Munich, Germany

Dr. O. Seeck
Deutsches Elektronen Synchrotron DESY
22603 Hamburg, Germany

Dr. N.-E. Weber[+]
Faculty of Physics
University of Bielefeld
33615 Bielefeld, Germany

Prof. A. Turchanin
Institute of Physical Chemistry
Friedrich-Schiller-Universität Jena
07743 Jena, Germany
E-mail: andrey.turchanin@uni-jena.de

Prof. A. Turchanin
Jena Center for Soft Matter (JCSM)
07743 Jena, Germany

Prof. A. Turchanin
Center for Energy and Environmental Chemistry
(CEEC) 07743, Jena, Germany

Prof. A. Turchanin
Abbe Center of Photonics (ACP)
07745 Jena, Germany

[+]Present address: Scienta Omicron GmbH, 65232 Taunusstein, Germany

**ADVANCED
SCIENCE NEWS**

www.advancedsciencenews.com

**ADVANCED
MATERIALS**

www.advmat.de

new solid substrates or suspended across macroscopic cavities and grids as freestanding structures. We characterize in detail the effect of the electron irradiation on structural and optical properties of pentacene nanofilms employing grazing incidence X-ray diffraction (GIXD), X-ray reflectometry (XR), UV–Vis and IR spectroscopy, helium ion microscopy (HIM), and atomic force microscopy (AFM). The functional electronic properties of the formed nanosheets are studied via electric transport measurements of the FET devices. We found that already about 5 nm (≈3–4 molecular layers) of crosslinking depth is sufficient to stabilize 50 nm thick pentacene films, whereas the remaining film preserves its pristine structure as well as electronic and optical properties and can be used for functional applications. The transferred pentacene nanosheets show superior charge injection characteristics in the FET devices in comparison to the pentacene films prepared by physical vapor deposition.

Low energy electron irradiation of aromatic self-assembled monolayers results in their lateral crosslinking and conversion into 2D carbon sheets - carbon nanomembranes (CNMs) - with a thickness of only one molecule.[11] The crosslinking is driven by primary electron irradiation as well as low energy secondary and photoelectrons produced in the substrate resulting in the dissociation of C−H bonds and subsequent formation of the new covalently bonded carbon network in the complete

monolayer, which significantly changes its structural and electronic properties.[12] Similar to graphene, fully crosslinked CNMs can be removed from their substrates and transferred onto new holey or solid substrates or stacked into vdW heterostructures as free-standing sheets.[13,14] As the penetration depth of low energy electrons can be precisely tuned in the range of a few nanometers,[15] we employ this effect to crosslink only the topmost layers of a ≈50 nm thick film of pentacene preserving the pristine structure of the deeper layers and therewith the functional electronic properties of the film. Moreover, the smooth bottom interface of the organic film remains accessible for electronic contact resulting in the lower contact resistance of the fabricated devices. In the following, we present the structural and functional characterization of the surface stabilized free-standing pentacene nanosheets prepared in this way.

First, we describe the essential steps to crosslink and transfer pentacene nanosheets, **Figure 1**a. We use a thin sacrificial polyvinyl-alcohol (PVA) layer deposited on a flat and inert substrate such as an oxidized Si wafer or a fused silica glass by spin coating and deposit a 50 nm pentacene film on this substrate by vacuum vapor deposition.[16] The deposited film is then irradiated in the same vacuum chamber with a defocused electron beam having an electron energy of $E_{irr} = 500$ eV and an irradiation dose of $D_{irr} = 3.0$ mC cm^{-2}. To detach the pentacene
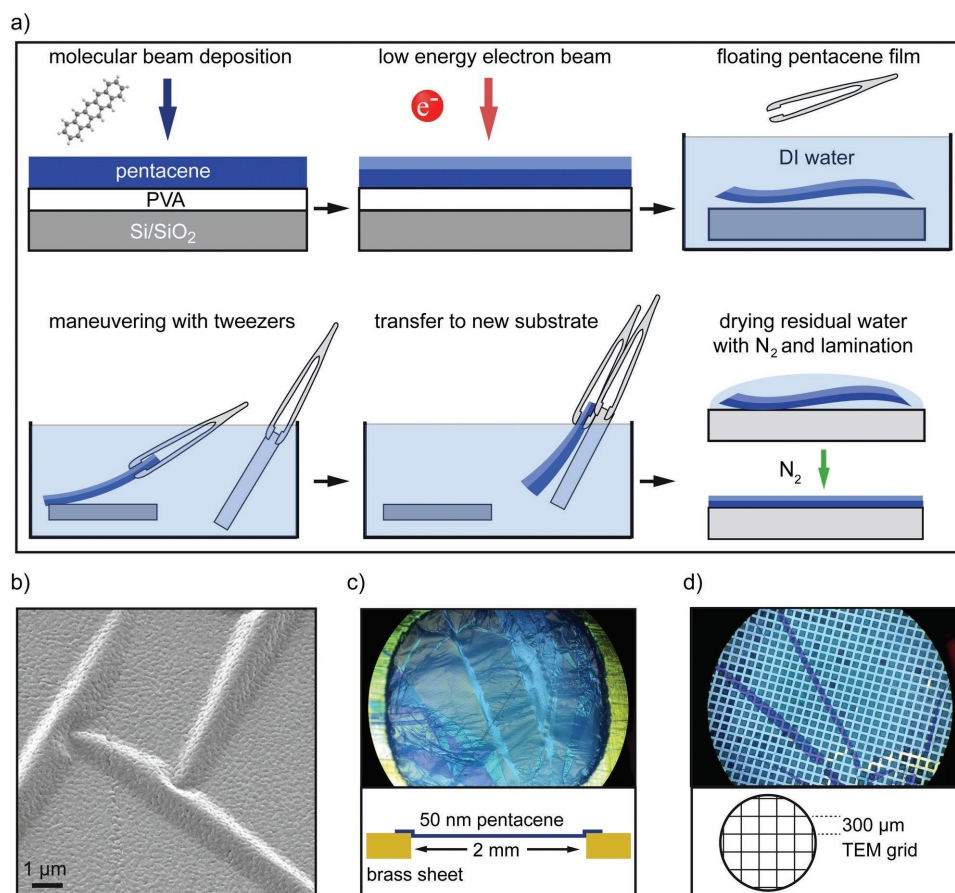
Figure 1. Transfer of thin pentacene films. a) Schematic representation of the transfer method. b) Helium ion microscopy (HIM) image of a crosslinked and transferred 20 nm pentacene film. c) Optical microscopy image of a 50 nm thin pentacene film spanned over a 2 mm hole in a 0.5 mm brass sheet. d) Optical microscopy image of a 50 nm thin pentacene film transferred onto a copper TEM grid (mesh width: 300 μm).

ADVANCED
SCIENCE NEWS
www.advancedsciencenews.com

ADVANCED
MATERIALS
www.advmat.de

film from the surface, the sample is removed from the vacuum chamber and immersed in deionized water. Since PVA is a water soluble polymer, the sacrificial PVA layer dissolves and the pentacene film remains free-floating in the solvent.[17,18] These freestanding films with areas up to a size of 1 cm^2 can then be picked up with tweezers, placed onto new substrates and removed from the water. The crosslinking step is essential for this procedure because pristine (non-irradiated) pentacene films disintegrate at the slightest touch by tweezers or during transfer through the water surface meniscus. After removing the wet nanosheet from water, it is possible to correct its position on the surface and flatten it out by gentle pulling. Upon drying in nitrogen flow, the nanosheets laminate firmly to the new surface, i.e., they adhere irreversibly by van der Waals forces. Note, the pentacene films are sufficiently mechanically stable so that no stabilizing polymeric film, as typically used for atomically thin sheets,[4,13] is necessary for their transfer. The HIM image in Figure 1b shows a pentacene nanosheet, which was transferred in this way on an oxidized silicon wafer. Folds and wrinkles are recognized indicating the sheet character of the pentacene. The characteristic terrace-like topography of pentacene is conserved after irradiation and transfer (cf. Figure S1, Supporting Information). In Figure 1c,d optical microscopy images of pentacene nanosheets spanning over holes with diameters of several millimeters are presented. The sheets are homogenous with some color variations originating from the wrinkle and folds due to transfer. In Figure 1c, a 50 nm pentacene nanosheet spans a 2 mm diameter hole in a brass sheet, whereas in Figure 1d the nanosheet spans a transmission electron microscope (TEM) grid with a mesh width of 300 µm. As we show in the following, this remarkable mechanical stability results from the lateral crosslinking of only the topmost 3–4 monolayers (ML) of the pentacene films.

To analyze the penetration depth of the crosslinking, we employ specular XR in combination with GIXD measurements.[19] As seen from the XR data presented in **Figure 2**, the pristine film shows the characteristic (0 0 L) reflections of the pentacene thin film phase (black curve).[20] After irradiation, the (0 0 L) peaks broaden and decrease in intensity (red curve). This observation indicates a reduction of the crystallinity due to the electron irradiation induced crosslinking. In comparison to XR, where the total thickness of the film contributes to the signal, in GIXD an evanescent X-ray wave selectively probes only the surface region (cf. Figure 2b). Experimentally, the probing depth is adjusted using the X-ray beam at subcritical incidence angle for total reflection, typically at less than a fraction of a degree from the surface. The smaller the angle, the more surface sensitive is the measurement. GIXD measurements for a pristine pentacene film and films irradiated at two different electron beam energies (E_{irr} = 300 and 800 eV, D_{irr} = 3.0 mC cm^{-2}, see Table 1, Supporting Information for details) are shown in Figure 2c. While there is still some GIXD intensity of the first truncation rod (1 1 L) after 300 eV irradiation, the signal vanishes almost completely after 800 eV irradiation. To quantify the number of disordered crosslinked layers, i.e., the number of layers on top of the film which do not contribute to the diffraction signal, we measure the GIXD signal under different incidence angles and model the diffracted intensities within the model of
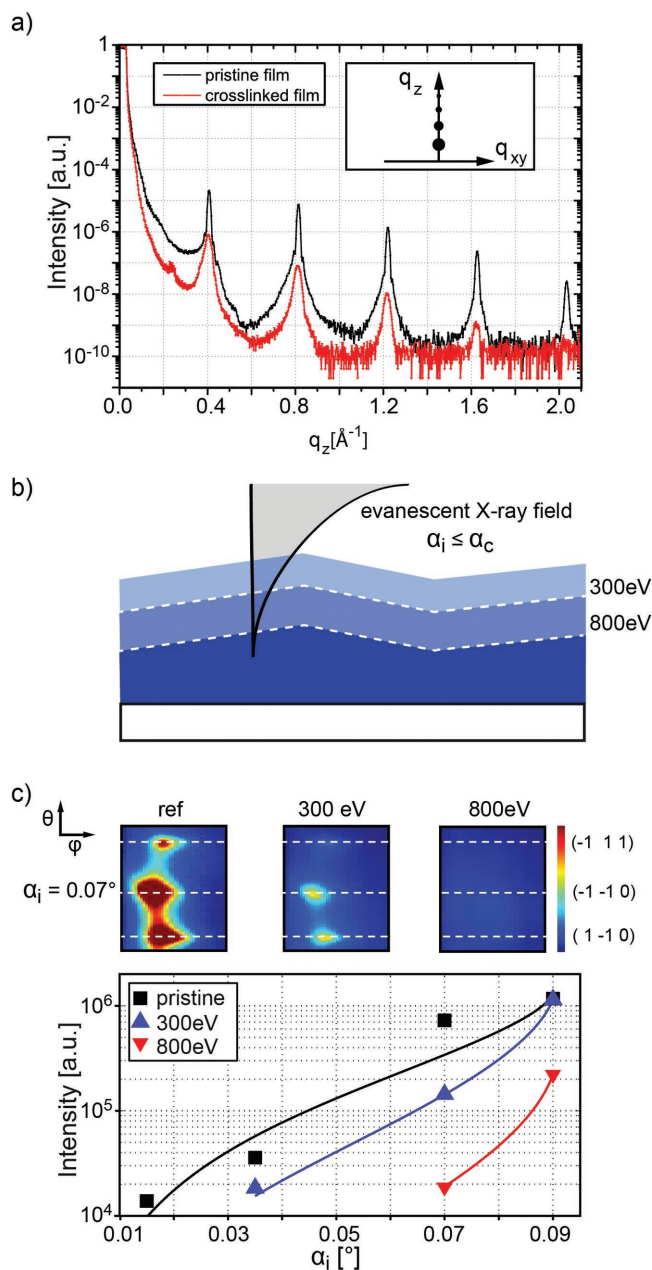
Figure 2. X-ray analysis of the influence of crosslinking on the crystal structure of pentacene thin films. a) Comparison of synchrotron specular X-ray reflectometry measurements of a pristine pentacene thin film (black) on SiO$_2$ and a strongly crosslinked film (red, 50 min at electron energy >700 eV, D = 7.5 mC cm^{-2}). The decreasing Bragg signal indicates that the crosslinked film contains less crystalline material. b) Schematic of the evanescent X-ray field penetrating the pentacene surface for different electron irradiation depths. c) GIXD measurements of the first pentacene truncation rod at different angles of incidence and different e-beam energies (here, θ is the out-of-plane angle and ϕ the in-plane angle). Top: exemplary GIXD data for pristine, 300 eV irradiated, and 800 eV irradiated pentacene at α_i = 0.07°. Bottom: the highest intensities of the (−1−10) peaks (middle peaks from raw data), plotted against the angles of incidence. The continuous lines represent the fit calculated from the DCGID model for truncation rods, including noncrystalline top layers.

**ADVANCED
SCIENCE NEWS**

www.advancedsciencenews.com

**ADVANCED
MATERIALS**

www.advmat.de
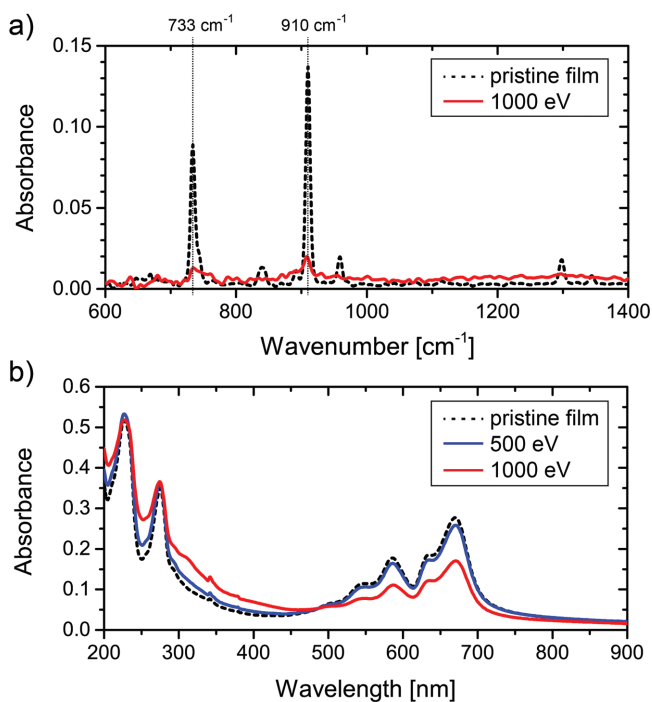
Figure 3. Spectroscopic characterization of the crosslinking process. a) FTIR spectra of a 23 nm pentacene film on Au before and after irradiation with 1 keV electrons (dose 10.3 mC cm^{-2}), shown as dashed black and red curve, respectively. b) UV–Vis measurements of a 50 nm pentacene film on fused silica, before and after irradiation with 500 eV and 1 keV electrons (dose of 3 and 10.3 mC cm^{-2}, respectively), shown as dashed black, blue and red curves, respectively.

depth controlled grazing incidence diffraction (DCGID) (Figure 2c).[21–24] Details on the fit routine are reported in Figure S2 (Supporting Information). We find that the observed intensities are in agreement with three disordered ML of pentacene (or 4.5 nm crosslinking depth) for 300 eV irradiation and five disordered monolayers pentacene (or 7.5 nm crosslinking depth) for the 800 eV sample. These data unambiguously show that only the topmost layers of the pentacene film lose their crystallinity due to the crosslinking, whereas the pristine crystallinity is preserved in the deeper layers of the film.

To get an insight into the crosslinking mechanisms, we applied Fourier transform infrared (FTIR) spectroscopy. As seen from the FTIR spectra (cf. **Figure 3**a), after irradiation the characteristic C—H vibrations of pentacene at 910 and 733 cm^{-1} are strongly diminished.[25,26] Such a behavior is indicative for the hydrogen abstraction via the cleavage of the C—H bonds and formation of new carbon bonds between the unsaturated adjacent aromatic moieties.[12] Next, we used UV–Vis spectroscopy to characterize the changes in the optical spectra. As seen from Figure 3b, the UV–Vis spectrum of a pristine pentacene film shows the characteristic absorption features in the spectral range of 500–700 nm.[25] After electron irradiation with two different electron energies (500 eV and 1 keV), the intensity of these characteristic absorbance features is decreased. This effect is stronger for the irradiation with higher energy electrons, which is in agreement with their higher penetration depth and therefore the formation of a thicker crosslinked layer. Using the

Lambert–Beer law and the corresponding inelastic mean free paths of 500 eV and 1 keV electrons, we estimate the thickness of the formed crosslinked layer to about 3 and 17 nm, respectively. The formation of the crosslinked layer is also in agreement with an increase of the intensity in the spectral range at smaller wave lengths (cf. Figure 3b), which is characteristic for the formation of amorphous carbon species.[27] To summarize the structural and optical study, we conclude that irradiation of pentacene films with electrons in the range of 300–500 eV results in the crosslinking of their topmost 3–4 MLs. These topmost layers have disordered, most probably amorphous, structure, whereas the deeper pentacene layers preserve their pristine crystallinity. Importantly, the formed crosslinked layer provides a sufficient mechanical stability to about 50 nm thick pentacene films in order to transfer them onto new solid and holey substrates as free-standing nanosheets.

In the following, we demonstrate that the formed pentacene nanosheets possess functional semiconducting properties and can be employed in effective field effect devices. To this end, we fabricated bottom-contact, bottom-gate pentacene FETs by vapor deposition of pentacene in vacuum onto the contact structures and studied electric transport properties of these devices before and after the irradiation, **Figure 4**a. After an irradiation with low energy electrons (E_{irr} = 350 eV, D_{irr} = 1.5 mC cm^{-2}) no significant alteration in the device performance in comparison to the nonirradiated devices is observed (Figure 4a). This demonstrates that the crosslinked layer does not penetrate into the conduction channel, which is typically confined at the semiconductor-dielectric interface (Figure 4b).[28] Only after extensive irradiation at higher electron energies and doses (E_{irr} = 700 eV, D_{irr} = 4.5 mC cm^{-2}) the device performance significantly decreases. In the next step, we transferred the pentacene nanosheets onto prefabricated transistor contact pads of varying bottom-contacts with channel widths of W_{ch} = 10 mm and channel lengths of L_{ch} = 5, 10, and 20 µm (see the details in the Experimental Section in the Supporting Information) and compared the device performance with transistor structures prepared via conventional physical vapor deposition. The AFM images of the contact regions in Figure 4b show the morphology on both types of devices. The typical obstructed pentacene growth (i.e., small grained, pillar-like 3D morphology) is observed by direct vapor deposition on gold contacts.[29] In contrast, the structure of the pentacene films grown on PVA and transferred after the crosslinking onto gold contacts is significantly more homogeneous and shows the characteristic Bragg peaks of the pentacene thin film phase (Figure S3, Supporting Information). The obstructed growth of pentacene on gold has a negative influence on the charge injection properties of pentacene devices and can only be reduced by a proper, often aggressive modification of the gold contacts.[29–33] The elongated pentacene structures formed on PVA most likely represent the lying phase pentacene.[34] First, we determine the total resistance R of the devices from the linear region of the output characteristics (Figure S4, Supporting Information) according to $R = V_D/I_D$. The total resistances for devices with different channel lengths are summarized in Figure 4c. The contact resistance is determined from extrapolation to zero channel length.[35,36] For a gate voltage of V_G = −15 V, the devices made of the transferred pentacene sheets have a

**ADVANCED
SCIENCE NEWS** _____
www.advancedsciencenews.com

**ADVANCED
MATERIALS**
www.advmat.de
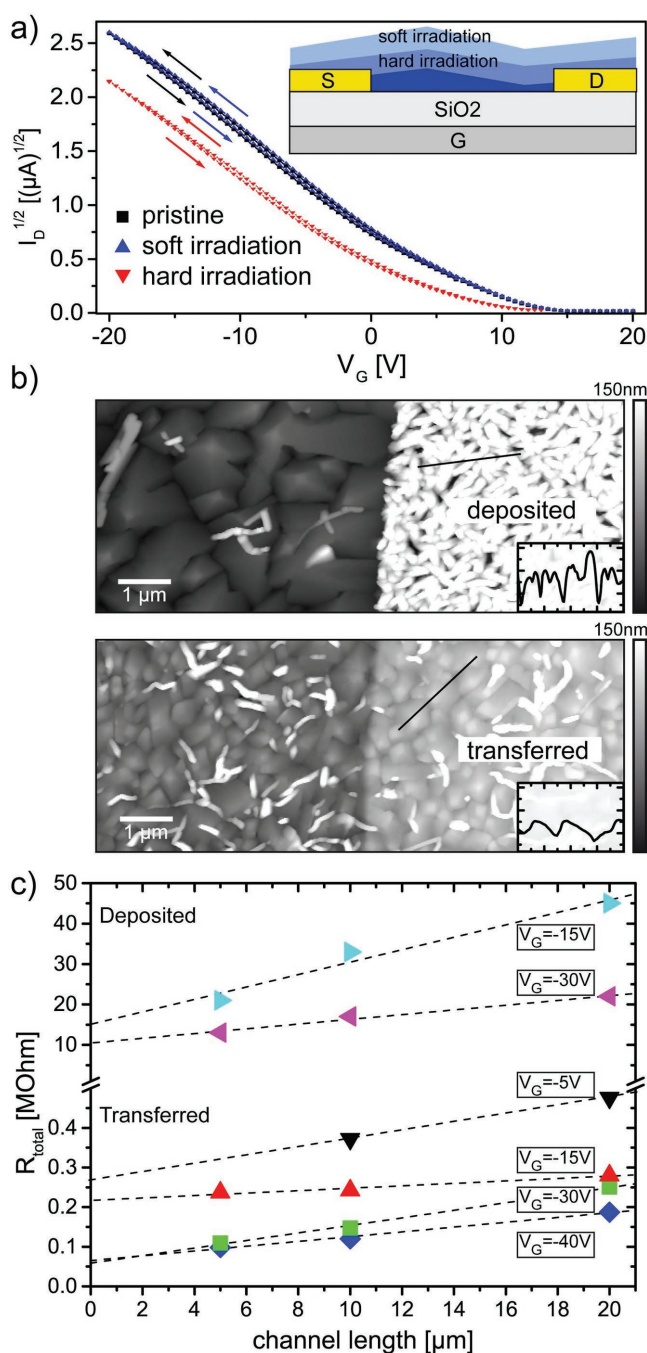
Figure 4. Characterization of the electronic properties in the field effect devices. Characteristic curves of a transistor irradiated at different electron energies and contact resistance analysis of deposited and transferred pentacene on bottom contact transistor geometry. a) Transfer curves of an organic field effect transistor (OFET) with pristine, partially crosslinked, and strongly crosslinked active layer ($V_D = -10$ V). The arrows indicate the sweep direction (inset: schematic of the transistor). When irradiated softly (low electron energy), only the top layers of the pentacene film are crosslinked, i.e., the conduction channel at the dielectric interface is not affected. After hard irradiation (high electron energy), the crosslinked region penetrates the conduction channel and the device performance is reduced. b) AFM height micrographs of the substrate—contact edge in a transistor channel. Pentacene was vapor deposited (top image), and nanosheet transferred (bottom image). The topography

contact resistance of $R_p = 0.22$ MΩ. This is almost two orders of magnitude less than the contact resistance of the transistors produced by the conventional pentacene vapor deposition on the test pads, which was $R_p = 15$ MΩ. This improvement is even more significant for larger gate voltages. Thus for $V_G = -30$ V the contact resistance of the devices made out for the transferred sheets is 0.057 versus 10 MΩ for devices prepared by vapor deposition. All vapor deposited films show nonideal saturation behavior, i.e., a drain current reduction I_D at larger drain voltages. On the other hand, the saturation behavior of the transferred films with 10 and 20 μm channel length is rather good; only the shortest channel (5 μm) shows some nonideal behavior. These findings demonstrate that the crosslinking and transfer technique of pentacene nanosheets enables the fabrication of thin film devices with superior contact characteristics (cf. Figure S4, Supporting Information) and improved saturation behavior for the 10 and 20 μm channel length. The mobilities, typically $\mu \approx 0.1$ cm^2 V^{-1} s^{-1} in our devices, stay largely unaffected, whether by electron irradiation (cf. Figure 4a) or by film transfer.

In summary, we have introduced a novel methodology to fabricate transferrable nanosheets of organic semiconductors with few tens of nanometers thickness via irradiation of their thin films with low energy electrons. The electron irradiation results in crosslinking of the topmost molecular layers, stabilizing the whole film and enabling its transfer as a nanosheet onto new substrates. Because of the low penetration depth of the crosslinking, the studied pentacene nanosheets preserve their functional semiconducting and optical properties. Moreover, employed in bottom contact FETs, they show a reduced contact resistance in comparison to devices fabricated via direct vapor deposition on the gold electrodes. The proposed methodology opens up new possibilities toward the fabrication of organic semiconductor devices with transferable organic semiconductor nanosheets from a variety of aromatic molecules. It paves the way toward free-standing organic field effect devices, an area which was reserved for single crystals so far, as well as to their integration with other 2D materials in hybrid devices.

Experimental Section

The defocused electron beam was produced using a Perkin Elmer low energy electron diffraction (LEED) gun (PHI Model 11-020 LEED Electronics System). Most experiments have been performed using an electron gun emission current of 5 mA. The doses (mC cm^{-2}) were estimated via the measured beam current I_B flowing through a

for the transferred film is unchanged on the gold electrode, while the vapor deposited film shows strong dewetting on the contact. The height scale of both AFM images is 150 nm. The insets show two height profiles above the contacts. The line cut is 2 μm, the y-axis covers 150 nm. c) Total channel resistance using vapor deposited pentacene (top) and nanosheet transferred pentacene (bottom), plotted against transistor channel lengths and evaluated for different applied gate voltages. The intersections of the linear fits with the ordinate indicate the extrapolated contact resistances. The error bars for each data point is less than 10% of their absolute values.

ground electrode: $D = \frac{I_B t}{A}$. For the used setup and an emission current of $I_{em} = 5$ mA, the current through an irradiated reference surface $A = 4$ mm² at the sample position was $\approx I_B = 100$ nA. Some experiments have also been performed with a reduced emission current of 2 mA after filament exchange and refocusing.

Further details for sample preparation and characterization are reported in the Supporting Information.

Supporting Information

Supporting Information is available from the Wiley Online Library or from the author.

Acknowledgements

Conflict of Interest

The authors declare no conflict of interest.

Keywords

[1] A. K. Geim, I. V. Grigorieva, *Nature* **2013**, *499*, 419.
[2] S. Z. Butler, S. M. Hollen, L. Y. Cao, Y. Cui, J. A. Gupta, H. R. Gutierrez, T. F. Heinz, S. S. Hong, J. X. Huang, A. F. Ismach, E. Johnston-Halperin, M. Kuno, V. V. Plashnitsa, R. D. Robinson, R. S. Ruoff, S. Salahuddin, J. Shan, L. Shi, M. G. Spencer, M. Terrones, W. Windl, J. E. Goldberger, *ACS Nano* **2013**, *7*, 2898.
[3] J. W. Suk, A. Kitt, C. W. Magnuson, Y. F. Hao, S. Ahmed, J. H. An, A. K. Swan, B. B. Goldberg, R. S. Ruoff, *ACS Nano* **2011**, *5*, 6916.
[4] A. C. Ferrari, F. Bonaccorso, V. Fal'ko, K. S. Novoselov, S. Roche, P. Boggild, S. Borini, F. H. L. Koppens, V. Palermo, N. Pugno, J. A. Garrido, R. Sordan, A. Bianco, L. Ballerini, M. Prato, E. Lidorikis, J. Kivioja, C. Marinelli, T. Ryhanen, A. Morpurgo, J. N. Coleman, V. Nicolosi, L. Colombo, A. Fert, M. Garcia-Hernandez, A. Bachtold, G. F. Schneider, F. Guinea, C. Dekker, M. Barbone, Z. Sun, C. Galiotis, A. N. Grigorenko, G. Konstantatos,

A. Kis, M. Katsnelson, L. Vandersypen, A. Loiseau, V. Morandi, D. Neumaier, E. Treossi, V. Pellegrini, M. Polini, A. Tredicucci, G. M. Williams, B. Hee Hong, J.-H. Ahn, J. Min Kim, H. Zirath, B. J. van Wees, H. van der Zant, L. Occhipinti, A. Di Matteo, I. A. Kinloch, T. Seyller, E. Quesnel, X. Feng, K. Teo, N. Rupesinghe, P. Hakonen, S. R. T. Neil, Q. Tannock, T. Lofwander, J. Kinaret, *Nanoscale* **2015**, *7*, 4598.
[5] F. Withers, O. Del Pozo-Zamudio, A. Mishchenko, A. P. Rooney, A. Gholinia, K. Watanabe, T. Taniguchi, S. J. Haigh, A. K. Geim, A. I. Tartakovskii, K. S. Novoselov, *Nat. Mater.* **2015**, *14*, 301.
[6] B. V. Lotsch, *Annu. Rev. Mater. Res.* **2015**, *45*, 85.
[7] I. S. Osborne, *Science* **2016**, *353*, 458.
[8] D. Jariwala, S. L. Howell, K.-S. Chen, J. Kang, V. K. Sangwan, S. A. Filippone, R. Turrisi, T. J. Marks, L. J. Lauhon, M. C. Hersam, *Nano Lett.* **2016**, *16*, 497.
[9] H. Klauk, *Organic Electronics: Materials, Manufacturing, and Applications*, Wiley-VCH, Weinheim, Germany **2006**.
[10] E. Menard, V. Podzorov, S. H. Hur, A. Gaur, M. E. Gershenson, J. A. Rogers, *Adv. Mater.* **2004**, *16*, 2097.
[11] A. Turchanin, A. Gölzhäuser, *Adv. Mater.* **2016**, *28*, 6075.
[12] A. Turchanin, D. Käfer, M. El-Desawy, C. Wöll, G. Witte, A. Gölzhäuser, *Langmuir* **2009**, *25*, 7342.
[13] A. Turchanin, A. Beyer, C. T. Nottbohm, X. H. Zhang, R. Stosch, A. Sologubenko, J. Mayer, P. Hinze, T. Weimann, A. Gölzhäuser, *Adv. Mater.* **2009**, *21*, 1233.
[14] C. T. Nottbohm, A. Turchanin, A. Beyer, R. Stosch, A. Gölzhäuser, *Small* **2011**, *7*, 874.
[15] S. Tanuma, C. J. Powell, D. R. Penn, *Surf. Interface Anal.* **1994**, *21*, 165.
[16] C.-C. Kuo, T. N. Jackson, *Appl. Phys. Lett.* **2009**, *94*, 3304.
[17] T. B. Singh, T. Meghdadi, S. Gunes, N. Marjanovic, G. Horowitz, P. Lang, S. Bauer, N. S. Sariciftci, *Adv. Mater.* **2005**, *17*, 2315.
[18] G. A. Salvatore, N. Munzenrieder, T. Kinkeldei, L. Petti, C. Zysset, I. Strebel, L. Buthe, G. Troster, *Nat. Commun.* **2014**, *5*, 2982.
[19] S. Schiefer, M. Huth, A. Dobrinevski, B. Nickel, *J. Am. Chem. Soc.* **2007**, *129*, 10316.
[20] B. Nickel, R. Barabash, R. Ruiz, N. Koch, A. Kahn, L. C. Feldman, R. F. Haglund, G. Scoles, *Phys. Rev. B* **2004**, *70*, 125401.
[21] H. Dosch, B. W. Batterman, D. C. Wack, *Phys. Rev. Lett.* **1986**, *56*, 1144.
[22] H. Dosch, *Phys. Rev. B* **1987**, *35*, 2137.
[23] G. H. Vineyard, *Phys. Rev. B* **1982**, *26*, 4146.
[24] I. K. Robinson, D. J. Tweet, *Rep. Prog. Phys.* **1992**, *55*, 599.
[25] C. Westermeier, A. Cernescu, S. Amarie, C. Liewald, F. Keilmann, B. Nickel, *Nat. Commun.* **2014**, *5*, 4101.
[26] D. M. Hudgins, S. A. Sandford, *J. Phys. Chem. A* **1998**, *102*, 344.
[27] N. D. Baydo an, *J. Mater. Sci. Eng. B* **2004**, *107*, 70.
[28] C. Rost, D. J. Gundlach, S. Karg, W. Riess, *J. Appl. Phys.* **2004**, *95*, 5782.
[29] D. Käfer, L. Ruppel, G. Witte, *Phys. Rev. B* **2007**, *75*, 085309.
[30] K. Hong, S. Y. Yang, C. Yang, S. H. Kim, D. Choi, C. E. Park, *Org. Electron.* **2008**, *9*, 864.
[31] Y. Tsuruma, A. Al-Mahboob, S. Ikeda, J. T. Sadowski, G. Yoshikawa, Y. Fujikawa, T. Sakurai, K. Saiki, *Adv. Mater.* **2009**, *21*, 4996.
[32] W. S. Hu, Y. T. Tao, Y. J. Hsu, D. H. Wei, Y. S. Wu, *Langmuir* **2005**, *21*, 2260.
[33] H. Kim, Z. Meihui, N. Battaglini, P. Lang, G. Horowitz, *Org. Electron.* **2013**, *14*, 2108.
[34] H. Yanagisawa, T. Tamaki, M. Nakamura, K. Kudo, *Thin Solid Films* **2004**, *464*, 398.
[35] D. J. Gundlach, L. Zhou, J. A. Nichols, T. N. Jackson, P. V. Necliudov, M. S. Shur, *J. Appl. Phys.* **2006**, *100*, 024509.
[36] G. Horowitz, P. Lang, M. Mottaghi, H. Aubin, *Adv. Funct. Mater.* **2004**, *14*, 1069.

A.8 SUB-MICRON PHASE COEXISTENCE IN SMALL-MOLECULE OR-GANIC THIN FILMS REVEALED BY INFRARED NANO-IMAGING

Christian Westermeier, Adrian Cernescu, Sergiu Amarie, Clemens Liewald, Fritz Keilmann, and Bert Nickel

Abstract

Controlling the domain size and degree of crystallization in organic films is highly important for electronic applications such as organic photovoltaics, but suitable nanoscale mapping is very difficult. Here we apply infrared-spectroscopic nano-imaging to directly determine the local crystallinity of organic thin films with 20-nm resolution. We find that state-of-the-art pentacene films (grown on SiO_2 at elevated temperature) are structurally not homogeneous but exhibit two interpenetrating phases at sub-micrometre scale, documented by a shifted vibrational resonance. We observe bulk-phase nucleation of distinct ellipsoidal shape within the dominant pentacene thin-film phase and also further growth during storage. A faint topographical contrast as well as X-ray analysis corroborates our interpretation. As bulk-phase nucleation obstructs carrier percolation paths within the thin-film phase, hitherto uncontrolled structural inhomogeneity might have caused conflicting reports about pentacene carrier mobility. Infrared-spectroscopic nano-imaging of nanoscale polymorphism should have many applications ranging from organic nanocomposites to geologic minerals.

Contribution

I measured the transistor characteristics and mapped the phase coexistence within the channel of a pentacene TFT, shown in Supplementary Figure 2.

Sub-micron phase coexistence in small-molecule organic thin films revealed by infrared nano-imaging

Christian Westermeier[1,2], Adrian Cernescu[1,3], Sergiu Amarie[3], Clemens Liewald[1], Fritz Keilmann[1] & Bert Nickel[1,2]

Controlling the domain size and degree of crystallization in organic films is highly important for electronic applications such as organic photovoltaics, but suitable nanoscale mapping is very difficult. Here we apply infrared-spectroscopic nano-imaging to directly determine the local crystallinity of organic thin films with 20-nm resolution. We find that state-of-the-art pentacene films (grown on SiO_2 at elevated temperature) are structurally not homogeneous but exhibit two interpenetrating phases at sub-micrometre scale, documented by a shifted vibrational resonance. We observe bulk-phase nucleation of distinct ellipsoidal shape within the dominant pentacene thin-film phase and also further growth during storage. A faint topographical contrast as well as X-ray analysis corroborates our interpretation. As bulk-phase nucleation obstructs carrier percolation paths within the thin-film phase, hitherto uncontrolled structural inhomogeneity might have caused conflicting reports about pentacene carrier mobility. Infrared-spectroscopic nano-imaging of nanoscale polymorphism should have many applications ranging from organic nanocomposites to geologic minerals.

[1] Fakultät für Physik and Center for NanoScience (CeNS), Ludwig-Maximilians-Universität München, Geschwister-Scholl-Platz 1, 80539 München, Germany. [2] Nanosystems Initiative Munich, Schellingstrasse 4, 80799 München, Germany. [3] Neaspec GmbH, Bunsenstrasse 5, 82152 Martinsried, Germany. Correspondence and requests for materials should be addressed to B.N. (email: nickel@lmu.de).

Highly ordered organic materials hold high promise for novel electronics[1–4]. Reproducible device performance rests on understanding the effect of molecular arrangement on charge-carrier mobility. Pentacene is one of the most characterized and best-performing materials for organic thin-film devices[2,5,6]. To maximize its mobility, the most crucial parameters for pentacene quality have been identified to be the substrate and its temperature during deposition[1,5–7]. On the one hand, substrate temperatures well above 50 °C result in larger grains of the film structure with characteristic lengths of microns[8]. On the other hand, deposition temperature also controls the abundance of several crystallographic phases, such as thin-film phase (TFP) and bulk phase (BP) pentacene[5,6,9].

Here we reveal the surprising lateral nanostructure of two coexisting pentacene polymorphs on a 300-nm scale, by mapping infrared absorption using a near-field infrared microscope[10]. We observe ellipse-shaped BP pentacene ubiquitously within the dominant TFP, uncorrelated with grain structure. Our finding may explain why the carrier mobility ceases to increase in pentacene thin films deposited at elevated substrate temperature despite increased grain size[5,11,12]; apparently, BP nucleation obstructs charge transport by scattering off polarons from inter-phase boundaries[1,13]. Furthermore, we observe that the BP pentacene grows over months at room temperature without a change of grain morphology, as we also corroborate by X-ray diffraction. The BP ellipses come with a subtle topographical depression, which earlier had led to interpretation of them as cracks[14,15]. Infrared nanoscopy clearly has a high potential for analyzing the molecular arrangement of organic thin films at the nanoscale and thus for better understanding organic electronic systems.

Results

X-ray diffraction shows recrystallization during storage. The crystallographic phases in pentacene films can be discriminated by their (001)-spacing of the molecular layers. For the TFP, the pentacene molecules are oriented almost perpendicularly on the substrate and the (001)-spacing amounts to 15.4 Å, while for the BP it is 14.4 Å[9,16,17] as the molecules are slightly tilted, shown in the inset of Fig. 1. The sample studied in Fig. 1 was grown at 65 °C to obtain large crystalline grains. After deposition, X-ray diffraction measurements showed that the film was dominated by TFP, with some weak fraction of BP (Fig. 1, yellow curve) as expected for deposition temperatures above 50 °C[5,18]. However, surprisingly, the BP fraction was found considerably increased at the expense of TFP (red curve) after the sample had been stored over 20 months in a desiccator at room temperature (23 °C). This observation by itself is an alarming signal for pentacene-based device development and calls for immediate attention.

Infrared nano-imaging reveals elliptic BP inclusions. As the X-ray experiment geometry does not provide lateral information, additional methods are needed to determine the domain geometries and to understand how the phase conversion takes place in detail. An atomic force microscopy (AFM) image of the stored sample is shown in Fig. 2a. The film exhibits a grainy structure on the expected characteristic lateral length scale of 2–5 μm[6]. On the one hand, there is the argument that larger grains are beneficial for high charge-carrier mobility, simply as any kind of grain boundary will naturally impose a barrier due to defects, lowering the mobility[6,7,13]. On the other hand, film deposition at increased substrate temperatures to obtain large grains led to diverging results of increased[1], almost unchanged[11], and even reduced[5] carrier mobility. In

addition, even for pentacene films deposited at constant substrate temperature, the mobility tends to saturate with increasing grain size[12,19]. In a similar direction, Shtein et al.[20] have reported that in some cases smaller grains allow for higher mobility, while others observed that post-annealing reduces mobility due to structure variation and nucleation of BP pentacene[21,22]. Unfortunately in the experimental studies, it remains unclear whether apparent individual grains as observed by AFM are single crystals, and in particular, whether and on what scale BP and TFP domains are arranged. Thus, resolving the lateral crystallinity and the organization of BP and TFP pentacene might resolve the conflicting reports on the interplay between growth temperature, apparent grain size and charge transport in pentacene films.

To map and contrast BP and TFP domains in pentacene thin-film devices, we employ scattering-type scanning near-field optical microscopy (s-SNOM) with mid-infrared illumination, as it is known from far-field measurements that the different packing of TFP and BP pentacene results in a small shift of infrared vibrational frequencies[23–25]. s-SNOM enhances AFM probing by an additional channel of local infrared spectroscopy and should allow imaging the local distribution of both phases with a lateral resolution given by the probing tip diameter of typically 20 nm (see Methods)[10]. The near-field infrared image of the stored pentacene film shown in Fig. 2b was recorded using mid-infrared illumination at 907.1 cm^{-1}, which is close to the resonance of BP pentacene[23]. Strikingly, the infrared map is not homogeneous at all but exhibits ubiquitous nanoscale features, at strong contrast, in the form of bright and highly elongated ellipsoids, which, according to the choice of the infrared frequency, originate from BP domains. These domains appear uncorrelated to the topographic morphology recorded simultaneously (Fig. 2a), as they even persist across grain boundaries. Many BP ellipsoids are oriented approximately perpendicularly with respect to their neighbours and appear to
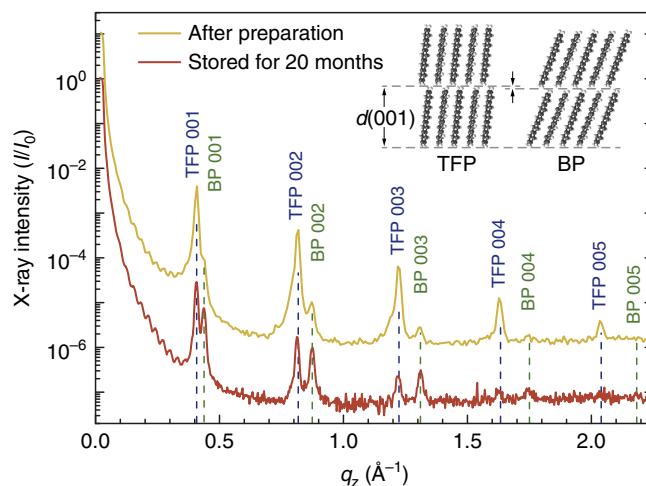
Figure 1 | Recrystallization in highly ordered pentacene film. X-ray diffraction of a 40-nm thick pentacene layer acquired right after fabrication (yellow curve), and after storage at room temperature for 20 months (red curve, vertically offset). The blue and green dashed lines indicate the positions of the (00L) Bragg peaks due to TFP and BP pentacene, respectively, corresponding to their well-known (001)-spacings of 15.4 and 14.4 Å (refs 5,9). Aging decreases TFP peaks and increases BP peaks. This observation clearly indicates a recrystallization from TFP to BP within the pentacene film. The two different molecular arrangements for TFP and BP, as well as their layer spacing d(001) perpendicular to the substrate are depicted in the inset.
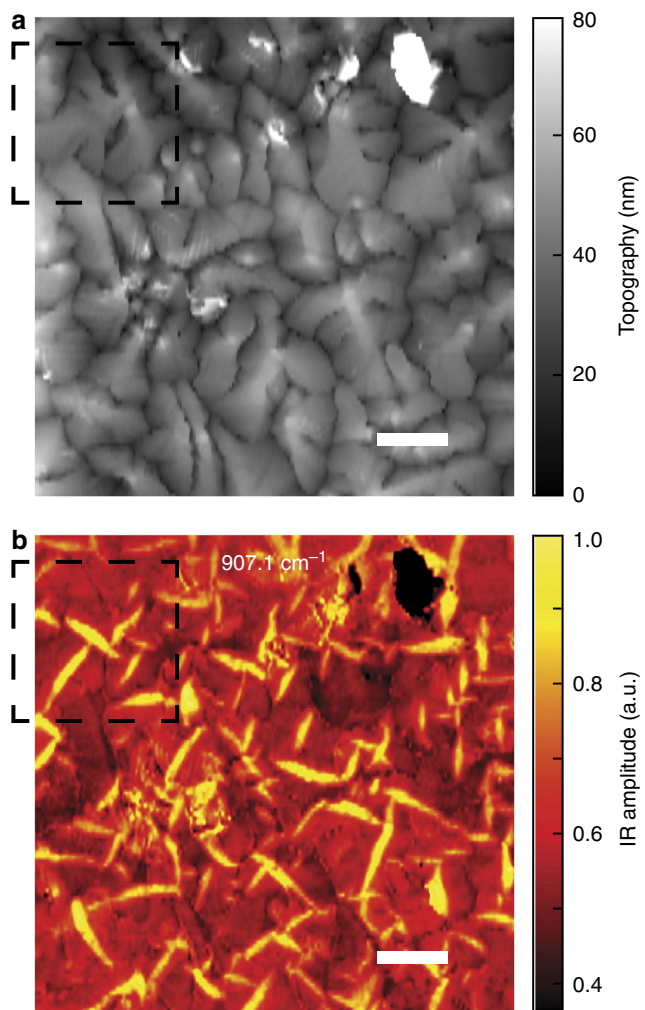
Figure 2 | Grain morphology and lateral distribution of two coexisting phases. (**a**) AFM topography (13.5 μm × 13.5 μm) showing a 40-nm thick pentacene film on SiO_2/Si substrate, after storage at room temperature for 20 months. (**b**) s-SNOM amplitude image at 907.1 cm^{-1}, recorded simultaneously, proves the coexistence of two phases of pentacene, which obviously persist across grain boundaries. The dashed square marks the section shown in Fig. 4. Scale bar, 2 μm.

stay mutually aligned within larger domains comprising several grains.

Crystalline packing of molecules shifts local infrared resonance. To investigate the spectral origin of this strong infrared contrast, we employ a fully spectroscopic mode of the s-SNOM, recently termed nano-FTIR (nanoscale Fourier transform infrared spectroscopy)[26,27] that registers broad near-field spectra at each sample position, here one on a BP ellipsoid and one on TFP next to it (Fig. 3, as marked in the left inset). A Lorentzian fit to each spectrum confirms the two distinctly different vibrational resonances on the BP ellipsoid, peaked at 906 cm^{-1} (green curve), and on the surrounding TFP, peaked at 904 cm^{-1} (blue curve). These frequencies agree well with literature values of TFP and BP pentacene[23,24]. A vertical, dashed line in the spectra of Fig. 3 indicates the specific frequency used for monochromatic imaging in Fig. 2b (907.1 cm^{-1}, CO_2 laser line P08). At this frequency, the nano-FTIR absorption on the BP ellipsoid (green curve, Fig. 3) is more
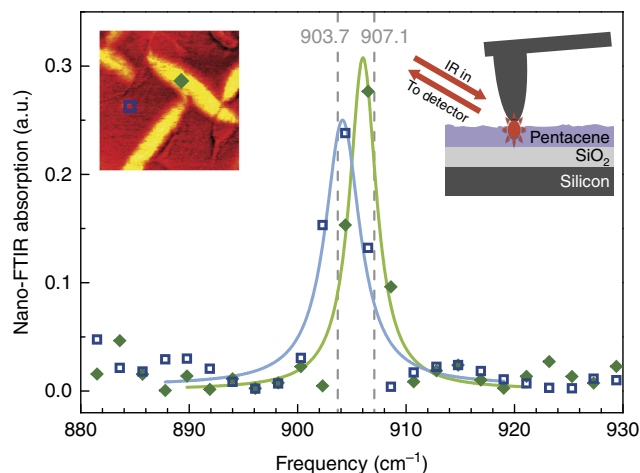
Figure 3 | Structural phases can be distinguished by an infrared resonance shift. Nano-FTIR spectra (data points) of a 40-nm thick pentacene film on SiO_2/Si substrate taken at two different positions that are marked in the left inset, taken from Fig. 4b (on ellipsoid—green and off ellipsoid—blue). For each spectrum, 20 interferograms with 5 min acquisition time each were averaged. We chose to record 4.8-mm long interferograms to attain 2.1 cm^{-1} spectral resolution (interferometer configuration as in ref. 26, Fig. 1). As seen from the Lorentzian fits (curves) to the data, the spectrum taken on the BP ellipsoid (green curve) clearly shows a higher resonance frequency (906 cm^{-1}) than that of surrounding TFP (904 cm^{-1}, blue curve). The CO_2 laser lines (P08, P12) used for monochromatic imaging (Figs 2 and 4) are indicated by vertical dashed lines. The right inset sketches the principle of back-scattering SNOM.

than twice as high compared with the surrounding TFP material (blue curve), explaining the bright contrast observed in Fig. 2b.

For a final verification of the optical response of the BP features observed in Fig. 2b, we applied the monochromatic imaging mode of the s-SNOM to a smaller sample area, with both the previous (Fig. 4a–c) and a slightly shifted illumination frequency (Fig. 4e,f). As expected, changing from 907.1 cm^{-1} to 903.7 cm^{-1}, near the TFP resonance[23,24], results in a reversion of the infrared amplitude contrast (*cf.* Fig. 4e). This invertible contrast proves that (i) infrared s-SNOM can selectively highlight either BP or TFP pentacene simply by choice of the infrared frequency, and that (ii) BP and TFP domains coexist on a *ca.* 300-nm length scale and seem to be not at all correlated to the well-known grain structure. This experimental finding is very surprising, as it allows us to conjecture that BP pentacene nucleates in the form of nanometre inclusions within, rather than on top of, TFP pentacene. BP seeds seem hidden in the morphology of the TFP and grow with storage time, as indicated by our X-ray analysis above (Fig. 1). In addition, s-SNOM imaging of a thick pentacene film (120 nm average thickness) shows that pentacene BP aggregates forming on top of the thick film[18] act as growth seeds for BP nucleation throughout the film underneath (see Supplementary Fig. 1). The strong infrared contrasts of our s-SNOM images appear homogeneous within BP ellipses as well as among ellipses. As the probing depth of s-SNOM is of the order of the tip diameter[10], here 20–30 nm, the observed homogeneity suggests that BP material in the ellipses is not mixed with TFP and extends through the full film depth.

Discussion

A close inspection of the AFM micrograph reveals that it is indeed possible to discern the BP ellipses also in topography, as
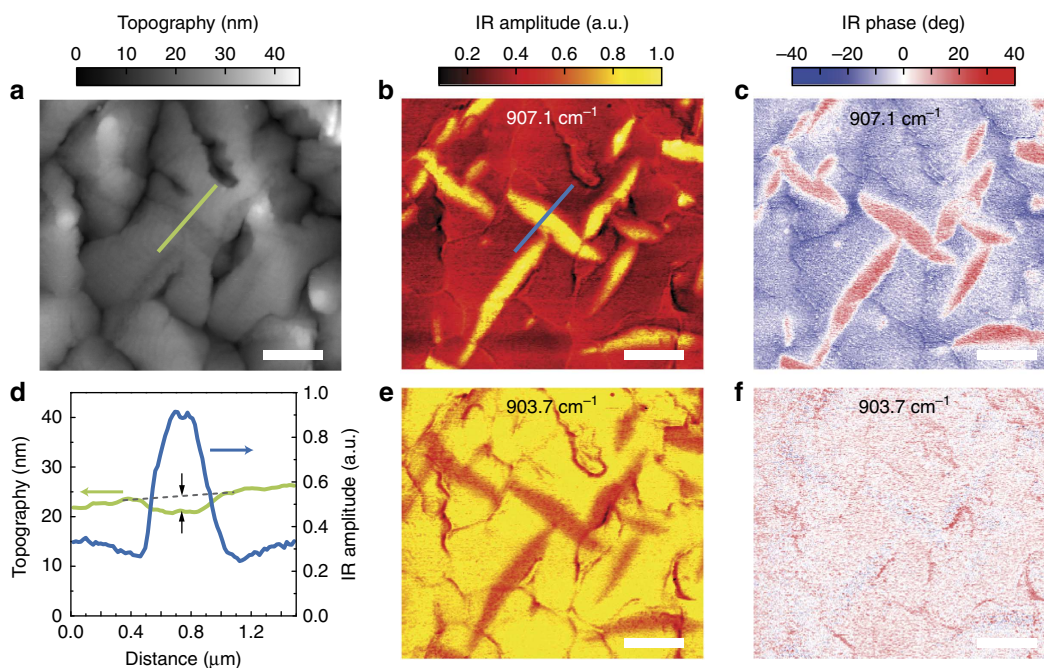
Figure 4 | Infrared contrast and topographic depression confirm BP nucleation. Two s-SNOM measurements (monochromatic imaging mode) of the same section of the pentacene film ($5\,\mu m \times 4.5\,\mu m$) marked by the dashed square in Fig. 2. The two repeats were conducted at different infrared illumination frequencies of $907.1\,cm^{-1}$ (**a**–**c**) and $903.7\,cm^{-1}$ (**e,f**), corresponding to the CO_2 laser lines P08 and P12, respectively. Characteristic BP pentacene ellipsoids appear both in the infrared amplitude (**b,e**) and phase (**c,f**) images. Clearly, changing the illumination frequency inverts the relative contrast between pentacene polymorphs in both the amplitude and phase images. Line profiles across a BP domain (**d**) illustrate a subtle depression in topography (green curve) marked with arrows, and a strong contrast in the infrared amplitude (blue curve). Scale bar, $1\,\mu m$.

subtle depressions of several nanometre depth (Fig. 4a), quantified in extracted line profiles (green curve, Fig. 4d). A similar observation had earlier been noted in the literature[14,15]. There, the depressions were interpreted as cracks in the pentacene film and thought to be induced by its greater contraction compared with the substrate on cooling down to room temperature after deposition. Our experiments indeed suggest an alternative mechanism, in which the mechanical stress is relaxed by a continuous conversion of TFP into BP pentacene at the interface boundaries. The direction of this phase change is determined by BP pentacene exhibiting a larger unit-cell footprint along the substrate plane compared with TFP[16,28], thus slowing the contraction and reducing the mechanical tension. In previous work, a phase transition from pentacene TFP to BP during storage under ambient air was related to the difference between the surface energies and the bulk energies of the two pentacene phases[29,30]. However, a theoretical study has already suggested that surface stress makes a contribution to this crystallization as well[31]. Here, the driving force is indeed the reduction of mechanical tension induced by the thermal contraction mismatch between pentacene and the substrate. Although our study focuses on pentacene on commonly used SiO_2 substrate, we expect a similar behaviour for other substrates that feature a thermal expansion coefficient different from the one of pentacene.

Our observation that the BP ellipsoids appear aligned along predominant, orthogonal directions (Fig. 2b, presumably the crystal axes of TFP) supports the conjectured evolution of BP from highly ordered TFP pentacene. The phase conversion from the initial, upright molecular orientation of TFP easily explains why the resulting BP has the molecules also upright on the substrate, as proven in X-ray diffraction by its $14.4\,\text{Å}$ (001)-spacing (Fig. 1). Indeed, this height is by $1\,\text{Å}$ smaller than that of

TFP, due to a larger tilt of the molecules (*cf.* inset Fig. 1)[9,16,17]. As the 40-nm thick pentacene sample consists of about 30 molecular layers, the accumulated topographical depression should be $\sim 3\,nm$, as is experimentally demonstrated in the AFM line profile (Fig. 4d, green line). This agreement confirms that the nanoscale BP ellipses penetrate the full film depth. Thus, despite our well-controlled growth of pentacene films with optimized topographical homogeneity, BP ellipses may well dissect percolation pathways in TFP and hinder carrier transport, a phenomenon that has escaped discovery so far in spite of the large number of studies on this material. The influence of BP crystallization on carrier mobility might be further investigated by recording the BP evolution in the channel of a working field-effect transistor (see Supplementary Fig. 2) or even by direct measurements of the local conductivity via the SNOM technique[32]. During storage of the pentacene sample, BP continues to grow at the expense of TFP pentacene (see Supplementary Fig. 3), which may turn out to be critical for the shelf life of pentacene electronic devices.

Altogether, our method of infrared contrasting at nanoscale resolution has straightforwardly clarified that the larger grains in pentacene films deposited at elevated substrate temperature ($65\,°C$) are subject to massive nucleation of nanometre-sized BP inclusions in the dominant TFP. We expect that the unique combination of molecular specificity (which includes sensitivity to molecular arrangement) and nanometre resolution offered by the infrared near-field interaction will allow to deepen our understanding of the nanostructure of conjugated and aromatic materials for organic electronics.

Our findings demonstrate that s-SNOM is ideally suited for monitoring polymorphism and phase coexistence in highly ordered organic films at 20-nm resolution. We also foresee great opportunities for infrared s-SNOM in the field of semi-crystalline

polymers, where the nanometer-scale coexistence of crystalline and amorphous phases[33,34] with fullerene domains[35,36] is discussed in the context of exciton and charge transport. Imaging of the acceptor and donor network in terms of structure and composition should considerably help to better understand organic photovoltaics.

Methods

Pentacene deposition. The pentacene samples were prepared on Si substrate on top of 20-nm thick thermally grown SiO_2. The Si/ SiO_2 substrates were successively cleaned by sonication in acetone and isopropyl alcohol for 10 min each, followed by thorough rinsing with deionized water and then dried with nitrogen. Molecular beam deposition was employed to prepare 40-nm thick films, using triple-sublimed pentacene (Sigma-Aldrich), at a deposition rate of $0.2\,\text{Å}\,\text{s}^{-1}$, a substrate temperature of $65\,°C$ and a pressure of about 2×10^{-6} mbar.

X-ray diffraction. X-ray intensity measurements were carried out by reflectometry using a laboratory X-ray diffractometer with a Mo-K_α source (wavelength $\lambda = 0.71\,\text{Å}$). The scattered X-ray intensity was normalized and plotted against the momentum transfer $q_z = (4\pi/\lambda)\sin\theta$, where λ is the wavelength and θ the scattering angle.

s-SNOM near-field microscope. We employed a commercial scattering near-field microscope (NeaSNOM, neaspec.com) equipped with a standard metallized tip (NCPt arrow, nanoandmore.com), operated in AFM tapping mode at 50 nm amplitude to modulate the near-field interaction between the tip and sample. The back-scattered infrared signal is detected simultaneously with the topography (see sketch in the right inset of Fig. 3). Lock-in and heterodyne detection at the $n = 3$ harmonic of the tapping frequency (~ 300 kHz) provides background-free near-field imaging. Monitoring of the infrared signal versus tip-sample separation (approach curves) was used to ensure the optimal working settings of the tapping amplitude, the demodulation order n and the focusing. In the monochromatic infrared near-field imaging mode (Figs 2 and 4) a line-tunable $^{13}C^{16}O_2$ laser attenuated to 10 mW was used for illumination. The acquisition time was 9 ms per pixel, requiring several minutes for a 300×300 pixel-sized image.

Nano-FTIR mode of s-SNOM. The spectroscopic mode of s-SNOM (Fig. 3) employs illumination by a coherent broadband mid-infrared beam (here $25\,\mu W$) from a home-built difference-frequency source driven by a <100-fs Er fibre laser (FFS.SYS-2B with FFS-CONT, toptica.com)[26]. Detection and spectral analysis of the back-scattered light is carried out via an asymmetric Michelson interferometer that generates, by online Fourier transformation, infrared amplitude and phase spectra simultaneously. Note that although common FTIR spectrometers are not equipped to determine the complete, complex material response, the nano-FTIR phase spectra valuably complement the amplitude spectra[26,27]. Specifically, nano-FTIR absorption by molecular vibrational resonance can be directly determined by multiplying the measured scattering amplitude with $\sin(\varphi)$, where φ is the measured scattering phase[27]. The work of F. Huth, et al.[27] also demonstrates that near-field infrared spectra of organic substances, that is, weak oscillators, exhibit indeed the same spectral positions, spectral widths and relative intensities as the corresponding far-field spectra.

References

1. Forrest, S. R. The path to ubiquitous and low-cost organic electronic appliances on plastic. *Nature* **428,** 911–918 (2004).
2. Klauk, H., Zschieschang, U., Pflaum, J. & Halik, M. Ultralow-power organic complementary circuits. *Nature* **445,** 745–748 (2007).
3. Sekitani, T., Zschieschang, U., Klauk, H. & Someya, T. Flexible organic transistors and circuits with extreme bending stability. *Nat. Mater.* **9,** 1015–1022 (2010).
4. Congreve, D. N. *et al.* External quantum efficiency above 100% in a singlet-exciton-fission–based organic photovoltaic cell. *Science* **340,** 334–337 (2013).
5. Dimitrakopoulos, C. D., Brown, A. R. & Pomp, A. Molecular beam deposited thin films of pentacene for organic field effect transistor applications. *J. Appl. Phys.* **80,** 2501–2508 (1996).
6. Knipp, D., Street, R. A., Völkel, A. & Ho, J. Pentacene thin film transistors on inorganic dielectrics: Morphology, structural properties, and electronic transport. *J. Appl. Phys.* **93,** 347–355 (2003).
7. Heringdorf, F., Reuter, M. C. & Tromp, R. M. Growth dynamics of pentacene thin films. *Nature* **412,** 517–520 (2001).
8. Westermeier, C., Fiebig, M. & Nickel, B. Mapping of trap densities and hotspots in pentacene thin-film transistors by frequency-resolved scanning photoresponse microscopy. *Adv. Mater.* **25,** 5719–5724 (2013).
9. Mattheus, C. C. *et al.* Identification of polymorphs of pentacene. *Synth. Met.* **138,** 475–481 (2003).

10. Keilmann, F. & Hillenbrand, R. in *Nano-Optics and Near-Field Optical Microscopy.* (eds Zayats, A. & Richards, D.) Ch. 11, 235–265 (Artech House, Norwood, 2009).
11. Lee, J., Kim, J. H. & Im, S. Effects of substrate temperature on the device properties of pentacene-based thin film transistors using Al_2O_{3+x} gate dielectric. *J. Appl. Phys.* **95,** 3733–3736 (2004).
12. Kitamura, M. & Arakawa, Y. Pentacene-based organic field-effect transistors. *J. Phys. Condens. Matter* **20,** 184011 (2008).
13. Horowitz, G. & Hajlaoui, M. E. Grain size dependent mobility in polycrystalline organic field-effect transistors. *Synth. Met.* **122,** 185–189 (2001).
14. Pesavento, P. V., Puntambekar, K. P., Frisbie, C. D., McKeen, J. C. & Ruden, P. P. Film and contact resistance in pentacene thin-film transistors: dependence on film thickness, electrode geometry, and correlation with hole mobility. *J. Appl. Phys.* **99,** 094504 (2006).
15. Ruiz, R. *et al.* Pentacene ultrathin film formation on reduced and oxidized Si surfaces. *Phys. Rev. B* **67,** 125406 (2003).
16. Campbell, R. B., Robertson, J. M. & Trotter, J. The crystal structure of hexacene, and a revision of the crystallographic data for tetracene and pentacene. *Acta Crystallogr.* **15,** 289–290 (1962).
17. Schiefer, S., Huth, M., Dobrinevski, A. & Nickel, B. Determination of the crystal structure of substrate-induced pentacene polymorphs in fiber structured thin films. *J. Am. Chem. Soc.* **129,** 10316–10317 (2007).
18. Bouchoms, I. P. M., Schoonveld, W. A., Vrijmoeth, J. & Klapwijk, T. M. Morphology identification of the thin film phases of vacuum evaporated pentacene on SiO_2 substrates. *Synth. Met.* **104,** 175–178 (1999).
19. Di Carlo, A., Piacenza, F., Bolognesi, A., Stadlober, B. & Maresch, H. Influence of grain sizes on the mobility of organic thin-film transistors. *Appl. Phys. Lett.* **86,** 263501 (2005).
20. Shtein, M., Mapel, J., Benziger, J. B. & Forrest, S. R. Effects of film morphology and gate dielectric surface preparation on the electrical characteristics of organic-vapor-phase-deposited pentacene thin-film transistors. *Appl. Phys. Lett.* **81,** 268–270 (2002).
21. Guo, D., Ikeda, S., Saiki, K., Miyazoe, H. & Terashima, K. Effect of annealing on the mobility and morphology of thermally activated pentacene thin film transistors. *J. Appl. Phys.* **99,** 094502 (2006).
22. Ji, T., Jung, S. & Varadan, V. K. On the correlation of postannealing induced phase transition in pentacene with carrier transport. *Org. Electron.* **9,** 895–898 (2008).
23. Hosoi, Y., Okamura, K., Kimura, Y., Ishii, H. & Niwano, M. Infrared spectroscopy of pentacene thin film on SiO_2 surface. *Appl. Surf. Sci.* **244,** 607–610 (2005).
24. Koch, N. *et al.* Evidence for temperature-dependent electron band dispersion in pentacene. *Phys. Rev. Lett.* **96,** 156803 (2006).
25. Salzmann, I. *et al.* Structural and electronic properties of pentacene-fullerene heterojunctions. *J. Appl. Phys.* **104,** 114518 (2008).
26. Amarie, S., Ganz, T. & Keilmann, F. Mid-infrared near-field spectroscopy. *Opt. Express* **17,** 21794–21801 (2009).
27. Huth, F. *et al.* Nano-FTIR absorption spectroscopy of molecular fingerprints at 20 nm spatial resolution. *Nano Lett.* **12,** 3973–3978 (2012).
28. Ruiz, R. *et al.* Structure of pentacene thin films. *Appl. Phys. Lett.* **85,** 4926–4928 (2004).
29. Drummy, L. F. & Martin, D. C. Thickness-driven orthorhombic to triclinic phase transformation in pentacene thin films. *Adv. Mater.* **17,** 903–907 (2005).
30. Di, C.-a. *et al.* Effect of dielectric layers on device stability of pentacene-based field-effect transistors. *Phys. Chem. Chem. Phys.* **11,** 7268–7273 (2009).
31. Yang, C. C., Li, S. & Armellin, J. Size and temperature dependence of phase stability in nanocrystalline pentacene thin films. *J. Phys. Chem. C* **111,** 17512–17515 (2007).
32. Keilmann, F., Huber, A. J. & Hillenbrand, R. Nanoscale conductivity contrast by scattering-type near-field optical microscopy in the visible, infrared and THz domains. *J. Infrared Millim. Terahertz Waves* **30,** 1255–1268 (2009).
33. Sirringhaus, H. *et al.* Two-dimensional charge transport in self-organized, high-mobility conjugated polymers. *Nature* **401,** 685–688 (1999).
34. Noriega, R. *et al.* A general relationship between disorder, aggregation and charge transport in conjugated polymers. *Nat. Mater.* **12,** 1038–1044 (2013).
35. Yu, G., Gao, J., Hummelen, J. C., Wudl, F. & Heeger, A. J. Polymer photovoltaic cells: enhanced efficiencies via a network of internal donor-acceptor heterojunctions. *Science* **270,** 1789–1791 (1995).
36. Park, S. H. *et al.* Bulk heterojunction solar cells with internal quantum efficiency approaching 100%. *Nat. Photon* **3,** 297–302 (2009).

Author contributions

All authors were involved in designing the research, performing the research and writing the paper.

Additional information

Supplementary Information accompanies this paper at http://www.nature.com/naturecommunications

Competing financial interests: F.K. is co-founder and scientific advisor of Neaspec GmbH, manufacturer of the s-SNOM setup used in this study. All other authors declare no competing financial interests.

Reprints and permission information is available online at http://npg.nature.com/reprintsandpermissions/

How to cite this article: Westermeier, C. *et al.* Sub-micron phase coexistence in small-molecule organic thin films revealed by infrared nano-imaging. *Nat. Commun.* 5:4101 doi: 10.1038/ncomms5101 (2014).

B

SUPPLEMENTARY MATERIAL FOR THE PUBLICATIONS

B.1 SUPPLEMENTARY MATERIAL FOR ALL-ELECTRONIC TERAHERTZ NANOSCOPY

Clemens Liewald, Stefan Mastel, Jeffrey Hesler, Andreas J. Huber, Rainer Hillenbrand, and Fritz Keilmann

All-electronic terahertz nanoscopy: supplementary material

Clemens Liewald,[1,2] **Stefan Mastel,**[3] **Jeffrey Hesler,**[4] **Andreas J. Huber,**[5]
Rainer Hillenbrand,[6,7] **Fritz Keilmann**[1,*]

[1]*Fakultät für Physik & Center for NanoScience (CeNS), Ludwig-Maximilians-Universität, 80539 München, Germany*

[2]*Nanosystems Initiative Munich, 80799 München, Germany*

[3]*CIC nanoGUNE, 20018 Donostia-San Sebastián, Spain*

[4]*Virginia Diodes Inc., Charlottesville, Virginia 22901, USA*

[5]*Neaspec GmbH, 82512 Martinsried, Germany*

[6]*CIC nanoGUNE and UPV/EHU, 20018 Donostia-San Sebastián, Spain*

[7]*IKERBARSQUE, Basque Foundation of Science, 48013 Bilbao, Spain*

Corresponding author: fritz.keilmann@lmu.de

This document provides supplementary information to "All-electronic terahertz nanoscopy," **https://doi.org/10.1364/OPTICA.5.000159.**

Principle of Mixer and Tapping Demodulation

The basic function of an electronic mixer is two-wave interference in a nonlinear device, resulting in an output wave whose frequency and phase are the differences of frequencies and of phases, respectively, of the incident waves. Of interest in our application is the case that one wave contains a modulation to be analyzed, while the other wave, the "local oscillator" is purely sinusoidal. Thus, the effect of mixing is that the modulation content of interest is transferred from the original frequency region (THz) to the region of the much smaller difference frequency (MHz) where the modulation analysis is technically easier. The present transceiver scheme uses two such transfers by two sequential mixers down to frequency zero, after which the original modulation of the THz wave at harmonics of the tapping frequency including phases stays fully preserved and ready to be analyzed by the NeaSNOM controller.
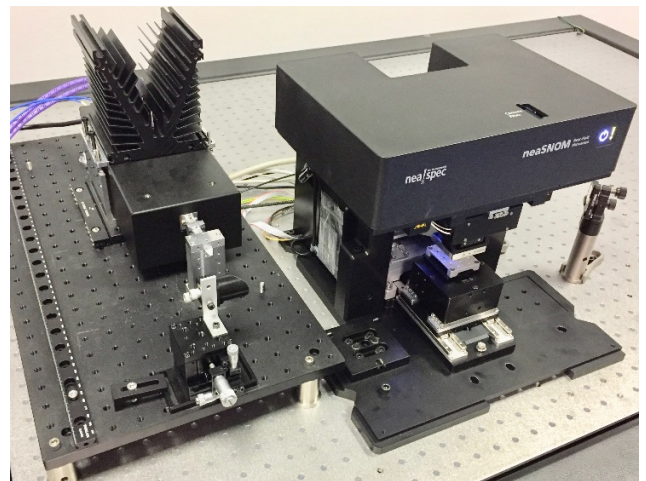
Fig. S1. Photograph of the THz transceiver head (left) aligned to the s-SNOM (right). The transfer paraboloidal mirror can be seen in the foreground, 5 cm from the transceiver's waveguide aperture.
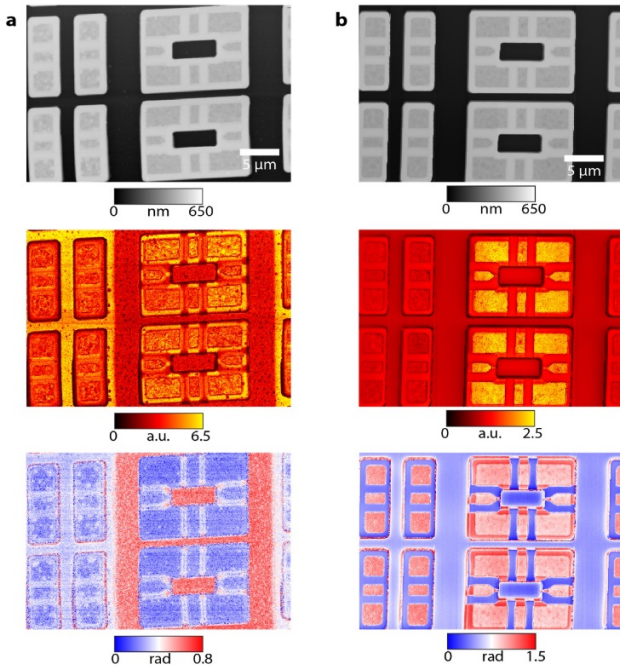
Fig. S2. Single-frequency THz and mid-infrared s-SNOM nano-images of Si exhibiting topographical as well as doping structures, topography (top), amplitude s_3 (mid), and phase φ_3 (bottom), **a**, at 0.6 THz (from which Fig. 2 is cut), acquisition time 144 min, **b**, at 27 THz (equiv. to 11.1 µm wavelength), acquisition time 48 min.
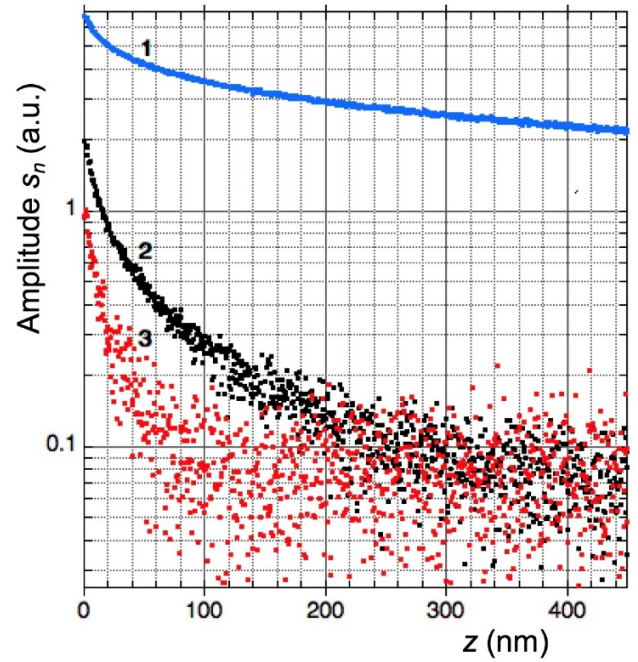
Fig. S3. Approach curves, i.e., simultaneously recorded 0.6 THz amplitude signals s_1, s_2 and s_3 as function of the tip-sample separation z, at sample position B (highly doped Si), tapping amplitude 170 nm, acquisition time 90 s.—The s_3 signal is seen to fluctuate by up to ca. ± 0.07 a.u. at the used integration time of 100 ms/experimental point; this value corresponds to a S/N ratio of 7 and 14 for s_3 and s_2 images, respectively, if acquired at 100 ms pixel time on Au or highly doped Si.

B.2   SUPPLEMENTARY MATERIAL FOR PHOTOCURRENT MICROSCOPY
      OF CONTACT RESISTANCE AND CHARGE CARRIER TRAPS IN
      ORGANIC FIELD-EFFECT TRANSISTORS

Supplemental material for

Photocurrent microscopy of contact resistance and charge carrier traps in organic field-effect transistors

C. Liewald,[1,2] D. Reiser,[1] C. Westermeier,[1] and B. Nickel[1,2,a]

[1]*Fakultät für Physik & Center for NanoScience (CeNS), Ludwig-Maximilians-Universität München,*

Geschwister-Scholl-Platz 1, 80539 Munich, Germany

[2]*Nanosystems Initiative Munich, Schellingstrasse 4, 80799 Munich, Germany*

A) Transfer curves of transistor II and extraction of the mobilities and threshold voltages.
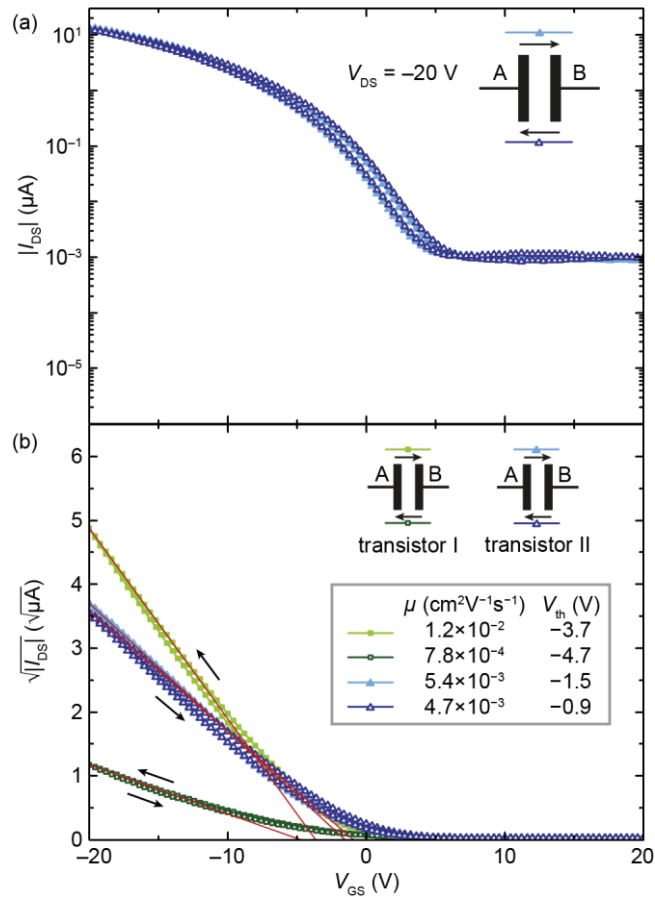
FIG. S1. (a) Transfer curves of transistor II for both polarities. The Femto amplifier was not calibrated correctly, resulting in a small offset current of 10^{-3} µA. Therefore, the turn-on voltage cannot be determined perfectly. In contrast to transistor I these curves are almost identical. (b) Extraction of the mobilities and threshold voltages out of a $(I_{DS})^{0.5}$ plot by linear approximation.

a) Electronic mail: nickel@lmu.de

To extract the mobilities and threshold voltages out of a $(I_{DS})^{0.5}$ plot in the saturation regime by linear approximation,

$$\mu = \left(\frac{\partial\sqrt{I_{DS}}}{\partial V_{GS}}\right)^2 \frac{2L}{W C_i}$$

can be used, with $L = 23$ µm the length of the transistor channel, $W = 900$ µm its width and $C_i = 3.8 \times 10^{-4}$ Fm^{-2} the capacitance of the insulator per area. Therefore with the slope of the $(I_{DS})^{0.5}$ plot, μ can be extracted. The intersection with the V_{GS} axis determines the threshold voltage[1].

B) SPCM maps of transistor II.
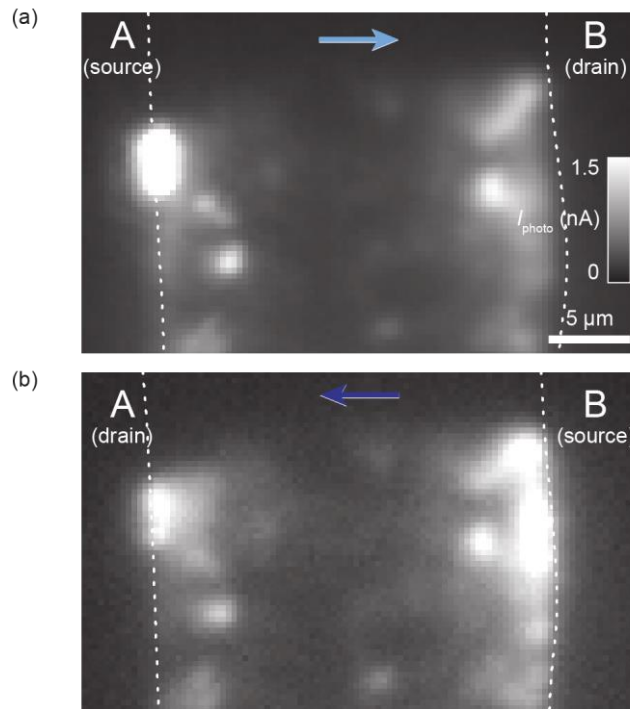
FIG. S2. SPCM maps of transistor II. The boundaries of the contacts A and B are indicated by the white, dotted lines. The arrows indicate the polarity of the electric field. (a) AB direction, (b) BA direction, recorded at $V_{DS} = -15$ V and $V_{GS} = -10$ V. Both maps show the same hotspots and an equal level of photoresponse over the whole channel. A slight increase of the signal at the respective source contact can be seen, indicating an additional contribution of photocurrent.

[1]   B. Nickel, M. Fiebig, S. Schiefer, M. Göllner, M. Huth, C. Erlen, and P. Lugli, Phys. Status Solidi A **205**, 526 (2008).

B.3 SUPPLEMENTARY MATERIAL FOR SCANNING PHOTOCURRENT MICROSCOPY OF ELECTRONS AND HOLES IN THE PIGMENT SEMICONDUCTOR EPINDOLIDIONE

Clemens Liewald, Simone Strohmair, Henrik Hecht, Eric Głowacki, and Bert Nickel

Supplementary Information

Scanning photocurrent microscopy of electrons and holes in the pigment semiconductor epindolidione

C. Liewald[a,b], S. Strohmair[a], H. Hecht[a], E. D. Głowacki[c], and B. Nickel[a,b,*]

[a] Faculty of Physics and CeNS, Ludwig-Maximilians-Universität München, 80539 Munich, Germany.

[b] Nanosystems Initiative Munich (NIM), 80799 Munich, Germany.

[c] Laboratory of Organic Electronics, Department of Science and Technology, Campus Norrköping,

Linköpings Universitet, Bredgatan 33, SE-601 74 Norrköping, Sweden.

[*] Corresponding author. E-Mail address: nickel@lmu.de (B. Nickel)
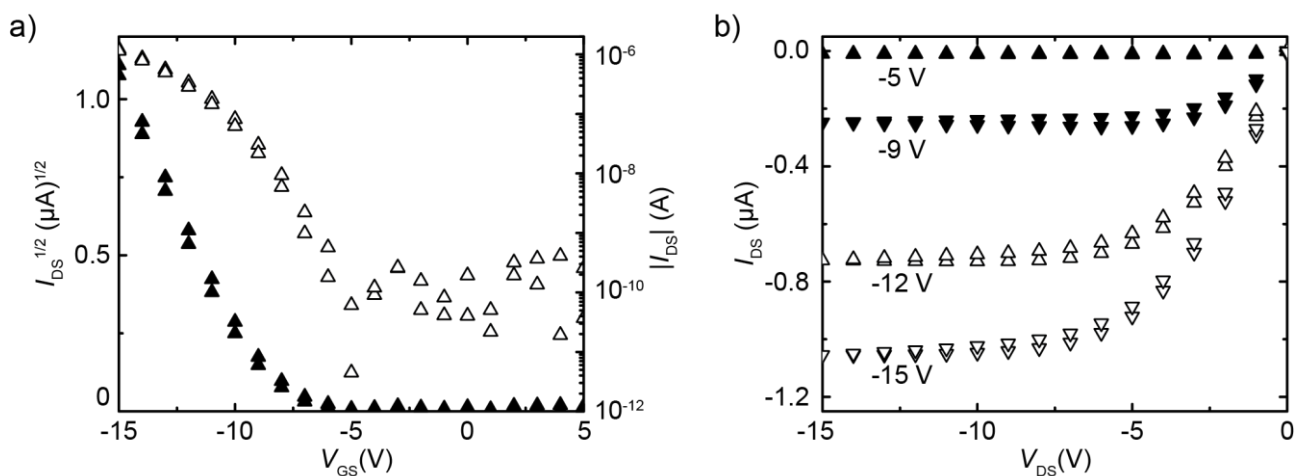
Figure S1 a) Transfer characteristics of the investigated transistor in the dark. **b)** Output characteristics I_{DS} vs. V_{DS} with different V_{GS} (-5 V, -9 V, -12 V, -15 V).
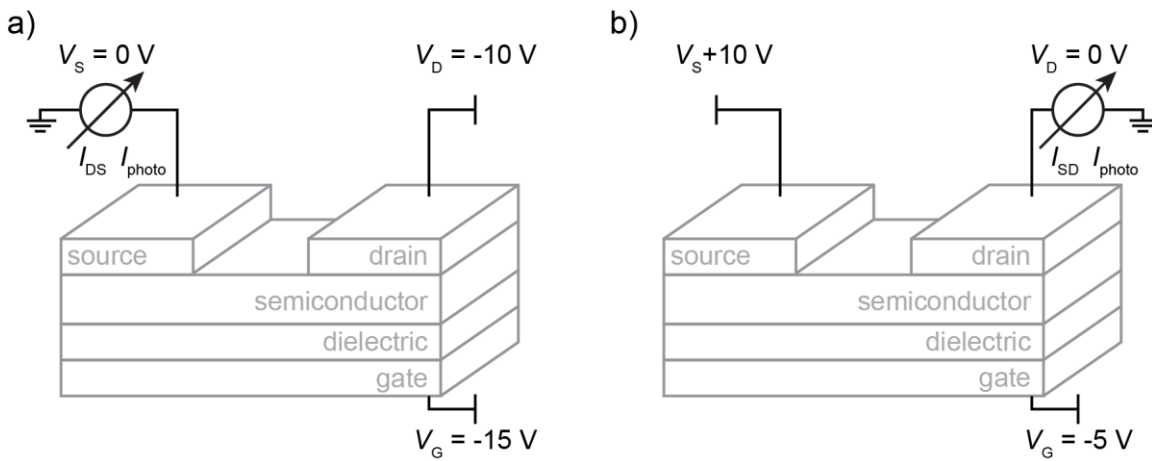
Figure S2 Equivalent circuit for V_{DS} = -10 V, V_{GS} = -15 V. **a)** Current measurement at the source. **b)** Current measurement at the drain. The same voltage differences (V_{DS} = V_D - V_S = -10 V, V_{GS} = V_G - V_S = -15 V, V_{GD} = V_G - V_D = -5 V) are present in both configurations. Configuration **a)** is typically used, while configuration **b)** is equivalent regarding potential differences, equally shifting the potential level for all three contacts. For V_{GS} = 5 V, the gate voltage has to be adjusted accordingly.
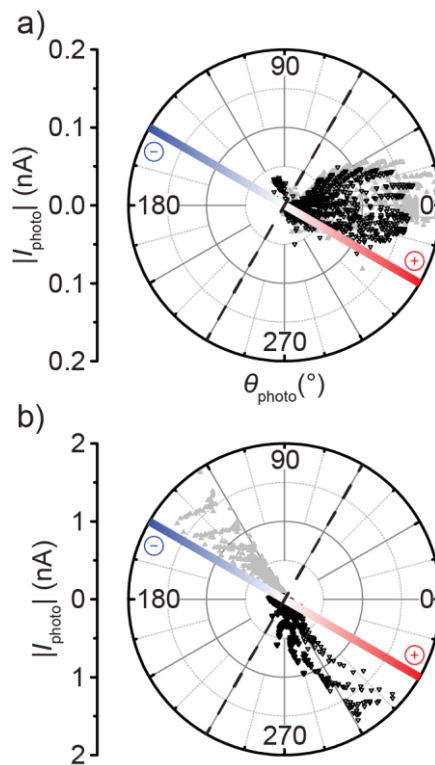
Figure S3 Polar plots of photocurrent line scans (same measurement as shown in Figure 3) for **a)** V_{GS} = 5 V and **b)** V_{DS} = -15 V. Photocurrent measurements at source (grey data points) and at the drain (black data points) are shown. For V_{GS} = 5 V, the measurements at the source and drain exhibit an equal photocurrent phase around 0°. For V_{GS} = -15 V, the phase difference between the consecutive measurements is approximately 180°. The projection I_{photo} = $|I_{photo}|$ × cos(θ_{photo} + 30°) of all measurement points onto the drawn color scale at -30°/330° is a compromise to equally display the measurements in Figure 3.
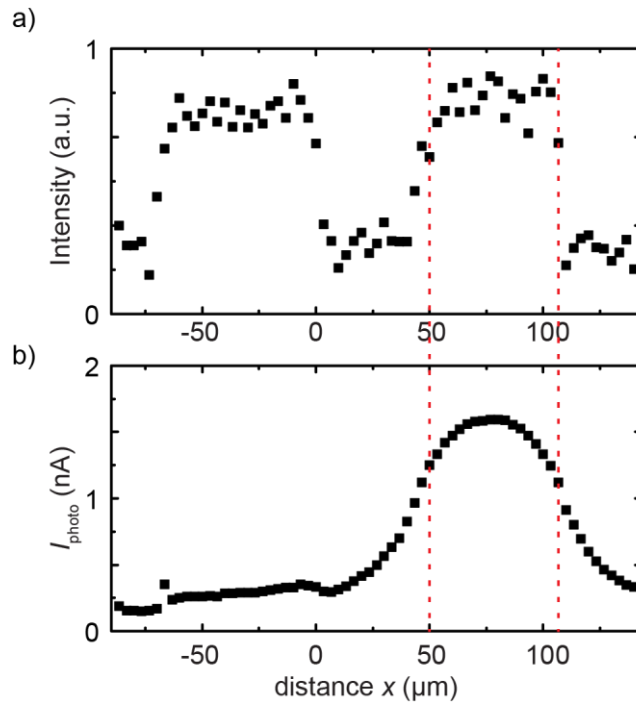
Figure S4 Line-scan of **a)** the reflected optical intensity and **b)** I_{photo} over the lateral transistor structure for V_{GS} = -15 V, V_{DS} = -10 V, and the Lock-in amplifier connected to the drain contact. The reflected intensity defines the edges of the contact. I_{photo} shows no sharp decrease but a substantial contribution when the laser was not illuminating the right contact.
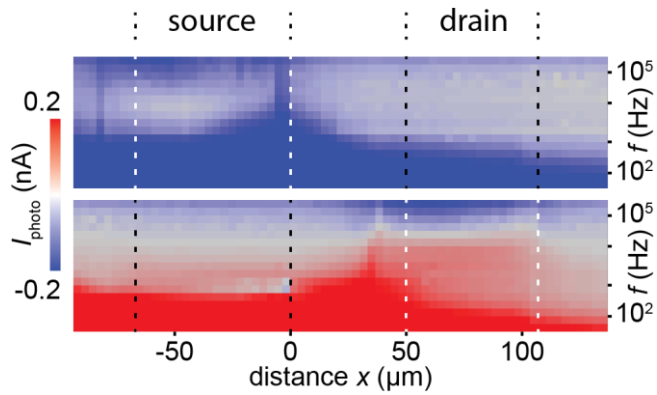
Figure S5 Line scans of frequency-resolved photocurrent I_{photo} for V_{GS} = -15 V (same measurement as shown in **Figure 3b**) with a lower color scale, revealing the negative component above 10^4 Hz. This component was measured at both contacts, source and drain, like the displacement current for V_{GS} = 5 V (**Figure 3a**). Dotted lines indicate the transistor channel (x = 0-50 μm) between the left source contact and the right drain contact; the contacts marked with white lines were connected to the transimpedance amplifier.

3

B.4 SUPPLEMENTARY MATERIAL FOR A RESISTOR NETWORK SIMULATION MODEL FOR LASER-SCANNING PHOTO-CURRENT MICROSCOPY TO QUANTIFY LOW CONDUCTANCE REGIONS IN ORGANIC THIN FILMS

Mohammed Darwish, Hakan Boysan, Clemens Liewald, Bert Nickel, and Alessio Gagliardi

Supplementary Information

A Resistor Network Simulation Model for Laser-Scanning Photo-Current Microscopy to quantify low conductance regions in Organic Thin Films

M. Darwish, H. Boysan, C. Liewald, B. Nickel, A. Gagliardi
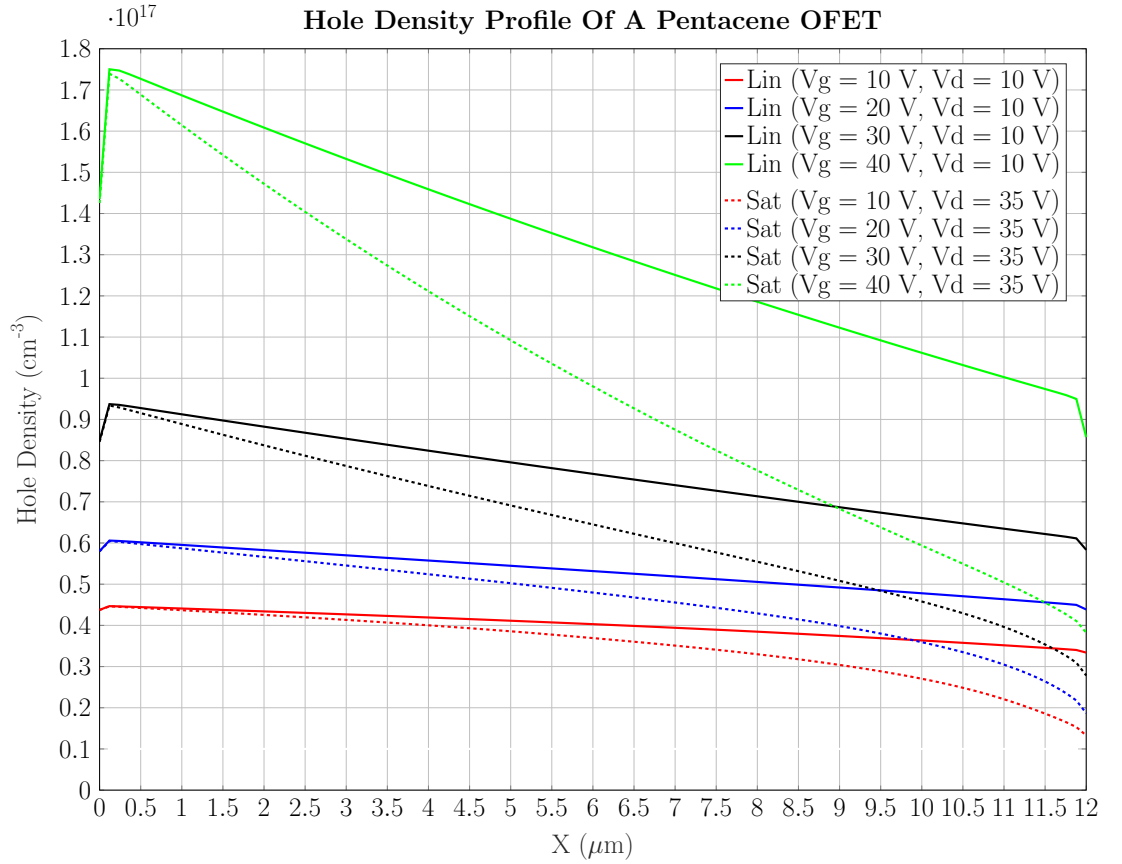
Figure S1: Illustration of the charge (i.e holes) density profile along a channel of a Pentacene OFET. Profiles are shown for both linear and saturation regimes. A linear drop is observed in both regimes, but also for the saturation regime the profiles shows a non-linear behaviour close to the drain contact. Concerning the operating point of the network model, we use the "blue" solid line at a gate voltage Vg = 20 V and drain voltage Vd = 10 V.
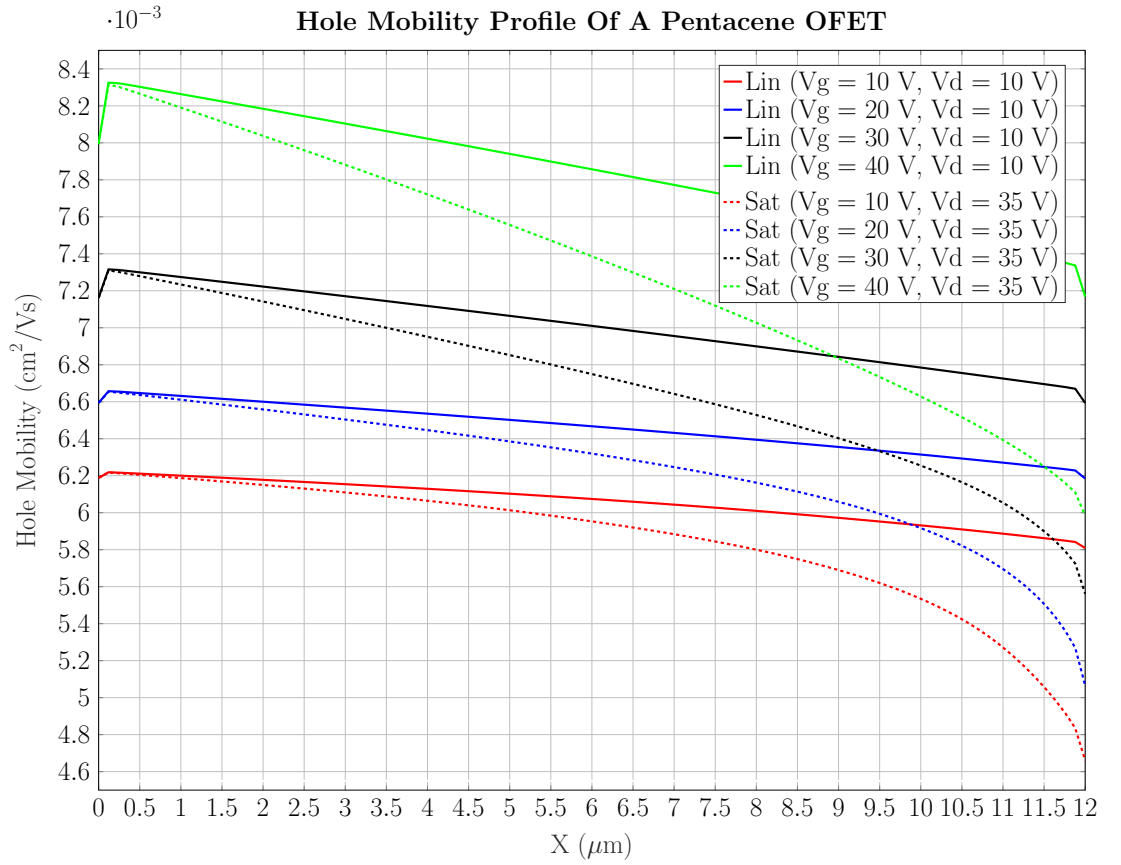
Figure S2: Illustration of the charge (i.e holes) mobility profile along a channel of a Pentacene OFET. Profiles are shown for both linear and saturation regimes. Given the operating point of the network model, we use the "blue" solid line represented by a gate voltage Vg = 20 V and a drain voltage Vd = 10 V, with an average charge mobility of approximately $6.5 \times 10^{-3}\,\mathrm{cm^2/Vs}$.

B.5 SUPPLEMENTARY MATERIAL FOR TRANSFERABLE ORGANIC SEMICONDUCTOR NANOSHEETS FOR APPLICATION IN ELECTRONIC DEVICES

Simon J. Noever, Michael Eder, Fabio del Giudice, Jan Martin, Franz X. Werkmeister, Stefan Hallwig, Stefan Fischer, Oliver Seeck, Nils-Eike Weber, Clemens Liewald, Fritz Keilmann, Andrey Turchanin, and Bert Nickel

ADVANCED MATERIALS

Supporting Information

Transferable Organic Semiconductor Nanosheets for Application in Electronic Devices

Simon J. Noever, Michael Eder, Fabio del Giudice, Jan Martin, Franz X. Werkmeister, Stefan Hallwig, Stefan Fischer, Oliver Seeck, Nils-Eike Weber, Clemens Liewald, Fritz Keilmann, Andrey Turchanin,* and Bert Nickel*

SUPPORTING INFORMATION

Transferable organic semiconductor nanosheets
for application in electronic devices

Simon J. Noever, Michael Eder, Fabio del Giudice, Jan Martin, Franz Werkmeister, Stefan Hallwig,

Stefan Fischer, Oliver Seeck, Nils-Eike Weber†, Clemens Liewald, Fritz Keilmann,

Andrey Turchanin* and Bert Nickel*

Dr. Simon J. Noever, Michael Eder, Stefan Fischer, Fabio del Giudice, Jan Martin,

Stefan Hallwig, Clemens Liewald, Franz Werkmeister, Dr. Fritz Keilmann, PD. Dr. Bert Nickel

Faculty of Physics and CeNS, Ludwig-Maximilians-Universität München, 80539 Munich,

Germany

Simon J. Noever, Clemens Liewald, PD. Dr. Bert Nickel

Nanosystems Initiative Munich (NIM), 80799 Munich, Germany

E-mail: nickel@physik.uni-muenchen.de

Dr. Oliver Seeck

Deutsches Elektronen Synchrotron DESY, 22603 Hamburg, Germany

Dr. Nils-Eike Weber

Faculty of Physics, University of Bielefeld, 33615 Bielefeld, Germany

Present Addresses: † Scienta Omicron GmbH, 65232 Taunusstein, Germany

Prof. Dr. Andrey Turchanin

Institute of Physical Chemistry, Friedrich-Schiller-Universität Jena, 07743 Jena, Germany

Jena Center for Soft Matter (JCSM), 07743 Jena, Germany

Center for Energy and Environmental Chemistry Jena (CEEC), 07743 Jena, Germany

Abbe Center of Photonics (ACP), 07745 Jena

E-mail: andrey.turchanin@uni-jena.de

Experimental

Sample preparation: For all experiments, the pentacene (Sigma Aldrich triple sublimed, additionally purified by Creaphys) thin films were deposited at a rate of ~ 0.1 Ås^{-1} under equal conditions. Sample temperatures were held at room temperature, while the chamber pressure was kept below $1 \cdot 10^{-7}$ mbar. The Si/SiO$_2$ substrates were cleaned *via* sonicating in acetone and isopropanol for 10 minutes, respectively. After thorough rinsing with DI water, the substrates were plasma cleaned using oxygen plasma (50 W for 30 s, LabAsh).

The PVA layers were produced using the following protocol: first a 5 % PVA (Fluka Polyvinyl alcohol 6-98) solution in DI water was prepared *via* stirring at 800 rpm at 75 °C for 3 hours. Afterwards, the solution was filtered using a standard folded paper filter, and spincast onto the substrates (here, oxidized, highly doped Si wafers) for 60 seconds at 4000 rpm, leading to layer thicknesses of ~ 200 nm. The brass sheet in Fig. 2 was cleaned with acetone and isopropanol prior to lamination with the pentacene film.

The gold structures for the SNOM samples (cf. SI) were defined *via* positive photolithography. First the sample surfaces were coated by LOR 3B (MicroChem) at 4000 rpm and soft baked for 3 minutes at 150 °C. A layer of S1813 G2 (Microposit) was spincast at 5000 rpm followed by a 3 minute soft bake at 115 °C. This photoresist was illuminated by a Karl Suss Maskaligner MJB3 and developed with Microposit 351 Developer, diluted with DI water 1:3. The structures (3 nm Cr, followed by 50 nm Au) were deposited *via* electron beam deposition at ~ 1 Ås^{-1}. For the lift off, Microposit 1165 remover was used, followed by rinsing in acetone and IPA.

Characterization: GIXD measurements were taken at the P08 beamline at PETRA III / DESY in Hamburg using an X-ray energy of 18 keV. The diffraction signal was recorded using a Perkin Elmer XRD 1621 detector. An oxidized Si wafer with a 300 nm SiO_2 layer served as substrate.

For the UV-VIS measurements, 50 nm pentacene films were deposited on fused silica, *i.e.* transparent glass substrates. The absorbance spectra were recorded using a PerkinElmer Lambda EZ201 spectrometer in wavelength scan mode. Each measurement was corrected by a baseline recorded with cleaned and bare silica substrates.

Vibrational spectroscopy data were recorded using a Nicolet Nexus FTIR equipped with a ThermoFisher SAGA grazing incidence accessory. A 23 nm pentacene layer was deposited onto a 100 nm Au film. Before each FTIR measurement, the atmosphere was allowed to stabilize for 10 minutes, and no nitrogen or dry air purge was used. Background spectra were recorded from a clean Au film and used for the automatic baseline correction of the Omnic v6.2 software.

The AFM micrographs were measured in tapping mode with a Veeco Dimension 3100 AFM and analyzed using Gwyddion 2.40. The SEM images were taken at a Zeiss-LEO 982.

Helium ion microscopy was conducted with a Carl Zeiss Orion Plus instrument employing secondary electrons collected by an Everhart-Thornley detector. For this image, the film was grown on a 300 nm Au/mica substrate, crosslinked *via* a high dose flood gun (electron energy: 300 eV, dose: 250 mC/cm^2) and transferred onto an oxidized Si wafer.

Transistor characteristics were recorded *via* a Keithley Instruments Source Meter 2612. The transfer curves in Fig. 4 were measured under high vacuum. The transistor had a channel width of 2 mm and a channel length of 50 μm. The contact resistance measurements were taken under

ambient conditions. The transistor layouts for the contact resistance measurements were Generation 4 test wafers, purchased from the Fraunhofer IPMS, which were cleaned using the same protocol as all Si/SiO$_2$ substrates. The gate-dielectric substrate consisted of n-doped Si (n ~ 3E17 cm^{-3}) topped by a 230 nm thick SiO$_2$ thermal oxide layer. 30 nm Au on a high work function ITO (indium tin oxide) adhesion layer served as source and drain contacts. The pentacene nanosheets were transferred to the test pads as described in Fig. 1 and stored in a desiccator to remove residual water.

Table T1: Specifications of crosslinked samples from main manuscript

Sample	electron energy	Emission current	irradiation time	approx. dose
GIXS sample 1	300 eV	5 mA	1200 seconds	3.0 mC/cm²
GIXS sample 2	800 eV	5 mA	1200 seconds	3.0 mC/cm²
TFT sample 1	350 eV	5 mA	600 seconds	1.5 mC/cm²
TFT sample 2	700 eV	5 mA	1800 seconds	4.5 mC/cm²
Spectroscopy sample 1	500 eV	2 mA	1200 seconds	3.0 mC/cm²
Spectroscopy sample 2	1000 eV	2 mA	1200 seconds	10.3 mC/cm²
All other samples	500 eV	5 mA	1200 seconds	3.0 mC/cm²
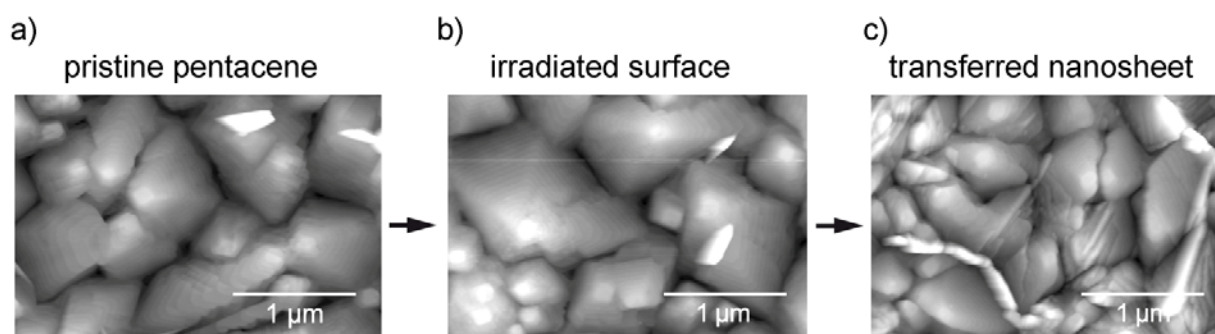
Figure S1: **AFM micrographs of pristine, irradiated and transferred pentacene surface.** a) The AFM height micrograph shows typical pyramidal growth mode of pentacene. b) After irradiation by a low energy electron (LEE) beam, AFM image indicates unchanged pentacene topography. c) After transfer to a new substrate, AFM image shows slightly disturbed topography from the transfer and drying, but otherwise unchanged characteristics. The z-scale for all AFM micrographs is 50 nm, the film thickness is 50 nm in all cases.
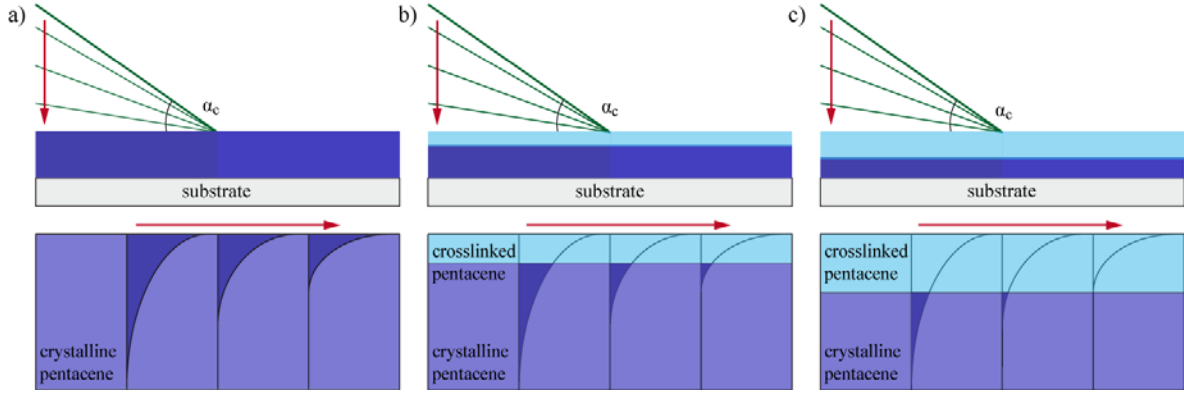
Figure S2: GIXD measurements Scheme of the grazing angle dependent penetration depth of the evanescent wave into pristine and crosslinked surfaces. The angle of incidence α_i controls the probe depth of the X-ray beam. Here, different angles below the critical angle for total reflection α_c are shown. With decreasing angle, the probe depth is more and more confined to the surface region.

The fitted total intensities of the scattered beam are calculated by the product of transmission functions and the structure factor as follows:

$$I = |T_i^2| S_{-p} |T_f^2|$$

The transmission functions calculate to:

$$T_{i,f} = \frac{2 \sin \alpha_{i,f}}{\sin \alpha_{i,f} + \sqrt{\sin^2 \alpha_{i,f} - \sin^2 \alpha_c}}$$

while the structure factor is given by the following term:

$$S_{-p} = \frac{\left| e^{\frac{-pa}{\Delta}} - e^{-iNQ_za} \right|^2}{|1 - e^{-iQ_za}|^2}$$

with p dead layers on top of the sample surface. N is the number of molecular layers within the film thickness (here, $N = 33$), Δ is the scattering depth of the evanescent wave, and $a = 15.4$Å is the lattice spacing in z-direction. $Q_z = q_z - 0.1909$ Å^{-1} is the momentum transfer parallel to the sample surface normal of the examined peak, corrected by the tilt of the unit cell with respect to said surface. This tilt was extracted from the detector image position of the first truncation rod peak, which is positioned at the sample horizon for upright crystal structures. The momentum

transfer can be calculated to:

$$q_z = k_i^z - k_f^z = \frac{2\pi}{\lambda}\left[\sqrt{\sin^2\alpha_i - 2\delta - 2i\beta} + \sqrt{\sin^2\alpha_f - 2\delta - 2i\beta}\right], \text{ with } 2\delta = \sin^2\alpha_c, \text{ and } 2i\beta =$$

$i\frac{\mu\lambda}{2\pi}$, where $\mu = 5.8 \cdot 10^{-9}\text{Å}^{-1}$ is the absorption factor (data taken from henke.lbl.gov). The scattering depth of the evanescent wave calculates to:

$$\Delta = \frac{\lambda}{2\pi(l_i + l_f)}, \text{ with } l_{i,f} = \frac{\sqrt{2}}{2}\sqrt{\left(2\delta - \sin^2\alpha_{i,f}\right) + \sqrt{(\sin^2\alpha_f - 2\delta)^2 + (2\beta)^2}}.$$

$\alpha_c = 0.0915°$ is the critical angle for pentacene (measured via X-ray reflection. α_i is the angle of incidence. The diffraction angle $\alpha_f = 1.149°$ was extracted from the detector data. The wavelength was set to $\lambda = 0.6888\text{Å}$, i.e. a photon energy $E_{ph} = 18keV$, for all experiments. For the whole fit, surface roughness and grain topography as well as exponential decay of electron beam inside the film are neglected. The fit parameters were the number of dead layers p and a scaling factor to normalize the intensities.
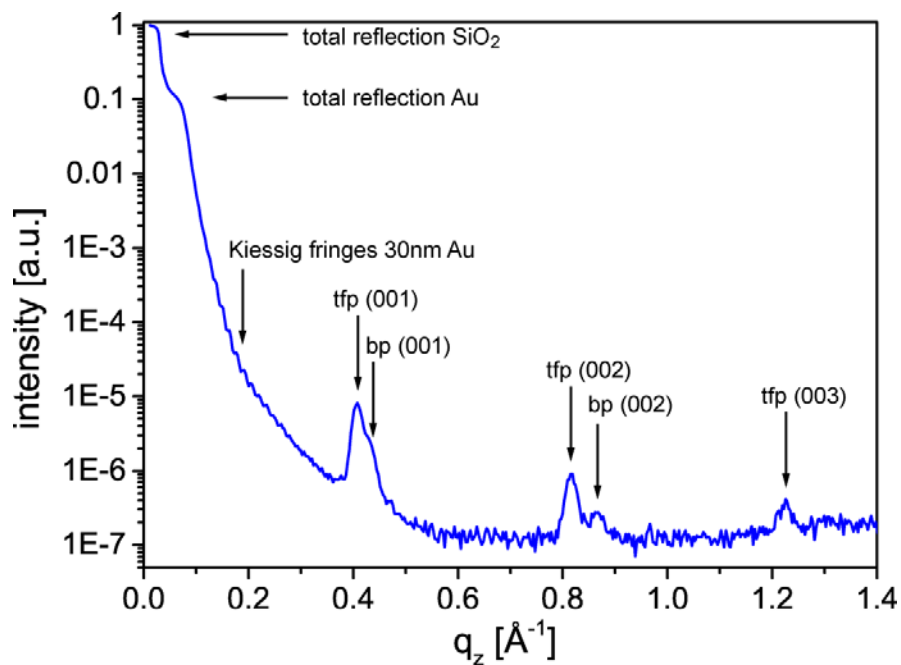
Figure S3: Crystallinity of transferred pentacene. In-house specular X-ray reflectometry measurement of crystalline pentacene after film transfer to an SiO_2 substrate with Au transistor structures. The dominant pentacene polymorph is thin film phase (tfp). The small bulk phase (bp) features are probably due to long storage. The overall small intensity of the Bragg features is due to the low signal to noise ratio (in-house compared to synchrotron) and the small flake size of ~ 2 mm.
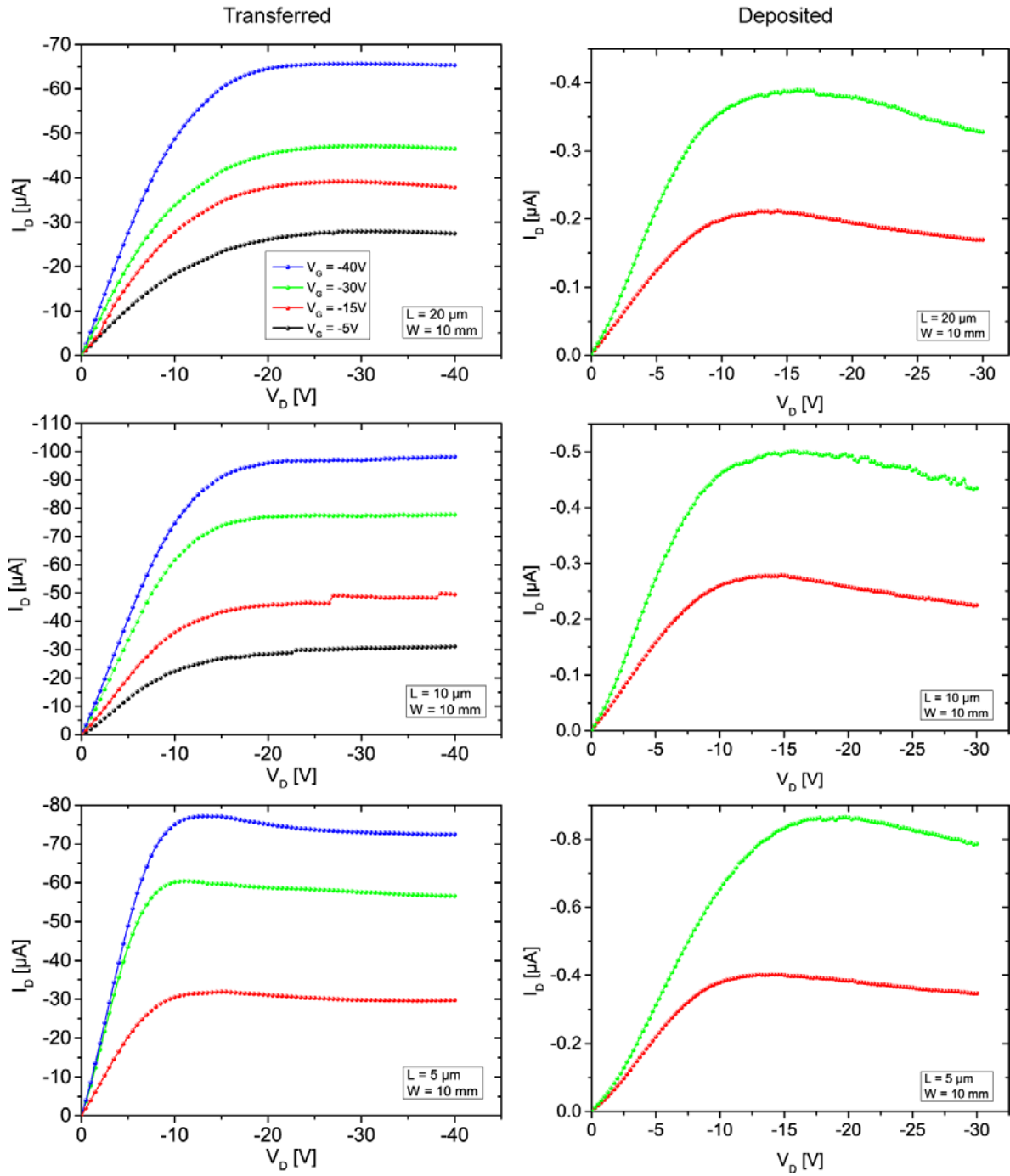
Figure S4: Output characteristics of transferred and deposited FETs for contact resistance evaluation. The source-drain sweeps were measured at room temperature under ambient conditions. From them, the necessary data is extracted to calculate the channel resistances, discussed in the main text.

B.6 SUPPLEMENTARY MATERIAL FOR SUB-MICRON PHASE CO-EXISTENCE IN SMALL-MOLECULE ORGANIC THIN FILMS RE-VEALED BY INFRARED NANO-IMAGING

Christian Westermeier, Adrian Cernescu, Sergiu Amarie, Clemens Liewald, Fritz Keilmann, and Bert Nickel
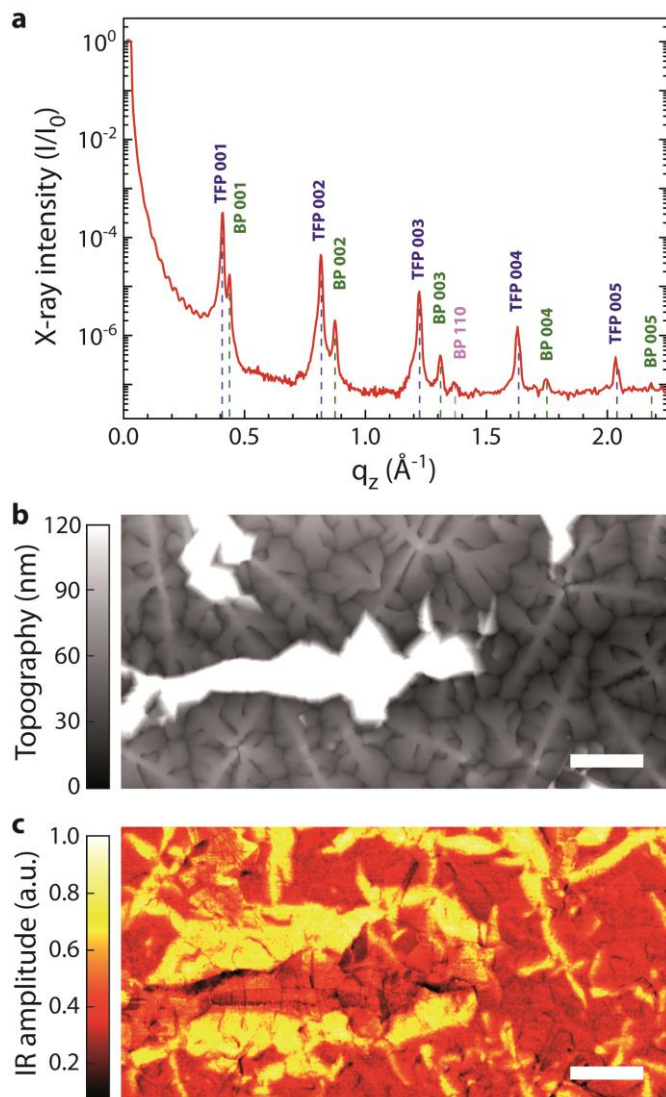
Supplementary Figure 1 | BP nucleation within pentacene TFP induced by aggregates of BP on top. (**a**) X-ray diffraction of a thick pentacene layer (average thickness 120 nm) deposited on SiO_2/ Si at a substrate temperature of 60 °C. The (110) Bragg peak indicated by the pink dashed line results from aggregates of horizontally orientated BP pentacene, that forms on top of the thin film in case of higher layer thicknesses[1-6]. (**b**) AFM topography and (**c**) simultaneously recorded s-SNOM amplitude image using IR illumination at 907.1 cm^{-1} close to resonance with BP pentacene. Scale bar, 2 µm. The sample exhibits the heterogeneous morphology (**b**) of an up to 300 nm thick pentacene film. Interestingly, the infrared image (**c**)

reveals a broad rim of BP pentacene (yellow colour) surrounding the elevated aggregates on top of the thin film. So far, aggregates forming on top of organic thin films in case of an increased layer thickness have usually not been considered to interfere with transport at the lower interface with the dielectric[7]. However, this BP distribution suggests that the aggregates on top act as growth seeds for BP nucleation and thus increase structural inhomogeneity throughout the thin film.
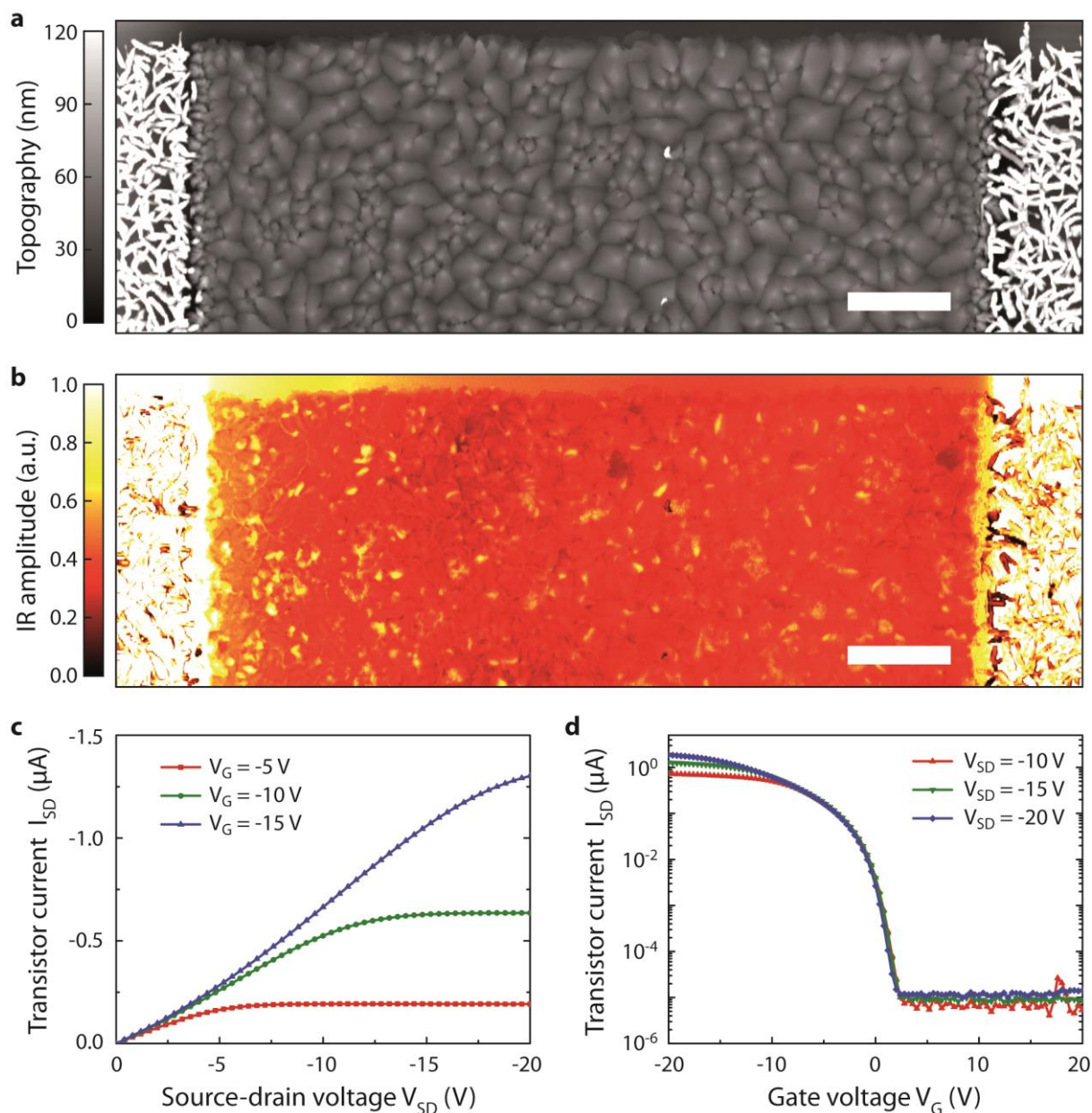
Supplementary Figure 2 | Mapping of phase coexistence within the channel of a pentacene TFT. (**a**) AFM topography and (**b**) simultaneously recorded s-SNOM amplitude image at 907.1 cm^{-1}. Scale bar, 3 μm. The measurement was conducted within the channel region of a working organic thin-film transistor (OTFT) in bottom-contact configuration. The pentacene film grown within the transistor channel shows homogeneous grain morphology (**a**) that is surrounded to the left and right by a filament-like growth on top of the gold electrodes. Indeed, the infrared imaging

technique reveals a distinct inhomogeneity inside the transistor channel (**b**), which mirrors the distribution of BP inclusions within the pentacene thin film.

(**c**) Conductance and (**d**) transconductance characteristics of the bottom-contact pentacene TFT used in this study.
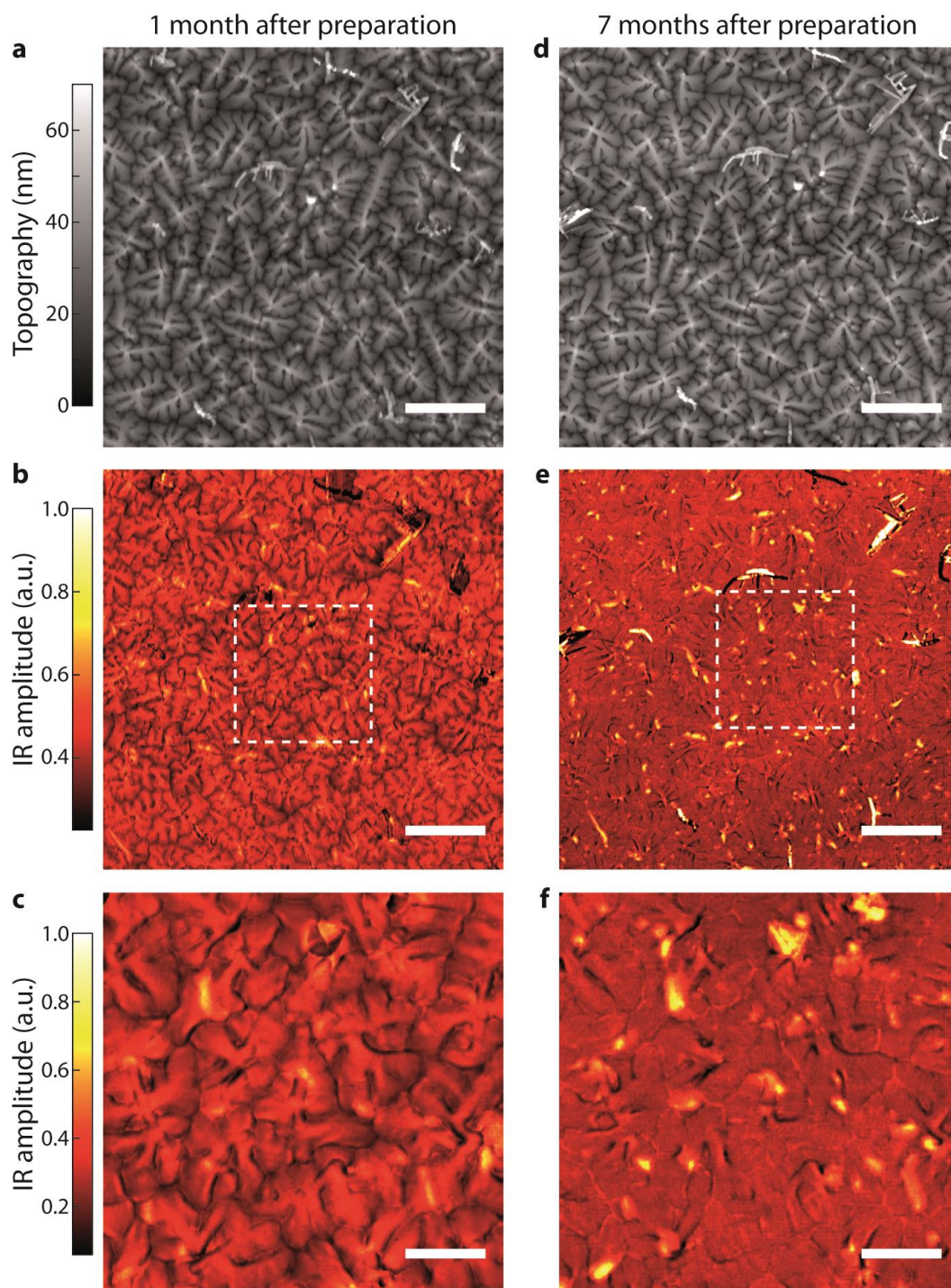
Supplementary Figure 3 | Monitoring recrystallization in pentacene film over time. A repeat of s-SNOM measurements (**a**,**b**,**c**) and (**d**,**e**,**f**) with a time interval of six months, showing the same section of a 60 nm thick pentacene film deposited on SiO$_2$/ Si at a substrate temperature of 30 °C. (**a**,**d**) AFM topography and (**b**,**c**,**e**,**f**) s-SNOM amplitude images using IR illumination at 907.1 cm^{-1}. The scale bars in

(**a**,**b**,**d**,**e**) denote 3 μm, and in (**c**,**f**) 1 μm. The dashed squares in (**b**,**e**) mark the enlarged section shown in (**c**,**f**). The first set of measurements shown on the left hand side (**a**,**b**,**c**) was carried out one month after fabrication of the pentacene film. These images can be compared with a repeated set of measurements on the right hand side (**d**,**e**,f) that was acquired after storing the samples at room temperature for another six months. Since the substrate temperature during pentacene deposition was only elevated up to 30 °C, i.e. slightly above room temperature, a relatively small number of BP inclusions are observed within the thin film after one month. The fraction of BP, however, clearly growths with storage time, as expected according to the continuous relaxation of mechanical stress within the film by conversion of TFP into BP pentacene.

Supplementary References

1. Bouchoms, I. P. M., Schoonveld, W. A., Vrijmoeth, J. & Klapwijk, T. M. Morphology identification of the thin film phases of vacuum evaporated pentacene on SiO_2 substrates. *Synth. Met.* **104,** 175-178 (1999).

2. Mattheus, C. C. *et al.* Polymorphism in pentacene. *Acta Cryst. Section C* **57,** 939-941 (2001); crystallographic data accessible at Crystallography Open Database (COD) ID: 2012157

3. Schiefer, S., Huth, M., Dobrinevski, A. & Nickel, B. Determination of the crystal structure of substrate-induced pentacene polymorphs in fiber structured thin films. *J. Am. Chem. Soc.* **129,** 10316-10317 (2007); crystallographic data accessible at Crystallography Open Database (COD) ID: 4109834

4. Downs, R. T. & Hall-Wallace, M. The American Mineralogist Crystal Structure Database. *Am. Mineral.* **88,** 247-250 (2003).

5. Gražulis, S. *et al.* Crystallography Open Database - an open-access collection of crystal structures. *J. Appl. Crystallogr.* **42,** 726-729 (2009).

6. Gražulis, S. *et al.* Crystallography Open Database (COD): an open-access collection of crystal structures and platform for world-wide collaboration. *Nucleic Acids Res.* **40,** D420-D427 (2012).

7. Drummy, L. F. & Martin, D. C. Thickness-driven orthorhombic to triclinic phase transformation in pentacene thin films. *Adv. Mater.* **17,** 903-907 (2005).

SAMPLE FABRICATION

In the following chapter, the fabrication steps of pentacene and Epi TFTs are described. The basic principle for the TFT fabrication is the formation of different functional layers on a cleaned substrate. The transistors in this work were produced with a bottom-gate and top-contacts.

C.1 PENTACENE TFTS

The pentacene TFTs were fabricated on cleaved pieces from a Si wafer, with thermally oxidized silicon dioxide (SiO_2) and cyclic olefin copolymer (COC) as the dielectric.

C.1.1 *Substrate preparation*

The SiO_2 layer needs to be electrically insulating and also $<100\,nm$ thin for measuring the local photocurrent properties of the transistor characteristics. Thicker SiO_2 leads to a non-local excitation of the pentacene layer via waveguide effects or surface plasmon polaritons [93–95]. High-quality substrates, tailored to these specific requirements, were produced by in-house thermal oxidation of bare Si wafers.

A arsenic doped wafer from *CrysTec*, with a polished front side and an etched back side, 5.08 cm (2 in) diameter, (100) crystal orientation, $<0.01\,\Omega\,cm$ specific resistance, and 275 μm thickness, was used as base material for the TFT fabrication. The wafer was thermally oxidized for 2.5 h so that a 82 nm thick dielectric layer of SiO_2 was formed on the front and back side. Then, individual wafer pieces of 7 mm x 6 mm were produced by scratching surface with a diamond
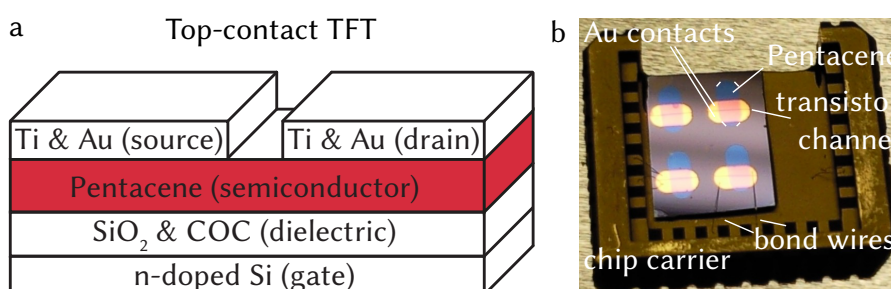
FIGURE 17: DESIGN OF TOP-CONTACT PENTACENE TRANSISTORS USED IN THIS WORK.
a) Schematic of the top-contact pentacene transistors. b) Overview of a sample with four transistor structures, glued into the chip carrier. The two transistors on the bottom are electrically connected to the chip carrier with bond wires.

scriber and successively cleaving the wafer. To remove the dielectric layer from the back side, the SiO_2 was etched with hydrofluoric acid (HF). During this step, it was ensured that the acid droplet did not reach the front side of the individual wafer pieces. Afterward, the HF was removed by rinsing with deionized water (DI water).

c.1.2   *Substrate cleaning*

The electrical characteristics of organic TFTs depend strongly on the interface quality between the dielectric and the semiconducting organic layer. Therefore, the samples were thoroughly cleaned with the following protocol:

- 10 min sonication in acetone

- 10 min sonication in isopropyl alcohol

- 2 x rinsing with DI water

In total, four glass beakers were used for this cleaning protocol. The beakers should be changed quickly between the cleaning steps, to avoid residua on the substrate surface.

After solvent cleaning, the samples were further treated with piranha cleaning. The piranha solution is prepared by mixing 3 parts of sulfuric acid (H_2SO_4) (98 %) with 1 part of H_2O_2 (30 %). This mixture exhibits a strong exothermic reaction to peroxymonosulfuric acid (H_2SO_5). The samples are put into the boiling piranha solution for 35 min and afterward 2 x rinsed with DI water.

The cleaned substrates were stored in DI water until the next fabrication steps. Immediately before the further processing, the samples were dried with dry nitrogen flow and cleaned with oxygen plasma for 3 min.

c.1.3   *COC deposition*

On the cleaned SiO_2 front side of the samples, a 5 nm thick layer of COC (*TOPAS 6013S-04*) was spin-coated from solution. The COC solution with a concentration of 0.25 wt% was prepared before, by dissolving COC in toluene. A clean COC solution can be used for several years if stored in glass bottles with glass caps. The solution was placed on the sample with a pipette, fully covering the SiO_2 surface, and rotated with a speed of 6000 rpm for 30 s. Afterward, the samples were thermally annealed on a hotplate at 100 °C for 2 min. The COC layer forms a smooth and hydrophobic surface and promotes a convenient crystal growth of pentacene [95, 96].

C.1.4   *Pentacene deposition*

After the COC deposition, the samples were immediately transferred into the pentacene evaporation chamber to avoid a contamination of the surface. The evaporation chamber was evacuated to a pressure of about 10^{-8} mbar and the home-made pentacene evaporation cell was heated with halogen lamps, until a deposition rate of about $0.1\,\text{Å}\,\text{s}^{-1}$ was obtained. After the target deposition rate was reached, the samples were exposed to the evaporated pentacene molecules and after about 50 min, a target pentacene thickness of 30 nm was reached. For optimal device performance, the purchased pentacene (*Sigma Aldrich triple-sublimed*) was purified with a gradual zone sublimation and afterward filled into the evaporation cells.

C.1.5   *Metal contact deposition*

To form the source/drain contacts on top of the pentacene layer, an optional layer of 2 nm Ti with $0.5\,\text{Å}\,\text{s}^{-1}$ deposition rate and a 30 nm thick Au layer with $1\,\text{Å}\,\text{s}^{-1}$ was deposited inside of an evaporation chamber. The dimensions of the source/drain contacts were defined by a shadow mask to form a transistor channel of 20 µm length and 1 mm width.

C.1.6   *Mounting inside chip carrier*

After the deposition of the source/drain contacts, the samples were mounted inside a chip carrier, fitting to the sample stage of the SPCM setup. Therefore, the back side of the silicon wafer was glued to the cavity of the chip carrier with conductive silver lacquer, to provide a mechanical adhesion together with an electrical connection to the gate contact. The source/drain contacts were electrically connected in a wedge bonder with aluminum (Al) bond wires. The Al wires were used because they can be bonded at a lower temperature compared to Au wires, preventing a melting of the COC layer and therefore giving a higher yield of successful bonds to the sample.

C.2   EPINDOLIDIONE TFTS

The Epi TFTs were fabricated on glass substrates after the protocol of Głowacki et al. [54]. A sputtered Al layer served as gate electrode, electrochemically oxidized aluminum oxide (Al_2O_3) and a TTC layer formed the dielectric.
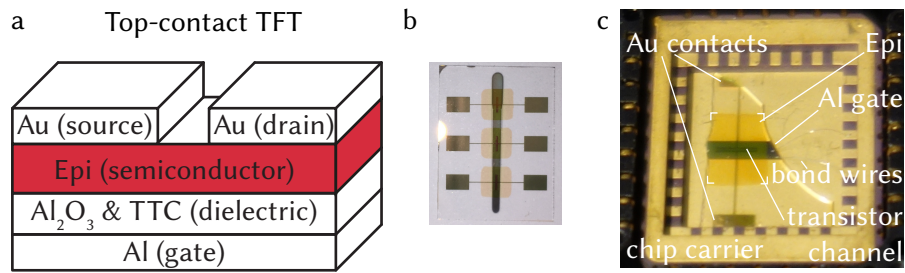
FIGURE 18: DESIGN OF TOP-CONTACT EPINDOLIDIONE TRANSISTORS USED IN THIS WORK.
a) Schematic of the top-contact Epi transistors. b) Overview of a sample with three
Epi transistors. c) Overview of a cleaved sample with one transistor, glued into the
chip carrier. The transistor is electrically connected to the chip carrier with bond
wires.

C.2.1 *Substrate cleaning*

Microscopical cover slips (*R. Langenbrinck, 01-1520/2*) with the dimensions 15 mm x 20 mm and 0.19 mm to 0.23 mm thickness were used as substrates for the produced Epi TFTs. The substrates were solvent cleaned, as described in appendix C.1.2, and stored in DI water until further fabrication.

- 10 min sonication in acetone

- 10 min sonication in isopropyl alcohol

- 2 x rinsing with DI water

C.2.2 *Aluminum gate deposition*

The bottom gate contact was deposited on the sample by radio frequency (RF) sputtering of 100 nm Al. For the sputtering process, argon plasma with a process pressure of about 2×10^{-2} mbar and an incident power of 30 W was used. The Al target was 10 min presputtered for cleaning purposes before the deposition process. Afterward, the Al film was formed with deposition rate of $9 \, nm \, s^{-1}$. The desired gate structure was defined by a shadow mask.

C.2.3 *Aluminum oxidation*

Electrochemical oxidation (anodization) of the sputtered Al layer was used to produce a 32 nm thin layer of Al_2O_3. Therefore, the substrate was fixed with a crocodile clip, which simultaneously provided an electrical contact to the Al layer. The sample was immersed into an acidic solution with the crocodile clip just above the surface of the solution. In addition, a grounded Pt wire was submerged into the solution as the counter electrode. The acidic solution with a potential of hydrogen (pH) value of 6 was obtained with the following recipe:

- 5 ml (10 %) of 0.1 M citric acid ($C_6H_8O_7$)

- 22 ml (44 %) of 0.1 M trisodium citrate ($Na_3C_6H_5O_7$)

- 23 ml (46 %) of DI water

Applying a positive voltage to the substrate, the Al is oxidized to Al_2O_3. The oxide is formed at the anode electrode and hydrogen is produced at the cathode electrode.

- $2\,Al + 3\,H_2O \longrightarrow Al_2O_3 + 6\,H^+ + 6\,e^-$

- $6\,H^+ + 6\,e^- \longrightarrow 3\,H_2$

With an oxidation rate of $1.6\,nm\,V^{-1}$, a 32 nm thick oxide layer was obtained by applying a voltage of 20 V. To avoid electrolysis, the voltage was increased slowly with $0.1\,V\,s^{-1}$ and kept constant at 20 V for 10 min. After the anodization process, the sample was rinsed with DI water and dried under nitrogen flow.

c.2.4 *TTC deposition*

The samples were mounted in an evaporation chamber for deposition of the oligoethylene TTC. The chamber was evacuated to a pressure of about $10^{-7}\,mbar$ and the home-made TTC evaporation cell was heated with halogen lamps [97]. When the desired deposition rate of $4\,\text{Å}\,s^{-1}$ was reached, a pressure rise to about $10^{-6}\,mbar$ was observed and the samples were exposed to the evaporated TTC molecules, forming a 34 nm thick layer. With a thinner TTC layer of 15 nm, lower operating gate voltages could have been reached. However, the fabricated samples with the thinner TTC layer showed an insufficient electrical isolation of the dielectric. After the TTC deposition, the samples were thermally annealed over night at 60 °C in an argon atmosphere.

c.2.5 *Epi deposition*

The active Epi layer was deposited in an evaporation chamber at a pressure around $10^{-7}\,mbar$. The home-made evaporation cell was heated with a halogen lamp to a temperature of 190 °C. At a deposition rate of $0.2\,\text{Å}\,s^{-1}$, the samples were exposed to the evaporated molecules, forming a layer of 90 nm thickness. The purified Epi molecules for this work were kindly provided by Eric D. Głowacki.

c.2.6 *Au contact deposition*

To form the source/drain contacts on top of the Epi layer, a 30 nm thick Au layer was deposited with a rate of $11\,\text{Å}\,s^{-1}$. This rather high

evaporation rate ensured a good electrical contact between the Au and the active Epi layer. The dimensions of the source/drain contacts were defined by a shadow mask to form a transistor channel of 50 μm length and 2 mm width.

C.2.7 *Mounting inside chip carrier*

To mount a fabricated transistor into a chip carrier, the samples were scratched with with a diamond scriber and carefully cleaved. The individual transistors were glued into the chip carrier, fitting to the sample stage of the SPCM setup. Therefore, the sample back side was glued into the cavity of the chip carrier with a two-component epoxy resin adhesive. The gate contact and the source/drain contacts were electrically connected in a wedge bonder with Al bond wires.

SETUP FOR PHOTOCURRENT MICROSCOPY

The following chapter describes the home-made setup for scanning photocurrent microscopy (SPCM). In this setup, light of visible wavelength is focused on an electrically connected TFT, and the response of the connected device on illumination is analyzed. The position of the device is controlled by a stack of three piezo motors (*AN-Px/z101/RES, ANC350* from *attocube*) and the position of the sample with respect to the laser beam is controlled with a charge-coupled device (CCD) camera (*sensicam qe* from *PCO*). This camera can also be used to record the luminescence of the sample during the SPCM maps. In addition, the luminescence can analyzed with a spectrometer. The reflected light from the sample is coupled back into the optical fiber and, after the fiber beam splitter, analyzed by a photodiode (*PDA36A* from *Thorlabs*). Our photocurrent setup spans a whole optical table, but these functionalities can also be implemented in a more compact microscope [98].

D.1 LIGHT SOURCES

For the illumination, different lasers are available. The laser should be chosen according to desired wavelength λ, matching the absorption of the investigated semiconductor. The laser beam is coupled into a single-mode optical fiber with a fiber beamsplitter, one part of the laser beam was used to measure the laser intensity. The other part of the fiber was guided through a polarization controller and was collimated by a lens into an objective.

Helium-Neon laser

The wavelength λ of the used line-tunable helium-neon (HeNe) gas laser (*30603* from *Research Electro-Optics*) can be selected from the available laser lines at 633 nm, 612 nm, 604 nm, 594 nm, and 543 nm. The light of this continuous-wave laser can be modulated by a mechanical chopper with frequencies up to 10 kHz.

iPulse diode laser

A diode laser (*iPulse* from *TOPTICA Photonics*) was added to the SPCM setup in course of this thesis. The laser emits at 488 nm wavelength and is remote controlled by a computer via a serial interface. It can be operate in continuous wave or pulsed mode, with pulse fre-

quencies up to 1 MHz. As this laser does not provide a reference output for synchronizing the illumination with the measurements, one part of the outcoming laser beam was used for generating the reference signal. For this purpose, the laser intensity was measured with a high speed photoreceiver (*Model 2107* from *New Focus*). The output voltage of this photoreceiver was amplified (*HVA-10M-60-B* from *FEMTO Messtechnik*) to generate transistor-transistor logic (TTL) compatible voltage levels.

Laser diode system

Laser diodes of different wavelengths can used with a laser system from *Newport*. This laser system consists of a laser diode mount (*Model 710*), which is connected to a pulsed laser diode driver (*LDP-3811*) and to a temperature controller (*Model 6100*). The laser diodes can be operated in continuous wave or pulsed mode, with pulse frequencies up to 1 MHz.

D.2   ELECTRICAL WIRING

To measure the response of the fabricated devices on illumination, the samples were electrically connected. One of the source/drain contacts was connected to a transimpedance amplifier (*DHPCA-100* from *FEMTO Messtechnik*), the other source/drain contact and the gate contact were connected to a voltage sources (*7651* from *Yokogawa*). The output voltage of the transimpedance amplifier was then analyzed by a digital multimeter (*34411A* from *Agilent Technologies*), a Lock-in amplifier (*Model 7280* from *Signal Recovery*), or a boxcar averager (*SR200 series* from *Stanford Research Systems*).

D.3   MEASUREMENT PROCEDURE

The response of an organic FET on illumination can be analyzed in the time domain and frequency domain. Both measurements require a proper reference signal to trigger the measurement or to lock to the pulse frequency.

Time domain measurements

Time domain measurements can be realized with an oscilloscope, a digital multimeter, or a boxcar averager. The used digital multimeter *34411A* from *Agilent Technologies* provided measurements with a much lower noise level, compared to oscilloscopes. A signal trace with 8000 samples and 20 µs integration time per sample can be acquired with the following settings:

```
 1  TRIG:SOUR EXT
    TRIG:COUN 1
    TRIG:DEL:AUTO 0
    TRIG:DEL 0
    TRIG:SLOP POS
 6
    SAMP:SOUR TIM
    SAMP:COUNT 8000
    SAMP:COUN:PRET 0


11  VOLT:DC:RANG:AUTO OFF
    VOLT:DC:RANG 0.1
    VOLT:DC:NPLC MIN
    VOLT:DC:NULL:STAT OFF
    VOLT:DC:ZERO:AUTO 0
16  SAMP:TIM MIN
```

Frequency domain measurements

Frequency domain measurements can be realized with a lock-in amplifier, analyzing the signal at a given reference frequency f. Neglecting all other frequencies, the lock-in amplifier can extract a clean signal from a noisy background. The integration time should be sufficiently large so that the amplifier can integrate over several periods of the signal. Two-phase lock-in amplifiers contain two detectors, producing orthogonal output signals X and Y. From these signals, the lock-in amplitude and phase, equivalent to the photocurrent amplitude $|\mathbf{I_{photo}}|$ and photocurrent phase $\Theta_{\texttt{photo}}$, can be calculated.

$$|\mathbf{I_{photo}}| = \sqrt{X^2 + Y^2} \qquad \Theta_{\texttt{photo}} = \texttt{arctan}(X/Y)$$

Amplitude and phase form the complex photocurrent $\mathbf{I_{photo}}$.

More details of this home-made SPCM setup can be found in my master's thesis [94], and in the master's theses of Daniel Reiser [83] and Simone Strohmair [85], which were conducted in course of this work.

BIBLIOGRAPHY

[1] M. Pope and C. Swenberg. *Electronic processes in organic crystals and polymers*. Oxford University Press, 1999. ISBN: 9780195129632.

[2] M. Schwoerer and H. C. Wolf. *Organic molecular solids*. John Wiley & Sons, 2007. ISBN: 3527405402.

[3] G. Schweicher, Y. Olivier, V. Lemaur, and Y. H. Geerts. "What Currently Limits Charge Carrier Mobility in Crystals of Molecular Semiconductors?"
In: *Israel Journal of Chemistry* 54.5-6 (2014), pp. 595–620. DOI: 10.1002/ijch.201400047.

[4] S. E. Root, S. Savagatrup, A. D. Printz, D. Rodriquez, and D. J. Lipomi. "Mechanical Properties of Organic Semiconductors for Stretchable, Highly Flexible, and Mechanically Robust Electronics."
In: *Chemical Reviews* 117.9 (2017), pp. 6467–6499. DOI: 10.1021/acs.chemrev.7b00003.

[5] L. L. Wang, D. Chen, K. Jiang, and G. Z. Shen. "New insights and perspectives into biological materials for flexible electronics."
In: *Chemical Society Reviews* 46.22 (2017), pp. 6764–6815. DOI: 10.1039/c7cs00278e.

[6] A. M. Pappa, O. Parlak, G. Scheiblin, P. Mailley, A. Salleo, and R. M. Owens. "Organic Electronics for Point-of-Care Metabolite Monitoring."
In: *Trends in Biotechnology* 36.1 (2018), pp. 45–59. DOI: 10.1016/j.tibtech.2017.10.022.

[7] M. Irimia-Vladu. ""Green" electronics: biodegradable and biocompatible materials and devices for sustainable future."
In: *Chemical Society Reviews* 43.2 (2014), pp. 588–610. DOI: 10.1039/c3cs60235d.

[8] O. Ostroverkhova. "Organic Optoelectronic Materials: Mechanisms and Applications."
In: *Chemical Reviews* 116.22 (2016), pp. 13279–13412. DOI: 10.1021/acs.chemrev.6b00127.

[9] S. Fukuzumi, Y. M. Lee, and W. Nam. "Artificial Photosynthesis for Production of ATP, NAD(P)H, and Hydrogen Peroxide."
In: *Chemphotochem* 2.3 (2018), pp. 121–135. DOI: 10.1002/cptc.201700146.

[10]   S. S. Lee and Y.-L. Loo. "Structural Complexities in the Active Layers of Organic Electronics."
In: *Annual Review of Chemical and Biomolecular Engineering* 1.1 (2010), pp. 59–78. DOI: 10.1146/annurev-chembioeng-073009-100851.

[11]   S. A. Burke, J. M. Topple, and P. Grutter. "Molecular dewetting on insulators."
In: *Journal of Physics-Condensed Matter* 21.42 (2009), p. 16. DOI: 10.1088/0953-8984/21/42/423101.

[12]   H. Chung and Y. Diao. "Polymorphism as an emerging design strategy for high performance organic electronics."
In: *Journal of Materials Chemistry C* 4.18 (2016), pp. 3915–3933. DOI: 10.1039/c5tc04390e.

[13]   I. Salzmann and G. Heimel. "Toward a comprehensive understanding of molecular doping organic semiconductors (review)."
In: *Journal of Electron Spectroscopy and Related Phenomena* 204 (2015), pp. 208–222. DOI: 10.1016/j.elspec.2015.05.001.

[14]   I. Salzmann, G. Heimel, M. Oehzelt, S. Winkler, and N. Koch. "Molecular Electrical Doping of Organic Semiconductors: Fundamental Mechanisms and Emerging Dopant Design Rules."
In: *Accounts of Chemical Research* 49.3 (2016), pp. 370–378. DOI: 10.1021/acs.accounts.5b00438.

[15]   A. C. Dürr, F. Schreiber, M. Kelsch, H. D. Carstanjen, and H. Dosch. "Morphology and thermal stability of metal contacts on crystalline organic thin films."
In: *Advanced Materials* 14.13-14 (2002), pp. 961–+. DOI: 10.1002/1521-4095(20020705)14:13/14<961::AID-ADMA961>3.0.CO;2-X.

[16]   A. Salleo, R. J. Kline, D. M. DeLongchamp, and M. L. Chabinyc. "Microstructural Characterization and Charge Transport in Thin Films of Conjugated Polymers."
In: *Advanced Materials* 22.34 (2010), pp. 3812–3838. DOI: 10.1002/adma.200903712.

[17]   C. R. McNeill. "Imaging the domain structure of organic semiconductor films."
In: *Journal of Polymer Science Part B: Polymer Physics* 49.13 (2011), pp. 909–919. DOI: 10.1002/polb.22270.

[18]   J. B. Gilchrist, S. Heutz, and D. W. McComb. "Revealing structure and electronic properties at organic interfaces using TEM."
In: *Current Opinion in Solid State & Materials Science* 21.2 (2017), pp. 68–76. DOI: 10.1016/j.cossms.2017.01.002.

[19] J. Rivnay, S. C. B. Mannsfeld, C. E. Miller, A. Salleo, and M. F. Toney. "Quantitative Determination of Organic Semiconductor Microstructure from the Molecular to Device Scale."
In: *Chemical Reviews* 112.10 (2012), pp. 5488–5519. DOI: 10.1021/cr3001109.

[20] V. Palermo, M. Palma, and P. Samori. "Electronic characterization of organic thin films by Kelvin probe force microscopy."
In: *Advanced Materials* 18.2 (2006), pp. 145–164. DOI: 10.1002/adma.200501394.

[21] F. Keilmann and R. Hillenbrand. "Near-field nanoscopy by elastic light scattering from a tip." In: *Nano-Optics and Near-Field Optical Microscopy*. Ed. by A. Z. Richards and D. Artech House, 2009. Chap. Near-field nanoscopy by elastic light scattering from a tip, pp. 235–265. ISBN: 978-1-59693-283-8.

[22] C. Westermeier, A. Cernescu, S. Amarie, C. Liewald, F. Keilmann, and B. Nickel. "Sub-micron phase coexistence in small-molecule organic thin films revealed by infrared nano-imaging."
In: *Nature Communications* 5 (2014), p. 4101. DOI: doi:10.1038/ncomms5101.

[23] R. Graham and D. Yu. "Scanning photocurrent microscopy in semiconductor nanostructures."
In: *Modern Physics Letters B* 27.25 (2013), p. 1330018. DOI: doi:10.1142/S0217984913300184.

[24] A. Masurkar and I. Kymissis. "Photocurrent measurements of pentacene-based devices."
In: *Applied Physics Reviews* 2.3 (2015), p. 031101. DOI: doi:http://dx.doi.org/10.1063/1.4926767.

[25] M. Fiebig, C. Erlen, M. Göllner, P. Lugli, and B. Nickel. "Spatially resolved photoresponse measurements on pentacene thin-film transistors."
In: *Applied Physics a-Materials Science & Processing* 95.1 (2009), pp. 113–117. DOI: 10.1007/s00339-008-5009-x.

[26] A. W. Tsen, F. Cicoira, G. G. Malliaras, and J. Park. "Photoelectrical imaging and characterization of point contacts in pentacene thin-film transistors."
In: *Applied Physics Letters* 97.2 (2010), p. 023308. DOI: 10.1063/1.3462914.

[27] Z. Jia, M. Shi, and I. Kymissis. "Study of Local Mobility in Pentacene Field-Effect Transistors Using Spatially Resolved Photocurrent Measurement."
In: *Ieee Electron Device Letters* 31.7 (2010), pp. 761–763. DOI: 10.1109/led.2010.2049559.

[28] C. Westermeier, M. Fiebig, and B. Nickel. "Mapping of trap densities and hotspots in pentacene thin-film transistors by frequency-resolved scanning photoresponse microscopy."
In: *Advanced Materials* 25.40 (2013), pp. 5719–24. DOI: 10.1002/adma.201300958.

[29] A. Giannopoulou and P. Kounavis. "Visualization of channel formation of organic field-effect transistors by scanning photocurrent microscopy."
In: *Organic Electronics* 58 (2018), pp. 167–177. DOI: 10.1016/j.orgel.2018.04.009.

[30] M. Iwamoto, T. Manaka, and D. Taguchi. "Probing and modeling of carrier motion in organic devices by electric-field-induced optical second-harmonic generation."
In: *Japanese Journal of Applied Physics* 53.10 (2014). DOI: 10.7567/jjap.53.100101.

[31] T. Manaka and M. Iwamoto. "Optical second-harmonic generation measurement for probing organic device operation."
In: *Light-Science & Applications* 5 (2016). DOI: 10.1038/lsa.2016.40.

[32] C. Liewald, S. J. Noever, S. Fischer, J. Roemer, T. U. Schülli, and B. Nickel. "Microdiffraction imaging—a suitable tool to characterize organic electronic devices."
In: *AIMS Materials Science* 2.4 (2015), pp. 369–378. DOI: 10.3934/matersci.2015.4.369.

[33] C. Liewald, S. Mastel, J. Hesler, A. J. Huber, R. Hillenbrand, and F. Keilmann. "All-electronic terahertz nanoscopy."
In: *Optica* 5.2 (2018), pp. 159–163. DOI: 10.1364/OPTICA.5.000159.

[34] C. Liewald, D. Reiser, C. Westermeier, and B. Nickel. "Photocurrent microscopy of contact resistance and charge carrier traps in organic field-effect transistors."
In: *Applied Physics Letters* 109.5 (2016), p. 053301. DOI: 10.1063/1.4960159.

[35] C. Liewald, S. Strohmair, H. Hecht, and B. Nickel. "Scanning photocurrent microscopy of electrons and holes in the pigment semiconductor epindolidione."
In: *Organic Electronics* 60 (2018), pp. 51–56. DOI: 10.1016/j.orgel.2018.05.032.

[36] S. M. Sze and K. K. Ng. *Physics of semiconductor devices*. John wiley & sons, 2006. ISBN: 0470068302.

[37] E. G. Bittle, J. I. Basham, T. N. Jackson, O. D. Jurchescu, and D. J. Gundlach. "Mobility overestimation due to gated contacts in organic field-effect transistors."

In: *Nature communications* 7 (2016), p. 10908. DOI: 10 . 1038 / ncomms10908.

[38] E. D. Głowacki, M. Irimia-Vladu, S. Bauer, and N. S. Sariciftci. "Hydrogen-bonds in molecular solids - from biological systems to organic electronics."
In: *Journal of Materials Chemistry B* 1.31 (2013), pp. 3742–3753. DOI: 10.1039/c3tb20193g.

[39] M. Gsänger, D. Bialas, L. Huang, M. Stolte, and F. Würthner. "Organic Semiconductors based on Dyes and Color Pigments."
In: *Advanced Materials* 28.19 (2016), pp. 3615–3645. DOI: 10.1002/adma.201505440.

[40] M. A. Romero, M. Martinez, and P. R. Herczfeld. "An analytical model for the photodetection mechanisms in high-electron mobility transistors."
In: *IEEE transactions on microwave theory and techniques* 44.12 (1996), pp. 2279–2287. DOI: 10.1109/22.556467.

[41] H.-S. Kang, C.-S. Choi, W.-Y. Choi, D.-H. Kim, and K.-S. Seo. "Characterization of phototransistor internal gain in metamorphic high-electron-mobility transistors."
In: *Applied Physics Letters* 84.19 (2004), pp. 3780–3782. DOI: 10 . 1063/1.1739278.

[42] K.-J. Baeg, M. Binda, D. Natali, M. Caironi, and Y.-Y. Noh. "Organic Light Detectors: Photodiodes and Phototransistors."
In: *Advanced Materials* 25.31 (2013), pp. 4267–4295. ISSN: 1521-4095. DOI: 10.1002/adma.201204979.

[43] L. Caranzi, G. Pace, M. Sassi, L. Beverina, and M. Caironi. "Transparent and Highly Responsive Phototransistors Based on a Solution-Processed, Nanometers-Thick Active Layer, Embedding a High-Mobility Electron-Transporting Polymer and a Hole-Trapping Molecule."
In: *ACS Applied Materials & Interfaces* 9.34 (2017), pp. 28785–28794. DOI: 10.1021/acsami.7b05259.

[44] T. W. Kelley, P. F. Baude, C. Gerlach, D. E. Ender, D. Muyres, M. A. Haase, D. E. Vogel, and S. D. Theiss. "Recent progress in organic electronics: Materials, devices, and processes."
In: *Chemistry of Materials* 16.23 (2004), pp. 4413–4422. DOI: 10 . 1021/cm049614j.

[45] N. A. Minder, S. Ono, Z. Chen, A. Facchetti, and A. F. Morpurgo. "Band-Like Electron Transport in Organic Transistors and Implication of the Molecular Structure for Performance Optimization."
In: *Advanced Materials* 24.4 (2012), pp. 503–508. DOI: 10.1002/adma.201103960.

[46] C. C. Mattheus, A. B. Dros, J. Baas, A. Meetsma, J. L. d. Boer, and T. T. M. Palstra. "Polymorphism in pentacene."
In: *Acta Crystallographica Section C* 57.8 (2001), pp. 939–941. DOI: doi:10.1107/S010827010100703X.

[47] R. B. Campbell, J. Trotter, and J. M. Robertson. "Crystal and molecular structure of pentacene."
In: *Acta Crystallographica* 14.7 (1961), pp. 705–711. DOI: 10.1107/s0365110x61002163.

[48] R. B. Campbell, J. Trotter, and Monteath.J. "Crystal structure of hexacene, and a revision of crystallographic data for tetracene and pentacene."
In: *Acta Crystallographica* 15.3 (1962), pp. 289–290. DOI: 10.1107/s0365110x62000699.

[49] S. Schiefer, M. Huth, A. Dobrinevski, and B. Nickel. "Determination of the crystal structure of substrate-induced pentacene polymorphs in fiber structured thin films."
In: *Journal of the American Chemical Society* 129.34 (2007), pp. 10316–+. DOI: 10.1021/ja0730516.

[50] C. Ambrosch-Draxl, D. Nabok, P. Puschnig, and C. Meisenbichler. "The role of polymorphism in organic thin films: oligoacenes investigated from first principles."
In: *New Journal of Physics* 11.12 (2009), p. 125010. DOI: 10.1088/1367-2630/11/12/125010.

[51] C. F. Macrae, I. J. Bruno, J. A. Chisholm, P. R. Edgington, P. McCabe, E. Pidcock, L. Rodriguez-Monge, R. Taylor, J. v. Streek, and P. A. Wood. "Mercury CSD 2.0–new features for the visualization and investigation of crystal structures."
In: *Journal of Applied Crystallography* 41.2 (2008), pp. 466–470. DOI: 10.1107/S0021889807067908.

[52] H. Marciniak, M. Fiebig, M. Huth, S. Schiefer, B. Nickel, F. Selmaier, and S. Lochbrunner. "Ultrafast Exciton Relaxation in Microcrystalline Pentacene Films."
In: *Physical Review Letters* 99.17 (2007), p. 176402. DOI: 10.1103/PhysRevLett.99.176402.

[53] M. W. B. Wilson, A. Rao, B. Ehrler, and R. H. Friend. "Singlet Exciton Fission in Polycrystalline Pentacene: From Photophysics toward Devices."
In: *Accounts of Chemical Research* 46.6 (2013), pp. 1330–1338. DOI: 10.1021/ar300345h.

[54] E. D. Głowacki, M. Irimia-Vladu, M. Kaltenbrunner, J. Gasiorowski, M. S. White, U. Monkowius, G. Romanazzi, G. P. Suranna, P. Mastrorilli, T. Sekitani, S. Bauer, T. Someya, L. Torsi, and N. S. Sariciftci. "Hydrogen-Bonded Semiconducting Pigments for Air-Stable Field-Effect Transistors."

In: *Advanced Materials* 25.11 (2013), pp. 1563–1569. DOI: 10.1002/adma.201204039.

[55]   E. D. Głowacki, G. Romanazzi, C. Yumusak, H. Coskun, U. Monkowius, G. Voss, M. Burian, R. T. Lechner, N. Demitri, G. J. Redhammer, N. Sünger, G. P. Suranna, and S. Sariciftci. "Epindolidiones—Versatile and Stable Hydrogen-Bonded Pigments for Organic Field-Effect Transistors and Light-Emitting Diodes." In: *Advanced Functional Materials* 25.5 (2015), pp. 776–787. DOI: 10.1002/adfm.201402539.

[56]   A. O. F. Jones, C. Röthel, R. Lassnig, O. N. Bedoya-Martínez, P. Christian, I. Salzmann, B. Kunert, A. Winkler, and R. Resel. "Solution of an elusive pigment crystal structure from a thin film: a combined X-ray diffraction and computational study." In: *CrystEngComm* 19.14 (2017), pp. 1902–1911. DOI: 10.1039/C7CE00227K.

[57]   M. Jakešová, D. H. Apaydin, M. Sytnyk, K. Oppelt, W. Heiss, N. S. Sariciftci, and E. D. Głowacki. "Hydrogen-Bonded Organic Semiconductors as Stable Photoelectrocatalysts for Efficient Hydrogen Peroxide Photosynthesis." In: *Advanced Functional Materials* 26.29 (2016), pp. 5248–5254. DOI: 10.1002/adfm.201601946.

[58]   E. D. Glowacki, R. R. Tangorra, H. Coskun, D. Farka, A. Operamolla, Y. Kanbur, F. Milano, L. Giotta, G. M. Farinola, and N. S. Sariciftci. "Bioconjugation of hydrogen-bonded organic semiconductors with functional proteins." In: *Journal of Materials Chemistry C* 3.25 (2015), pp. 6554–6564. DOI: 10.1039/C5TC00556F.

[59]   J. Als-Nielsen and D. McMorrow. *Elements of modern X-ray physics*. John Wiley & Sons, 2011. ISBN: 1119970156.

[60]   G. A. Chahine, M. I. Richard, R. A. Homs-Regojo, T. N. Tran-Caliste, D. Carbone, V. L. R. Jaques, R. Grifone, P. Boesecke, J. Katzer, I. Costina, H. Djazouli, T. Schroeder, and T. U. Schülli. "Imaging of strain and lattice orientation by quick scanning X-ray microscopy combined with three-dimensional reciprocal space mapping." In: *Journal of Applied Crystallography* 47 (2014), pp. 762–769. DOI: 10.1107/s1600576714004506.

[61]   Y. Nakayama, Y. Mizuno, T. Hosokai, T. Koganezawa, R. Tsuruta, A. Hinderhofer, A. Gerlach, K. Broch, V. Belova, H. Frank, M. Yamamoto, J. Niederhausen, H. Glowatzki, J. P. Rabe, N. Koch, H. Ishii, F. Schreiber, and N. Ueno. "Epitaxial Growth of an Organic p-n Heterojunction: C-60 on Single-Crystal Pentacene." In: *Acs Applied Materials & Interfaces* 8.21 (2016), pp. 13499–13505. DOI: 10.1021/acsami.6b02744.

[62]   D. W. Breiby, O. Bunk, J. W. Andreasen, H. T. Lemke, and M. M. Nielsen. "Simulating X-ray diffraction of textured films."
In: *Journal of Applied Crystallography* 41 (2008), pp. 262–271. DOI: 10.1107/s0021889808001064.

[63]   C. Hub, M. Burkhardt, M. Halik, G. Tzvetkov, and R. Fink. "In situ STXM investigations of pentacene-based OFETs during operation."
In: *Journal of Materials Chemistry* 20.23 (2010), pp. 4884–4887. DOI: 10.1039/c0jm00423e.

[64]   B. Bräuer, R. Kukreja, A. Virkar, H. B. Akkerman, A. Fognini, T. Tyliszczak, and Z. N. Bao. "Carrier mobility in pentacene as a function of grain size and orientation derived from scanning transmission X-ray microscopy."
In: *Organic Electronics* 12.11 (2011), pp. 1936–1942. DOI: 10.1016/j.orgel.2011.08.007.

[65]   X. Du. "Spectromicroscopic Insights into the Morphology and Interfaces of Operational Organic Electronic Devices." Dissertation. Friedrich-Alexander-Universität Erlangen-Nürnberg, 2017.

[66]   A. Cvitkovic, N. Ocelic, and R. Hillenbrand. "Analytical model for quantitative prediction of material contrasts inscattering-type near-field optical microscopy."
In: *Optics Express* 15.14 (2007), pp. 8550–8565. DOI: 10.1364/OE.15.008550.

[67]   F. Keilmann, A. J. Huber, and R. Hillenbrand. "Nanoscale Conductivity Contrast by Scattering-Type Near-Field Optical Microscopy in the Visible, Infrared and THz Domains."
In: *Journal of Infrared Millimeter and Terahertz Waves* 30.12 (2009), pp. 1255–1268. DOI: 10.1007/s10762-009-9525-3.

[68]   M. Liu, A. J. Sternbach, and D. Basov. "Nanoscale electrodynamics of strongly correlated quantum materials."
In: *Reports on Progress in Physics* 80.1 (2016), p. 014501. DOI: 10.1088/0034-4885/80/1/014501.

[69]   T. Taimre, M. Nikolić, K. Bertling, Y. L. Lim, T. Bosch, and A. D. Rakić. "Laser feedback interferometry: a tutorial on the self-mixing effect for coherent sensing."
In: *Advances in Optics and Photonics* 7.3 (2015), pp. 570–631. DOI: 10.1364/AOP.7.000570.

[70]   P. Dean, O. Mitrofanov, J. Keeley, I. Kundu, L. Li, E. H. Linfield, and A. Giles Davies. "Apertureless near-field terahertz imaging using the self-mixing effect in a quantum cascade laser."
In: *Applied Physics Letters* 108.9 (2016), p. 091113. DOI: 10.1063/1.4943088.

[71] G. Masetti, M. Severi, and S. Solmi. "Modeling of carrier mobility against carrier concentration in arsenic-, phosphorus-, and boron-doped silicon."
In: *IEEE Trans. Electron Devices* 30 (1983), pp. 764–769. DOI: 10.1109/T-ED.1983.21207.

[72] C. Tanase, E. J. Meijer, P. W. M. Blom, and D. M. de Leeuw. "Unification of the Hole Transport in Polymeric Field-Effect Transistors and Light-Emitting Diodes."
In: *Physical Review Letters* 91.21 (2003), p. 216601. DOI: 10.1103/PhysRevLett.91.216601.

[73] W. F. Pasveer, J. Cottaar, C. Tanase, R. Coehoorn, P. A. Bobbert, P. W. M. Blom, D. M. de Leeuw, and M. A. J. Michels. "Unified Description of Charge-Carrier Mobilities in Disordered Semiconducting Polymers."
In: *Physical Review Letters* 94.20 (2005), p. 206601. DOI: 10.1103/PhysRevLett.94.206601.

[74] D. M. Riffe. "Temperature dependence of silicon carrier effective masses with application to femtosecond reflectivity measurements."
In: *Journal of the Optical Society of America B* 19.5 (2002), pp. 1092–1100. DOI: 10.1364/JOSAB.19.001092.

[75] F. A. Hegmann, R. R. Tykwinski, K. P. H. Lui, J. E. Bullock, and J. E. Anthony. "Picosecond Transient Photoconductivity in Functionalized Pentacene Molecular Crystals Probed by Terahertz Pulse Spectroscopy."
In: *Physical Review Letters* 89.22 (2002), p. 227403. DOI: 10.1103/PhysRevLett.89.227403.

[76] E. Hendry, J. M. Schins, L. P. Candeias, L. D. A. Siebbeles, and M. Bonn. "Efficiency of Exciton and Charge Carrier Photogeneration in a Semiconducting Polymer."
In: *Physical Review Letters* 92.19 (2004), p. 196601. DOI: 10.1103/PhysRevLett.92.196601.

[77] O. Ostroverkhova, D. G. Cooke, S. Shcherbyna, R. F. Egerton, F. A. Hegmann, R. R. Tykwinski, and J. E. Anthony. "Bandlike transport in pentacene and functionalized pentacene thin films revealed by subpicosecond transient photoconductivity measurements."
In: *Physical Review B* 71.3 (2005), p. 035204. DOI: 10.1103/PhysRevB.71.035204.

[78] S. G. Engelbrecht, M. Prinz, T. R. Arend, and R. Kersting. "Terahertz spectroscopy on hole transport in pentacene thin films."
In: *Applied Physics Letters* 105.1 (2014). DOI: 10.1063/1.4887237.

[79]   T. R. Arend, A. Wimmer, G. Schweicher, B. Chattopadhyay, Y. H. Geerts, and R. Kersting. "Band Transport and Trapping in Didodecyl 1 benzothieno 3,2-b 1 benzothiophene Probed by Terahertz Spectroscopy."
In: *Journal of Physical Chemistry Letters* 8.21 (2017), pp. 5444–5449. DOI: 10.1021/acs.jpclett.7b02304.

[80]   C. H. Kim, O. Yaghmazadeh, D. Tondelier, Y. B. Jeong, Y. Bonnassieux, and G. Horowitz. "Capacitive behavior of pentacene-based diodes: Quasistatic dielectric constant and dielectric strength."
In: *Journal of Applied Physics* 109.8 (2011), p. 083710. DOI: 10.1063/1.3574661.

[81]   A. A. Govyadinov, S. Mastel, F. Golmar, A. Chuvilin, R. S. Carney, and R. Hillenbrand. "Recovery of Permittivity and Depth from Near-Field Data as a Step toward Infrared Nanotomography."
In: *Acs Nano* 8.7 (2014), pp. 6911–6921. DOI: 10.1021/nn5016314.

[82]   H. Méndez, G. Heimel, A. Opitz, K. Sauer, P. Barkowski, M. Oehzelt, J. Soeda, T. Okamoto, J. Takeya, J. Arlin, J. Balandier, Y. Geerts, N. Koch, and I. Salzmann. "Doping of Organic Semiconductors: Impact of Dopant Strength and Electronic Coupling."
In: *Angewandte Chemie International Edition* 52.30 (2013), pp. 7751–7755. DOI: doi:10.1002/anie.201302396.

[83]   D. Reiser. "Besetzen und Leeren von Fallenzuständen in Pentacen-Feldeffekttransistoren mittels Photostrommikroskopie."
Masterarbeit. Ludwig-Maximilians-Universität München, 2015.

[84]   M. Darwish, H. Boysan, C. Liewald, B. Nickel, and A. Gagliardi. "A resistor network simulation model for laser-scanning photocurrent microscopy to quantify low conductance regions in organic thin films."
In: *Organic Electronics* 62 (2018), pp. 474 –480. DOI: 10.1016/j.orgel.2018.08.002.

[85]   S. Strohmair. "Photoconductance and Photogeneration of Free Charge Carriers in Epindolidione." Masterarbeit. Ludwig-Maximilians-Universität München, 2017.

[86]   D. Jariwala, S. L. Howell, K.-S. Chen, J. Kang, V. K. Sangwan, S. A. Filippone, R. Turrisi, T. J. Marks, L. J. Lauhon, and M. C. Hersam. "Hybrid, Gate-Tunable, van der Waals p–n Heterojunctions from Pentacene and MoS2."
In: *Nano Lett.* 16.1 (2016), pp. 497–503. ISSN: 1530-6984. DOI: 10.1021/acs.nanolett.5b04141.

[87]   Q. Ren, Q. Xu, H. Xia, X. Luo, F. Zhao, L. Sun, Y. Li, W. Lv, L. Du, Y. Peng, and Z. Zhao. "High performance photoresponsive field-effect transistors based on MoS2/pentacene heterojunction."

In: *Organic Electronics* 51 (2017), pp. 142–148. ISSN: 1566-1199. DOI: https://doi.org/10.1016/j.orgel.2017.07.022.

[88] J. Dong, F. J. Liu, F. Wang, J. W. Wang, M. L. Li, Y. Wen, L. Wang, G. T. Wang, J. He, and C. Jiang. "Configuration-dependent anti-ambipolar van der Waals p-n heterostructures based on pentacene single crystal and MoS2."
In: *Nanoscale* 9.22 (2017), pp. 7519–7525. ISSN: 2040-3364. DOI: 10.1039/c7nr01822c.

[89] X. Liu, J. Gu, K. Ding, D. J. Fan, X. E. Hu, Y. W. Tseng, Y. H. Lee, V. Menon, and S. R. Forrest. "Photoresponse of an Organic Semiconductor/Two-Dimensional Transition Metal Dichalcogenide Heterojunction."
In: *Nano Letters* 17.5 (2017), pp. 3176–3181. ISSN: 1530-6984. DOI: 10.1021/acs.nanolett.7b00695.

[90] T. Zhu, L. Yuan, Y. Zhao, M. Zhou, Y. Wan, J. Mei, and L. Huang. "Highly mobile charge-transfer excitons in two-dimensional WS_2/tetracene heterostructures."
In: *Science Advances* 4.1 (2018). DOI: 10.1126/sciadv.aao3104.

[91] S. J. Noever, M. Eder, F. del Giudice, J. Martin, F. X. Werkmeister, S. Hallwig, S. Fischer, O. Seeck, N.-E. Weber, C. Liewald, F. Keilmann, A. Turchanin, and B. Nickel. "Transferable Organic Semiconductor Nanosheets for Application in Electronic Devices."
In: *Advanced Materials* 29.26 (2017), p. 1606283. DOI: 10.1002/adma.201606283.

[92] M. C. Giordano, S. Mastel, C. Liewald, L. L. Columbo, M. Brambilla, L. Viti, A. Politano, K. Zhang, L. Li, A. G. Davies, E. H. Linfield, R. Hillenbrand, F. Keilmann, G. Scamarcio, and M. S. Vitiello. "Phase-resolved terahertz self-detection near-field microscopy."
In: *Optics express* 26.14 (2018), pp. 18423–18435. DOI: 10.1364/OE.26.018423.

[93] S. Hallwig. "Charakterisierung von Fallendichten in organischen Feldeffekttransistoren mit Photostrommikroskopie." Diplomarbeit. Ludwig-Maximilians-Universität München, 2012.

[94] C. Liewald. "Optoelektronische und strukturelle Eigenschaften von Pentacen-Transistoren." Masterarbeit. Ludwig-Maximilians-Universität München, 2014.

[95] C. Westermeier. "Organic Molecular Semiconductors: Structure and Charge Transport at the Nanoscale." Dissertation. Ludwig-Maximilians-Universität München, 2015.

[96] C. Liewald. "Optimierung und Charakterisierung von Polymer-Zwischenschichten für organische Feldeffekttransistoren." Bachelorarbeit. Ludwig-Maximilians-Universität München, 2011.

[97] M. Göllner. "Double-Gate Pentacene Thin Film Transistors for Biosensing." Dissertation. Ludwig-Maximilians-Universität München, 2011.

[98] A. D. Sanctis, G. F. Jones, N. J. Townsend, M. F. Craciun, and S. Russo. "An integrated and multi-purpose microscope for the characterization of atomically thin optoelectronic devices." In: *Review of Scientific Instruments* 88.5 (2017), p. 055102. DOI: 10.1063/1.4982358.

Bert Nickel, ich danke Dir für die Betreuung meiner Promotion, deine guten Ideen und die ausführlichen Diskussionen, für das angenehme Gruppenklima und auch für die Freiheit, meine eigenen Ideen zu verfolgen zu können.

Fritz Keilmann, mein lieber Bundesbruder, ich danke Dir von ganzem Herzen für unsere Zusammenarbeit. Mit Deinen vielen wissenschaftlichen Kontakten hast du für mich eine neue Welt eröffnet. Die Alptip-Treffen auf der Drehmöser Hütte werden mir ebenso in Erinnerung bleiben, wie deine Zielstrebigkeit bei der Veröffentlichung unserer Ergebnisse.

Joachim Rädler, vielen Dank für die gute Atmosphäre an Deinem Lehrstuhl, besonders auch für die jährliche Winterschule in Antholz mit der perfekten Kombination aus wissenschaftlichen Vorträgen, Diskussionen und Teambuilding durch Langlaufen und Gaudi-Biathlon.

Christian Westermeier, deine Betreuung und Unterstützung während meiner Bachelor- und Masterarbeit war einfach super, ich konnte richtig viel von Dir lernen. Vielen Dank für die Zeit, die du Dir genommen hast, um meine Fragen und Probleme zu lösen.

Vielen Dank an meine Studenten Daniel Reiser, Paul Scheibenbogen, Felix Blanck, Simone Strohmair, Henrik Hecht für die gute und spannende Arbeit in den Laboren und speziell auch Daniel, Simone und Henrik für eure wertvollen Beiträge zu unseren Veröffentlichungen!

Der gesamten Nickel-Gruppe, danke für die tolle Zeit. Simon Noever, Stefan Fischer und Franz Werkmeister, von euch und eurer Generation konnte ich mir so einiges abschauen. Janina Roemer, Philip Böhm und Ida Simson, danke für die gegenseitige Unterstützung und gute Laune in der Gruppe. Martina Ober, danke für die erfrischende Atmosphäre im Büro. Batuhan Kalkan, have a good time doing your PhD here in this group, the photocurrent setup will be in good hands.

Yasin Durmaz, thank you for assembling the new SNOM setup and all the best for your PhD thesis.

Danke an alle Leute vom Lehrstuhl Rädler für die gute Zeit!

Rainer Hillenbrand, vielen Dank für die gute Zusammenarbeit, für dein umfassendes Wissen zur Nahfeldmikroskopie und deine klaren Gedanken.

Stefan Mastel, danke für die gute Zeit und deine Hilfe bei den Experimenten in den Laboren von Neaspec.

Jeffrey Hesler, thank you for your enthusiasm to visit us, and to go back to the lab for conducting experiments together.

Vielen Dank an die neaspec GmbH, speziell an Andreas Huber, Sergiu Amarie, Max Eisele, Adrian Cernescu und Florian Huth, für die gute Zusammenarbeit, die Möglichkeit, in euren Laboren messen zu können und die Unterstüzung meiner Teilnahme an der CLEO2018.

Eric Głowacki, thank you so much for our collaboration on the Epi project, especially for you enthusiasm for science as a young professor.

Susi Kempter und Gerlinde Schwake, vielen, vielen Dank für die tolle Atmosphäre im Büro, euer offenes Ohr, für das Gehirntraining und für die French Press.

Stefan Manus, herzlichen Dank für die erhellenden Einblicke in die Elektrotechnik, die Reparatur unserer kaputten Geräte und für deinen riesigen Fundus, in dem Du zu jeder Fragestellung das passende Messgerät findest.

Philipp Altpeter für das hervorragende Management des Reinraums und die Unterstützung bei der Probenpräparation und Analyse.

Dieter Braun, danke für die goldene Espressomaschine mit selbstgerösteten Bohnen und dem direkten Zugang zum Salinenhof. Ich werde es schmerzlich vermissen!

Meiner Frau Verena, danke für die gemeinsame Zeit, die ich mit dir verbringe und genieße.

Meinen Eltern Heinz und Annemarie, danke für die vielfältige Unterstützung, und meinen Geschwister Judith und Manuel mit der Rasselbande an Nichten und Neffen für die schöne Zeit.

Den guten Freunden, auch Bruderschaft genannt, für die jährlich fixen Events und Treffen in der Heimat, bei denen ich meine Wurzeln nicht vergesse.

Zuletzt noch ein Hoch auf die Musik, die mir eine Ergänzung zur Physik bietet. *6 for Chords*, danke für die coolen Auftritte und Erfahrungen, die wir als Vokalensemble machen, dem Jungen Chor und dem Akademischen Gesangverein München vielen Dank für die abwechslungsreiche Zeit.